August 2020

# Speciation, Transport, and Fate of Heavy Metals in Soils from a Civil War Battlefield: Development of a Novel MAE-GF-AAS Method

Shawn Christopher Salske
*University of Wisconsin-Milwaukee*

# SPECIATION, TRANSPORT, AND FATE OF HEAVY METALS IN SOILS FROM A CIVIL WAR BATTLEFIELD: DEVELOPMENT OF A NOVEL MAE-GF-AAS METHOD

by

Shawn C. Salske

A Thesis Submitted in

Partial Fulfillment of the

Requirements for the Degree of

Master of Science

in Chemistry

at

The University of Wisconsin-Milwaukee

August 2020

ABSTRACT
SPECIATION, TRANSPORT, AND FATE OF HEAVY METALS IN SOILS FROM A CIVIL WAR BATTLEFIELD: DEVELOPMENT OF A NOVEL MAE-GF-AAS METHOD

by
Shawn C. Salske

The University of Wisconsin-Milwaukee, 2020
Under the Supervision of Professor Joseph H. Aldstadt, III

The research herein will describe a novel method to better understand heavy metal contamination over long periods of time by studying soils for which the spatial and temporal dimensions are relatively well-defined. This work is based on the ability to pin-point the initial time and place of contamination on an American Civil War battlefield, where the firearms left distinctive chemical signatures (e.g., dropped and impacted bullets and percussion caps). The abundance and distribution of Copper and Mercury was measured in soil core samples collected at Manassas National Battlefield (Manassas, VA, USA) transecting the line occupied by an infantry regiment, a site where the study could be compared to recent archaeological studies as well as prior studies of Pb at this site.

This study developed, optimized, validated, and applied a novel Microwave-Assisted Extraction (MAE) method based on European Community Bureau of Reference (BCR) methodology for soil samples. Trace (low parts per billion) levels were quantified from soil cores by Graphite Furnace Atomic Absorption Spectroscopy (GF-AAS), supported by isotopic studies using Inductively Coupled Plasma-Mass Spectrometry (ICP-MS) to classify Cu, Hg, and Pb as: (a) mobile, (b) carbonate-bound, (c) metal oxide-bound, (d) organically complexed, and (e) refractory-bound. To optimize

the method, key factors were studied including MAE conditions to improve upon the standard BCR methodology and AAS conditions including the use of a permanent modifier consisting of a mixture of W and Ru.

Significant concentrations of Cu, Pb, and Hg (> 100 parts per billion) were found in the battlefield transect. From this study of the Manassas soil cores, Cu, Pb, and Hg can be reliably quantified, and the depth at which the analytes were quantified coincides with deposition in 1862 where there is a clear correlation between the deposited toxic metals and historical accounts of unit positions. Trends in transport and fate were inferred for the physico-chemical speciation of Cu, Pb, and Hg through the transect of the battlefield revealing that each has a unique transport mechanism controlled by different factors. The Cu and Pb clearly migrated predominantly as metal oxide- and organic-bound species whereas Hg was migrating mainly as an ORG-complexed species that were found primarily in the shallow layers. First-order rate constants for the migration of three Cu species (carbonate-, metal oxide-, and organic-bound) were calculated and compared to those from previous studies with Pb. By utilizing the novel methodology developed in this study, regulatory organizations can more accurately evaluate the risk imposed by contaminated sites on surrounding communities.

TABLE OF CONTENTS

## LIST OF FIGURES

## LIST OF TABLES

## LIST OF ABBREVIATIONS

AAS — Atomic Absorption Spectroscopy

ACW — American Civil War

AFS — Atomic Fluorescence Spectroscopy

BCR — European Union's Community Bureau of Reference

BF — Brawner Farm

CAT — Concentrated Acid Treatment

CO3 — Carbonate fraction in the BCR method

CRC — Collision-Reaction Cell

CRM — Certified Reference Material

DC — Direct Current

ET-AAS — Electrothermal Atomic Absorption Spectroscopy

EU — European Union

EXΔ — Exchangeable fraction in the BCR method

GF — Graphite Furnace

GF-AAS — Graphite Furnace Atomic Absorption Spectroscopy

HCL — Hollow Cathode Lamp

HDPE — High-Density Polyethylene

HDPP — High-Density Polypropylene

ICP — Inductively Coupled Plasma

ICP-MS — Inductively Coupled Mass Spectrometry

i.d. — Inner Diameter

KED — Kinetic Energy Discrimination

MAE — Microwave-Assisted Extraction

MDL — Minimum Detectable Level

MF — Magnetic Field

MOX — Metal Oxide fraction in the BCR method

MS — Mass Spectrometry

m/z — Mass-to-Charge Ratio

n — Number of replicates

NOM — Natural Organic Matter

NPS — National Park Service

ORG — Organic fraction in the BCR method

PMT — Photomultiplier Tube

ppb — Parts Per Billion

ppm — Parts Per Million

PTFE — Polytetrafluoroethylene

QMS — Quadrupole Mass Analyzer

QC — Quality Control

RF — Radio Frequency

RFC — Refractory fraction in the BCR method

RSD — Relative Standard Deviation

S/N — Signal-to-Noise Ratio

SRM — Standard Reference Material

THGA — Transversely Heated Graphite Furnace

TME — Total Metal Extraction

μ — Mean

μ — Cation-Exchange Capacity

w/w — Weight/Weight

18 MΩ-cm — Reagent Water

# ACKNOWLEDGEMENTS

Special thanks to my committee members Dr. J. Aldstadt, Dr. M. Dietz, and Dr. A. Pacheco. I would also like thank my analytical chemistry research group in the UW-Milwaukee Department of Chemistry, 2017 (Fall) – 2020 (Spring) under the supervision and instruction of Dr. J. Aldstadt. I would like to thank Dr. J. Aldstadt for his generous time and energy in helping me put this work together. His foresight in recognizing that I had the potential and ability to achieve this goal and to finish this research project is greatly appreciated. I would also like to thank my family and friends for their support in getting through this project.

# Introduction

## 1.1 Environmental

### 1.1.1 Toxic Metals

Trace metal contaminants in the environment resulting from human activity are of great interest because of their toxicity at low concentrations.[1] Human exposure to these toxic metals is primarily through inhalation or ingestion, but their transport and toxicity is dependent upon the chemical species that is present.[2-4] Additionally, the variability of soils has a significant influence on the mobility and bioavailability of these toxins.[2-4]

Copper (Cu), Lead (Pb), and Mercury (Hg) are of particular concern, with an increased interest in Pb and Hg because of their toxicity.[5] An understanding of the natural and artificial sources, their movement, transformations (in various ecosystems), as well as the entire cycle in the atmosphere, hydrosphere, lithosphere, and biosphere is necessary in the evaluation of the environmental impacts.[6-8] In this section, a review of these factors will be presented for Cu, Pb, and Hg. To assess the transport and fate of toxic metals in the environment, it is a worthwhile endeavor to study the transport of toxic metals to assess risk.

### 1.1.2 Speciation of Toxic Metals

Most studies investigating toxic metals in the environment focused on the total metal concentrations with the assumption that all forms of a given metal have an

environmental impact.[9] Because the environment is a dynamic system, to assess the impact of toxic metals one needs to consider their sources, fate in the environment, mechanism of transport, toxic effect on the environment, and their physical as well as their chemical speciation.[8] The importance of these studies is evident by the number of publications, which also displays that no clear explanation exists, as of yet, in regard to these factors. By studying soils for which the spatial and temporal dimensions are defined, this study addresses some of these questions by developing a model to better understand heavy metal contamination over long periods of time.

Four primary areas of study for environmental metal contamination include: speciation, effects, transport, and fate. Physical and chemical variations in the structure in which metals exist is referred to as "speciation". Physical speciation of Cu, Pb, and Hg include complex associations with organic matter such as with humic acids in soils.[10] The study of toxicology and ecosystem impact is referred to as "effects", whereas geochemical processes controlling the movement of a metal in the environment is commonly referred to as "transport and fate".

Knowledge of the spatial and temporal dimensions is essential to fully understand these four interdependent areas. Typically, these dimensions are not well-defined. The introduction of heavy metals into the environment can be classified temporally, as either *single input* or *continuous input*, and can be classified spatially, as either a *point source* or a *non-point source.* Consider a storage tank containing leaded gasoline that ruptured; this would be described as a *single-input, point source* contamination. On the other hand, for example, a factory discharging pollutants directly into the environment from a discrete source, such as a smokestack or a liquid

pipe which discharges into a river, would be described as *continuous-input, point sources*. A final example is soil polluted by the combustion products of leaded gasoline along a highway, which would be classified as a *continuous input, non-point source*.

The physico-chemical speciation of a heavy metal changes over time, thereby altering its transport efficiency and toxicological effects. Kinetic studies are often complicated by the poorly defined temporal input from the source. Without an initial event it is difficult to establish the time of release, therefore it is not clear *when* the particular physico-chemical forms of a heavy metal were produced, and thus determining the rate at which they have been transported cannot be reliably assessed. Laboratory simulations such as accelerated decay experiments, where heavy metals are added to a sample matrix (soil column), provide some insight into the kinetic dimensions.[11] With these studies, they tend to be poor substitutes for soils that have been genuinely aged over long periods of time.[11] For laboratory-aged soils, Dijkstra *et al*. stated that "…model predictions shown rely strongly on model parameters derived in the laboratory for well-characterized materials, while the conditions met in natural, heterogeneous soils may be very different from these model systems".[12]

Additional studies examining trace metals in soil have used soil cores up to 25 cm, but as a bulk sample, with a limitation of only three sites spread ~500 m apart.[13] A shooting range in Blacksburg, VA was studied as a continuous input source with soil cores ~ 1 m, quantified at 20 cm increments.[5] In Vienna, Austria, soil cores were quantified for total metal and not the speciated forms for Pb and Cd.[14]

### 1.1.3 Why Study the Soil from a Civil War Battle?

The American Civil War (ACW), 1861-1865, was the costliest in US history, with over 600,000 deaths.[15] A typical ACW battle is not ideal for studying Cu, Pb, or Hg contamination of soil as a *single input, point source* area because the typical battle involved extensive maneuvering and dynamic battle positions. However, several battles were atypical in that the forces engaged were stationary and therefore suitable for studying a *single input, point source* of toxic metals.

On August 28, 1862, Confederate forces occupied a strong defensive position near Manassas Junction, VA, which is approximately 25 miles west of Washington, D.C.[16,17] As evening approached, a Federal force approached the Confederate position near the Brawner family's farm and was suddenly attacked (Figure 1).[16]

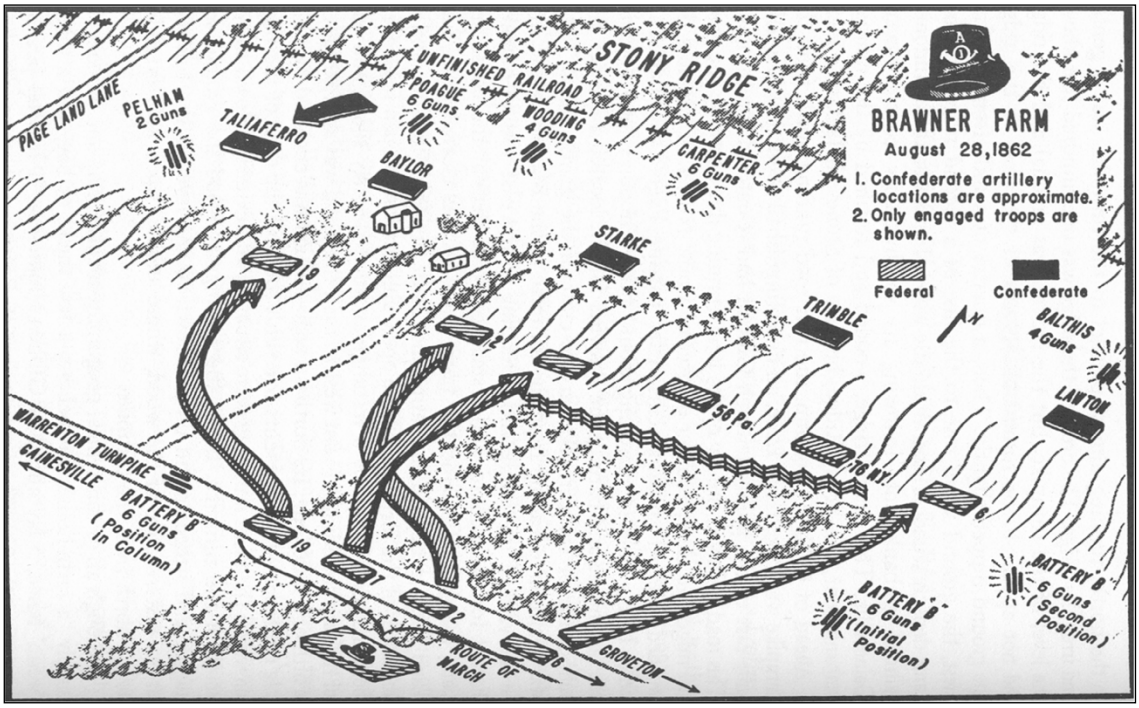

Figure 1. Troop movements and positions at Brawner Farm.[18]

The opposing battle lines stood face to face in one of the "…hardest close quarter fights of the whole war", with roughly 2,100 Federals facing 5,200 Confederate troops "…as if they were on parade awaiting inspection, and volleyed away at the murderous range of less than 100 yards for two solid hours".[16] As darkness drew near, the battle lines withdrew revealing the overwhelming losses, with a casualty rate of ~30% on both sides of the armies.[19]

The Brawner Farm battlefield was selected as an ideal location for this study because: (a) the volume of rifle fire was high (as evidenced by a ~30% casualty rate), (b) the battle lines remained relatively static ($\pm\ 5\ m$), and (c) no additional fighting, cultivation, or development has occurred on the Brawner Farm battlefield since the time of the battle.[20] The ability to pin-point the initial time and place of toxic metal input in the environment is thus achievable for the Battle of Brawner Farm because the battle was well documented, relatively static, and lasted only two hours. The Cu, Pb, and Hg introduced to the Brawner Farm soil created a linear source at a precise time.

### 1.1.4 Chemical Signatures in Brawner Farm Soil

From traditional archaeological methods of collection, objects and debris from the battlefield have been identified.[20] In addition, the firearms also left distinctive chemical signatures. Because of variability in Pb bullet manufacturing, after extended firing of a black powder rifle, a residue accumulates in the barrel and bullets that were too large to fit were commonly discarded.[21] In addition, brass percussion caps were

discarded after each fired bullet. Thus the dropped bullets and spent percussion caps underwent weathering processes in the soil, thereby leaving traces of Cu, Zn, and Hg in their wake.[21]

#### 1.1.4.1 Pb Bullets

There are two primary types of Pb bullets being used today: Pb shot used in shotguns and standard Pb bullets used in rifles and pistols. The composition of Pb shot contains (w/w): 97% Pb, 2% Sb, 0.5% As, 0.5% Ni whereas Pb bullets encased ("jacketed") in a Cu alloy casing contains (w/w) 90% Pb, 9% Cu, and 1% Zn.[5]

During the ACW, Pb was mined and refined on-site and therefore the composition of the bullets was determined by the region of origin. For example, the Number 2 Mine in Balmat, NY, was a source of Pb for the Union army.[22] The ore from this mine contained 0.5%(w/w) Pb in the form of PbS also known as galena, whereas the Confederacy obtained their Pb from the Wytheville mines in Wythe County, VA which contained 0.8% Pb.[23]

#### 1.1.4.2 Percussion Caps

The percussion cap was invented in 1817 by Joseph Egg.[21] It is a single-use ignition device used on muzzle loading firearms. The caps consisted of a brass cylinder with one closed end containing a shock-sensitive explosive material, $Hg(CNO)_2$, which was covered with a protective foil paper (Figure 2).[21] Before this development, firearms

used flintlock ignition system in which a flint-on-steel spark ignited a pan of priming powder to detonate the main powder charge behind the bullet.[21]

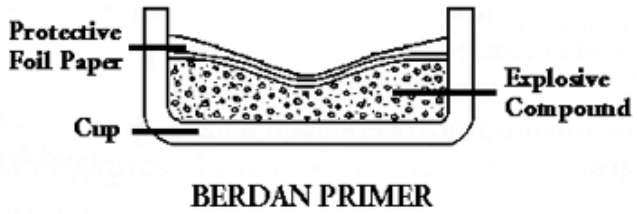


Figure 2. Schematic cross-sectional diagram of a percussion cap.[24]

The percussion cap is a small cylinder made of brass which is an alloy of Cu and Zn (70% Cu, 30% Zn) containing a shock-sensitive "primary" explosive material, Mercury Fulminate, $Hg(CNO)_2$. The explosive is covered with a thin foil to seal and protect it from the elements.[24] Because flintlock firearms are prone to misfire in wet weather, the introduction of the percussion cap enabled reliable firing in any weather condition.[24]

The formation of $Hg(CNO)_2$ involves the dissolution of Hg in nitric acid and the addition of ethanol.[25,26] Firearms incorporated the percussion cap by placing it over a hollow metal "nipple" at the rear end of the gun barrel.[21,24] Pulling the trigger releases a hammer that strikes the percussion cap and ignites the explosive primer (the "primary explosive"), and then the flame travels through the hollow nipple to ignite the main powder charge (the "secondary explosive").[21,24] The undisputed reign of $Hg(CNO)_2$ as a detonator began to be challenged in the 1920s, when effective alternatives began to

emerge which proved to be more efficient, non-corrosive, less toxic, and more stable over time, especially Lead Azide ($PbN_3)_2$) and Lead Styphnate ($C_6H(NO_3)_3Pb(OH)_2$).[21,38]

With effective alternatives being developed, the impact of years of Hg contamination of soils surrounding an abandoned $Hg(CNO)_2$ production plant were investigated.[27] Hg tends to accumulate in the soil surface and is mainly retained by sorption onto organic compounds, which occurs in the pH range from 3 to 5, such that an increase in pH decreased sorption because increases in the dissolved organic matter complexed with Hg.[27] Hg can undergo changes in speciation that are either physiochemically or biologically induced, and therefore result in changes in solubility, toxicity, and bioavailability.[27] The weathering of Hg disposed in soils may redistribute into other chemical forms, thus facilitating its dispersal in the watersheds.[27] This complicates the characterization of these contaminated sites, due to the heterogeneous distribution of Hg in a complex environmental sample.[27]

In this work, contaminated soils at Brawner Farm originating from the single-use brass ignition device and residual Hg from the explosive compound $Hg(CNO)_2$ were investigated.

### 1.1.5 Cu, Pb, and Hg Properties and Speciation

The symbol for Copper (Cu) is derived from the Latin word *cuprum* for "from the island of Cyprus," which was the leading supplier of Cu in the Mediterranean area at the time of the Roman empire.[28] Cu has an atomic number of 29 and is located in Group 11 of the periodic table.[7,28] Metallic Cu is reddish-brown in color; it crystallizes

as a face-centered cubic structure.[7] The most common oxidation states of Cu are +1, cuprous ion, and +2, cupric ion, in most inorganic compounds.[7,28]

The symbol for Lead (Pb) is derived from the Latin word *plumbum*, which arose because of the use of Pb pipes in plumbing in ancient Rome.[28] Pb has atomic number 82 and is located in Group 14 of the periodic table.[7,28] Metallic Pb is bluish-white in color and has a bright luster; it crystallizes as a face-centered cubic structure.[6,7] With four valence electrons, Pb is most commonly found in the +2 oxidation state in most inorganic compounds.[8,7,28]

The symbol for Mercury (Hg) is derived from the Latin name for the metal, *hydrargyrum*, meaning "liquid silver".[28] Hg has an atomic number of 80 and is located in Group 12 of the periodic table.[7,28] Hg is a silver-white metal that is a liquid at room temperature; it crystallizes as a simple trigonal structure.[7] In compounds, Hg is found in the oxidation states of +1, mercurous ion, which is a diatomic ion ($Hg_2^{2+}$) and +2, mercuric ion, which is a monatomic ion ($Hg^{2+}$).[7,28]

Studies have indicated that when Pb bullets come into contact with soil, they can be converted into dissolved and particulate species through oxidation, carbonation, and hydration reactions.[29] These mechanism can be useful to understand the weathering of Cu and Hg as well.[30] According to D.G. Strawn at the University of Idaho, three main processes are involved in determining the fate of metals in soils: (1) sorption of the metals by soil particles, (2) desorption of the metals from soil particles, and (3) precipitation of the metal into the soil matrix.[31]

Soil pH and organic matter influence the distributions of metal in soils and the mobility decreases with increasing pH.[29] At an elevated pH organic matter becomes

soluble and forms dissolved organic carbon-complexes thereby decreasing metal mobility.[29] Soil organic matter can form chemical bonds with metals due to the high surface area and the presence of Lewis bases, for example, such as functional groups that contain amines, carboxyls, and phenols.[31]

A three-step mechanism for the weathering of metallic Pb in soil, suggested by L. Q. Ma at the University of Florida, is shown in Equations 1, 2, and 3.[30] The following reactions, although Pb-specific, can be useful to understand the weathering of Cu and Hg as well. Oxidation, carbonation, and dissolution reactions are in Equations 1, 2, and 3, respectively.

$$2\,\mathrm{Pb(s)} + \mathrm{O_2(g)} \rightarrow 2\,\mathrm{PbO(s)} \quad [1]$$

$$\mathrm{PbO_{(s)}} + \mathrm{H_2CO_{3(aq)}} \rightarrow \mathrm{PbCO_{3(s)}} + \mathrm{H_2O_{(l)}} \quad [2]$$

$$3\,\mathrm{PbO_{(s)}} + 2\,\mathrm{H_2CO_{3(aq)}} \rightarrow \mathrm{Pb_3(CO_3)_2(OH)_{2(s)}} + \mathrm{H_2O_{(l)}} \quad [3]$$

With the use of a sequential extraction scheme, as described below, the forms of Cu, Pb, and Hg can be quantified from the Brawner Farm soil, and the speciation can be determined for genuine soils samples.

### 1.1.6 Sources, Toxicity, and Physiological Impact of Cu, Hg, and Pb

Cu is ubiquitous in the environment and naturally occurs in many food sources such as nuts, meats, and grains. Cu is one of the micronutrients essential to human health, and is incorporated into metalloenzymes that are involved in hemoglobin

formation, carbohydrate metabolism, the cross-linking of collagen, the antioxidant defense mechanism, and several other metabolic processes.[3,7] Cu is commonly found in drinking water (because of Cu plumbing fixtures, and water pipes), soil, and airborne dust. The most common environmental sources are coal-fired power stations, waste incinerators, sewage treatment processes, production and application of agricultural fertilizers, and by factories that make or use Cu or Cu compounds. Naturally-occurring Cu levels in the earth's crust are approximately 50 μg $g^{-1}$ on average.[3,7] Exposure studies suggest that the threshold for gastrointestinal symptoms is between 4 and 6 mg $L^{-1}$ (parts per million or ppm).[32] The US EPA's Office of Water regulates Cu in drinking water at < 1.3 ppm, and the recommended dietary allowance of Cu is 0.9 mg/day or 0.013 mg/kg/day for adults.[3,32,33] Exposure to excessive levels of Cu can result in a number of adverse health effects including liver and kidney damage, anemia, immunotoxicity, and developmental toxicity.[3,32]

Hg is ranked the third most toxic element on the planet after As and Pb.[34] Naturally-occurring Hg levels in the Earth's crust are 0.085 μg $g^{-1}$.[7] The most common source of Hg is coal-burning power plants.[4] Exposure from atmospheric Hg can lead to the human consumption of Hg by settling out of air into water or onto land where it can be washed into water.[4,35] Hg is regulated in drinking water at< 0.002 mg $L^{-1}$.[35] Hg vapor is invisible, odorless, and toxic, and once deposited, certain microorganisms can change it into methylmercury, which is a highly toxic form.[36] Subsequently, Hg can be ingested by smaller creatures and bioaccumulated through the food web, particularly in larger fish.[36] Exposure to Hg in humans is primarily by eating fish and shellfish that have high levels of methylmercury.[36] Common exposure to elemental Hg includes

dental amalgams, thermometers, fossil fuel emissions, incandescent lights, batteries, and incineration of medical waste.[34] Mercury exposure at high levels can harm the brain, heart, kidneys, lungs, and immune system of people of all ages.[34] High levels of methylmercury in a developing fetus as well as children impairs neurological development.[3,34]

Substantial increases in environmental Pb concentrations and the widespread contamination of soils has remained a persistent threat to human health since prior to the Industrial Revolution from sources including non-iron smelters, battery factories, and other industrial plants.[37] Naturally-occurring Pb levels in the Earth's crust are between 10-20 μg $g^{-1}$.[7,29] Anthropogenic Pb deposition in soils is found near the surface, typically at depths between 0-5 cm.[14] Pb exposure in humans is commonly from drinking water and agricultural produce, as well as the ingestion of Pb-based paint. [2,37] The three most common sources of Pb poisoning are deteriorating Pb-based paint, Pb-contaminated dust, and Pb-contaminated residential soil.[2] In a healthy adult, the toxicity of Pb should not exceed 35-45 μg in 100 mL of blood, and this level is lower for pregnant women — not to exceed 20 μg in 100 mL.[8,38] The primary adverse effect of Pb poisoning in humans (more prevalent in children than adults) is the damaging effects to the central nervous system.[8,38]

## 1.2 Analytical

The novel method used for this study was a *linear, single input, point source* deposition of trace metals (Cu, Pb, and Hg) at a known *initial* time of input. Sampling sites transect the battle line which permits the evaluation of horizontal migration patterns including the vertical deposition of metals. To distinguish the non-labile, organically complexed, and free ionic Cu, Pb, and Hg, a sequential extraction method was applied to soil core fractions from the Brawner Farm battlefield. The deterioration of percussion caps and bullets can be identified through isotopic analysis and quantified by atomic absorption spectroscopy (AAS) and mass spectrometry (MS).

### 1.2.1 Sequential Extraction Method

Early studies of trace metals in environmental samples prior to the institution of sequential extraction schemes was predominantly restricted to the determination of total metal concentrations. This approach is simplistic because the environment inherently exists as a dynamic system where the physical and chemical speciation is complex. The implementation of total metal extraction provides insight into the maximum potential amount of contamination but provides little information on environmental mobility or bioavailability.[39] To confront this information gap, sequential extraction schemes were developed in the 1970's to gather more detailed information on the speciation, transport, and fate of trace metals in environmental soils and sediments. The scheme most widely used was introduced by A. Tessier at the University of Quebec in 1979 as a means to study the partitioning of particulate trace

metals in fluvial sediments.[9,40] In Tessier's approach, samples are subjected to a series of extractions thereby releasing the metal from various "compartments".

Tessier's fundamental idea was that the transport and fate of a metal within an environmental solid is dependent upon the type and composition of the solid material in which it resides. Soil for example exhibits a unique complexity of water, organic, as well as inorganic neutrals and ions in the solid, liquid, and gas phases.[41] To further emphasize the complexity of examining metal migration in soil, Tessier classified soil into 12 distinctive orders.[41] Tessier's sequential extraction scheme concentrated on five primary "compartments": exchangeable, carbonate-bound, metal oxide-bound, organic-bound, and refractory-bound.[9] Tessier's method was based upon progressively increasing the strength of the extraction reagent to release the metals from the environmental solids.[40]

Tessier's scheme incorporated five different extraction steps: (1) exchangeable fraction released by using 1.0 M $MgCl_2$, (2) carbonate-bound fraction released with 1.0 M sodium acetate adjusted to pH 5 with acetic acid, (3) Fe-Mn oxide-bound fraction released by using 0.04 M ammonium hydroxide hydrochloride in 25% (v/v) acetic acid, (4) organic matter-bound fraction released by using 0.02 M nitric acid with 30% (v/v) hydrogen peroxide followed by 3.2 M ammonium acetate, and (5) residual or refractory-bound fraction released by HF-$HClO_4$.[9]

Tessier's sequential extraction approach simulates natural and anthropogenic environmental conditions to successively solubilize distinctive mineralogical fractions by the use of selective reagents.[42-44] Nevertheless, criticism of the method includes a lack of uniformity, variable selectivity, and inadequate quality control procedures.[40,42-44]

Interpretation of results from these studies has progressed to be predominantly reagent-specific because of the variety of procedures employed in the speciation studies.[42]

Sequential extraction schemes have characteristic uncertainties, including the concentration and type of extraction reagents, the pH of extraction solutions, temperature, extraction time, centrifuging conditions, mixing procedures, and so forth. The BCR procedure was capable of distinguishing between metals associated with anthropogenic origin and metals of natural geochemical origin, and consisted of: (1) 0.11 M acetic acid, (2) 0.10 M ammonium hydroxide hydrochloric acid at pH 2.0 adjusted with concentrated $HNO_3$, and (3) 30% (v/v) $H_2O_2$ and 1 M ammonium acetate adjusted to pH 2 with concentrated $HNO_3$.[44] The BCR subsequently developed a SRM for lake sediment that was certified for Cd, Cr, Cu, Ni, Pb, and Zn (CRM 601).[40,44-46] Across the EU labs, reproducibility errors were encountered for Ni and Pb.[44] In particular, the difficulties encountered were associated with calibration errors, variety of shaking as well as speed, pH, and the temperature at which the oxidizing agents were added in the organic-bound fraction.[44] A "modified" three-step BCR extraction scheme was then developed as a result of an interlaboratory study, which was conducted to modify and optimize the three-step BCR extraction scheme through examining these factors to establish and correct the sources of error.[43] Results from the interlaboratory study using CRM 601 discovered irreproducibility in Step 2 (Fe-Mn oxide-bound fraction).[43] To address this concern the reagent concentration was increased to 0.50 M $NH_4OH$ in HCl and the pH was adjusted with $HNO_3$.[43]

#### 1.2.1.1 Extraction Using Microwave Energy

A major disadvantage of sequential extraction is that it is a time-consuming process. For example, the BCR procedure involves three periods of overnight shaking. Together with *Aqua Regia* digestion of the residue for determining the refractory-bound metals (Step 5), an entire week is typically required to obtain results from a batch of samples. Thus, there has been considerable interest in developing new approaches that are faster, and microwave technology has provided an opportunity to reduce extraction time as an alternative to conventional BCR procedures.

The use of microwave energy for the extraction of trace metals was first implemented in 1975 by Samara, Morris, and Koirtyohann as an alternative to conventional wet ashing.[47] In wet ashing, a sample is placed in a mixture of $HNO_3$ and $HCLO_4$ and then placed inside an oven and "ashed" (i.e., destruction of organic matter) for a specific time. Progress of the digestion can be followed visually and is terminated when perchloric acid fumes appear (~200 °C).[47] The primary disadvantage of wet ashing is the danger of explosion if the procedures are not strictly followed.[47] To minimize these problems, Samara *et al.* used a commercially available microwave oven. The oven was rated at 600 W with a 1-inch diameter hole drilled through the side of the oven and liner to accommodate a glass exhaust port connected to an evacuation system.[47]

Modern microwave-assisted extraction (MAE) systems are designed specifically for laboratory use with a typical maximum power output of 1200 W at a frequency of 2450 MHz and are designed with a fluoropolymer-coated microwave cavity, a cavity

exhaust fan and tubing to vent fumes, as well as computer control of power, temperature, and pressure.[48] Pressure and temperature are measured by a water manometer and an optical fiber, respectively, that are placed inside the reaction vessel.[48] Reaction vessels are made of Teflon, which is stable up to 210 ºC and a maximum pressure of 350 psi.[48] Reaction vessels (14 total) are made of Teflon, which is stable up to 210 ºC and a maximum pressure of 350 psi.[48] A schematic diagram of the instrument used in this study is shown in Figure 3.

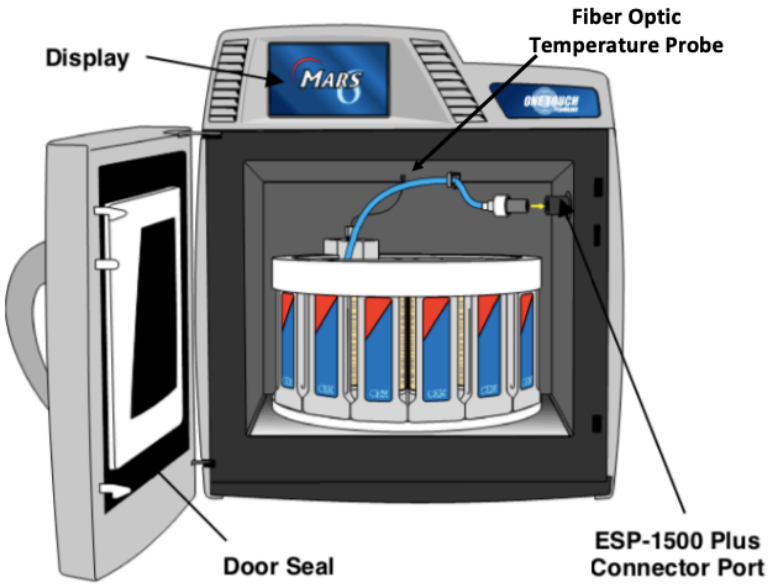


Figure 3. Schematic diagram of CEM Corportation's MARS 5 microwave extractor.[48]

#### 1.2.1.2 Microwave-assisted Extraction Principles

In MAE, radiation is absorbed by the solvent and sample leading to heating by ionic conduction and dipole rotation. Ionic conduction is a result of resistive heating of the solution as ions migrate under a changing electric field. Dipole rotation involves rearrangement of the molecular dipoles under the influence of the oscillating electric

field. Molecular dipoles are unable to realign with the oscillating field and undergo vibrations that create frictional heating. This process allows the heating to be applied in a focused manner towards the matrix of interest which results in desorption of analytes and dissolution in the solvent.[49-51]

The ability of a material to absorb microwaves is a function of its dielectric loss factor, which is related to the efficiency of converting microwave energy into heat and is a function of the permittivity of the material.[50] Polar solvents, such as water and small alcohols, have higher dielectric constants than nonpolar solvents so they will absorb microwave energy with a greater efficiency.[50] In MAE, the microwave irradiation directly heats the absorbing material with minimal reliance on conductive and convective heat transfer.[50] Factors that have been shown to influence microwave assisted extraction include solvent polarity, sample volume, extraction time, power, and temperature.[49-51] MAE procedures simulating the Tessier extraction have been developed for a variety of solids, including lake sediment, river sediment, sewage sludge, and fly ash.[52-55]

There is considerable merit in the development of these rapid approaches to extraction of environmental solids. Because of the complex nature of sequential extraction and sample variability, the development of a microwave-assisted procedure that gives similar performance to BCR-based schemes has been error-prone. This arises because the physical processes involved in MAE are different from those used in conventional Tessier-based BCR schemes, which are predicated on mechanical agitation at room temperature. More probable is the acceptance of standard protocols using the same reagents as the BCR procedures with individualized extraction factors to be optimized for specific sample types.[50]

In this work, optimized methods were developed for the Brawner Farm soil, adjusting the factors that influence extraction, primarily on the basis of replicating certified values from reference materials and subsequently applying the method to real samples. A comparison of the conventional and microwave-assisted BCR extraction procedures is shown in Figure 4 utilizing the same reagents, although extraction times are 20 min with MAE and 24 hrs. with conventional agitation. Whether MAE can provide accurate results in a more practical time frame was investigated.

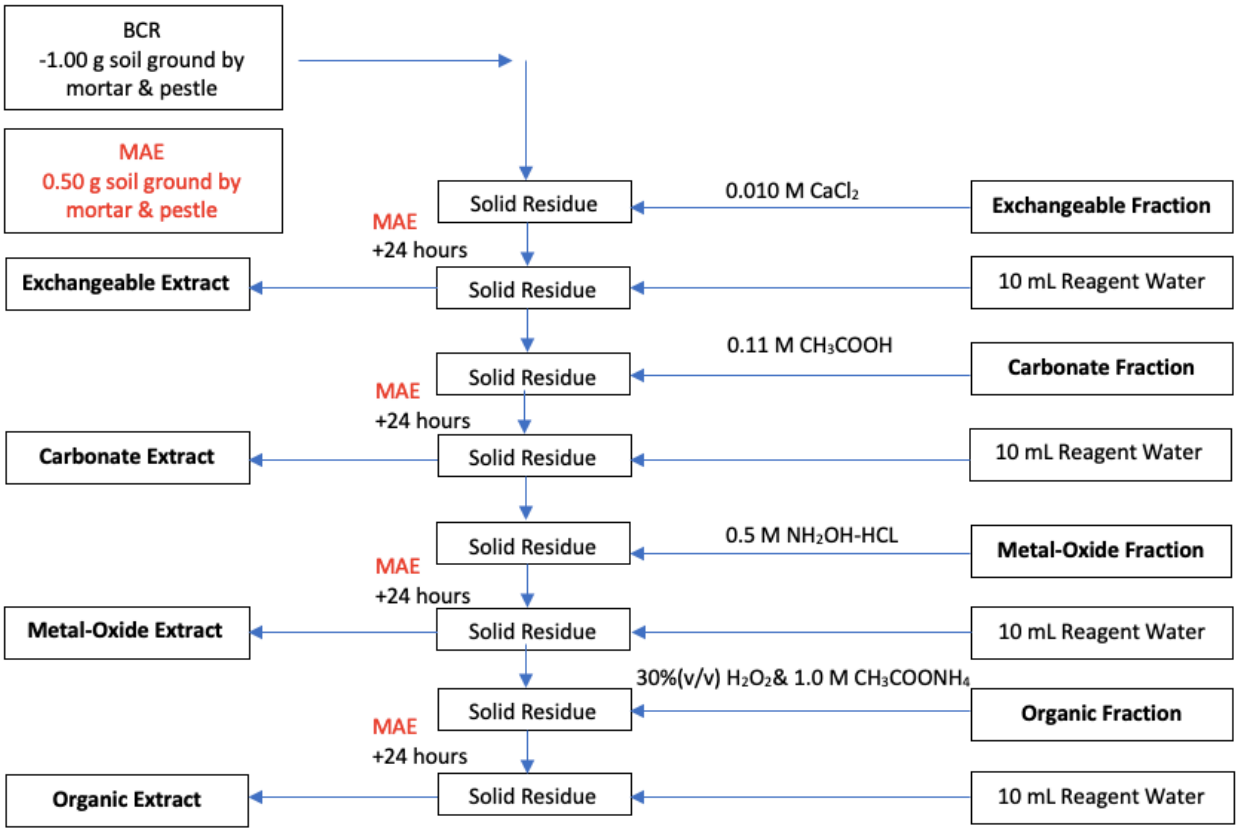


Figure 4. Comparison of the conventional and microwave-assisted BCR extraction procedures.

### 1.2.2 Quantification of Cu, Pb, and Hg

#### 1.2.2.1 Graphite Furnace Atomic Absorption Spectroscopy (GF-AAS)

Quantification for the speciation studies in this work was accomplished by Electrothermal Atomic Absorption Spectroscopy (ET-AAS), which is also known commonly as Graphite Furnace AAS (GF-AAS). The fundamental concept of GF-AAS is an electrically heated furnace which dissociates metal compounds into free gaseous atoms.[56] The heated furnace is based on the "King furnace", which was first described by A.S. King in 1908 consisting of a graphite tube heated to 3,000˚C in an evacuated chamber.[57] The prototype electrically-heated graphite tube placed in a chamber of an inert gas was referred to as the graphite furnace (GF), introduced in 1961 by B.V. L'vov.[58-60] In 1968, H. Massman engineered a simpler GF with a temperature gradient program that became the foundation for modern GFs.[59-62] Massman's design permitted higher heating rates and consequently increased sensitivity to the picogram range.[60,61]

The initial designs of the Massman furnace were restricted to the sample being deposited on the wall of the graphite furnace.[62] The mechanism that drives the metal from the surface of the wall into the gas phase is reliant upon the analyte reaching the temperature of vaporization.[61] Vaporization from the wall of the GF into the gas phase is predominantly matrix dependent, and consequently the temperature will vary depending upon the constituents of the matrix, which typically results in interferences.[58,61,63] To address these interferences, L'vov developed a GF which contained a suspended platform for the sample aliquot.[56,59] The platform had minimal contact with the furnace wall so that it was primarily heated by radiation from the

furnace tube.[56,62] With this modification, the temperature achieved by the platform was delayed relative to the temperature inside the GF such that the analyte was atomized at a higher constant temperature. This allowed for a more efficient decomposition of molecules, therefore causes reduction in the vapor-phase interferences.[59]

In comparison to Flame AA, GF-AAS has an improved sensitivity of ~4-5 orders of magnitude, resulting in ~2-3 orders improvement in the detection limit.[56,64,65] These improvements are rationalized by the fact that in GF-AAS, a discrete sample volume is vaporized, and the entire sample is atomized through pulsed heating, thereby creating a higher concentration of atoms for detection.[56,65] Nevertheless, the effects of condensation may still be problematic in GF-AAS. Condensation was addressed by the introduction of a transversely heated furnace (THA).[56,66] The electrodes in THA are positioned to contact the sides of the furnace rather than the ends, which delivers a more uniform temperature gradient.[67] The main advantage of the THA design is its high sensitivity and decreased sample volume requirement.[64] The sample volumes are typically 10-20 μL and the sensitivity is in the low ng $g^{-1}$ range, comparable to Inductively Coupled Mass Spectrometry (ICP-MS). The general mechanism for the chemical and physical processes which result in the formation of gaseous, neutral atoms is shown in Equation 4.[65]

$$\text{Metal Compound (aq)} \rightarrow \text{Metal Salt (s)} \rightarrow \text{Metal Oxide (s)} \rightarrow \text{Metal (s)} \rightarrow \text{Metal (g)} \qquad [4]$$

This mechanism starts with elimination of the solvent from the aqueous sample. A ~10-20 µL sample is injected onto the L'vov platform, which is typically ~25-30 mm in length and ~5-7 mm in diameter. The mechanism (Equation 4) is predicated on the changes caused by the stepwise temperature gradient. Following the evaporation of the solvent to form the salt, the oxidative atmosphere creates the Oxide which is then decomposed to the elemental form. When the temperature reaches the metal's vaporization point, the free, gaseous, neutral analyte is homogeneously desorbed as a gas from the surface of the furnace into the light path of the HCL The absorption signal acquired during the last step in the mechanism is the time-based variation in the atom population which produces the transient signal to yield a plot of absorbance versus time.[56,65] GF-AAS is one of the recommended methodologies which the USEPA approves for the determination of trace metals in a variety of environmental samples, including As, Se, Cd, Cu, Pb, Tl, Sb, Ag, Be, and Cr.[68]

However, there are inherent challenges in GF-AAS because the reactions shown in Equation 4 do not completely reach equilibrium.[64] The atomic population responsible for absorption must be representative of the original sample.[64] A sample vaporized from a complex mixture produces a small signal relative to potentially interfering matrix species, so the high background noise must be minimized.[56,64,65] Despite these difficulties in GF-AAS, careful optimization of the method conditions can still produce reliable and consistent results, as will be shown in this study.

#### 1.2.2.2 Inductively Coupled Plasma-Mass Spectrometry

Inductively Coupled Plasma-Mass Spectrometry (ICP-MS) is a multi-element atomic technique preferred for trace metal analysis because of its low detection limits (pg $g^{-1}$), high sensitivities, and quantitative multi-element (isotopic) capabilities.[69,70] The ICP-MS process can be broken down into six stages: (1) sample introduction by nebulization, (2) ICP torch atomization and ionization, (3) interface to the MS, (4) transport through ion lenses, (5) separation of ions according to their mass-to-charge (m/z) ratios, and (6) and ion detection.[69,70]

##### 1.2.2.2.1 Sample Introduction

ICP-MS samples are typically, but not limited to, the liquid form.[71] Liquid samples are typically introduced by a peristaltic pump, nebulizer, and spray chamber or as a solid particulate aerosol generated electrothermally or by laser ablation.[69-71] For liquids, the nebulizer converts the sample into a fine aerosol mist in an enclosed spray chamber, using a stream of Ar gas for efficient ionization for introduction to the ICP.[69-71] The aerosol flows through the central injector tube of the ICP torch, shown in Figure 5 and Figure 6.[69-71]

##### 1.2.2.2.2 ICP Torch Atomization and Ionization

The ICP is a highly ionized gas generated by the interaction of a strong electromagnetic field with Ar gas flowing through a quartz glass torch.[69-71] The electromagnetic field is generated by 40 MHz radio frequency (RF) energy transmitted

from a Cu induction coil that encircles the open end of the torch, as shown in Figure 5.[69,70,72] When a high voltage spark is applied by a Tesla coil, the Ar gas is ionized. The spark introduces electrons ($e^-$) into the Ar gas stream, $e^-$ are accelerated by the changing magnetic field (MF) at high RF, $e^-$ collide with Ar atoms causing the release of an $e^-$ and the formation of Ar ion ($Ar^+$), the $e^-$ is further accelerated by the MF. This process continues as the release rate of $e^-$ from collisions is balanced by rate of recombination ($Ar^+ + e^-$), forming a high temperature (~6000-10,000° K) plasma that becomes self-sustaining.[69,70,72] The ICP torch consists of three concentric tubes through which high-purity Ar flows at different rates.[69,70] The outermost tube (Main Plasma Gas: Ar flow ~15 L $min^{-1}$) provides most of the plasma-forming Ar and prevents direct contact of the plasma with the torch walls.[69,70,72] The medial tube (Auxiliary Gas: Ar flow ~ 0.75 L $min^{-1}$) controls the spacing of the plasma relative to the open end of the torch.[69,70,72] The central tube (Nebulizer Gas: Ar flow ~ 1 L $min^{-1}$) transfers the sample aerosol from the spray chamber into the central region of the plasma (6500°K), where it is rapidly (~2 ms) dried, dissociated, and atomized, thereby effectively destroying molecular species and generating positive ions, as depicted in Figure 5 and Figure 6.[69,70,72]

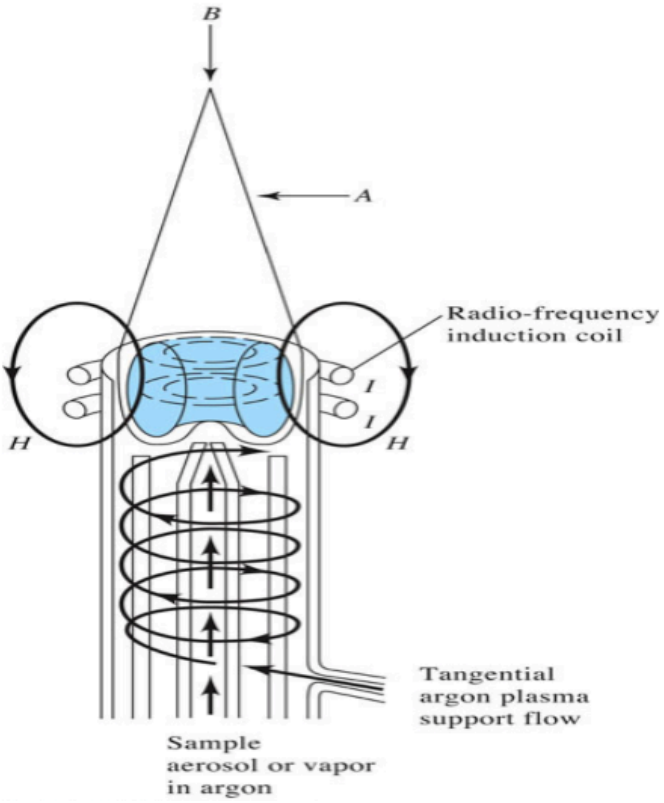


Figure 5. ICP torch schematic (Skoog, Holler, and Crouch 2007).[71]

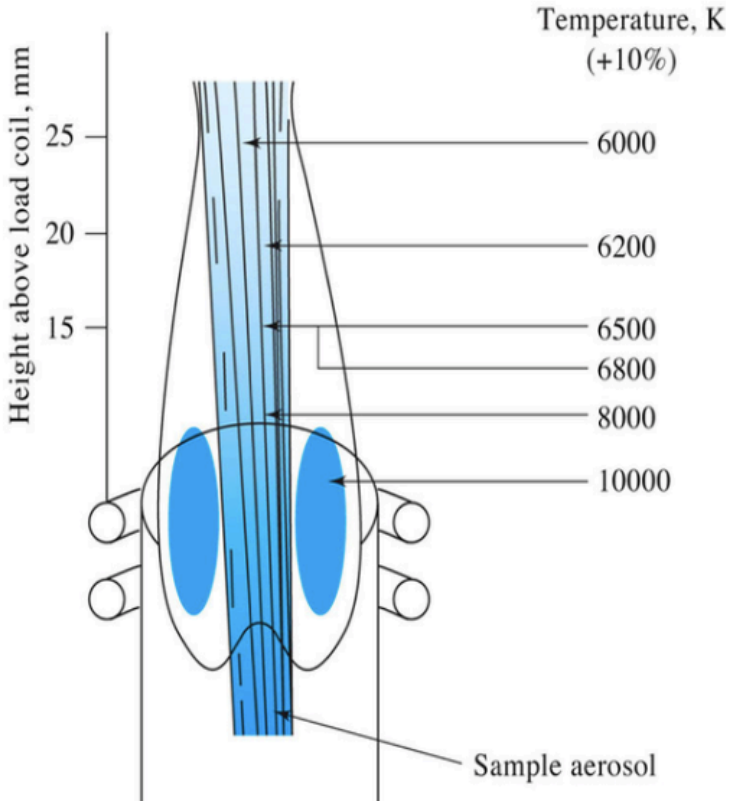


Figure 6. ICP torch temperature schematic (Skoog, Holler, and Crouch 2007).[71]

#### 1.2.2.2.3 MS Interface Region

The sample ions created by the ICP pass through the torch-MS interface region through two conical disks ("cones"), typically made of Ni or Pt where the gas begins to cool.[69,70,72] Each cone contains a small central orifice; the outer "sampler" cone orifice is ~2.5 times the size of the inner skimmer cone (~1mm).[72] The interface region is under vacuum, and the pressure is reduced from atmospheric pressure in the ICP to ~2 Torr in the interface region. The incoming ion beam will thus dramatically expand beyond the sampler cone such that the skimmer cone collects an ion distribution that is representative of the central, analyte-rich portion of the plasma.[69,70,72] The interface vacuum also serves to remove most of the neutral Ar atoms.[70]

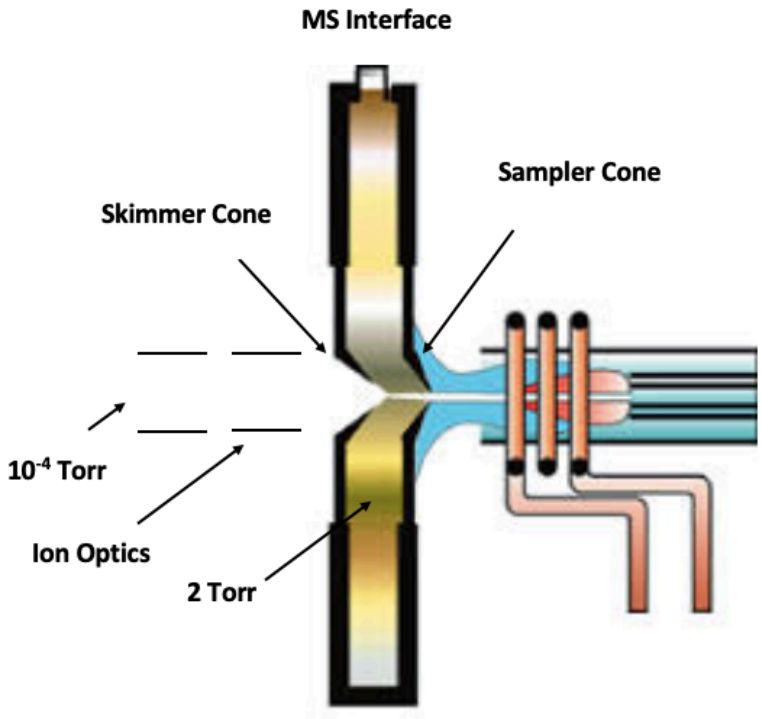


Figure 7. MS ICP torch interface region.[70,72]

#### 1.2.2.2.4 Ion Lens Optics

The narrow ion beam emerging from the skimmer cone is then directed by a sequence of "ion lenses", which consist of several positively charged plates (typically stainless steel).[70,72] A second vacuum stage using turbomolecular pumps further reduces the pressure to $10^{-4}$ Torr in ion lens region Figure 7.[69,70,72] The ion lenses have two primary purposes: (1) separation of positively charged ions from undesired neutral species and photons emitted by the ICP, and (2) further focusing and narrowing of the ion beam for introduction to the mass analyzer.[74] The composition of the ion beam is ideally only analyte cations in this low vacuum environment — neutral species should have been pumped away within the torch-MS interface, whereas negatively charged species are lost to the ion lenses.[74] In most modern designs, the resulting positively charged ion beam then passes through the collision-reaction cell (CRC) which removes polyatomic interferences by using a non-reactive gas (helium) and a process called kinetic energy discrimination (KED).[70,72] KED exploits the fact that all polyatomic ions are larger than analyte ions of the same mass. KED creates a potential energy barrier at the CRC exit using ion lenses. Because the exit of the CRC is more positive than the entrance, this slightly repels ions back into the cell. As the sample ions pass through the CRC, they encounter neutral helium atoms and collide emerging with lower kinetic energy. The potential energy barrier prevents them from leaving the cell, therefore they are excluded from the ion beam and ejected from the cell.[70,72] Finally, the ion beam enters the quadrupole mass analyzer.[70,72] An additional turbomolecular pump is used to

achieve a further pressure reductions of $10^{-6}$ Torr in the mass analyzer region to create a collision-free path to the detector.[70,72]

#### 1.2.2.2.5 Ion Detection

Most ICP-MS instruments use a quadrupole mass analyzer (QMS) because the mass resolution is sufficient for most applications. The QMS filters non-analyte, matrix, and interfering ions in general, allowing only desired analyte ions consisting of a single mass-to-charge ratio (m/z) sequentially transmitted to the ion detector.[71] A QMS consists of four parallel conductive rods made of gold-coated ceramic or molybdenum.[72] RF and direct current (DC) potentials are applied to each set of opposing rods as a means to produce an electrostatic field between the rods, as shown in Figure 8.[74] The electrostatic field controls the trajectories of ions entering the quadrupole based upon their inertial mass and charge.[74] The trajectories can be optimized to allow only analyte ions of a specific m/z to pass to the detector.[70] By changing the applied RF/DC voltages, the quadrupole can either scan the entire m/z range or “jump” selectively from target m/z to target m/z to measure elemental ion abundances.[70]

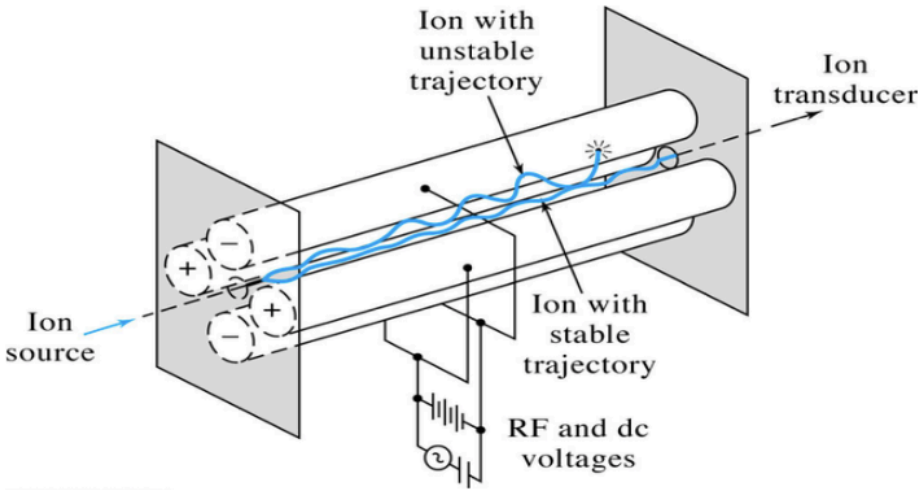


Figure 8. Schematic diagram of a quadrupole mass analyzer.[71]

The ion detector is an electron multiplier that receives and amplifies the ion signal. Electron multipliers consist of a series of dynodes which emit electrons when their surface is struck by analyte ions.[69,70,72] For example, positive ions are attracted to the first negative dynode of the detector, and upon impact, emit secondary electrons from the dynode surface.[70,72] The electrons are then attracted to the positively charged second dynode, where more electrons are emitted upon impact.[70,72] The electron emission process continues in this manner throughout the entire cascade of individual dynodes (usually 12-24), resulting in an amplified signal.[70,72] The ion detector has a linear range from pg $g^{-1}$ to 100's of µg $g^{-1}$ for a single multi-element analysis.[74] A schematic diagram of the instrument is shown in Figure 19 (Section 2.8).

The primary objective of this study was to develop a robust model for the transport of heavy metals in soil by application of a novel MAE-GF-AAS method. By utilizing this study, regulatory organizations could more accurately evaluate the risk imposed by contaminated sites on surrounding communities in the future.

## 1.3 Thesis

The objective of this study was to develop a novel MAE-GF-AAS method to study the abundance, distribution, speciation, and mobility of several heavy metals in soil from a well-defined input source. In the following, Cu, Pb, and Hg in soil at Brawner Farm are investigated, and transport rates for several different types of Cu species are estimated. The EU's BCR sequential extraction procedure was applied to the fractionated core samples by developing an optimized MAE method. Cu, Pb, and Hg at low parts per billion (ng $g^{-1}$) levels was determined primarily by GF-AAS and ICP-MS. In previous studies, core samples had been dated radiometrically by using the $^{210}Pb$ method, and geochemical characterization of the cores (soil type, cation-exchange capacity, pH, etc.) was also made to better understand the soil conditions under which Cu, Pb, and Hg was transformed and transported.[73,74]

# Chapter 2 Experimental

## 2.1 Reagents

Chemical reagents used in this work were of Trace Metal grade or higher for all acids, and all other reagents were ACS grade or higher (Sigma-Aldrich, St. Louis, MO). Reagent water (18 MΩ-cm) was prepared using a Milli-Q Gradient water purification system from deionized water. All glassware and plasticware was washed with Citranox detergent (Alconox, New York, NY) and soaked in 5% (v/v) nitric acid for a minimum of 48 hours, followed by copious rinsing with reagent water. All open containers were either inverted and covered with Parafilm or filled with reagent water and capped for storage.

### 2.1.1 Reagents for Sequential Extraction Studies

#### 2.1.1.1 Standard Solutions for Graphite Furnace Atomic Absorption Spectroscopy (GF-AAS)

Stock standard solutions in this work were prepared from aqueous 1000 mg $L^{-1}$ standard solutions of Cu and Pb (Sigma-Aldrich). A 1000 µg $L^{-1}$ Cu standard solution was prepared by dilution of a 1000 mg $L^{-1}$ Cu standard in a 1000 mL glass volumetric flask, diluted to the mark with 1% (v/v) nitric acid (Sigma Aldrich), followed by transferring to a 1000 mL high-density polyethylene (HDPE) bottle and stored at room temperature. A 100 µg $L^{-1}$ Cu solution was prepared daily by dilution of the 1000 µg $L^{-1}$ Cu standard solution.

#### 2.1.1.2 Exchangeable Fraction – Mobile

The first extraction step, the "exchangeable" fraction (hereafter denoted EXΔ), required aqueous 0.010 M calcium chloride dihydrate (Sigma-Aldrich), which was stored at room temperature indefinitely in glass. The standard solutions used for instrument calibrations were prepared on the day of use by dilution of the stock standards using 0.010 M calcium chloride dihydrate as the diluent.

#### 2.1.1.3 Acid-Soluble Fraction – Carbonate-bound

The second extraction step, the "carbonate-bound" fraction, (hereafter denoted CO3), required aqueous 0.11 M acetic acid prepared from glacial acetic acid (Sigma-Aldrich). This was also stored at room temperature indefinitely in a HDPE container. The standard solutions used for instrument calibrations were prepared on the day of use by dilution of the stock standards using 0.11 M acetic acid as the diluent.

#### 2.1.1.4 Acid-Reducible Fraction – Oxides-bound

The third extraction step, the "oxides-bound" fraction (hereafter denoted MOX), required aqueous 0.50 M hydroxylamine hydrochloride, and 1.0 M nitric acid (Sigma-Aldrich). This was prepared on the day of use from reagent hydroxylamine hydrochloride (Sigma-Aldrich) and stored at room temperature in glass. The standard solutions used for instrument calibrations were also prepared on the day of use by

dilution of the stock standards using 0.50 M hydroxylamine hydrochloride as the diluent.

#### 2.1.1.5 Oxidizable Fraction – Oxide-bound

The fourth extraction step, the "organic-bound" fraction (hereafter denoted ORG), required two extraction solutions. First, the soil sample was exposed to aqueous 30% (v/v) hydrogen peroxide (Sigma-Aldrich) which was stored in the manufacture's plastic bottle at room temperature. This was followed by 1.0 M ammonium acetate with pH adjusted to 2.0 ± 0.1 with concentrated nitric acid (Sigma-Aldrich). This was stored at room temperature indefinitely in glass. The standard solutions used for instrument calibrations were prepared on the day of use by dilution of the stock standards using 1.0 M ammonium acetate as the diluent.

### 2.1.2 Chemical Modifiers

Two chemical modifiers were used to improve the lifetime and performance of the graphite furnace. The "conventional" chemical modifier, which was added to each sample, was 100 mM ammonium nitrate (Sigma-Aldrich), prepared from reagent ammonium nitrate in 1% nitric acid (Sigma-Aldrich), which could be stored indefinitely at room temperature in HDPE bottle. The "permanent" chemical modifier, which was added directly to the graphite furnace, was a 1:1 mixture of a 500 mg $kg^{-1}$ solution of Ruthenium and Tungsten (Sigma Aldrich). Ruthenium was prepared from ammonium hexachlororhodate(III), and tungsten was prepared from sodium tungstate dihydrate;

both solutions were made up separately in 2% (v/v) nitric acid. The metal salts (50.0 mg each) were dissolved in a 10.0 mL volumetric flask and diluted to volume, followed by transferring 1.0 mL of each into a second 10.0 mL volumetric flask and diluting to volume. This mixture was prepared on the day of use and stored at room temperature in a HDPE bottle. These solutions needed to be prepared on the day of use for two reasons. First, the solution of sodium tungstate dihydrate formed a yellow precipitate after standing overnight, and second, the solution of ammonium hexachlororhodate(III) in 2% (v/v) nitric acid, would stay suspended for several hours and after standing overnight, would settle out of solution.

### 2.1.3 Standard Solutions for Inductively Coupled Plasma-Mass Spectrometry (ICP-MS)

The standard solutions used for instrument calibrations were prepared on the day of use by dilution of the stock standards. Certified atomic absorption standards for Au, Cu, Hg, In, Pb, and W obtained from Sigma Aldrich (Milwaukee, WI, USA) were prepared in the same manner as the GF-AAS standards.

## 2.2 Sample Collection and Treatment

### 2.2.1 Soil Core Sampling

In 2004 and 2007, soil cores were taken at the Brawner Farm battlefield in Prince William County, Virginia, by J. Aldstadt (a total of four separate trips). Map of

troop movements and unit positions at the Brawner Farm are shown in Figure 9. Sample collection followed a straight line that included the relatively flat area (ridge) where the primary infantry fighting occurred, followed by sampling down the subsequent slope of the hill, as a means to determine the degree of horizontal and vertical migration in that direction. Specifically, core samples were chosen that transected the battle-line starting at ~25 yards north of the battle-line and continued in a straight line southward for ~125 yards.

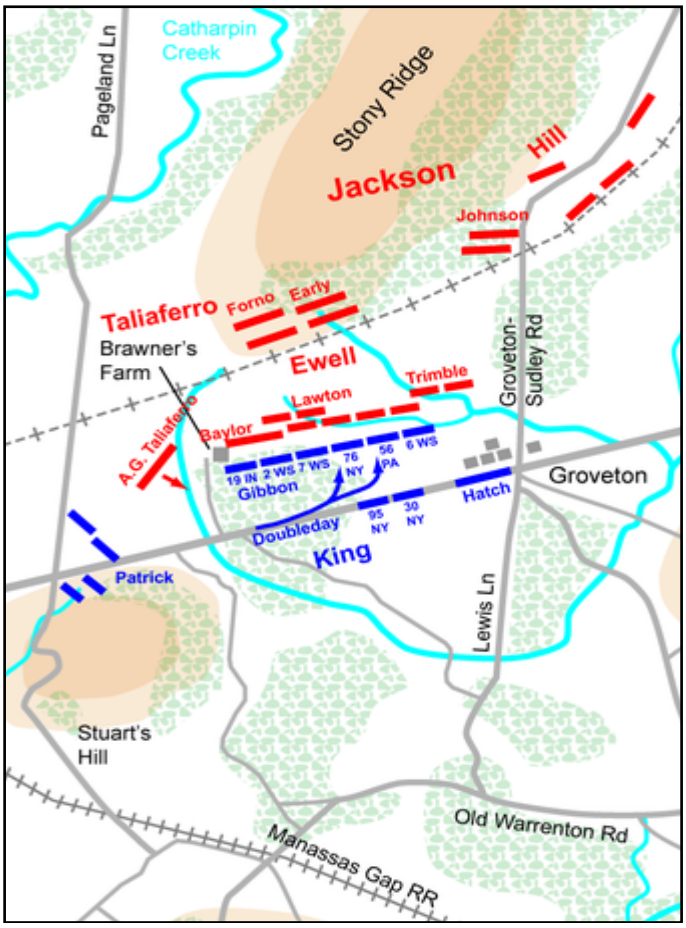


Figure 9. Unit positions at Brawner Farm. Map of troop movements at the Brawner Farm on the evening of August 28, 1862. Drawn by H. Jespersen. Graphic source file is available at http://www.posix.com/CWmaps/

The sampling line was located ~46 yards east the National Park Service (NPS) building which was built upon the original foundation of the Brawner family's farmhouse. To describe the terrain, when looking south of the conifer trees, the terrain starts to slope steeply and then gradually levels off approaching the Lee Highway (Warrenton Pike) which is located ~700 yards from the ridge. Looking south toward the Warrenton Turnpike, the sampling (transect) line is shown in Figure 10.

Figure 10. This is a photograph of the sampling area, and the view is looking south along the sampling line (orange flags); the nearest flag is sampling site #10. Yew trees can be seen at center-left, informational plaques at center-right, and the Warrenton Turnpike is visible in the distance. Photograph was taken by J. Aldstadt, August 2004.

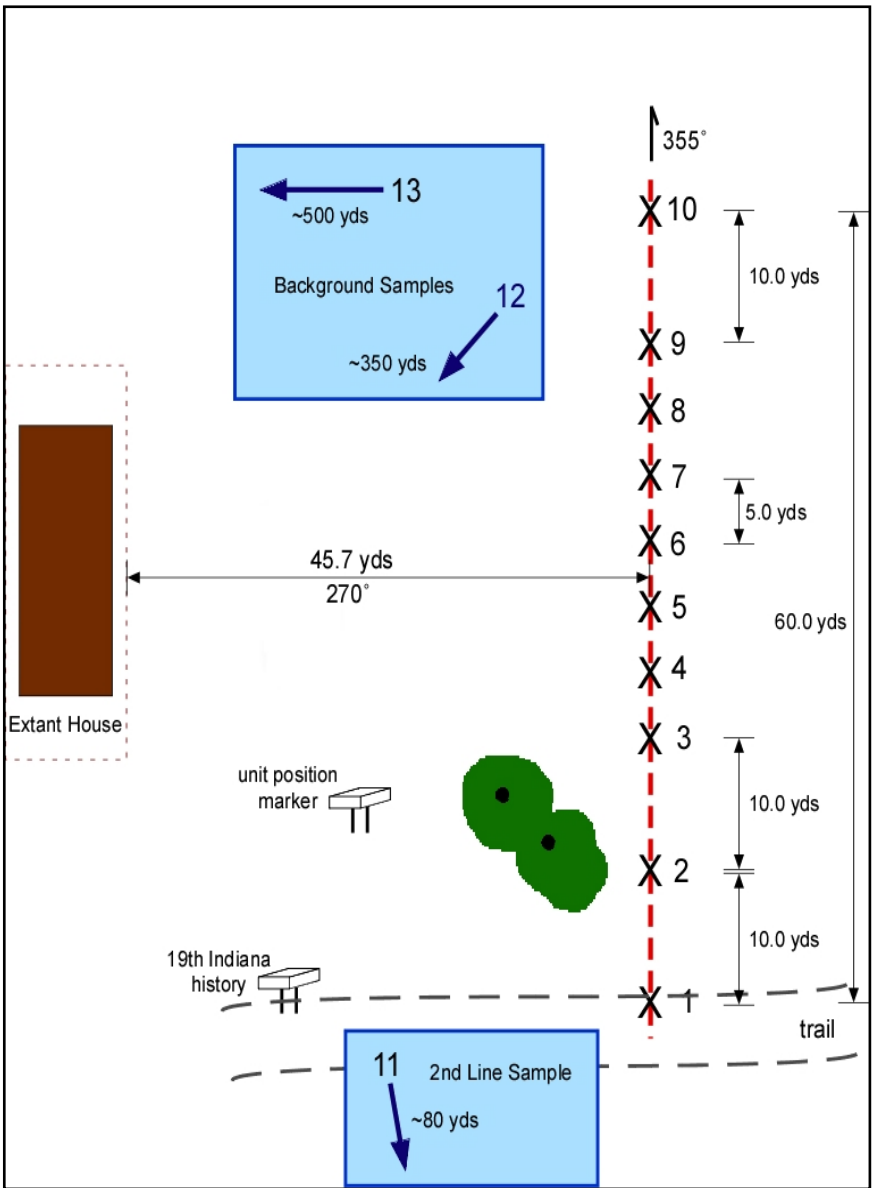


Figure 11. This is a map of the locations at which the core samples were collected, the sampling area shown transects where the heaviest fighting took place. Continuing south sampling sites 12-24 were taken at 10-yard intervals.

The locations at which the core samples were collected is shown Figure 11; note that the sampling area transects where the heaviest fighting took place. A stainless-steel soil coring device (Forestry Suppliers, Jackson, MS) with the use of a polycarbonate liner with a 1.6 cm inner diameter (i.d.) was inserted into the device and used to collect soil cores. To prevent shifting of the soil specimen during transport,

tissue paper (i.e., Kim-Wipes™) was inserted into the portion of the tube that did not contain soil. An orange cap was used to designate the top of the soil column and a blue cap to distinguish the bottom of the core. Both ends were sealed with Para-Film™ and stored at room temperature, as shown in Figure 13. The soil cores were placed horizontally during storage to prevent vertical migration of the material within the soil column. Depending on the hardness of the soil, cores were collected to a depth of 12″ where possible. Labeling of the cores started with the year, followed by the core location number, and ending with a capital letter (e.g., “A”) to denote replicate samples.

Figure 12. A photograph of the sampling area (the view is looking west toward the reconstructed Brawner house, perpendicular to the sampling line). The informational plaques can be seen at center-left and yew trees to the right. Photograph was taken by E. Christensen, June 2008.


Figure 13. A Photograph of a typical soil core sample. An orange cap was used to designate the top of the soil column and a blue cap to distinguish the bottom of the core. Photograph was taken by T. Grundl, September 2007.

### 2.2.2 Soil Core Fractionation

In preparation for subsequent extraction procedures, soil cores from the battlefield were fractionated. Soil cores were measured, and depending on the depth of the core, a 5" polystyrene weigh boat was, starting at 0-1 and continuing (1-2, 2-3, 3-4, etc.) to designate 1.0-inch sub-sections of the core, until the total depth was reached. A small 3" grove was cut and removed from one side of each weigh boat to allow for easy transfer of material. All tools used in fractionating the cores were plastic to avoid contamination by metals. Using tweezers, the parafilm, orange cap, and tissue paper were removed. Holding the core tube horizontally over the last 1.0-inch weigh boat, the blue cap was removed as a means to collect soil the soil that inadvertently spilled from the end of the tube. Next, using a rubber stopper attached to a 0.5˝

diameter plastic rod, the soil core was gently pushed within the tube towards the top edge. Before pushing the soil out of the tube, the designated polystyrene weigh boat was placed below the tube, and using a permanent marker, 1-inch fractions were marked on the outside of the tube. Then the first 1˝ fraction of the core was exposed, and using a plastic knife, the core was gently sawed until it fractured, thus collecting it in the weigh boat. This procedure was continued, using a new weigh boat and knife for each fraction, until the entire length of the soil core sample was fractionated.

After fractioning, each sub-sample was further ground with a porcelain mortar and pestle. All objects that were unable to be ground (e.g., stone, metal, etc.) were separated and saved, while all organic matter (e.g., grass, roots, etc.) were separated and discarded. Any remaining soil material from the mortar and pestle was transferred into the weigh boat using a Kim-Wipe™. After each sub-sample the mortar and pestle was washed vigorously in hot soapy water using Citranox detergent (Alconox, New York, NY) with a stiff brush; grinding a few grams of “clean” sand (Sigma Aldrich), and rinsing copiously with hot tap water, followed by copious rinsing with reagent water and drying thoroughly with clean Kim-Wipes™. The National Park Service (NPS) expressly noted that any human remains (e.g., bone fragments, teeth, etc.) found needed to be returned; none such material was found. The sub-samples were then poured into a polyethylene Zip-Loc™ bag and sealed tightly and stored at room temperature. Labeling bags began with the initials for Brawner Farm (BF), followed by the two-digit year when the sample was taken, one- or two-digit sample core location and replicate letter. Followed by sub-sample identification, ending with the two-digit

day, abbreviated month, and two-digit year that fractionation took place. An example is as follows:

BF07-21A 3-4″ 28-FEB-19

That is, this core was sampled at Brawner Farm in 2007 at site #21. It was the first replicate sample that was collected, the sub-sample was between 3.0 and 4.0 inches (±0.25 inches) and was fractionated on February 28, 2019.

## 2.3 Extraction Methods

### 2.3.1 Sequential Extraction – Conventional BCR Method

All fractionated sub-samples were subjected to a modified sequential extraction procedure that was developed by the Standards, Measurements, and Testing Program of the European Union (EU), formerly named the Community Bureau of Reference of the European Commission (BCR).[44] The basic theory of sequential extraction is to apply a series of chemical extractants to a given sample. Each extract dissolves different components within the sample, thereby releasing the metals.[1] In this way, a series of well-defined extracts can be studied. Minor changes that were applied are specified below in the descriptions of each step in the BCR method.

#### 2.3.1.1 Sample Preparation

For each core, the pulverized soil sub-samples were placed into a weigh boat and dried at ~110°C for 1 hr, then 1.000 ± 0.001 g was weighed for each fraction and transferred to a 50 mL HDPE centrifuge tube (commonly referred to as "Falcon" tubes,

manufactured by Becton-Dickinson). Any remaining sample was returned to the respective storage bag. Following the same procedure for drying and weighing, a blank sand “uncontaminated” sample (Sigma Aldrich) was also prepared and exposed through each step in the BCR method.

#### 2.3.1.2 BCR Step One: The Exchangeable Fraction

The first extract, 40.0 ± 0.5 mL of 0.010 M Calcium Chloride extraction solution, (prepared as described in Section 2.1.1.2) was added to 1.000 ± 0.001 g of soil. To ensure complete dissolution of the soil sample, the Falcon tube was inverted ~10x followed by vortexing for ~1 min. Then the sample was placed in a rotary shaker for at a minimum of 16 hr at room temperature at a rate of ~40 cycles per min. The extract was separated from the solid material by centrifugation at 3000 g for 20 min, followed by decanting the supernatant liquid into a labeled 125 mL PE bottle and stored at 4°C until analysis.

The remaining solid pellet was washed with 10 mL of 18 MΩ-cm water, the Falcon tube was inverted ~10x followed by vortexing for ~1 min followed by rotation for 15 min, and then centrifugation at 3000 g for 20 min. The supernatant from the washing was decanted and added to the previous extract, using caution to avoid disturbing the solid residue. The remaining soil pellet in the Falcon tube was saved for the next BCR step.

Note: hereafter the term "work-up" will be used to describe the rotation, centrifugation, supernatant isolation, and washing steps described above.

#### 2.3.1.3 BCR Step Two: The Carbonate-bound Fraction

To the same 50 mL Falcon tube containing the soil pellet from Step One of the BCR, 40.0 ± 0.5 mL of the 0.11 M Acetic Acid extraction solution (prepared as described in Section 2.1.1.3) was added and the sample was then "worked-up".

#### 2.3.1.4 BCR Step Three: The Metal Oxide-bound Fraction

To the same 50 mL Falcon tube containing the soil pellet from step two of the BCR, 40.0 ± 0.5 mL of the 0.50 M Hydroxylamine Hydrochloride extraction solution (prepared as described in Section 2.1.1.4) was added and the sample was then "worked-up".

#### 2.3.1.5 BCR Step Four: The Organic-bound Fraction

To the same 50 mL Falcon tube containing the soil pellet from step three of the BCR, 10.0 ± 0.5 mL of 30% (v/v) hydrogen peroxide (Sigma Aldrich) was added in small (~1 mL) aliquots to avoid loss due to vigorous reaction. The cap was placed loosely on top of the Falcon tube and the sample was allowed to digest for at least 1 hr. at room temperature with swirling occasionally ~10 min.

Then the Falcon tube was suspended in a water bath and the sample continued to digest for at least 1 hr. at 85°C with occasional swirling during the first 30 min. The cap of the Falcon tube was removed and the sample continued to heat at 85°C, until

the sample volume was reduced to less than 3 mL. Note: this step required several hours to reduce the volume.

Next, a 10.0 ± 0.5 mL aliquot of 30% (v/v) hydrogen peroxide (Sigma Aldrich) was added to the Falcon tube, the tube was capped, inverted ~10x followed by vortexing for ~1 min, and then returned to the water bath, and digested for at least 1 hr. at 85°C with occasional swirling during the first 30 min The cap of the Falcon tube was removed and the sample continued to heat at 85°C, until the sample volume was reduced to less than 1 mL. Note: special care needed to be taken to watch and make sure the samples did not dry completely. The remaining soil pellet was allowed to cool to room temperature.

To the same 50 mL Falcon tube containing the cooled soil pellet, 50.0 ± 0.5 mL of the 1.0 M Ammonium Acetate extraction solution (prepared as described in Section 2.1.1.5) was added and the sample was then "worked-up".

#### 2.3.1.6 BCR Step Five: The Residual Fraction —Total Metal Extraction (TME)

The remaining soil pellet in the Falcon tube was saved for the last BCR step the "residual fraction". The residual fraction was analyzed to determine the "refractory" (i.e., immobile) metals (hereafter denoted RFC), present in the soil aside from the battle. The remaining pellet was subjected to a total metal extraction procedure using aqua regia as the chemical leaching reagent. This method is based on the *aqua regia* extraction protocol.[44]

#### 2.3.1.6.1 Sample Preparation — TME

The remaining soil pellet in the Falcon tube was spread evenly in a polystyrene weigh boat and dried for 1 hr. at ~110°C. The sample was weighed and then transferred to a 250 mL round bottom borosilicate glass flask, and the water content of an air-dried sub-sample was determined according to the ISO Norm 11466 and recorded.[44]

#### 2.3.1.6.2 Treatment with *Aqua Regia*

In the fume hood, 1.0 mL of 18 MΩ-cm water was added to the 250 mL round bottom borosilicate glass flask containing the soil sample, to obtain a slurry. This was followed by adding the *aqua regia* solution to the flask, this was done drop by drop while mixing, first starting with 21 mL of 11.7 M HCl (TraceMetal grade, Sigma Aldrich), then followed by 7 mL of 15.8 M $HNO_3$ (TraceMetal grade, Sigma Aldrich), again adding the acid very slowly while swirling. Next, 15.0 mL of 0.5 M $HNO_3$ (TraceMetal grade, Sigma Aldrich) was added to the 250 mL flask, the reflux condenser was placed on top of the reaction vessel, swirled gently for several minutes, and then allowed to stand uncovered in the fume hood for a minimum of 16 hr at room temperature, to allow for the slow oxidation of RFC matter in the soil.

Following the digestion period, the glass water cooled reflux condenser (effective length of 200-mm) was placed on top of the 250 mL round bottom flask. Water lines were connected in series to ensure that the connections were secure and cold water flowed properly through the condenser. The temperature of the reaction

mixture was raised slowly, until reflux conditions were reached, and this was maintained for 2 hr. The condensation zone was kept lower that 1/3 of the height of the condenser, to prevent the loss of sample.

The extraction vessel was allowed to cool slowly to room temperature by maintaining cold water flow through the condenser as the refluxing period was complete. The remaining slurry was quantitatively transferred to a 50 mL HDPE centrifuge tube using a disposable pipette. The reaction vessel was rinsed with 10 mL of 0.5 M $HNO_3$ (TraceMetal grade, Sigma Aldrich) to ensure quantitative transfer. Following transfer, the extract was centrifuged at 3,000 g for 20 min, and then the supernatant was decanted into a 125 mL HDPE graduated cylinder. Using ~3.0 mL of 18 MΩ-cm water, the soil pellet was rinsed, centrifuged at 3,000 g for 20 min, followed by decanting the supernatant into the 125 mL HDPE graduated cylinder and the exact volume (±0.0 mL). The sample was then transferred to a 100 mL HDPE bottle and stored at 4°C until analysis.

### 2.3.2 BCR Method: Microwave-Assisted Extraction (MAE)

The MARS 5 microwave-assisted extractor was used for digesting, dissolving, hydrolyzing, or drying a wide range of materials.[48] The primary purpose is the rapid preparation of samples for analysis by atomic absorption (AA), inductively coupled plasma (ICP) spectroscopy, and gas or liquid chromatography.[48]

The speciation of Cu in soil was determined by a novel MAE method. This method is a modified sequential extraction procedure, originally developed by the

Standards, Measurements and Testing Program of the European Union (EU) (formerly named the Community Bureau of Reference of the European Commission BCR).[43] The sequential extraction process is the same as described above, but instead uses microwaves to accelerate the process. Several changes were made which are specified below in the descriptions of each step in the BCR MAE method.

#### 2.3.2.1 Sample Preparation for MAE

For each core, the pulverized soil sub-samples were placed into a weigh boat and dried at ~110°C for 1 hr, then 0.500 ± 0.001 g was weighed for each fraction and transferred to a HP500 MAE vessel. Remaining sample was returned to the respective plastic storage bag. Following the same procedure for drying and weighing, a blank sand "uncontaminated" sample (Sigma Aldrich) was prepared and subjected to each step in the BCR method.

#### 2.3.2.2 Number of Vessels

The total number of vessels used in MAE-BCR was based on the length of the soil cores. The longest core that was collected was 13 inches, and with a blank sample, a consistent 14 vessels in the microwave was used for extractions. If the core was less than 13 inches the remaining vessels would be filled with 20.0 mL of 18 MΩ-cm water. The carrousel holds 14 vessels (including 1 control vessel), methods run to full capacity for each extraction.

#### 2.3.2.3 BCR Step One: The Exchangeable Fraction MAE

The first extract, 20.0 ± 0.5 mL of 0.010 M Calcium Chloride extraction solution (prepared as described in Section 2.1.1.2) was added to 0.500 ± 0.001 g of soil in the HP500 MAE vessel. All vessels were capped, placed in carousel, the top bolt was tightened snugly (~3/4 turn) with a crescent wrench. The safety vent film was inspected that it was properly seated in vent cap, and in good condition (14 total vessels, 1 control, 13 additional). Note: if any vessels were unused 20.0 mL of 18 MΩ-cm water was placed in the vessel. Next, the temperature probe was attached and carousel was place in microwave (use caution when tightening top, if overtightened could damage the probe), at this time the pressure probe was attached to the control vessel (proper position of the pressure probe is vital to ensure that the pressure sensor does not get tangled during extraction). Ensure the exhaust hose is in the fume hood. The microwave settings are as follows: using the ramp to temperature method, with 10 min ramp time to 115°C, hold at 115°C for 10 min (1200 Watts at 100% power). When MAE is complete, allow time to cool (~20 min), remove temperature and pressure probes (place in respective containers). Note: use caution and slowly vent any excess pressure in the fume hood, wear acid resistant gloves (may need to leave in the microwave and allow additional time to cool).

Next, the contents were quantitatively transferred to a 50 mL Falcon tube, use 5.0 mL 18 MΩ-cm water to ensure quantitative transfer (keep the same 50 mL centrifuge tube for each sub-sample fraction throughout the procedure), centrifuge at 3000 g for 20 min, decant the supernatant into a 125 mL PE bottle. Wash the pellet

with 5.0 mL 18 MΩ-cm water, the Falcon tube was inverted ~10x followed by vortexing for ~1 min to ensure good dissolution, centrifuge at 3000g for 20 min, the supernatant from the washing was decanted and added to the previous extract, and store at 4˚C until analysis. The remaining soil pellet in the Falcon tube was saved for the next BCR step.

Note: hereafter the term "work-up" will be used to describe the MAE preparation, extraction, centrifugation, supernatant isolation, and washing steps described above.

#### 2.3.2.4 BCR Step Two: The Carbonate-bound Fraction MAE

To the same 50 mL Falcon tube containing the soil pellet from step one of the BCR, a total of 20.0 ± 0.5 mL of the 0.11 M Acetic Acid extraction solution (prepared as described in Section 2.1.1.2) was added in separate 10.0 mL increments to quantitatively transfer the pellet back into HP500 MAE vessel, as in step one the sample was "worked-up".

#### 2.3.2.5 BCR Step Three: The Metal Oxide-bound Fraction MAE

To the same 50 mL Falcon tube containing the soil pellet from step one of the BCR, a total of 20.0 ± 0.5 mL of the 0.50 M Hydroxylamine Hydrochloride extraction solution (prepared as described in Section 0) was added in separate 10.0 mL increments to quantitatively transfer the pellet back into HP500 MAE vessel, as in step one the sample was "worked-up".

Table 1. Microwave settings for BCR extraction, Steps One-three.

| Watts | Power | Ramp Time to 115°C | Hold |
|---|---|---|---|
| 1200 | 100% | 10 min | 10 min |

#### 2.3.2.6 BCR Step Four: The Organic-bound Fraction MAE

To the same 50 mL Falcon tube containing the soil pellet from step three of the BCR, add a total of 10.0 ± 0.5 mL of 30% (v/v) hydrogen peroxide (Sigma Aldrich) added in small (~1 mL) aliquots to avoid loss due to vigorous reaction. To ensure quantitative transfer back into HP500 MAE vessel aliquot 5.0 mL at a time. The microwave settings are as follows 7 min ramp time to 75°C, hold at 75°C for 10 s (300 Watts at 60% power). When MAE is complete, and properly cooled Add 10.0 mL 0.5 mL of the 1.0 M Ammonium Acetate extraction solution (prepared as described in Section 2.1.1.5) and the sample was "worked-up" using the same microwave settings.

Table 2. Microwave settings for BCR Step Four: ORG-Fraction.

| Watts | Power | Ramp Time to 75°C | Hold |
|---|---|---|---|
| 300 | 60% | 7 min | 10 s |

### 2.3.3 MAE Method for Hg

Trace Hg in soil was determined by MAE-ICP-MS.

#### 2.3.3.1 Sample Preparation

For each core, the pulverized soil sub-samples were placed into a weigh boat and dried at ~110°C for 1 hr, then 1.000 ± 0.001 g was weighed for each fraction, recorded in lab the notebook, and transferred to a HP500 MAE vessel. Any remaining

sample was returned to the respective plastic storage bag. Following the same procedure for drying and weighing a blank sand “uncontaminated” sample (Sigma Aldrich) was prepared and exposed through each step in the BCR method.

#### 2.3.3.2 Hg extraction by MAE

The extraction solution (concentrated nitric acid, 20.0 ± 0.5 mL) (hereafter denoted CAT-[Hg] for “concentrated acid treatment”) was added to 1.000 ± 0.001 g of soil in the HP500 MAE vessel. All vessels were capped, placed in the carousel, and the top bolt was tightened snugly. The safety vent film was inspected to make sure that it was properly seated in the vent cap and in good condition (14 total vessels). Note: If any vessels were unused, then 20.0 mL of 18 MΩ-cm water was placed in the vessel. Next, the temperature probe was attached and the carousel was placed in the microwave. The pressure probe was also attached to the control vessel. The microwave settings for the "ramp-to-temperature" method were: 5 min ramp time to 80°C, hold at 80°C for 15 min (1200 Watts at 100% power). When MAE is complete, the vessel was cooled (~20 min).

Next, the contents were quantitatively transferred to a 50 mL Falcon tube using 5.0 mL of 18 MΩ-cm water to ensure quantitative transfer. The extract was centrifuged at 3000 g for 20 min, the supernatant was then decanted into a 125 mL PE bottle. The pellet was then washed with 5.0 mL of 18 MΩ-cm water, the Falcon tube was inverted ~10x followed by vortexing for ~1 min to ensure good dissolution, centrifuged at 3000g

for 20 min, the supernatant from the washing was decanted and added to the previous extract, and stored at 4˚C until analysis.

## 2.4 Determination Method

### 2.4.1 Instrumentation

The primary instrument for the determination of Cu and Pb in soil was a Perkin-Elmer Model 4100ZL Atomic Absorption Spectrometer (Perkin Elmer, Waltham, MA). The 4100ZL is equipped with a transversely heated graphite furnace (THGA) and uses a Zeeman (longitudinal AC) background correction system. This model is automated for multi-element analysis by using four hollow cathode lamps (HCL) in a turret, an autosampler (Model AS-70), a recirculating water cooler, and a fume extraction system. A schematic drawing of the GF-AAS instrument is shown in in Figure 14. The system design includes a single light source from a HCL, a monochromator, and a photomultiplier tube (PMT) detector.

The line source was a single-element HCL for Cu (Model 14-386-100A) set at a current of 10 mA with a wavelength of 324.8 nm as the primary emission line and Pb (Model 14-386-101F) set at a current of 10 mA with a wavelength of 283.3 nm as the primary emission line. Both HCLs were obtained from FisherScientific. A schematic diagram of the HCL is shown in Figure 15.

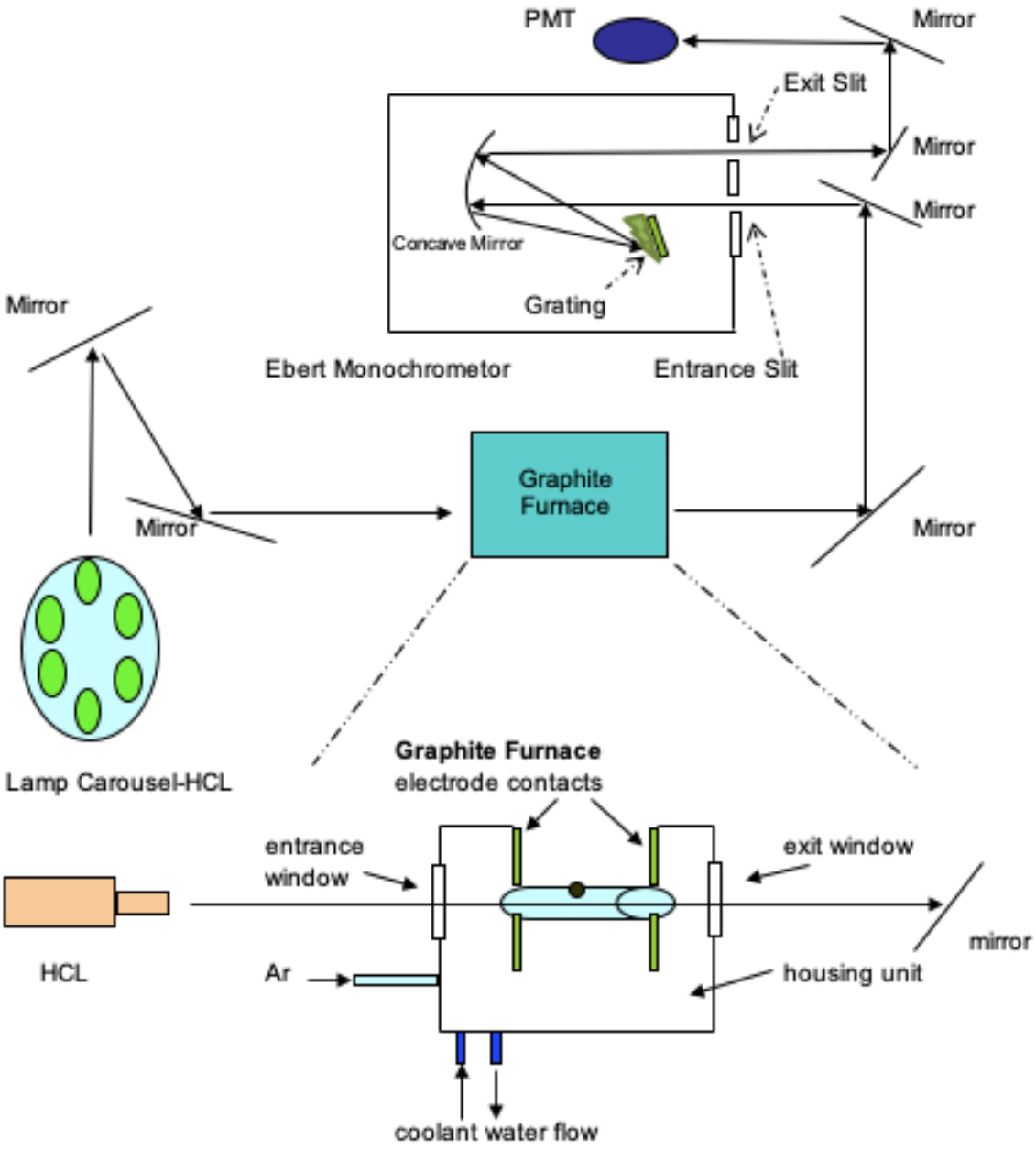


Figure 14. Schematic diagram of the GF-AAS.

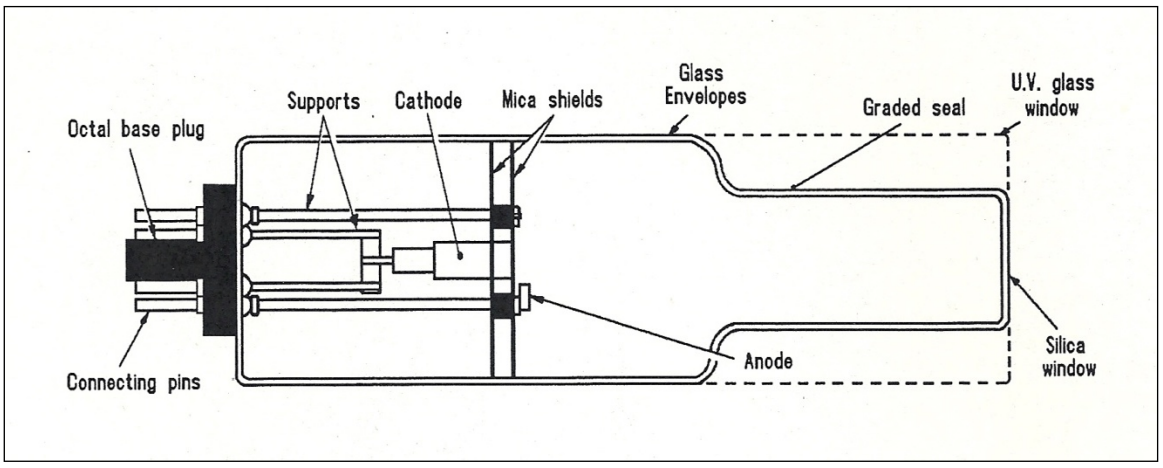


Figure 15. Schematic diagram of a HCL. *Methods Manual for Atomic Absorption Spectroscopy*, Issue 3; Thermo Elemental, Cambridge, UK, 2001.

The GF-AAS optical system uses an Ebert-design monochromator with a linear dispersion of 1.6 nm $mm^{-1}$. The monochromator employed a grating with 1800 lines/mm with a wavelength range from 190-870 nm. The instrumental software offers three settings for the slit width: 0.2, 0.7, and 2.0 nm. For this study, the monochromator was set to a slit width of 0.7 nm. A photomultiplier tube PMT was used as the detector.

#### 2.4.1.1 Graphite Furnace

The graphite platform cuvette is referred to as the “furnace”, whereas the aperture that contains the cuvette is referred to as the “furnace head”. Schematic diagrams of the graphite furnace and the furnace head are shown in Figure 16 and Figure 17, respectively. In this work, the furnace used was a transversely-heated graphite furnace (THGA, Perkin Elmer) with an integrated L’vov platform. The

transversely-heated furnace provides uniform temperature distribution which significantly reduces "memory effects", and also improves the atomization efficiency.

The instrument also used a water-cooling pump for temperature control of the furnace electrodes, and a fume extraction to minimize analyst exposure to toxic vapors that were released by the system.

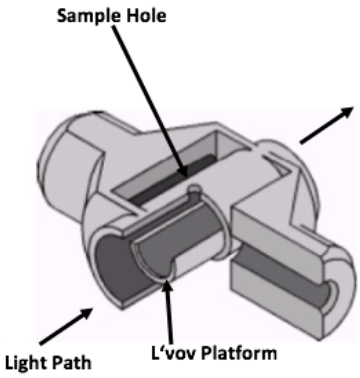


Figure 16. Schematic diagram of the graphite platform cuvette. The furnace used in this work was a transversely heated graphite furnace (THGA, Perkin Elmer) with an integrated L'vov platform (www.perkinelmer.com).

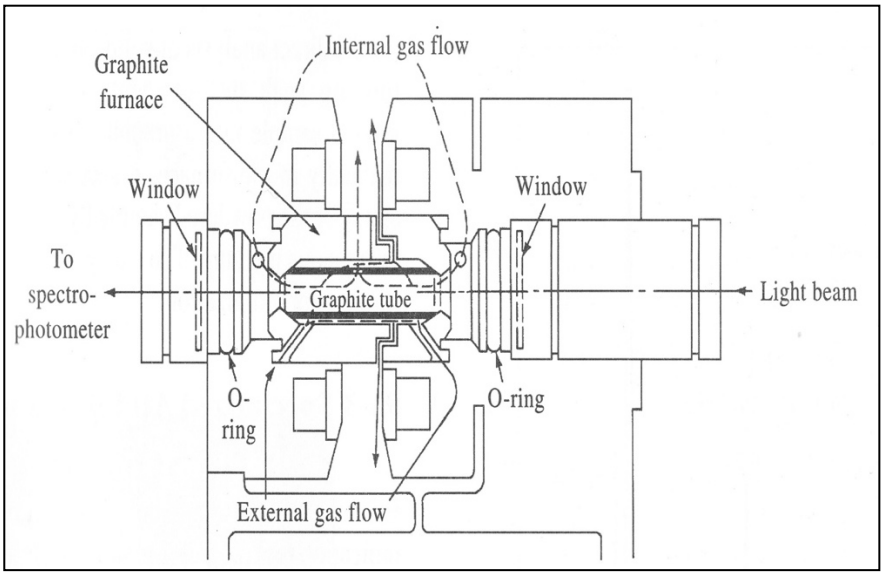


Figure 17. Furnace head shown with graphite platform cuvette in place. Skoog, D.A., Leary, J.J. Principles of Instrumental Analysis, 4th ed.; Harcourt Brace College Publishers: New York, 1992; p. 210.

#### 2.4.1.2 Light Sources

The HCL source was used at an operating current of 10 mA at a wavelength of 324.8 nm for Cu and 283.3 nm for Pb. For background correction, a Zeeman (longitudinally AC) system provided correction by maintaining the high energy throughput and thereby eliminated the need for a polarizer or other energy-reducing components in the optical system.

#### 2.4.1.3 Autosampler

The AS-70 carousel-styled autosampler accommodated up to 40 high-density polypropylene (HDPP) sample cups for unknown extracts, and 6 reagent cups (also HDPP) that could be used for matrix modifiers, standard additions, dilutions, automatic standard preparations, and/or blanks. The autosampler included a wash cycle with 1.0% (v/v) nitric acid between samples, and was able to handle normal or even viscous sample solutions. The rate of solution uptake was controlled by a 100 µL syringe pump. The autosampler carousel had an integrated 1 L wash reservoir which contained 1.0% (v/v) $HNO_3$ in combination with a 1 L waste reservoir.

The sample was introduced onto the L'vov platform of the graphite cuvette through a 0.5 mm inner diameter (i.d.) polytetrafluoroethylene (PTFE) capillary probe which was attached to the syringe pump. The total volume of solution used for each aliquot was 15 µL. The deposited sample was then exposed to a stepwise temperature program. The program resistively heated the furnace to atomize the sample, followed by cycling back to the initial temperature.

#### 2.4.1.4 Software

The spectrometer system and accessories were controlled through the AA WinLab data software (Perkin-Elmer, 1998). The computer was an Omni Tech Intel® Pentium 2 processor, with 327 KB of RAM running Microsoft Windows NT (version 4.00.1381).

#### 2.4.1.5 Temperature Program Procedure for GF-AAS

The temperature program consisted of five separate stages; a general schematic diagram is shown in Figure 18 for Cu and Pb. Also shown in

Table 3 and Table 4 are the temperature programs for Cu and Pb, respectively. The temperature program for Cu was: the injection temperature was set at 20°C, followed by a drying step, where the temperature ramped to a temperature of 140°C in 20s and was held at that temperature for 35 s. This step removed the solvent from the sample solution, as well as prevented the sample from boiling and subsequent spreading which could lead to sample loss. This was followed by the pyrolysis step, or ashing step, in which the temperature was ramped to a 1200°C in 10 s, and then held at this temperature for 20 s.

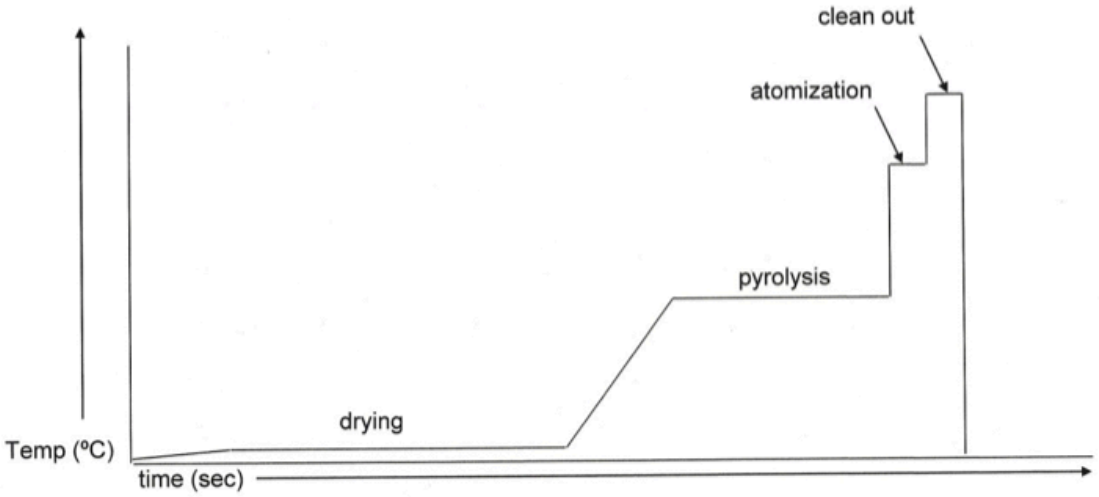


Figure 18. Temperature program for the graphite furnace for Cu and Pb.

Table 3. Temperature program for the graphite furnace for Cu.

| | Temp.(°C) | Ramp Time (s) | Hold Time (s) | Gas | Gas Flow |
|---|---|---|---|---|---|
| Injection | 20 | - | - | - | - |
| Drying | 140 | 20 | 35 | N2 | 0.3 mL $min^{-1}$ |
| Ashing | 1200 | 10 | 20 | N2 | 0.3 mL $min^{-1}$ |
| Atomization | 2000 | 1 | 5 | - | - |
| Clean out | 2200 | 1 | 3 | N2 | 0.3 mL $min^{-1}$ |
| N2 = 99.995% | - | - | - | - | - |

Table 4. Temperature program for the graphite furnace for Pb.

| | Temp.(°C) | Ramp Time (Sec.) | Hold Time (Sec.) | Gas | Gas Flow |
|---|---|---|---|---|---|
| Injection | 20 | - | - | - | - |
| Drying | 120 | 12 | 30 | N2 | 0.3 mL $min^{-1}$ |
| Ashing | 1000 | 12 | 20 | N2 | 0.3 mL $min^{-1}$ |
| Atomization | 1800 | 1 | 3 | - | - |
| Clean out | 2200 | 1 | 3 | N2 | 0.3 mL $min^{-1}$ |
| N2 = 99.995% | - | - | - | - | - |

The pyrolysis stage was performed to eliminate as much of the sample matrix components as possible without loss of the analyte. The next stage in the temperature program is the atomization stage, in which the analyte produces a cloud of free gaseous ground state atoms, and the absorption measurement is obtained. The temperature was stepped to 2000°C in 1 s and held there for 5 s. During the atomization stage, all $N_2$ flow was stopped and the absorption measurement was made. Following the atomization stage, "clean-out" was accomplished by stepping the temperature to 2450°C in 1 s and held at this temperature for 3 s. This stage efficiently eliminates all impurities that had accumulated from the previous stages. Next, the instrument used a water-cooling pump for temperature control of the furnace electrodes that cycled the temperature of the furnace back to 20°C to prepare for the next sample. The total time of the temperature program was 95 s for Cu, and 82 s for Pb, as shown in Table 3 and Table 4, respectively.

## 2.5 Validation of Methods

To validate the conventional and modern BCR extraction-GF-AAS methods for Cu and Pb, a lake sediment standard reference material (SRM) BCR 701 was used, from the Community Bureau of Reference, the former reference materials programme of the European Commission, Geel, Belgium. To validate the MAE-ICP-MS method for Hg, a waterway sediment SRM 1944 was used, from the National Institute of Standards and Technology (NIST, Gaithersburg, MD, USA).

## 2.6 Data Treatment

### 2.6.1 Data Acquisition

Data analysis was performed on a MacBook Air personal computer with a 1.6 GHz Intel Core i5 processor. The response from the GF-AAS was reported as peak area, and data was transferred to Excel 2019 (Microsoft, Redmond, Washington, USA) for analysis.

### 2.6.2 Calculations for trace metals in soil by GF-AAS

The Equations (5-7) given below describe the calculation of the analyte concentration in the original sample matrix from its concentration as measured. The calculations in performing data analysis for the BCR extractions steps for the GF-AAS are shown in Equations 5 and 6 below.

$$\boldsymbol{C_e = \frac{C*V*df}{W}} \quad [5]$$

Where:

$C_e$ is the element concentration in the original sample

C is the concentration of the element in the sample solution (from calibration model)

V is the volume of the undiluted sample solution

W is the weight of the sample in g

df is the dilution factor given below in Equation 6

$$\boldsymbol{df = \frac{volume\ of\ diluted\ sample\ solution}{volume\ of\ aliquot\ taken\ for\ dilution}} \quad [6]$$

Using Equation 5 and 6, Equation 7 provides an example for the MOX-bound fraction for Site 9, 0-1" using the conventional BCR method as follows:

$$C_e = \frac{(31.733\,\frac{ug}{L}) * (15 * 10^{-6} L) * (\frac{50\,mL}{0.01\,mL})}{1.0013\,g} = \left(2.37691\ \frac{\mu g}{g}\right)\left(\frac{10^3 ng}{\mu g}\right) = 2376.91\,\frac{ng}{g} \quad [7]$$

Below are some additional notes to help understand this calculation:

Injection volume: $15\ \mu\text{L}\ \ (10\ \mu\text{L of sample}, 5\ \mu\text{L of modifier})$

Total volume of 0.50 M hydroxylamine hydrochloride + wash = 40 mL + 10 mL respectively.

Mass of soil: 1.0013 g

Calibration model: y = 0.0015x + 0.0062

Average absorbance (3 replicates) – blank : y = 0.0538

Solving for x in $\frac{\mu g}{L}$ = 31.733 = $(31.733\ \text{ppb}) = \left(31.733\ \frac{\mu g}{L}\right)$

### 2.6.3 Calculation to Validate [Hg] in SRM by MAE ICP-MS

For the standard reference material (SRM) 1944, New York – New Jersey Waterway Sediment, Equation 8 was used to validate the certified value for Hg. The certified value for mercury was $3.4 \pm 0.5\,\frac{\text{mg}}{\text{kg}}$ , or $3.4 \pm 0.5\ \frac{\text{mg Hg}}{\text{kg of SRM}}$ . Equation 8 is similar to Equation 5, but the difference is that when using the ICP-MS, the exact sample volume taken into the nebulizer is unknown due to the peristaltic pump. Shown below are the steps I used to determine my concentration.

$$C_e = \frac{C * V_m * df}{W} \quad [8]$$

Where:

$C_e$ is the element concentration in the original sample ($\frac{\text{mg}}{\text{kg}}$)

C is the concentration of the element in the sample solution (from calibration model) ($\frac{\text{g analyte}}{\text{g extractant}}$)

$V_m$ is the total mass of the undiluted sample solution

W is the weight of the sample in g

df is the dilution factor shown above in Equation 6

Using Equations 6 and 8, an example calculation to validate [Hg] in SRM 1944 by MAE ICP-MS is shown in Equation 9:

$$C_e = \frac{\left(\frac{5.555\ g\ Hg}{1*10^9 g\ extractant}\right)*(33.31\ g\ undiluted\ sample\ solution)*\left(\frac{50\ mL}{2.5\ mL}\right)}{1.0017\ g\ SRM} =$$

$$\left(3.6945\ \frac{g\ Hg}{g\ SRM}\right)\left(\frac{10^3 mg}{g}\right)\left(\frac{10^3\ g}{1\ kg}\right) = 3.70\frac{mg}{kg} \quad [9]$$

Below are some additional notes to help understand this calculation:

Mass of SRM: 1.0017 g

Calibration curve y = 6.956623x-4.639375

Average intensity (3 replicates) – blank : y = 34.003

Solving for x in $\frac{\text{g analyte}}{\text{g extractant}} = 5.555 = (5.555\ \text{ppb}) = \left(\frac{5.555\ \text{g Hg}}{1*10^9 \text{g extractant}}\right)$

Vm the total mass of the undiluted sample = 28.32g + 4.99g = 33.31 g

$$20.0\ \text{mL Conc. HN}O_3\ \left(\frac{1..416\ \text{g}}{\text{mL}}\right) = 28.32\ \text{g}$$

$$5.0\ \text{mL H2O}\ \left(\frac{0.998\ \text{g}}{\text{mL}}\right) = 4.99\ \text{g}$$

Total volume MAE extract: 25 mL (20.0 mL Conc $HNO_3$, 5.0 mL 18 MΩ-cm H2O)

Dilution 1:20: 2.5 mL extract diluted to 50 mL with 18 MΩ-cm water

## 2.7 GF-AAS System

Quantitation was based on the integrated absorbance or peak area because of the variable nature of the atomization absorbance vs. time profiles.[75] The rate of atomization is sensitive to changes in the sample matrix complexity, this leads to imprecision in the measurement of peak height, therefore the integrated peak area signal was used in this work to eliminate the error peak height contributes.[75]

## 2.8 Inductively Coupled Plasma-Mass Spectrometry (ICP-MS)

The primary instrument for the determination of Hg used in this work was the Inductively Coupled Plasma-Mass Spectrometry (ICP-MS). This instrument was also was used for the determination of other trace metal analytes from the Brawner Farm soil core extracts from the conventional and modern MAE BCR methods, the total metal extraction method, as well as Hg MAE method. The extracts were subjected to elemental analysis over the m/z range of 50-238 as "full scans". The instrument employs a quadrupole mass analyzer, an instrument schematic is shown in Figure 19.

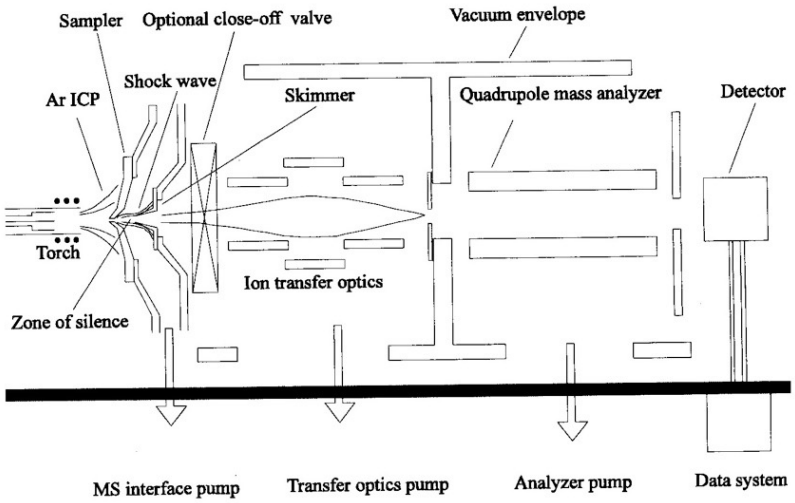


Figure 19. Schematic diagram of ICP-MS with quadrupole mass analyzer.[71]

### 2.8.1 ICP-MS Procedure

Table 5. ICP-MS Operating Conditions on the Micromass instrument

| ICP-MS Operating Conditions | |
|---|---|
| Instrument | Micromass Platfrom ICP |
| Number of Replicates | 4 |
| Dwell Time | 4 s |
| Integration Time | 1.5 min |
| | |
| Plasma Conditions | |
| Plasma Gas Flow | 13.00 L $min^{-1}$ |
| Nebulizer Gas Flow | 1.00 L $min^{-1}$ |
| Sample Flow | 0.95 L $min^{-1}$ |
| Hexapole Gas Flow - He | 3.5 L $min^{-1}$ |
| Hexapole Gas Flow – $H_2$ | 3.5 L $min^{-1}$ |
| Forward Power | 1350 W |
| Ion Energy | 2 eV |

## Chapter 3 Results and Discussion

In the following pages, the chemical speciation and transport of Cu, Pb, and Hg in soil from the BF battlefield is examined by various MAE methods and analyzed by GF-AAS as well as ICP-MS. The primary focus for this study is separated into two aspects: (1) development of analytical methods for the extraction and quantification of the metals from soil, and (2) study of the environmental chemistry in terms of the trends that were observed in the speciation, abundance, distribution, and transport of Cu, Pb, and Hg in BF soil.

The following questions are addressed in the analytical section for this study:

- Is it possible to reliably extract and quantify Cu, Pb, Hg in the BF soil core samples at trace (low ppb) levels?
- Does the BCR method reveal the chemical speciation of Cu in the soil cores?

The following questions are addressed in the environmental section for this study:

- How does the Cu distribution, as determined by MAE-BCR-GF-AAS, suggest a transport mechanism?
- How does the Cu distribution differ from Pb, as determined previously by BCR-GF-AAS?
- What is the mass balance for Cu at BF? How does this compare to Pb?
- Can the Cu and Pb distributions be useful in pin-pointing the infantry unit positions during the battle?
- How does the distribution and abundance of Hg in BF soil compare to the Cu and Pb results?

## 3.1 Development of Analytical Methods

The development of analytical methods to determine the concentration of Cu, Pb, and Hg in the soil fractions obtained by sequential extraction will be discussed. GF-AAS methods were developed, optimized, and then validated for the conventional BCR extraction method as well as for the MAE-based methods.

### 3.1.1 GF-AAS Method Development and Optimization

The GF-AAS method was required to address the first question in this study: to reliably quantify Cu, Pb, Hg at trace levels. Because of the variety of sample extracts examined in this study, the key GF-AAS method conditions were optimized: primarily the hollow cathode lamps (HCLs), means of sample introduction, and furnace programing including temperature gradients as well as the injection, atomization, and clean-out temperatures are discussed. The effect of conventional and permanent modifiers on the response and lifetime of the furnace was also examined.

#### 3.1.1.1 Hollow Cathode Lamp

The HCL source was initially set at 100% of the maximum rating defined by the manufacture at an operating current of 10 mA. If the operating current is set too high, it can prematurely wear out the lamp, and also cause distortions in the observed response by decreasing the absorbance profiles or causing double peaks to appear. In this work, operating currents of 60%, 80%, and 100% were investigated by using a 50 ng $g^{-1}$ Cu standard diluted in 1% (v/v) $HNO_3$ (Table 6). The 60% operating current

showed a slight decrease in absorbance, while no statistically significant difference was observed for 80% and 100% responses, so 60% was used for further studies.

Table 6. Optimization of current for the Cu HCL comparing the absorbances of three different operating currents; (n = 4 at the 95% confidence level).

| Standard | 60% (6 mA) | 80% (8 mA) | 100% (10 mA) |
|---|---|---|---|
| 50 ppb Cu | 0.301 ± 0.016 | 0.327 ± 0.028 | 0.329 ± 0.033 |

#### 3.1.1.2 Sample Introduction

As described in section 2.4.1.3 (Autosampler), a carousel-style autosampler with a connecting mechanical arm was used for sample deposition into the furnace. The standard and sample solutions consisted of a 15 µL drop that was distributed over the L'vov platform surface and occupied a surface area that was dependent upon the nature of the solvent and the characteristics of the surface.[56] Figure 20 shows the correct deposition of the an aqueous solution to produce a hemisphere because of its high surface tension. To ensure that the solution was precisely and accurately delivered into the furnace, the capillary probe was manually positioned 2-3 mm above the platform surface shown (Figure 21).[65] The sample deposition and capillary tip positioning were manually checked every 15 samples to ensure that the sample formed a well-defined droplet as it was deposited in the cavity of the platform.

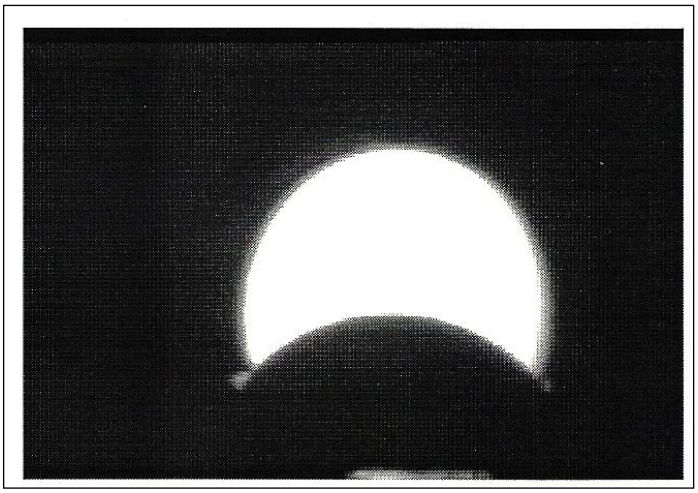

Figure 20. Aqueous samples correctly deposited on the platform will form a droplet, as observed along the optical axis. (From *Methods Manual for Atomic Absorption Spectroscopy*, Issue 3; Thermo Elemental, Cambridge, UK, 2001.)

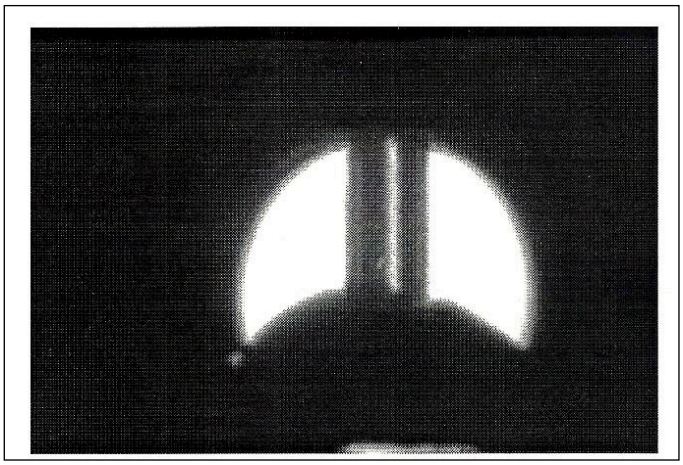

Figure 21. Optimal capillary tip position for deposition of the sample into the cavity of the platform. Sample was not observed running back up the tip of the sample probe. (From *Methods Manual for Atomic Absorption Spectroscopy*, Issue 3; Thermo Elemental, Cambridge, UK, 2001.)

### 3.1.1.3 Furnace Programming

The GF-AAS experiment is based upon the presence of gaseous analyte atoms in the ground state for the desired valence electronic transition (e.g., 324.8 nm for Cu, 283.3 nm for Pb, and 253.7 for Hg). For Cu, absorption of the incident photon by the ground state ($Cu^{\circ}_{(g)}$) is measured, and relaxation of the excited state ($Cu^{\circ}_{(g)}$) to the ground state is accompanied by evolution of heat, as represented by Equation 10:

$$\boldsymbol{Cu^{\circ}_{(g)} + h\nu \rightarrow Cu^{*}_{(g)} \rightarrow Cu^{\circ}_{(g)} + \Delta} \qquad [10]$$

In GF-AAS, ideally the purpose of the furnace is to red convert all of the Cu species in the sample to $Cu^{\circ}(g)$. A schematic diagram of the temperature program developed for the graphite furnace is shown in Figure 14. The furnace is operated in four consecutive stages. The initial "drying stage" is intended to remove the solvent while preventing loss of the analyte. This is accomplished by heating the furnace slowly through the solvent's boiling point. The next step in the furnace program is the "pyrolysis (ashing) stage" in which the temperature is ramped at a faster rate as a means to remove interfering matrix components, again without loss of the analyte. The subsequent stage in the temperature program is the "atomization stage" in which a cloud of gaseous Cu atoms in the ground state are created. The HCL is tuned for the absorbance measurement of this form of the analyte, Cu*(g).

During the atomization stage, the temperature rate is >1,000°C s-1 and the $N_2$ flow through the furnace is stopped to isolate Cu*(g). After the atomization stage, a

final "clean out" stage is executed in which the temperature of the furnace is stepped to a high temperature as a means to remove contaminants. To prepare the furnace for the next sample (20℃ at injection), water at room temperature flowed at a constant rate of 1.7 L $min^{-1}$ around the electrode contacts.

#### 3.1.1.3.1 Drying Stage

The primary aim of the drying stage in GF-AAS is to de-solvate the 15 µL drop deposited on the platform surface by the autosampler. An aqueous solution will produce a residue of microcrystals in the furnace from the salts of the acids used in its preparation.[56,76] Optimization of the temperature gradient for the drying stage was studied to ensure consistent and uniform formation of the microcrystals between sample depositions — that is, to avoid "splattering" of the sample solution.[73] The temperature during the drying stage was held constant to ensure that all of the solvent had uniformly evaporated.

#### 3.1.1.3.2 Pyrolysis Stage

The purpose of the pyrolysis or ashing stage is to create a matrix-free environment without loss of analyte. In GF-AAS, it is important to use as high of a pyrolysis temperature as possible to lessen matrix effects. For this study, a pyrolysis temperature of 1200°C was chosen as the optimal temperature for Cu and 1000°C for Pb.[73]

#### 3.1.1.3.3 Atomization Stage

The theory of analyte atomization within the semi-enclosed furnace is that the formation of free gaseous neutral atoms in the ground state must be rapid compared to the analyte dissipation time.[56,57,59] The absorbance signal is proportional to density of free metal atoms within the furnace volume, integrated over the length of the furnace area that they occupy.[56,59,61] The optimized atomization temperature for Cu was 2000°C and 1800°C for Pb.[73]

#### 3.1.1.3.4 Clean-Out Stage

In the final stage of the temperature program, the temperature of the furnace was stepped to a very high temperature to remove residual material that could remain between firings of the furnace. However, setting too high of a temperature would adversely affect the lifetime of the furnace. The clean-out temperature was adjusted to 2200°C for Cu with no significant difference in the observed absorbance between firings. The clean-out temperature for Pb was also 2200°C based on previous optimization work.[73]

#### 3.1.1.3.5 Sheath Gas

To minimize the amount of atmospheric gases entering the furnace, predominantly oxygen, a constant internal flow of 99.995% (v/v) $N_2$ gas flowed through the cuvette and the furnace head.[67] The reaction of oxygen and carbon within the furnace causes oxidation of the carbon in the graphite lattice.[77-80] From this reaction it

causes an increase in the number of highly active sites on the graphite surface by the formation of CO and/or $CO_2$..[56,80,81] The presence of oxygen forms stable oxides of the analyte, thus reducing the free atom population, as shown in Equation 11.[76,79-81]

$$2\,Cu^{\circ}_{(g)} + O_2{}^{\circ}_{(g)} \rightarrow 2\,CuO_{(g)} \quad [11]$$

Oxygen can be introduced into the furnace through diffusion of air, as well as through decomposition of oxyanion salts of the analyte and/or the sample matrix.[56,77] The nitrogen gas flow prevents oxidation of the graphite by flushing the oxygen out through the two apertures within the furnace head as well as the sample introduction hole, as shown in Figure 16.[65] Flow rate settings ranged from 0.200 L $min^{-1}$ to 0.300 L $min^{-1}$. The higher flow rate was used for this study to enhance the removal of oxygen from the system.

#### 3.1.1.4 Chemical Interferences

The term chemical interference broadly describes the interaction of the analyte and matrix components occurring within the graphite furnace. However, other physical processes may be occurring (Figure 22).[67,82,83] There are two types of chemical interferences: condensed phase and vapor phase[65,84] Vapor-phase chemical interferences occur when a matrix contaminant reacts with the analyte and prevents its quantitative conversion into gaseous neutral ground-state atoms (Figure 4).

A vapor-phase chemical interference is either lost during the pyrolysis step or does not dissociate into gaseous neutral ground-state atoms during the furnace program, this is often caused if the temperature is set too high during the pyrolysis step.[56,82] In the determination of Cu, chloride ions are a common vapor-phase chemical interference.[59,65]

In addition, secondary effects of analyte adsorption-desorption can occur as the analyte migrates to the cooler ends of the tube, causing a recombination of the analyte with a matrix interferent, which can then re-vaporize resulting in loss of the analyte.[56,82]

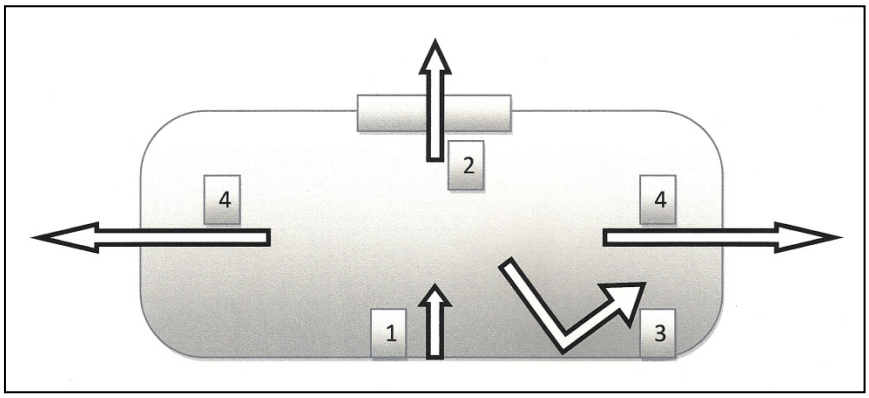


Figure 22. Physical processes occurring within the atomizer: (1) primary generation; (2) irreversible analyte loss through the dosing hole; (3) analyte adsorption-desorption at the furnace platform; (4) irreversible analyte loss through the furnace ends and/or condensation from the cooler ends of the furnace.[56]

A condensed phase chemical interference occurs when there is incomplete vaporization of the condensed phase of a non-volatile molecular species containing the analyte.[66] Occlusion is the formation of a microcrystal of the analyte with the interfering matrix component. The microcrystals are swept away upon vaporization prior to the atomization step.[56] RFC compound formation can also cause incomplete atomization,

e.g., CuO.[76,84] In addition, if a matrix interferent remains after the drying or pyrolysis stage or if there are "memory effects" from the previous heating cycle, the gaseous products of its decomposition may rapidly expand during atomization, resulting in the loss of the analyte from the furnace.[68,82]

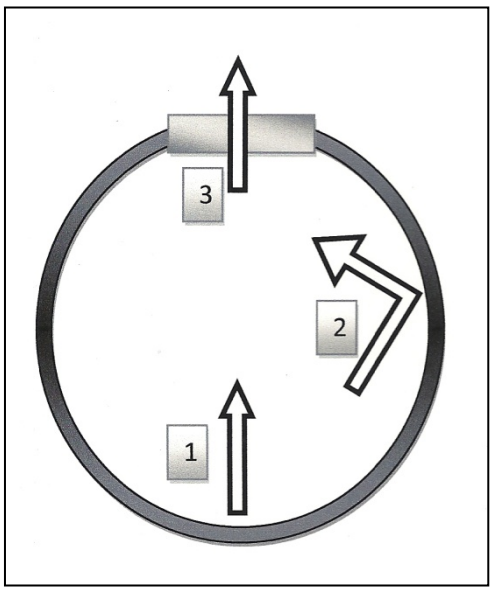


Figure 23. Chemical processes occurring within the atomizer volume: (1) homogeneous gas-phase reactions consuming and producing free analyte atoms; (2) heterogeneous reactions of analyte vapor with the furnace wall producing and consuming free analyte atoms.[56]

#### 3.1.1.5 Matrix Modifiers

Matrix modifiers were introduced in 1975 to combat chemical and physical interferences. Chemical modifiers are added to samples and standards to either increase matrix volatility or decrease analyte volatility.[64] Chemical modifiers are designed to minimize the formation of molecular species during the atomization step. They also permit the use of a higher pyrolysis temperature to vaporize more of the matrix components thereby preventing interference.[65]

There are two types of chemical modifiers: conventional and permanent. Conventional modifiers are intended to either stabilize the analyte at a higher temperature during pyrolysis or to atomize the sample matrix at a lower temperature. Conventional modifiers are intended to produce a matrix-free environment during the formation of a cloud of neutral ground-state gaseous analyte atoms. Though the process is not well understood, permanent modifiers react with the surface of the platform by forming a coating of intermetallic compounds with high melting points to stabilize the analyte at higher pyrolysis temperature.[56,85,86] In this study, 100 mM $NH_4NO_3$ in 1% (v/v) $HNO_3$ was added to each sample and standard.

A permanent modifier is retained through multiple firing cycles if it is stable on the graphite surface. Because of their high melting points, the six platinum group metals (Pd, Pt, Ir, Os, Ru, and Rh), as well as carbide-forming elements such as Zr, Nb, Ta, and W, have been commonly used as permanent modifiers.[85] These metals have stable exceptional catalytic activity and are resistant to degradation.[85] A permanent modifier can be deposited in a simple way by injecting the modifier solution directly onto the platform, applying a temperature program, and then repeating this cycle to deposit a total of ~400-500 µg of the modifier onto the platform surface.[81]

The principal benefits of permanent modifiers over conventional modifiers are the elimination of volatile impurities during graphite pre-treatment (pyrolysis) which contributes to lower modifier background noise.[37] With lower noise this leads to improved detection limits, as well as enhanced signal stability because of the reduction in the number of re-calibrations that are required, thus extending the lifetime of the graphite furnace.[37] For Ru, the formation of an intermetallic compound (e.g., CuRu2,

PbRu2) has been proposed as the stabilizing mechanism.[85] The use of W for the determination of As, Cd, and Pb in complex matrices has also been studied.[37]

For this work, the permanent modifier (36 µL of a 500 mg $kg^{-1}$ solution of a 1:1 mixture of W and Ru) was deposited onto the graphite surface and subjected to the temperature program listed in Table 7.[73] After 28 cycles, a layer of 500 µg of W carbide was deposited onto the surface, as well as 500 µg of Ru was permeated into crystal lattice of the graphite furnace platform.[87]

Table 7. Temperature program for the deposition of 500 mg $kg^{-1}$ solution of a 1:1 mixture of W and Ru onto the graphite surface, with an injection temperature of 20°C.[73]

| Step | Temperature/°C | Time/s | Ar flow $L^{-1}$ $min^{-1}$ |
|---|---|---|---|
| 1 | 98 | 5 | 3 |
| 2 | 120 | 20 | 3 |
| 3 | 1000 | 15 | 3 |
| 4 | 1000 | 3.5 | 3 |
| 5 | 1000 | 3 | 0 |
| 6 | 2000 | 1.5 | 0 |
| 7 | 2000 | 3 | 0 |
| 8 | 2000 | 3 | 3 |
| 9 | 40 | 20 | 3 |

### 3.1.2 MAE Method Development and Optimization

To address the first question in this study — is it possible to reliably extract Cu, Pb, Hg at trace levels — factors that influence the extraction efficiency for the individual types of BCR soil extractants were studied. For MAE, optimization of the temperature program, number of vessels, and the applied power were examined.

#### 3.1.2.1 MAE Performance Testing

A monthly performance test was run on the MAE system (CEM Mars5) to ensure that the extractor was functioning properly. For the temperature sensor and pressure probes, reagent water (50.0 mL) was placed in the HP500 control vessel with the temperature and pressure sensors attached (no other vessels were inside of the MAE system during this test). The five-stage "QC ESP/EST" method was then run and a passing result (200 ±10°C) was observed (Table 8). In addition to testing the probes, the volume of water remaining in the vessel was measured to determine if any leakage had occurred during the test.

Table 8. Performance test protocol for the MARS 5 microwave extractor using the preprogramed QC ESP/EST test.

| Stage | Ramp Time (min) | Hold Time (min) | Final Pressure (psi) | Final Temperature (°C) |
|---|---|---|---|---|
| 1 | 5 | 2 | 120 | 175 |
| 2 | 2 | 2 | 140 | 180 |
| 3 | 2 | 2 | 160 | 187 |
| 4 | 2 | 2 | 180 | 192 |
| 5 | 2 | 2 | 200 | 197 |

#### 3.1.2.2 Temperature Model

For a general understanding of the MARS 5 microwave extractor, a temperature model was created using 20.0 mL of 18 MΩ-cm water placed in each extraction vessel (14 total) using the ramp-to-temperature method. With this method the power will adjust to reach the final temperature at a given rate determined by the ramp time. To determine the amount of time to reach 150°C at 300, 600, 900, and 1200 W, the ramp-

to-temperature method (Table 9, Figure 24) used a ramp time of 1 s (to ensure that the microwave would operate at 100% power) and hold time of 50 min (to allow sufficient time to reach temperature).

Table 9. Microwave settings for temperature model.

| Watts | Power | Ramp Time to 150°C | Hold |
|---|---|---|---|
| 300 | 100% | 1 s | 50 min |
| 600 | 100% | 1 s | 50 min |
| 900 | 100% | 1 s | 50 min |
| 1200 | 100% | 1 s | 50 min |

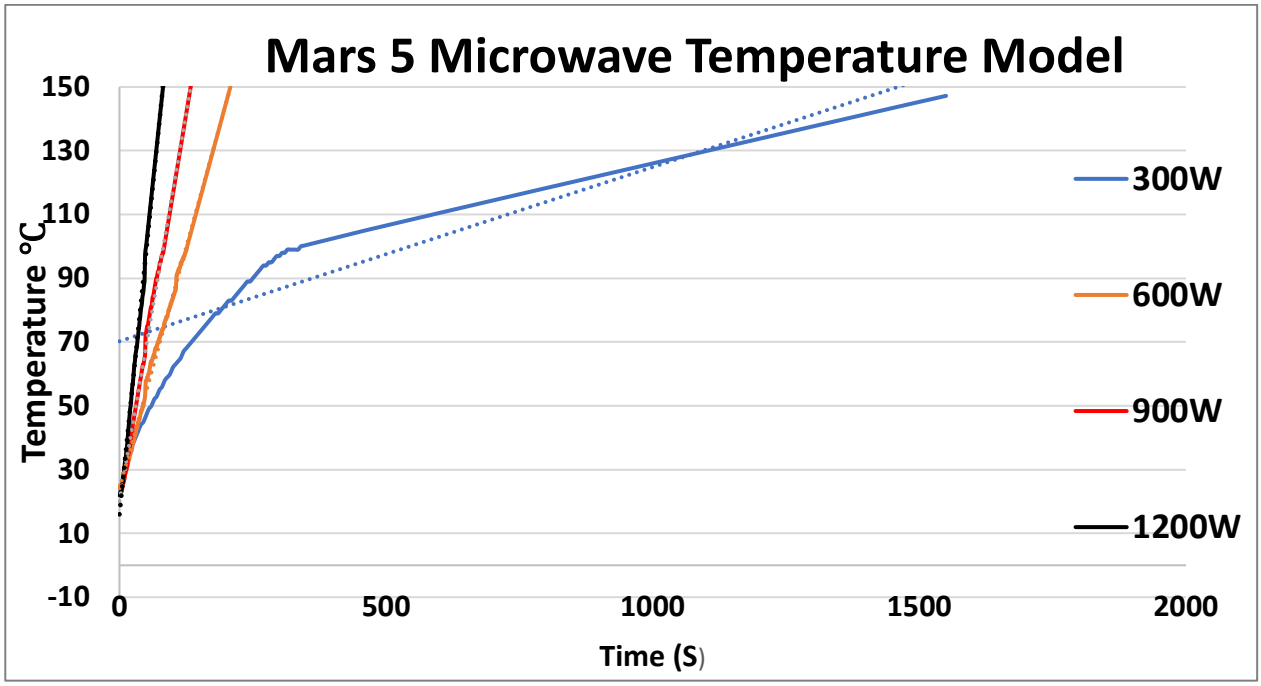


Figure 24. Temperature program models for MAE at various power settings.

From the model shown in Figure 24, 300 W was reached at 150°C in 1550 s (25 min), while 1200 W was reached at 150°C in 150 s (2.5 min). The slopes and y-intercepts are shown in Table 10.

Table 10. Slopes and y-intercepts for MAE temperature program models at various power settings.

| Power (W) | Slope | y-intercept |
|---|---|---|
| 300 | 0.0546 | 70.251 |
| 600 | 0.6042 | 24.173 |
| 900 | 0.9712 | 20.141 |
| 1200 | 1.6445 | 16.002 |

### 3.1.2.3 Power Settings

Using the general guidelines shown in Table 11 from the MARS 5 instrument manual, the power settings for the MAEs was kept constant at 1200 W.[50,88] The optimization methods from the literature are shown in Table 12 which used a lower power (180 W). By increasing to 1200 W, an efficient procedure to reach the final temperature for all 14 vessels was realized.

Table 11. General guidelines for the number of vessels and the recommended power settings.

| General Guidelines | |
|---|---|
| # of Vessels | Power (W) |
| 1 - 2 | 300 |
| 3 - 5 | 600 |
| 6 or more | 1200 |

### 3.1.2.4 Cu Method Development

To develop an optimal BCR MAE method, the extraction reagents and temperature program were studied. Many methods have been reported for BCR extractions using MAE (Table 12).

Table 12. Literature methods for BCR MAE of Cu. For the methods shown, the differences include the solvent, volume, ramp time, final temperature, and hold times.

| Mass of soil (g) | Step | Solvent | Volume (mL) | Power (W) | Ramp Time (min) | Final Temperature (ºC) | Hold Time (s) | Ref. |
|---|---|---|---|---|---|---|---|---|
| 0.5 | EXΔ-[Cu] | 0.01 M Calcium Chloride | 20 | 180 | 35 | 70 | 100 | 89 |
| 0.5 | EXΔ-[Cu] | 0.01 M Calcium Chloride | 20 | 180 | 7 | 70 | 100 | 90 |
| 0.5 | EXΔ-[Cu] | 1.0 M Magnesium Chloride PH 7 | 4 | 180 | 7 | 75 | 30 | 91 |
| 0.5 | CO3-[Cu] | 0.11 M Acetic Acid | 20 | 180 | 35 | 70 | 100 | 89 |
| 0.5 | CO3-[Cu] | 0.11 M Acetic Acid | 20 | 180 | 7 | 70 | 100 | 90 |
| 0.5 | CO3-[Cu] | 1.0 M Sodium Acetate | 4 | 180 | 7 | 75 | 30 | 91 |
| 0.5 | MOX-[Cu] | 0.50 M Hydroxylamine Hydrochloride | 20 | 180 | 35 | 70 | 100 | 89 |
| 0.5 | MOX-[Cu] | 0.50 M Hydroxylamine Hydrochloride | 20 | 180 | 7 | 70 | 100 | 90 |
| 0.5 | MOX-[Cu] | 0.04 M Hydroxylamine Hydrochloride in 25% (v/v) Acetic Acid | 4 | 180 | 7 | 75 | 30 | 91 |
| 0.5 | ORG-[Cu] (1) | 35% (v/v) $H_2O_2$ | 10 | 180 | 35 | 70 | 100 | 89 |
| 0.5 | ORG-[Cu] (2) | 1.0 M Ammonium Acetate | 10 | 180 | 35 | 70 | 100 | 89 |
| 0.5 | ORG-[Cu] (1) | 8.8 M $H_2O_2$ | 10 | 180 | 7 | 75 | 10 | 90 |
| 0.5 | ORG-[Cu] (2) | 1.0 M Ammonium Acetate | 10 | 180 | - | - | - | 90 |
| 0.5 | ORG-[Cu] (1) | 30% (v/v) H2O2 | 4 | 180 | 7 | 80 | 30 | 91 |
| 0.5 | ORG-[Cu] (2) | 3.2 M Ammonium Acetate in 20% (w/w) Nitric Acid | 2.5 | 180 | 7 | 80 | 10 | 91 |

There are significant variations in the solvent type, solvent volume, ramp time, final temperature, and hold time (Table 12). To verify these methods, the authors used

BCR SRMs 483 (sewage sludge), 701 (lake sediment), and/or 601 (lake sediment). To develop the method used in this study, a comparison for the MAE of Cu was studied (Table 13).

Table 13. MAE of Cu, using SRM BCR 483 (sewage sludge), BCR SRM 701 (lake sediment), and BCR SRM 601 (lake sediment) for methods shown in Table 12.

| Certified/Analyzed | CO3 mg $kg^{-1}$ | MOX mg $kg^{-1}$ | ORG mg $kg^{-1}$ | Ref. |
|---|---|---|---|---|
| BCR SRM 483 | 16.8 ± 1.5 | 141.0 ± 20.0 | 132.0 ± 29.0 | 91 |
| Analyzed | 16.2 ± 1.3 | 145.0± 11.2 | 130.0± 11.8 | 91 |
| BCR SRM 701 | 49.3 ± 1.7 | 124 ± 3.0 | 55 ± 4.0 | 89 |
| Analyzed | 48.0 ± 0.3 | 59.0± 1.1 | 212.0± 1.5 | 89 |
| BCR SRM 601 | 10.5 ± 0.8 | 72.8 ± 4.9 | 78.6 ± 8.9 | 90 |
| Analyzed | 5.32 ± 0.32 | 1.58± 0.16 | 62.2± 1.2 | 90 |

From Table 13 the method used (Table 12) for SRM 483 was validated for each fraction.[91] For SRM 701, [Cu] was validated for the CO3-bound fraction, while [Cu] was low for the metal-oxide bound and high for the ORG-bound fractions.[89] For SRM 601, [Cu] was low for all three fractions, especially for the metal-oxide bound fraction.[90] Although SRM 483 was validated, the solvents used in Reference 90 varied compared to the conventional BCR method.[44] In the present study, as a means to compare Cu to prior studies of Pb, the solvents chosen were those used in Reference 89 (which was

the same as the conventional method for Pb), and MAE program used in Reference 91 (validated with SRM 483).

A factorial design was developed (Table 14), in which the maximum final temperature was varied from 80°C to 150°C. The power was set to 1200 W (Table 11), ramp times varied between 3-10 min (based on Figure 24), and total extraction time was kept constant at 20 min.

Table 14. MAE factorial design of ramp-to-temperature optimization for Cu.

| | **Low Temperature** | **Medium Temperature** | **High Temperature** |
|---|---|---|---|
| Short Ramp | Ramp to 80°C in 3 min, hold for 17 min | Ramp to 110°C in 3 min, hold for 17 min | Ramp to 150°C in 3 min, hold for 17 min |
| Medium Ramp | Ramp to 80°C in 5 min, hold for 15 min | Ramp to 110°C in 5 min, hold for 15 min | Ramp to 150°C in 5 min, hold for 15 min |
| Long ramp | Ramp to 80°C in 10 min, hold for 10 min | Ramp to 110°C in 10 min, hold for 10 min | Ramp to 150°C in 10 min, hold for 10 min |

Because of the high cost and limited quantity of SRMs, soil core 32 was used as "representative" to determine the optimal extraction conditions before further validation of SRM BCR 701 by the optimized GF-AAS method. The optimal conditions were determined for MOX-bound fraction because it contained the highest level of Cu (Table 13): 110°C, 10 min ramp time, and 10 min hold time at 110°C. The results for the extraction are shown in Table 14 using the calibration model (Figure 94 in Appendix B).

### 3.1.3 Chemical Speciation of Cu

#### 3.1.3.1 Bi-modal Distribution of Cu

During the development of the BCR MAE GF-AAS method, soil core 32 (38.9 m) was used to determine the optimal extraction conditions. In developing an extraction method, it is important to define key factors (e.g., temperature, power, time) and consider what the response should look like. This experiment was designed such that a gradual or sharp increase in [Cu] to a plateau was expected as shown in Figure 25.

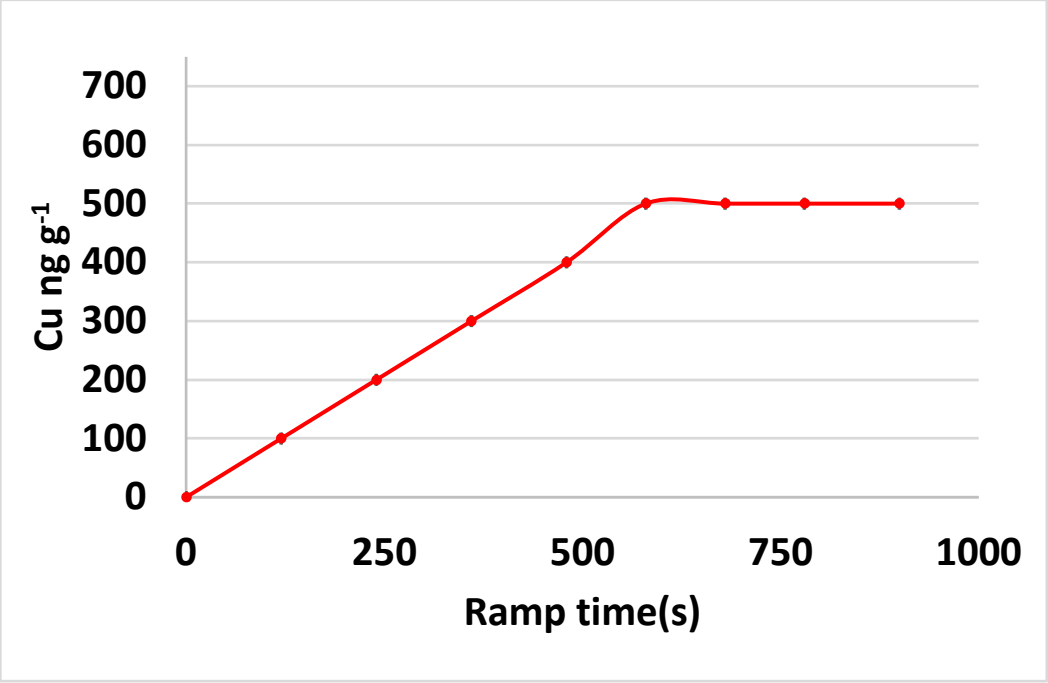


Figure 25. Expected unimodal release of Cu with increasing ramp time for the method development of the BCR MAE GF-AAS method.

However, a bimodal release of Cu with increasing ramp time was observed (Figure 26).

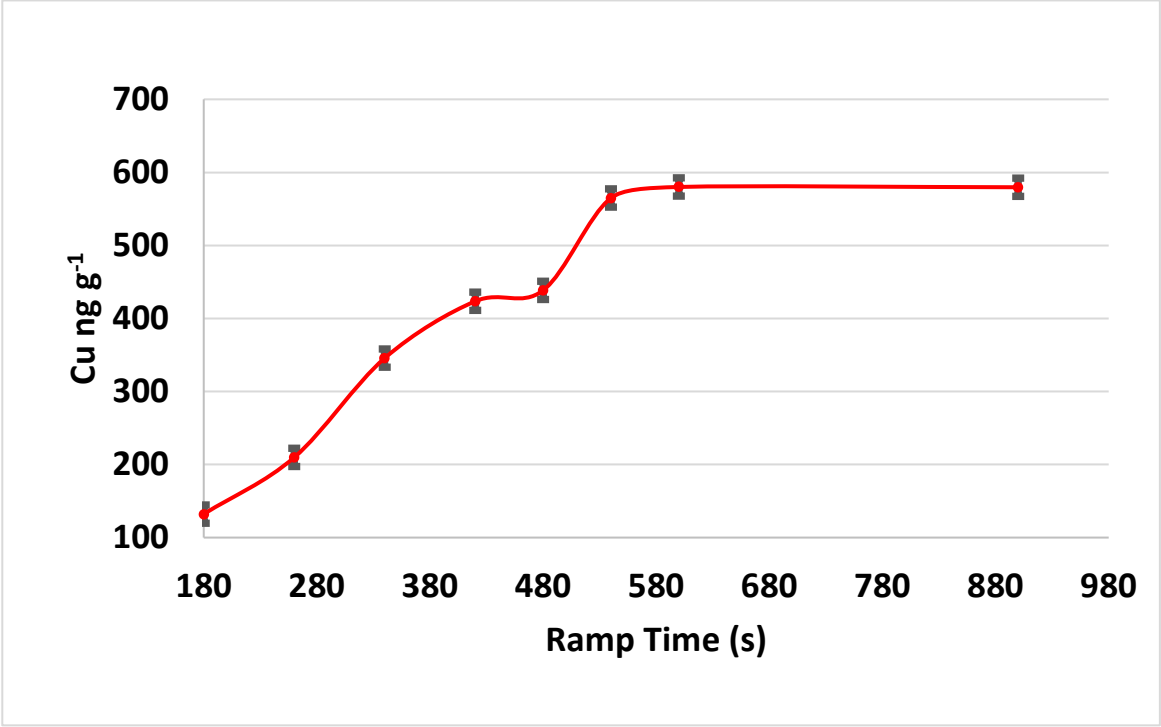


Figure 26. For soil core 32 (6-7”), a bimodal release of Cu with increasing ramp time was observed; (n=3) at the 95% confidence level.

One theory is that the microwave is able to extract the RFC-[Cu] because it is more energetic. A model for a soil particle with two different kinds of Cu is shown in Figure 27, with an outer layer that is labile Cu (1%, i.e., easily released) and an inner layer of refractory Cu (>99%, i.e., immobile) which is presumably in the form of Fe oxides.

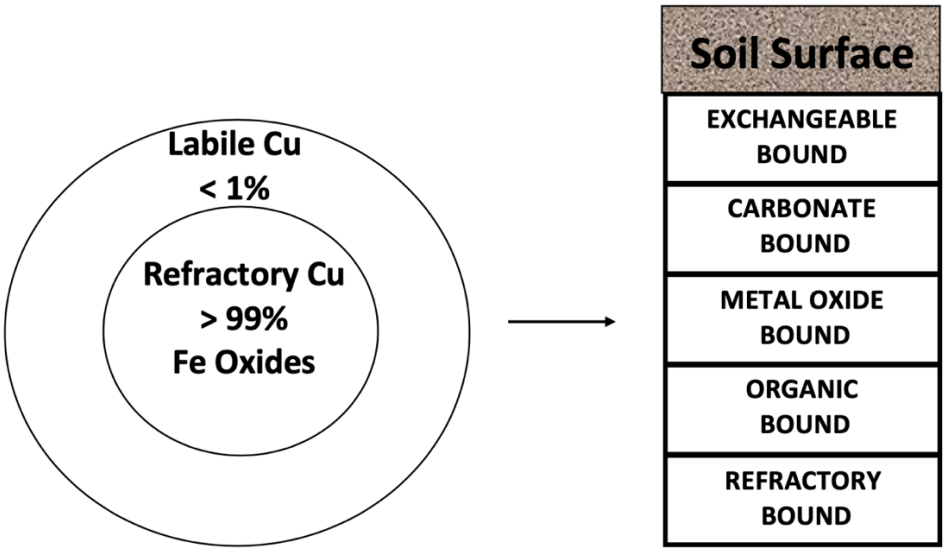


Figure 27. Cross-sectional diagram of a soil particle in which the Cu is speciated into EXΔ-, CO3-, MOX-, ORG-, AND RFC-bound fractions.

This observation has not been reported in the literature and therefore represents a significant bias in the MAE method. Methods that have been published in the literature have reported a shorter extraction time at decreased power and temperature, but this appears to introduce a major error. The published MAE methods have been promoted because they are faster but appear to be inaccurate. Thus, there is a need to more thoroughly investigate this effect at longer extraction times at increased power and higher temperature.

Conventional extraction is only able to release approximately 1% of the non-RFC-[Cu] (i.e., not observing RFC-[Cu] because MAE is not used). For this study, A comparison of conventional and MAE BCR extraction methods (Figure 28 and Table 15) reveals that MAE BCR extracts are 28.31, 44.76 and 41.85% higher in [Cu] as compared to the conventional method for the CO3-, MOX-, AND ORG-bound fractions,

respectively. These results clearly show that a significant error is introduced by the MAE method when applied to the BCR procedure. These results are also further revealing in that the highest amount of Cu is released in the MOX-bound fraction. This observation clearly supports the interpretation of this study that refractory-bound MOX species are the primary source of the MAE-bias error. Furthermore, ORG-Cu species are also quite significant, suggesting that there are also two major forms of these as well, i.e., "loosely-" (extractable by the conventional BCR method) and "tightly-" (extractable by the MAE-BCR method) bound forms of ORG-Cu that can be distinguished by using the MAE approach.

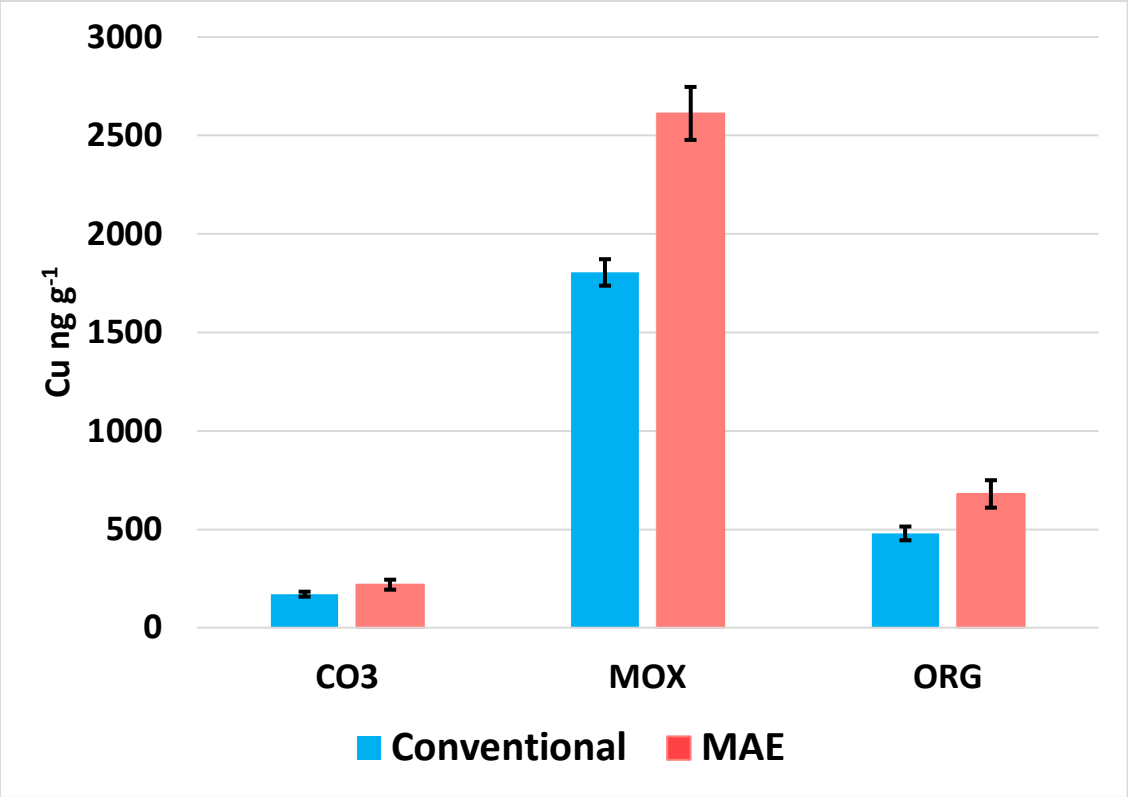


Figure 28. Mass balance for soil core 32, comparing conventional and MAE BCR for CO3-, MOX-, and ORG-[Cu]; (n=3) at the 95% confidence level.

Table 15. Mass balance for soil core 32, comparing conventional and MAE BCR for CO3, MOX, AND ORG-[Cu]; (n=3) at the 95% confidence level.

| Extraction Method | CO3 (ng $g^{-1}$) | MOX (ng $g^{-1}$) | ORG (ng $g^{-1}$) |
|---|---|---|---|
| Conventional | 170.30 ± 12.68 | 1804.51 ± 67.25 | 478.94 ± 34.90 |
| Microwave | 218.51 ± 25.36 | 2612.13 ± 134.50 | 679.38 ± 69.80 |
| % Difference | 28.31% | 44.76% | 41.85% |

Furthermore, besides the analytical implications of the MAE bias error, there are environmental chemistry implications as well in terms of bioavailability. Because RFC-[Cu] is found more deeply within the soil particle, it is not considered to be "bioavailable". Rather than the "natural weathering" which the BCR method is designed to reflect, REF-Cu can become "bioavailable" when ingested by an organism. The low pH of gastrointestinal tracts in most organisms (including, of course humans) will readily release the RFC-[Cu] from soil particles. Fe oxide-bound MOX species appear to be the principal culprits — Fe oxides present relatively deeply within the soil particle very tenaciously bind Cu, as described below.

#### 3.1.3.2 Bi-modal Distribution of Cu, Fe, and Mn

The bimodal release of Cu was further investigated by ICP-MS using soil core 32 for the MOX-bound fraction. Similarly, to the bimodal study described above, the extractions were performed by varying the ramp time (3-10 min) with a final extraction temperature of 110°C. Two distinct increases in [Cu] were observed as a function of ramp time throughout the soil core (at depths of 3-7 in) as shown in Figure 29.

Soil core 32 was analyzed for Fe and Mn at depths of 3-4 in and 4-5 in, and the increases in Cu correlate to increases in Fe but show no correlation to Mn (Figure 30), thereby clearly showing that iron oxides were released as ramp time increased.

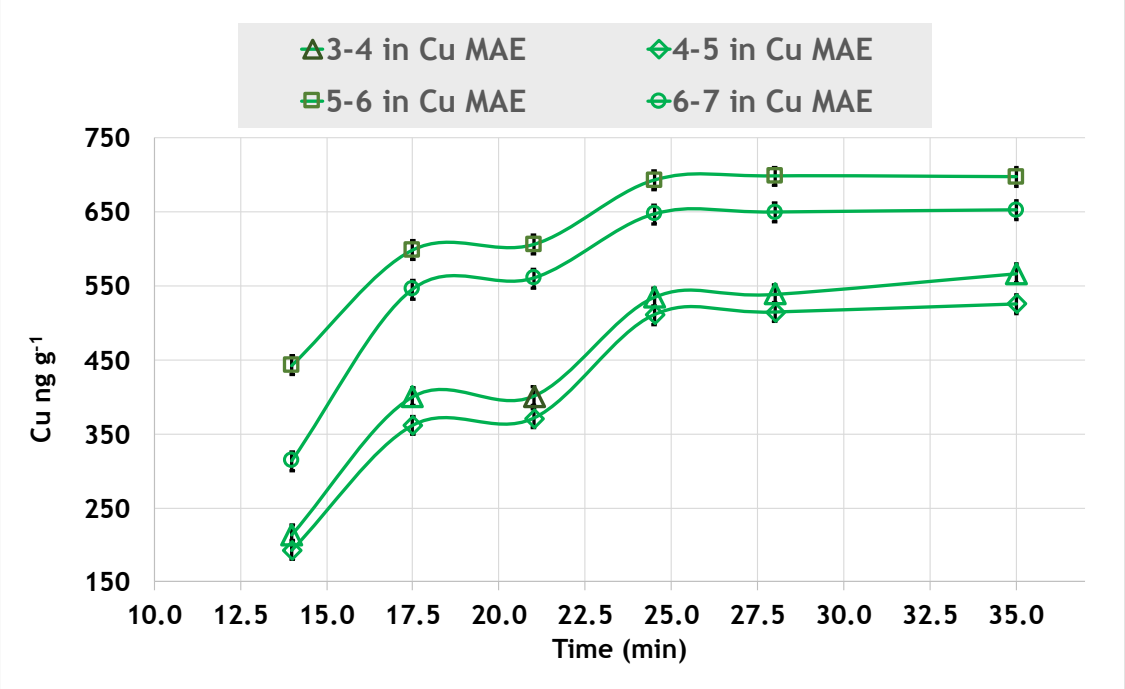


Figure 29. Bi-modal release Cu for soil core 32 using the MAE BCR method for the MOX fraction by ICP-MS; (n=3) at the 95% confidence level.

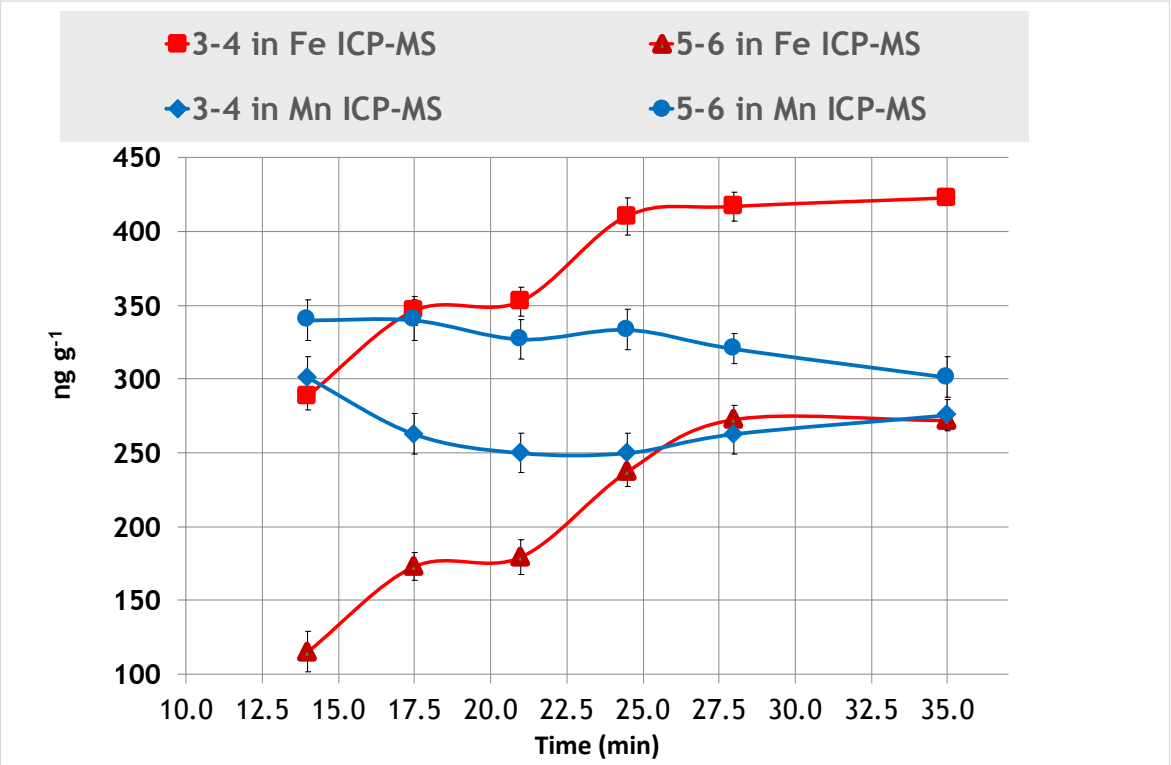


Figure 30. Bi-modal release Fe for soil core 32, using MAE BCR method for the MOX fraction by ICP-MS; (n=3) at the 95% confidence level.

Although it is not bioavailable as defined by the BCR procedure, the accurate determination of trace metals by the application of the MAE method should be studied more thoroughly for a variety of soil types for Cu as well as for other metals of interest.

Another well-known source of error in the BCR method was initially described by Tipping *et al.* in 1985. These works reported the problem of re-adsorption during extraction, where metal is initially released by the extracting reagent but then re-precipitated onto the solid phase by the time that the procedure is completed.[92] As Tipping and co-workers concluded: "These findings mean that considerable care must be taken when attempting to employ selective chemical extraction to evaluate metal oxide interactions in the environment". To investigate this potential source of error, the

cooling of the vessel after the MAE method was completed was studied to determine if readorption occurred in the present study.

To determine if the [Cu] decreased by re-adorption onto the soil particles as the extraction vessel cooled, two methods were used— a 10 min ramp time/10 min hold time at either 80°C or 110°C. After the MAE process was complete, the vessel was vented, centrifuged, and a thermometer was placed in the vessel. For every decrease of 10°C, 10 µL of supernatant was removed and the [Cu] was determined by GF-AAS. The [Cu] readsorption was observed to be negligible, as shown by a constant [Cu] as the solution cooled (Figure 31).

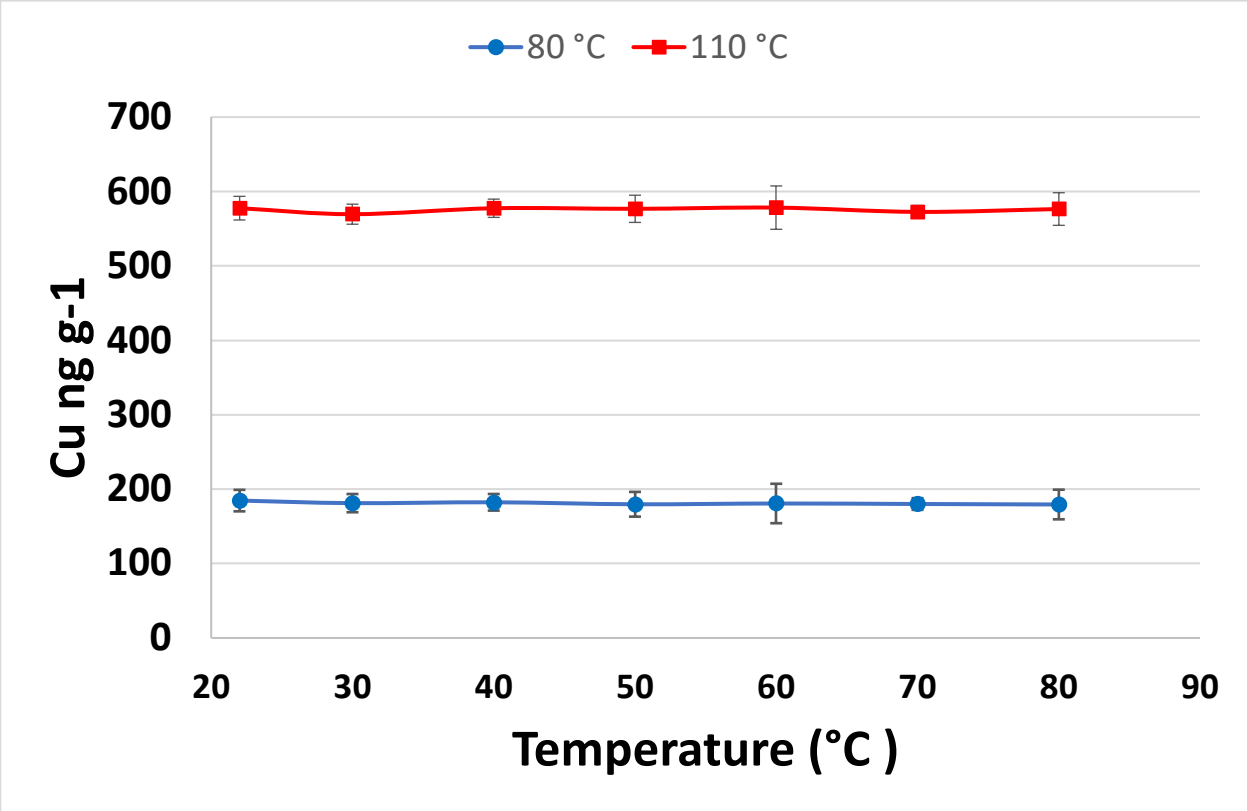


Figure 31. Cu readsorption in soil core 32 (6-7”) was negligible as the solution cooled; (n=3) at the 95% confidence level.

Thus, for trace metal determination by MAE, there is a critical need to know that even though the method is fast, a significant bias is introduced from the otherwise BCR-inaccessible species (principally MOX- and ORG-bound species). This observation that further investigations are needed to elucidate the molecular structures that are present and the mechanisms of Cu release. In the Tipping *et al.* study, Ca, Zn, and Ba were predominantly associated with the MOX-bound species, while Pb was primarily associated with Fe-bound species.[92] This study also suggested that similar results would be expected for other strongly adsorbed metals such as Cu. The structures or mechanisms were not defined by Tipping *et al.*, but provided the insight that iron oxides are preferentially complexed with Pb (and presumably Cu) and then released differently by the MOX reagent ($NH_2OH$•HCl).[92]

Because there are many types of iron oxides, the structures present and mechanism of binding are undoubtedly to be complex for a given metal of interest.[8] It has been noted that the formation of crystalline iron minerals is strongly inhibited by the presence of high natural organic matter (NOM).[93] In studies of aqueous Fe(II), it was observed that NOM strongly impacts the mechanism of Fe mineral transformations and Fe atom exchange.[93]

The BF soil was found that it generally had a high ORG content in the upper 3-4 inches and a high clay content below 4 inches.[73] With the layering of NOM to clay, the primary mechanism and the structures involved for the formation and transformation of RFC-[Cu] is difficult to study, i.e, the processes occur over a long period of time. It is widely acknowledged that these studies are poor substitutes for soils that have been

genuinely aged over long periods of time.[11] Thus with the complexity of the various forms of Fe oxides, the mechanisms and structures are poorly understood.

Following the bi-modal distribution study described previously in this section, the optimal MAE conditions were determined (Table 16) using the calibration model (Figure 94 in Appendix B).

Table 16. Factorial design for the ramp-to-temperature optimization using the MOX-bound fraction of core 32 (5-6 in); (n=3) at the 95% confidence level.

| | **Low Temperature ($ng\ g^{-1}$)** | **Medium Temperature ($ng\ g^{-1}$)** | **High Temperature ($ng\ g^{-1}$)** |
|---|---|---|---|
| Short Ramp | 54.1 ± 3.5 | 132.1 ± 4.0 | 117.1 ± 4.3 |
| Medium Ramp | 64.3 ± 5.1 | 423.6 ± 7.6 | 405.6 ± 9.1 |
| Long ramp | 71.3 ± 6.3 | 580.0 ± 9.3 | 551.4 ± 10.3 |

The optimized MAE BCR-GF-AAS method was applied to BCR SRM 701 (Table 17) using the calibration models for the BCR extracts (Figure 95-Figure 97 in Appendix B). The results were within the range of the certified values, thereby validating the method for all four steps in the BCR procedure.

Table 17. Validation of the MAE BCR method by using SRM 701; (n=3) at the 95% confidence level.

| | CO3-[Cu] $mg\ kg^{-1}$ | MOX-[Cu] $mg\ kg^{-1}$ | ORG-[Cu] $mg\ kg^{-1}$ |
|---|---|---|---|
| BCR SRM 701 | 49.3 ± 1.7 | 124 ± 3.0 | 55 ± 4.0 |
| Calibration | 48.60 ± 6.58 | 126.17 ± 11.18 | 54.41 ± 5.35 |
| % RSD | 5.5 | 3.6 | 4.0 |

### 3.1.3.3 Hg Method Development

As performed for Cu, an optimal MAE ICP-MS method for Hg was developed. The BCR extraction reagents and MAE temperature program were optimized. Several methods have been reported for Hg extraction by using MAE (Figure 32, Table 18). The factorial design used in the optimization study is shown in Table 20.

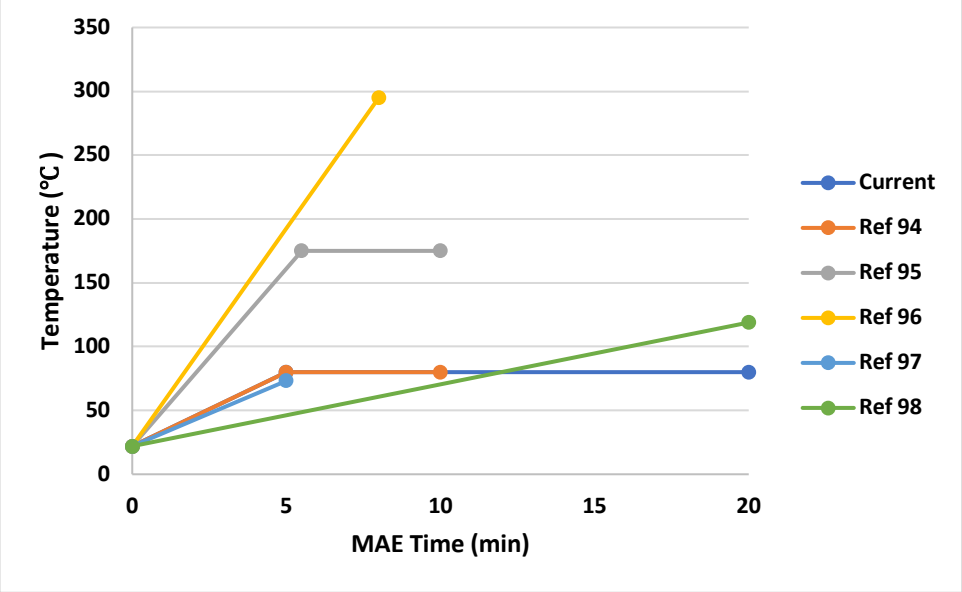


Figure 32. Comparison of published methods for MAE of Hg.

Table 18. Published methods for MAE of Hg in environmental solids.

| Mass of soil (g) | Solvent | Volume (mL) | Power (W) | Ramp Time (min) | Final Temperature (°C) | Hold Time (min) | Ref. |
|---|---|---|---|---|---|---|---|
| 1.0 | 6 M $HNO_3$ | 10.0 | - | 5 | 80 | 5 | 94 |
| 1.0 | 4 M $HNO_3$ | 10.0 | 1000 | 5.5 | 100 | 4.5 | 95 |
| 0.7 | Conc. $HNO_3$ & $H_2O$ | 10.0 & 4.5 | 570 | 8 | 295 | 0 | 96 |
| 0.1 | Conc. $HNO_3$ | 5.0 | 60 | 5 | 75 | 15 | 97 |
| 0.2 | $CH_3OH$ & 6M HCl | 5.0 & 100 uL | 40 | 20 | 120 | 0 | 98 |

Not surprisingly, there are variations in the published methods as observed for Cu (Figure 32, Table 18). To validate these methods, the authors used CRM 580 (estuarine sediment), CRM 277 (estuarine sediment), and PACS-1 (lake sediment).

Table 19. MAE of Hg, using CRM 580 (estuarine sediment), 277 (estuarine sediment), and PACS-1 (lake sediment) for methods in Table 18.

| Certified Reference Material | Certified Hg mg $kg^{-1}$ | Observed Hg mg $kg^{-1}$ | Ref. |
|---|---|---|---|
| CRM 277 | 1.77 ± 0.06 μg $g^{-1}$ | 1.73 ± 0.04 μg $g^{-1}$ | 96 |
| CRM 580 | 132.0 ± 3.0 | 129.0 ± 6.5 | 94 |
| CRM 580 | 132.0 ± 3.0 | 133.0± 4.0 | 95 |
| CRM 580 | 132.0 ± 3.0 | 17.08 ± 0.64 | 98 |
| CRM PACS-1 | 4.57 ± 0.16 | 4.46 ± 0.12 | 97 |

As shown in Table 19 and Table 18, the methods were validated for CAT-[Hg] except by Park.[98] In the present work, a modified MAE factorial design was developed (Table 20) with the following factors kept constant: 1.000 g of soil, 20.0 mL conc. $HNO_3$, 14 vessels (2.3.2.2), 1200 W (Table 11), and total extraction time of 20 min.[96-98]

Table 20. MAE factorial design of ramp-to-temperature optimization for Hg.

| | **Low Temperature** | **Medium Temperature** | **High Temperature** |
|---|---|---|---|
| Short Ramp | Ramp to 80°C in 2 min, hold for 18 min | Ramp to 150°C in 2 min, hold for 18 min | Ramp to 200°C in 2 min, hold for 18 min |
| Medium Ramp | Ramp to 80°C in 5 min, hold for 15 min | Ramp to 150°C in 5 min, hold for 15 min | Ramp to 200°C in 5 min, hold for 15 min |
| Long ramp | Ramp to 80°C in 10 min, hold for 10 min | Ramp to 150°C in 10 min, hold for 10 min | Ramp to 200°C in 10 min, hold for 10 min |

For validation of the factorial design (Table 20), NIST SRM 1944 "New Jersey Waterway Sediment" was tested. The certified value for Hg was 3.4 ± 0.5 mg/kg. Optimal conditions used in this work were: 80°C, 5 min ramp time, and 15 min hold time at 80°C. ICP-MS was used for quantification of Hg. The results for the extraction are shown in Table 21 using a calibration model (see Figure 98 in Appendix B). The method was certified in this work at the lowest temperature (80°C) and a 5 min ramp time, the former as a precaution in working with concentrated $HNO_3$.

Table 21. MAE factorial design for the ramp-to-temperature optimization for Hg using NIST SRM 1944 by ICP-MS; (n=3) at the 95% confidence level.

| | **Low Temperature (mg kg-1)** | **Medium Temperature (mg kg-1)** | **High Temperature (mg kg-1)** |
|---|---|---|---|
| Short Ramp | 3.66 ± 0.46 | -0.10 ± 0.5 | 1.21 ± 0.70 |
| Medium Ramp | 3.26 ± 0.31 | 2.61± 1.90 | 0.41 ± 0.28 |
| Long ramp | 3.13 ± 1.05 | -0.04 ± 0.25 | 0.11 ± 0.40 |

### 3.1.4 Validation of the Conventional Method for Pb

The optimized conventional BCR-GF-AAS method for Pb described in prior work for the soil core samples was applied to BCR SRM 701.[73] The results (Table 22)

were within the range of certified values using the calibration models (Figure 99, Figure 100, and Figure 101 in Appendix B), thereby validating the method for all four steps in the BCR method for Pb as well as Cu.

Table 22. Validation of the MAE BCR method for Pb by using SRM 701; (n=3) at the 95% confidence level.

| | CO3-[Pb] mg $kg^{-1}$ | MOX-[Pb] mg $kg^{-1}$ | ORG-[Pb] mg $kg^{-1}$ |
|---|---|---|---|
| BCR SRM 701 | 3.18 ± 0.21 | 126 ± 3 | 9.3 ± 2.0 |
| Calibration | 2.98 ± 1.23 | 127.66 ± 6.90 | 9.08 ± 2.44 |
| % RSD | 6.67 | 2.17 | 4.20 |

### 3.1.5 Method Performance

#### 3.1.5.1 Quantification Models

The second question in this study was whether the BCR method revealed the chemical speciation of Cu, Pb, and Hg in the soil cores. Conventional calibrations were performed on the day of analysis for each of the BCR extractions of the soil samples to reliably determine chemical speciation. Quality control (QC) samples were intermittently included to ensure that the calibration was maintained throughout the day. For example, a 50 ppb Cu standard in 1% (v/v) nitric acid was measured after every 15 unknown samples.

##### 3.1.5.1.1 Exchangeable Cu

The concentrations that were measured in the EXΔ-[Cu] extracts in the soil samples were below the MDL of the GF-AAS method. This was not surprising given

that similar results were observed in the earlier Pb study.[73] An example of a calibration model for EXΔ-[Cu] in soil core samples is provided in Figure 102 in Appendix B.

#### 3.1.5.1.2 Carbonate-bound Cu

CO3-[Cu] extracts of soil samples were determined using calibration models (Figure 103-Figure 106 in Appendix B). Absorbance readings were collected over a period of 41 weeks (Table 23). The drift of the calibration model parameters over this period of time is shown in Figure 33 and Figure 34. The sensitivities (0.0041 ± 0.0003) and y-axis intercepts (0.0054 ± 0.0005) reveal excellent precision with negligible drift. The results for the QC samples (Table 24) show that the calibration model was stable during a given day of measurement and the observed drift was negligible (Figure 35) further demonstrating that the BCR-GF-AAS method for the CO3-[Cu] was acceptable.

Table 23. Model parameter values over time of $CH_3COOH$ extraction of the CO3-[Cu] soil core samples.

| Date | Slope | y-Intercept/b |
|---|---|---|
| Feb 3, 2019 | 0.0041 | 0.0057 |
| Jun 22, 2019 | 0.0041 | 0.0057 |
| July 7, 2019 | 0.0046 | 0.0048 |
| Nov 17, 2019 | 0.0037 | 0.0058 |

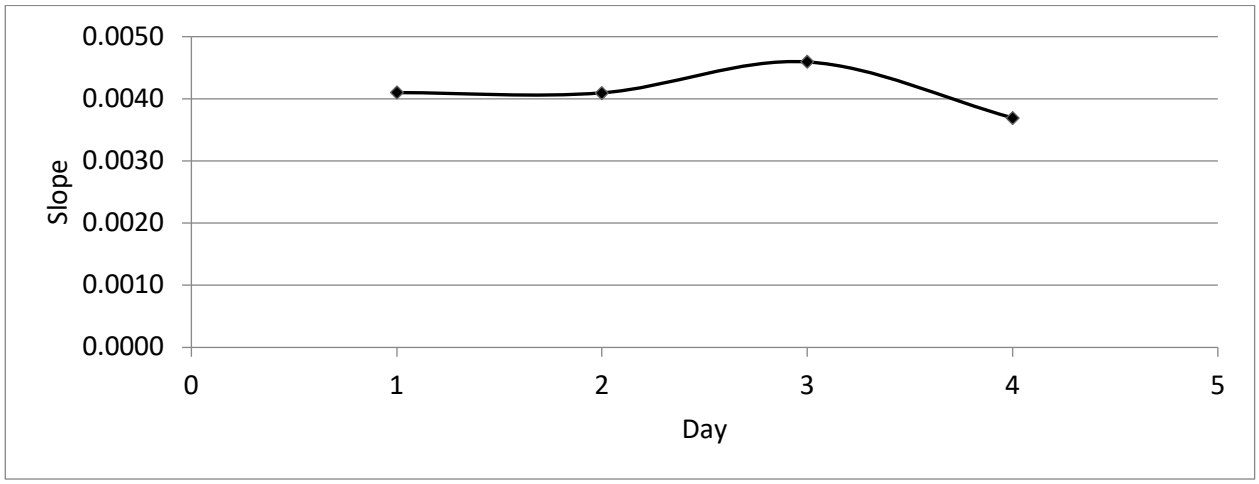


Figure 33. Method sensitivity changes for the $CH_3COOH$ extraction of the CO3-[Cu] soil core samples.

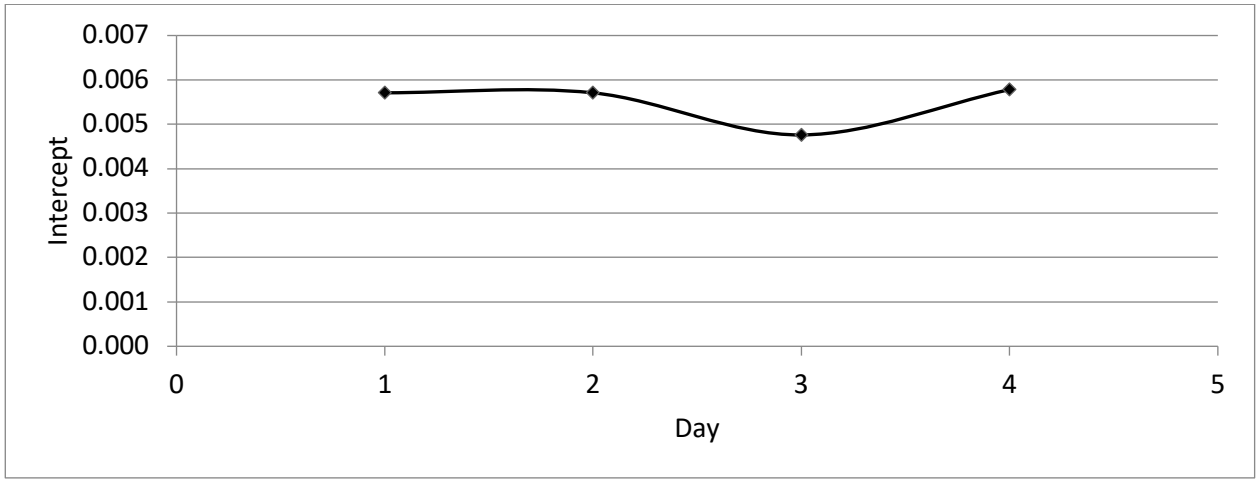


Figure 34. Y-axis intercept changes for $CH_3COOH$ extraction of the CO3-[Cu] soil core samples.

Table 24. Quality control samples for the CO3-bound soil core samples; (n=3).

| QC Sample/ng $g^{-1}$ | Cu/ng $g^{-1}$ | RSD |
|---|---|---|
| 6.0 | 6.01 | 3.81 |
| 10.0 | 9.86 | 2.18 |

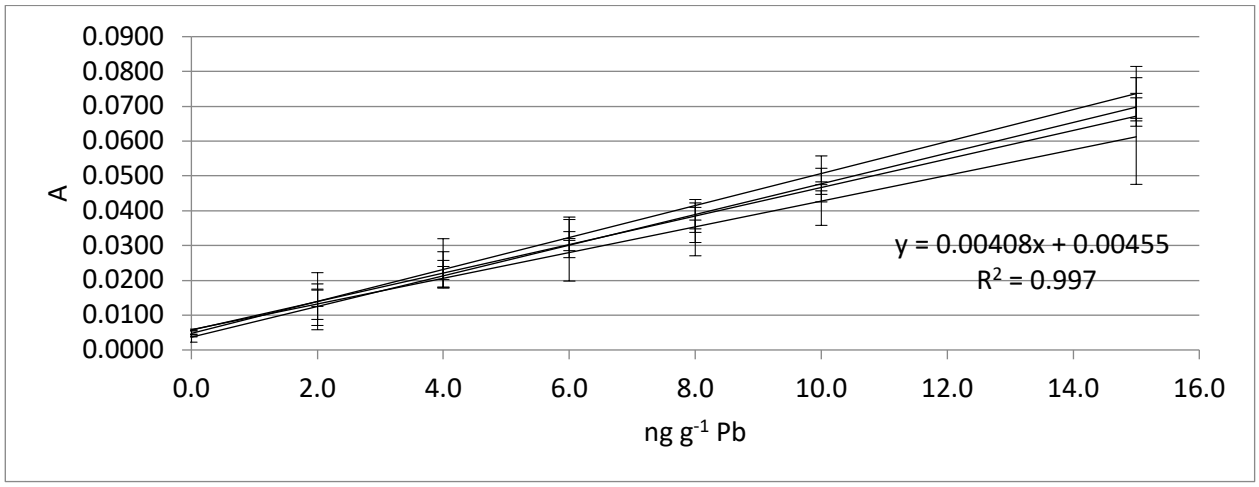


Figure 35. Overlay of the calibration models that were used for $CH_3COOH$ extraction of the CO3-[Cu] in the soil core samples.

#### 3.1.5.1.3 Metal Oxide-bound Cu

MOX-[Cu] extracts of soil samples were determined using calibration models (Figure 107-Figure 114 in Appendix B). Absorbance readings were collected over an eighteen-month period and the parameters of the models are shown in Table 25. The sensitivities (0.0024 ± 0.0004) reveal excellent precision with negligible drift over the eighteen-month period. The y-axis intercepts (0.0078 ± 0.0041) displayed an increased drift with approximately 80% variability over the eighteen-month period (Figure 36, Figure 37). The variation in the y-axis intercept is presumed to be due to random variability.

The calibration model was accurately reflecting the concentration of the samples/standards during the analysis period (Table 26). A composite of all the calibration models constructed (Figure 38) shows only a relatively low degree of drift, thus the methodology for the MOX-[Cu] extraction was robust for this study.

Table 25. Model parameters values for the hydrogen peroxide (oxidative) extraction of the ORG-[Cu] soil core samples.

| Date | Slope | y-Intercept/b |
|---|---|---|
| Jun 24, 2018 | 0.0025 | 0.0012 |
| Jul 7, 2018 | 0.0025 | 0.0113 |
| Feb 3, 2019 | 0.0023 | 0.0129 |
| Mar 12, 2019 | 0.0027 | 0.0095 |
| Jun 28, 2019 | 0.0027 | 0.0098 |
| Jul 22, 2019 | 0.0015 | 0.0050 |
| Nov 17, 2019 | 0.0023 | 0.0032 |
| Nov 19, 2019 | 0.0026 | 0.0095 |

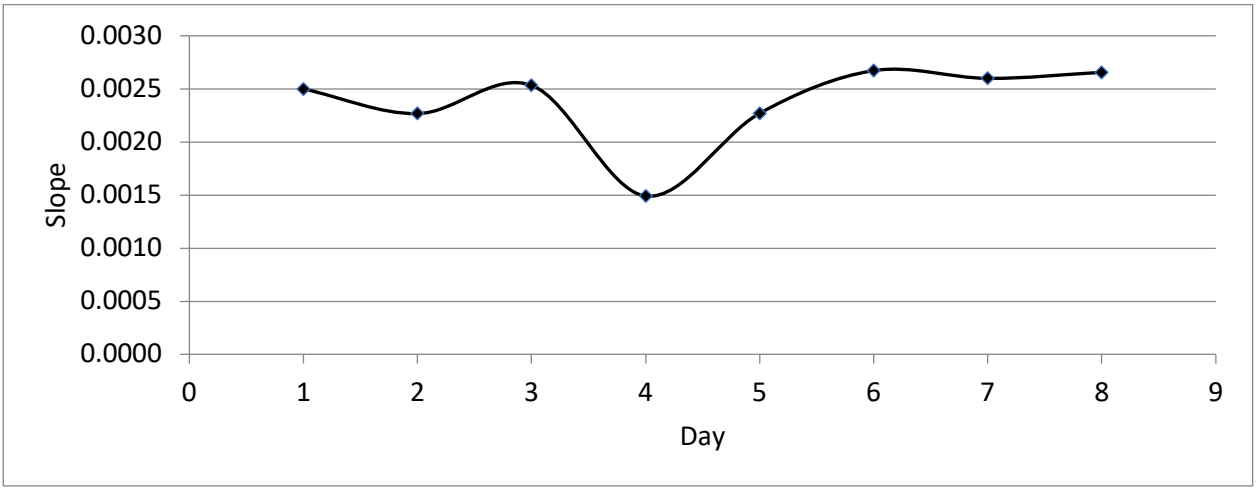


Figure 36. Variation in method sensitivity of the hydroxylamine-hydrochloride extraction of the MOX-[Cu] soil core samples.

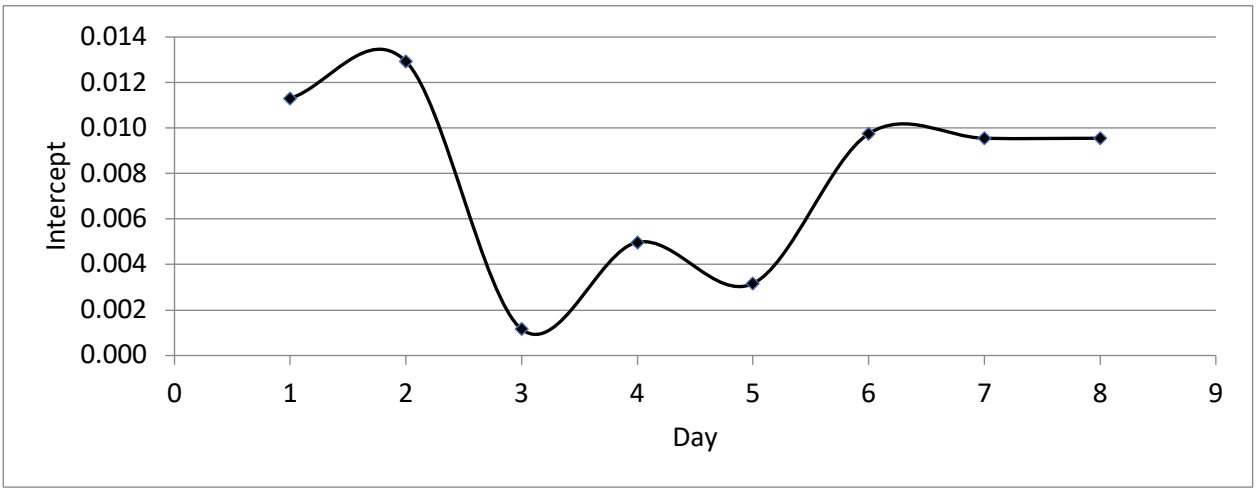

Figure 37. Variation in y-axis intercept of hydroxylamine-hydrochloride extraction of the MOX-[Cu] soil core samples.

Table 26. Quality control samples for the MOX-bound soil core samples.

| QC Sample/ng $g^{-1}$ | Cu/ng $g^{-1}$ | RSD |
|---|---|---|
| 15.0 | 15.04 | 4.19 |
| 50.0 | 55.32 | 2.54 |

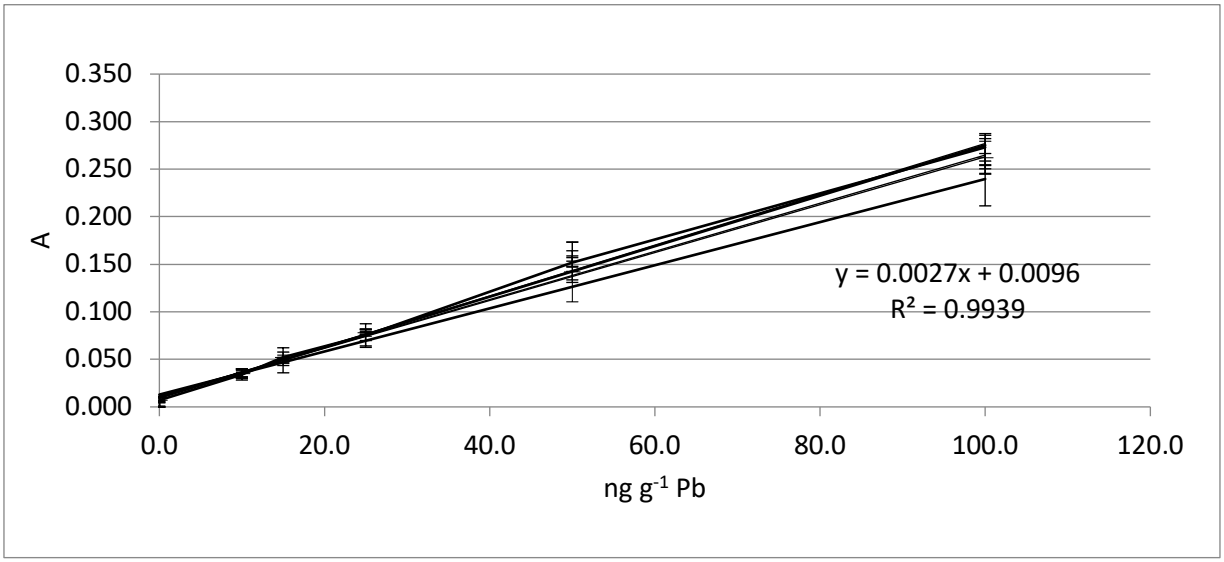


Figure 38. Overlay of the calibration models that were used for the hydroxylamine-hydrochloride extraction of MOX-[Cu] in the soil core samples.

#### 3.1.5.1.4 Organic-bound Cu

Calibration models for the hydrogen peroxide extraction of the ORG-[Cu] in soil core samples is shown in Figure 115-Figure 124 (Appendix B). Absorbance readings were collected over an eighteen-month period and the values for the calibration model parameters are shown in

Table 27. The sensitivities (0.0028 ± 0.0002 L $ng^{-1}$) revealed excellent precision with negligible drift over the eighteen-month time period. The y-axis intercept (0.0157 ±

0.004) also displayed excellent precision. The variation, or drift, in calibration model parameters can be seen in Figure 39 and Figure 40.

The calibration model was accurately reflecting the concentration of the samples/standards during the analysis period (Table 28). A composite of all the calibration models collected (Table 27 and Figure 41) shows a slight drift, thus it can be concluded that the methodology for the hydrogen peroxide, oxidative extraction of the ORG-[Cu] was acceptable for this study.

Table 27. Model parameters values for the hydrogen peroxide (oxidative) extraction of the ORG-[Cu] soil core samples.

| Date | Slope | y-Intercept/b |
|---|---|---|
| Jun 24, 2018 | 0.0028 | 0.0192 |
| Jun 26, 2018 | 0.0027 | 0.0131 |
| Jul 7, 2018 | 0.0028 | 0.0250 |
| Feb 3, 2019 | 0.0031 | 0.0127 |
| Mar 12, 2019 | 0.0028 | 0.0163 |
| Jun 28, 2019 | 0.0028 | 0.0161 |
| Jul 22, 2019 | 0.0024 | 0.0139 |
| Aug 1, 2019 | 0.0033 | 0.0136 |
| Nov 17, 2019 | 0.0033 | 0.0104 |
| Nov 19, 2019 | 0.0025 | 0.0172 |

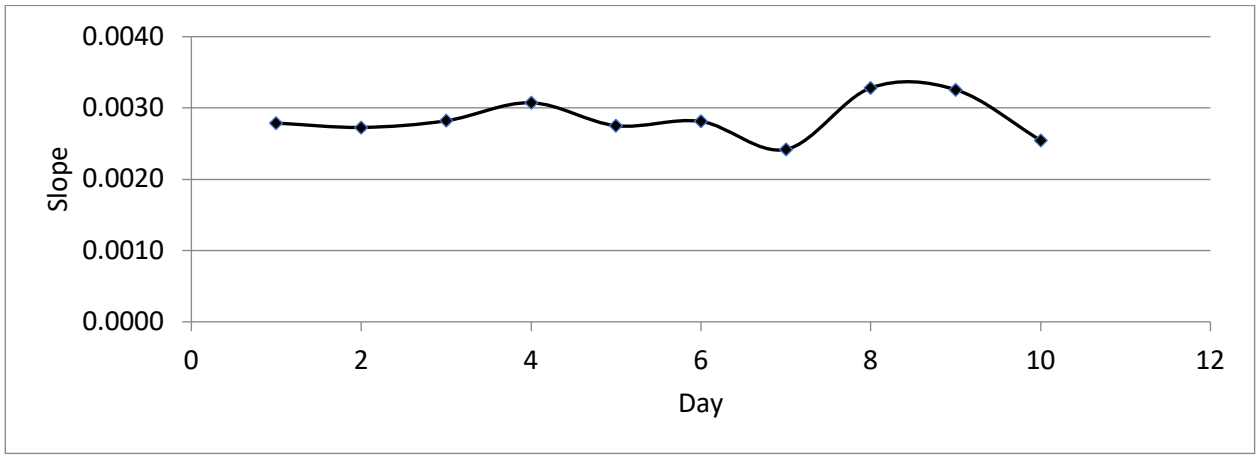


Figure 39. Variation in method sensitivity for the hydrogen peroxide (oxidative) extraction of the ORG-[Cu] soil core samples.

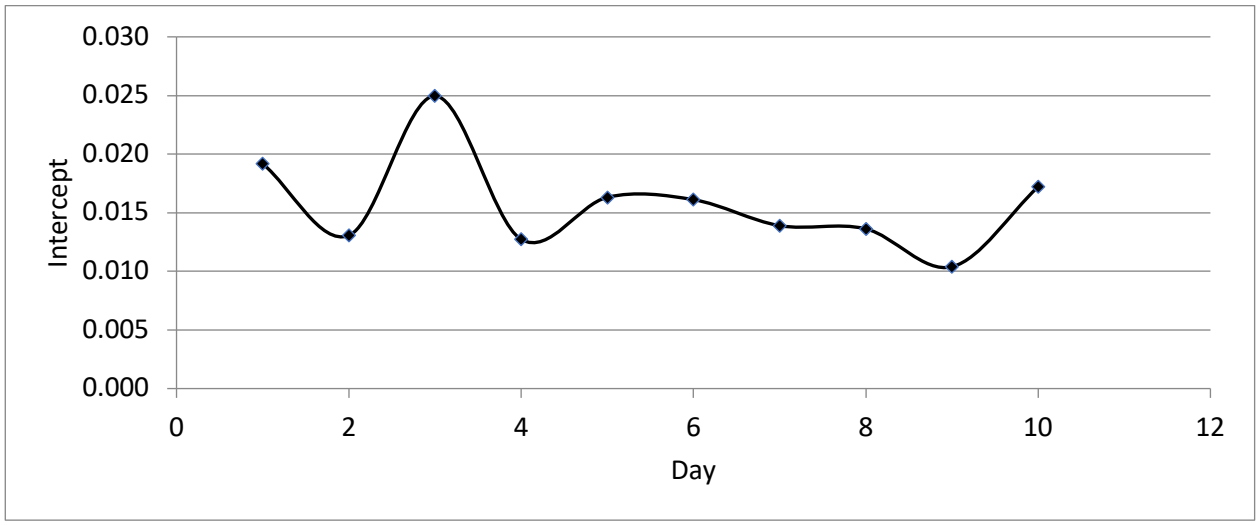


Figure 40. Changes in y-axis intercept for the hydrogen peroxide (oxidative) extraction of the ORG-[Cu] soil core samples.

Table 28. Quality control samples for the ORG-bound soil core samples; (n=3).

| QC Sample/ng $g^{-1}$ | Cu/ng $g^{-1}$ | RSD |
|---|---|---|
| 15.0 | 15.24 | 5.69 |
| 25.0 | 25.04 | 4.49 |

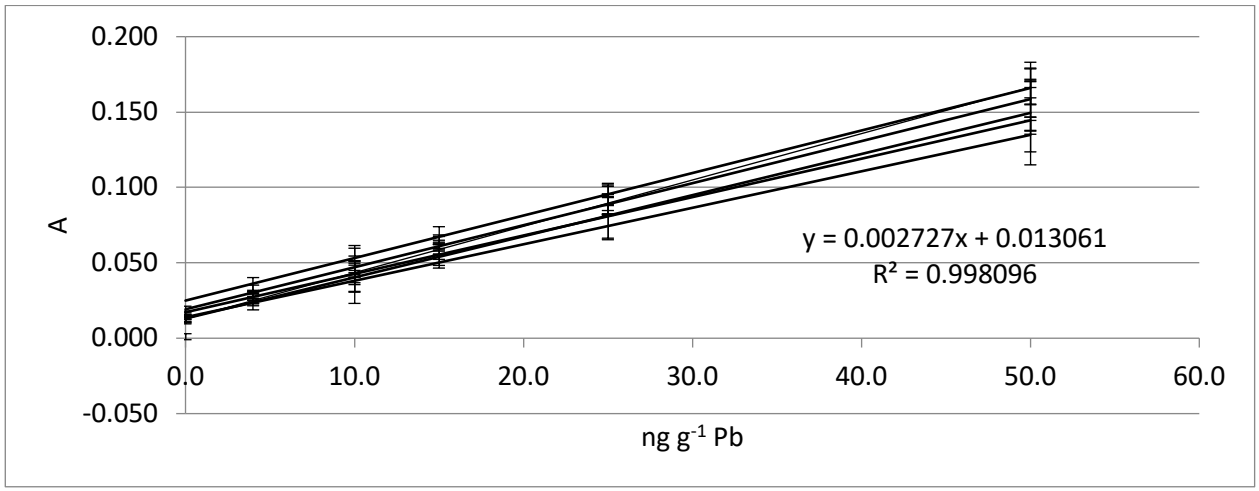


Figure 41. Overlay of the calibration models that were used for the hydrogen peroxide (oxidative) extraction of ORG-[Cu] in the soil core samples.

Figure 42 and Figure 43 are a composite of the model parameters for all of the Cu BCR extractions, excluding the EXΔ fraction.

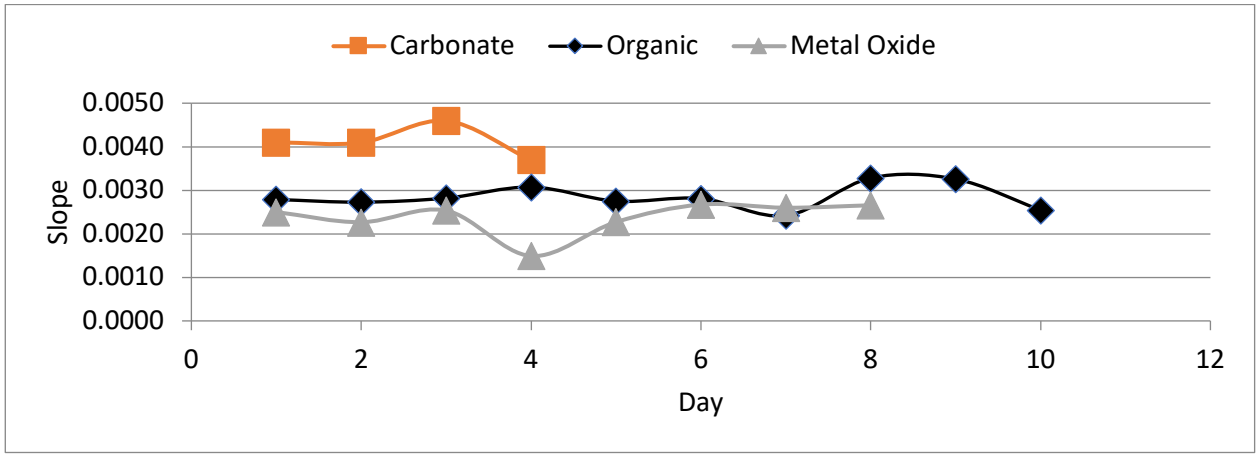


Figure 42. Variation in method sensitivity for the BCR extractions of the soil core samples.

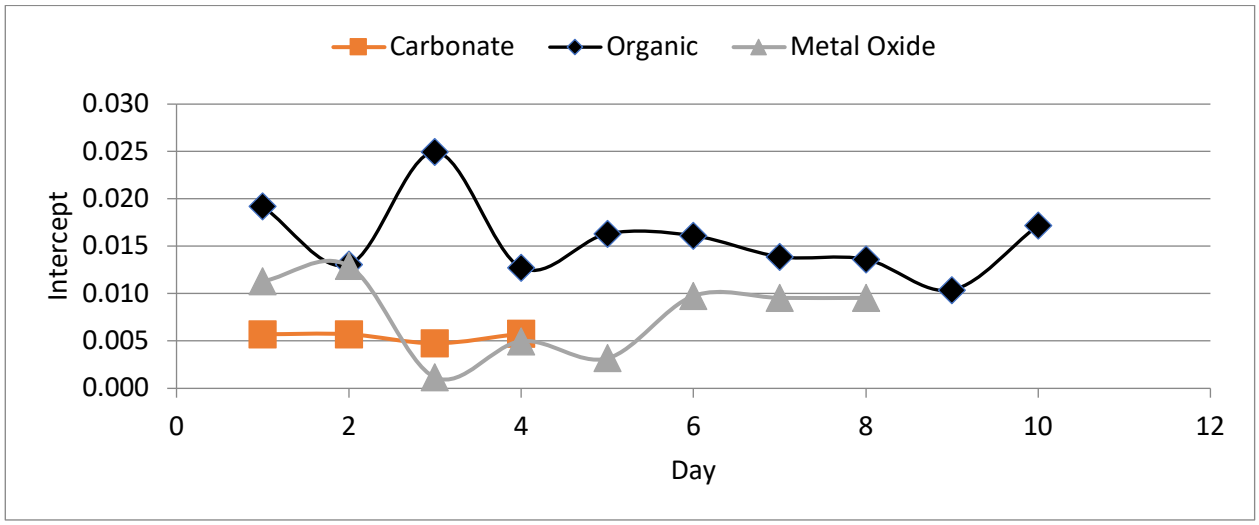

Figure 43. Changes in y-axis intercept for the BCR extractions of the soil core samples.

#### 3.1.5.1.5 Exchangeable Pb

The Pb concentrations that were measured in the EXΔ extracts in the soil samples were below the detection limits of the GF-AAS. This was consistent with results observed in the earlier Pb study.[73] An example of a calibration model for EXΔ-[Pb] samples is provided in Figure 125 in Appendix B.

#### 3.1.5.1.6 Carbonate-bound Pb

CO3-[Pb] extracts of soil samples were determined using a calibration model (Figure 126 in Appendix B). The results for the QC samples (Table 29) show that the calibration model was stable during the day of measurements demonstrating that the BCR-GF-AAS method for the CO3-[Pb] was acceptable.

Table 29. Quality control samples for the CO3-bound soil core samples; (n=3).

| QC Sample/ng $g^{-1}$ | Pb/ng $g^{-1}$ | RSD |
|---|---|---|
| 6.0 | 5.89 | 6.84 |
| 10.0 | 9.65 | 4.98 |

#### 3.1.5.1.7 Metal Oxide-bound Pb

MOX-[Pb] extracts of soil samples were determined using a calibration model (Figure 127 in Appendix B). The calibration model was accurately reflecting the concentration of the samples/standards during the analysis period (Table 30). One can therefore conclude that the methodology for the MOX-[Pb] extraction was robust for this study.

Table 30. Quality control samples for the MOX-bound soil core samples; (n=3).

| QC Sample/ng $g^{-1}$ | Pb/ng $g^{-1}$ | RSD |
|---|---|---|
| 15.0 | 15.07 | 4.17 |
| 50.0 | 50.82 | 2.43 |

#### 3.1.5.1.8 Organic-bound Pb

Calibration model for the hydrogen peroxide extraction of the ORG-[Pb] in soil core samples is shown in Figure 128 (Appendix B). The calibration model was accurately reflecting the concentration of the samples/standards during the analysis period (Table 31), thus it can be concluded that the methodology for the hydrogen peroxide, oxidative extraction of the ORG-[Pb] was acceptable for this study.

Table 31. Quality control samples for the ORG-bound soil core samples; (n=3).

| QC Sample/ng $g^{-1}$ | Pb/ng $g^{-1}$ | RSD |
|---|---|---|
| 15.0 | 14.91 | 2.99 |
| 25.0 | 25.14 | 2.50 |

### 3.1.6 [CAT]-Hg by MAE ICP-MS

Concentrated $HNO_3$ extraction of CAT-[Hg] in soil samples was done using a calibration model (Figure 129 in Appendix B). The results for the QC samples (Table 32-Table 34) show the calibration model being maintained during a given day of measurement. One can therefore conclude that the methodology for Hg determination by ICP-MS was acceptable.

Table 32. Quality control samples for Hg in soil core samples 6; (n=3).

| QC Sample/ng $g^{-1}$ | Hg/ng $g^{-1}$ | RSD |
|---|---|---|
| 25.0 | 25.83 | 2.53 |
| 50.0 | 50.76 | 3.00 |

Table 33. Quality control samples for Hg in soil core samples 2; (n=3).

| QC Sample/ng $g^{-1}$ | Hg/ng $g^{-1}$ | RSD |
|---|---|---|
| 25.0 | 26.31 | 3.00 |
| 50.0 | 50.88 | 2.60 |

Table 34. Quality control samples for Hg in soil core samples 21; (n=3).

| QC Sample/ng $g^{-1}$ | Hg/ng $g^{-1}$ | RSD |
|---|---|---|
| 25.0 | 25.64 | 5.64 |
| 50.0 | 51.24 | 3.00 |

### 3.1.7 Speciated Hg by MAE-BCR ICP-MS

EXΔ-, CO3-, MOX-, and ORG-[Hg] in soil samples were determined using a calibration model (Figure 130 in Appendix B). The results for the QC samples (Table 35) show the calibration model being maintained during the day of measurements. One can therefore conclude that the MAE BCR-ICP-MS methodology for the Hg was acceptable.

Table 35. Quality control samples for Hg in soil core samples 2; (n=3).

| QC Sample/ng $g^{-1}$ | Hg/ng $g^{-1}$ | RSD |
|---|---|---|
| 25.0 | 25.32 | 3.84 |
| 50.0 | 50.78 | 2.10 |

### 3.1.8 Background Levels of Copper

To reliably quantify [Cu] in the soil core samples, background samples were studied for each of the BCR steps using the optimized MAE method. Two soil cores were collected ~1000 m west of the Brawner house (Figure 11 in Chapter 2.2.1).

Site 13 (Ridge, Figure 44, Table 36), and Site 28 (Pines, Figure 45, Table 37). The general trend for background [Cu] is as follows: EXΔ-[Cu] < 1 ng $g^{-1}$, CO3-[Cu] < 3 ng $g^{-1}$, MOX-[Cu] ~46 ng $g^{-1}$. The differences were shown in the ORG-bound fraction, core 28 (Pines), [Cu] was 19.07 ± 0.42 ng $g^{-1}$, BF04-13B (Ridge), [Cu] was 3.38 ± 0.33 ng $g^{-1}$. The increased [ORG-[Cu]] (Figure 45) is presumed to originate from increases in the amount of ORG-M within the pine forest, which is very rich in humic material extending vertically downwards, such that the humic acids bind with metals.[99] This is why the [Cu]

for the ORG fraction is highest in the first inch because that is where the humic acid concentrations are the highest (essentially pure humic acid). Not only in the pine forest, but also from the covering of grass and weeds on the surface, more humic acid is prevalent in the top layer, as observed on the Ridge (Figure 44).

For the subsequent measurements in this work, the background concentration for each of the BCR steps was subtracted by using results from Site 13 as the representative sample, omitting the results from Site 28, because of possible increased interaction of humic acids within the pine forest.

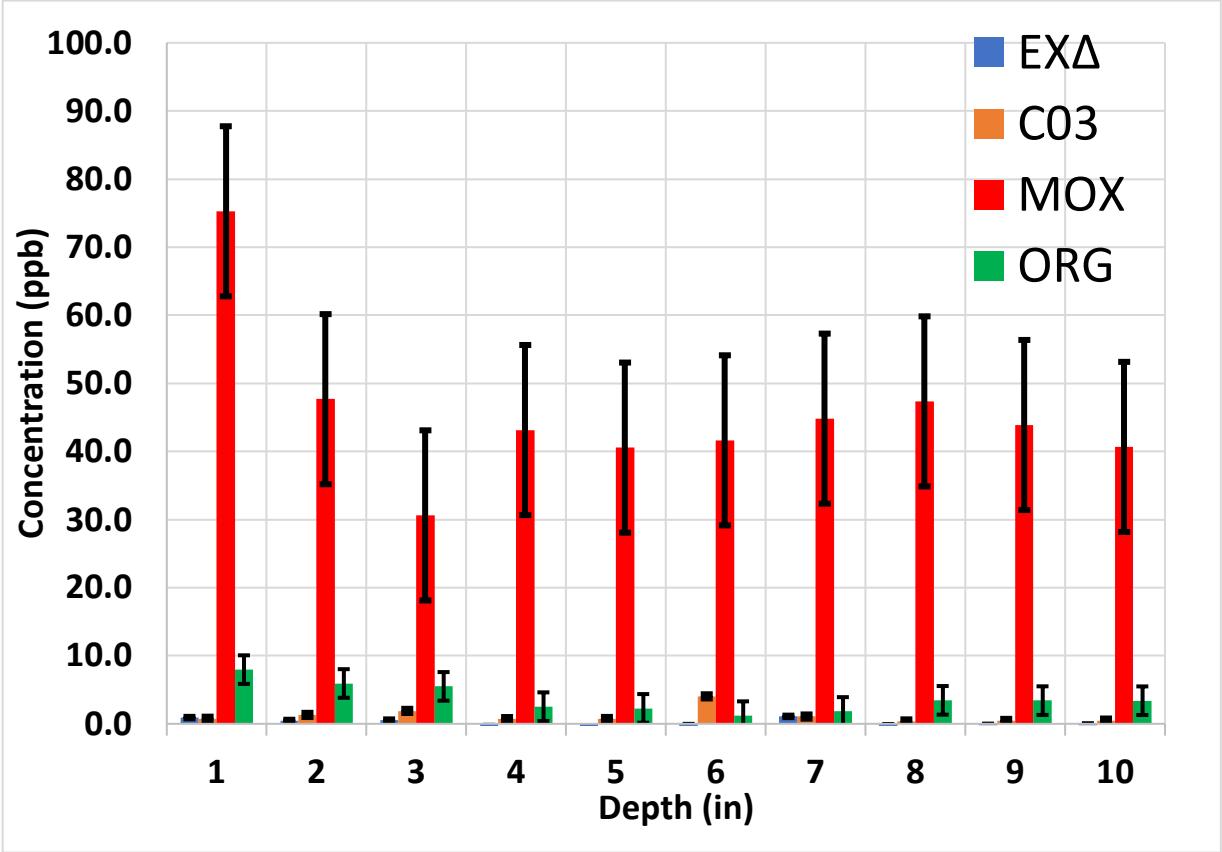


Figure 44. Background Cu for soil core 13 using the MAE BCR method (n=10) at the 95% confidence level.

Table 36. Results for the determination of background Cu in soil core 13 using the MAE BCR method (n=10) at the 95% confidence level.

| EXΔ-[Cu] ng $g^{-1}$ | CO3-[Cu] ng $g^{-1}$ | MOX-[Cu] ng $g^{-1}$ | ORG-[Cu] ng $g^{-1}$ |
|---|---|---|---|
| 0.20 ± 0.02 | 1.35 ± 0.13 | 46.38 ± 2.01 | 3.38 ± 0.33 |

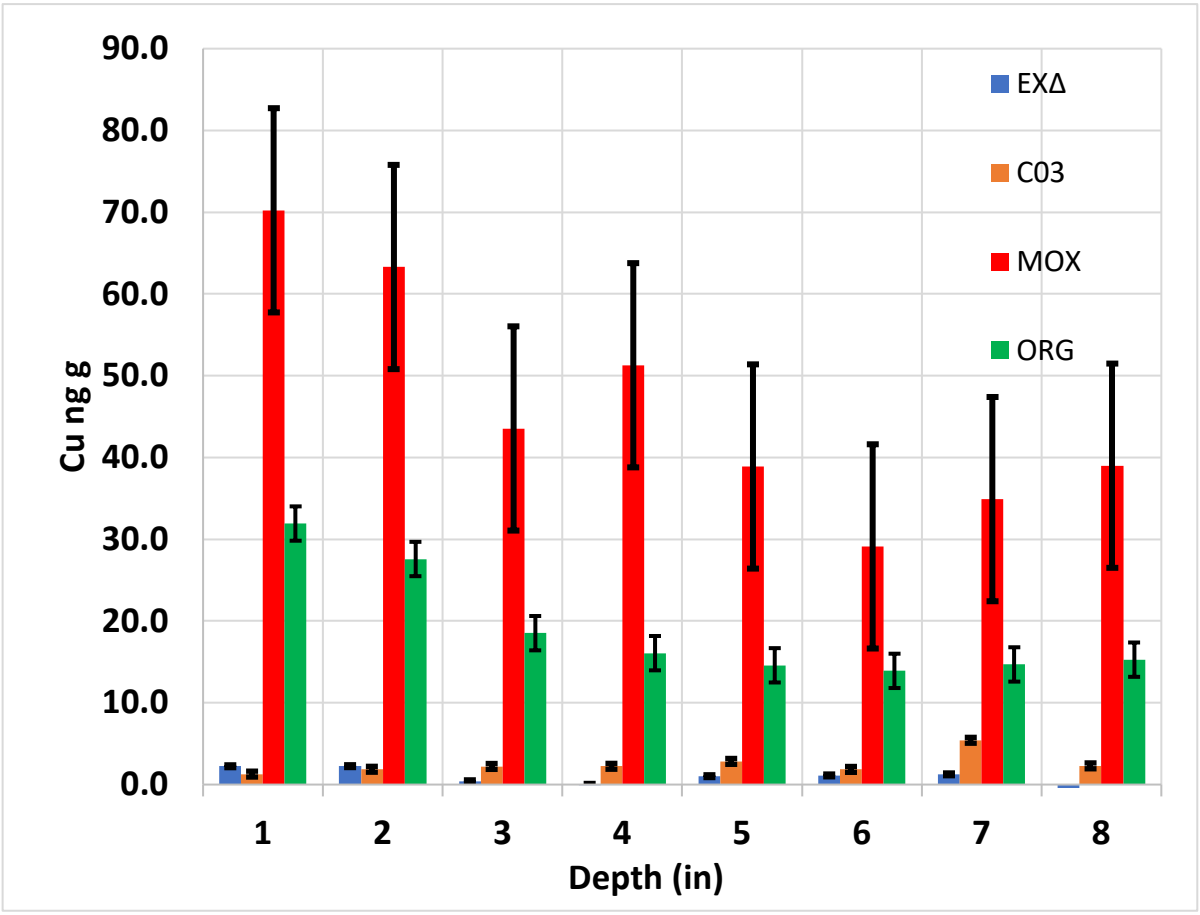


Figure 45. Background Cu for soil core 28 using the MAE BCR method (n=10) at the 95% confidence level.

Table 37. Results for the determination of background Cu in soil core 28 using the MAE BCR method (n=10) at the 95% confidence level.

| EXΔ-[Cu] ng $g^{-1}$ | CO3-[Cu] ng $g^{-1}$ | MOX-[Cu] ng $g^{-1}$ | ORG-[Cu] ng $g^{-1}$ |
|---|---|---|---|
| 0.96 ± 0.02 | 2.50 ± 0.10 | 46.29 ± 1.92 | 19.07 ± 0.42 |

### 3.1.9 ICP-MS: Hg Interference

When analyzing Hg by ICP-MS, the literature suggests that Hg is subject to a tungsten oxide (WO) interference in the direct ICP-MS analysis of soil or sediment samples.[100-103] A similar type of WO interference can be observed for each W isotope and subsequent Hg interference as shown in Table 38.

Table 38. Tungsten (W) and Mercury (Hg) isotopes and their relative abundances.[101]

| Isotope | % Abundance |
|---|---|
| W 180 | 0.12 |
| W 182 | 26.50 |
| W 183 | 14.30 |
| W 184 | 30.64 |
| W 186 | 28.43 |
| Hg 196 | 0.15 |
| Hg 198 | 9.97 |
| Hg 199 | 16.87 |
| Hg 200 | 23.10 |
| Hg 201 | 13.18 |
| Hg 202 | 29.86 |
| Hg 204 | 6.87 |

To investigate WO interferences, a standard calibration model (Figure 131 in Appendix B) for 25-250 ppb W in 1% (v/v) nitric acid (Sigma Aldrich) was constructed. The quantitative method for ICP-MS measured from 50-238 m/z using a 1.0 ppm Au addition as used in the Hg method.[104] A low ppm amount of Au is added to stabilize Hg compounds because the Au ion acts as a strong oxidizing agent that converts Hg species to soluble mercuric ion ($Hg^{2+}$).[105]

The range of interest for the potential WO interferences to Hgare between 180-204 m/z. The W isotopic fingerprint is confirmed from the mass spectrum in Figure 133 and Table 39 for 25 ppb W, such that the isotopic abundance and measured intensities agree, with no detectable WO interferences present for Hg isotopes (note that the peak at 197 m/z is from the 1.0 ppm Au standard). The same trend is seen for 50-250 ppb standards (the spectra can be found in Figure 134-Figure 136 in Appendix C).

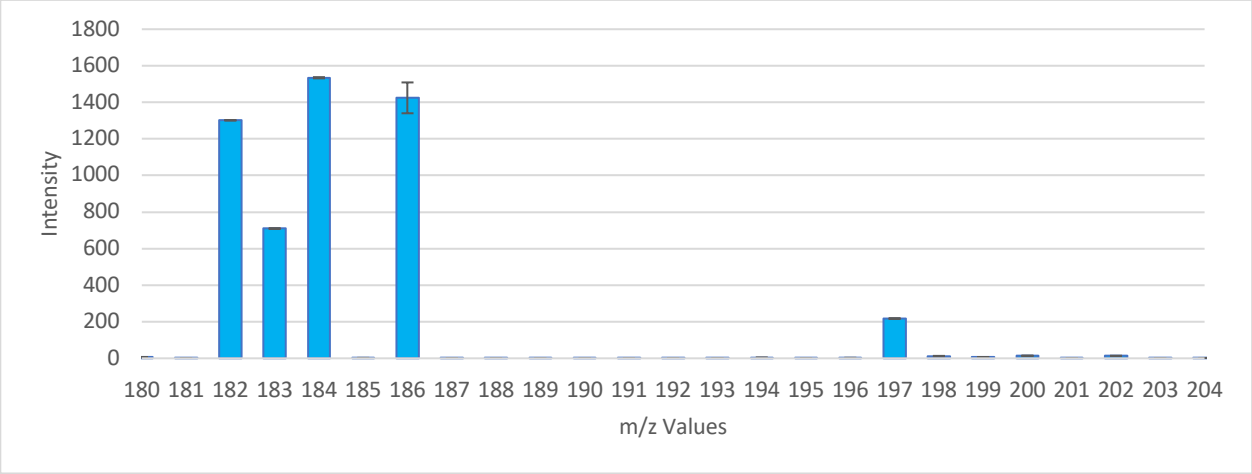


Figure 46. ICP-MS spectrum for a W standard (25 ppb); (n=3) at the 95% confidence level.

Table 39. Confirmation of W isotopic fingerprint for 25 ppb W standard.[101]

| Isotope | % Abundance | W Intensity | % Total W Intensity | % Difference |
|---|---|---|---|---|
| W 180 | 0.12 | 6.23 | 0.13 | 4.25 |
| W 182 | 26.50 | 1301.73 | 26.16 | 1.30 |
| W 183 | 14.30 | 709.75 | 14.26 | 0.27 |
| W 184 | 30.64 | 1534.50 | 30.83 | 0.63 |
| W 186 | 28.43 | 1424.61 | 28.62 | 0.69 |
| Total | 99.99 | 4976.80 | - | - |

To further investigate the WO interferences, a combined standard calibration model (Figure 132 in Appendix B) for W and Hg was created in the range from 25-250 ppb in 1% (v/v) $HNO_3$ with 1.0 ppm Au addition.[104] The W and Hg isotopic fingerprints are confirmed from the mass spectrum in Figure 137 and Table 42, with no detectable WO interferences present for Hg isotopes. The same trend is seen for the standards (the spectra can be found in Figure 134-Figure 136 in Appendix C).

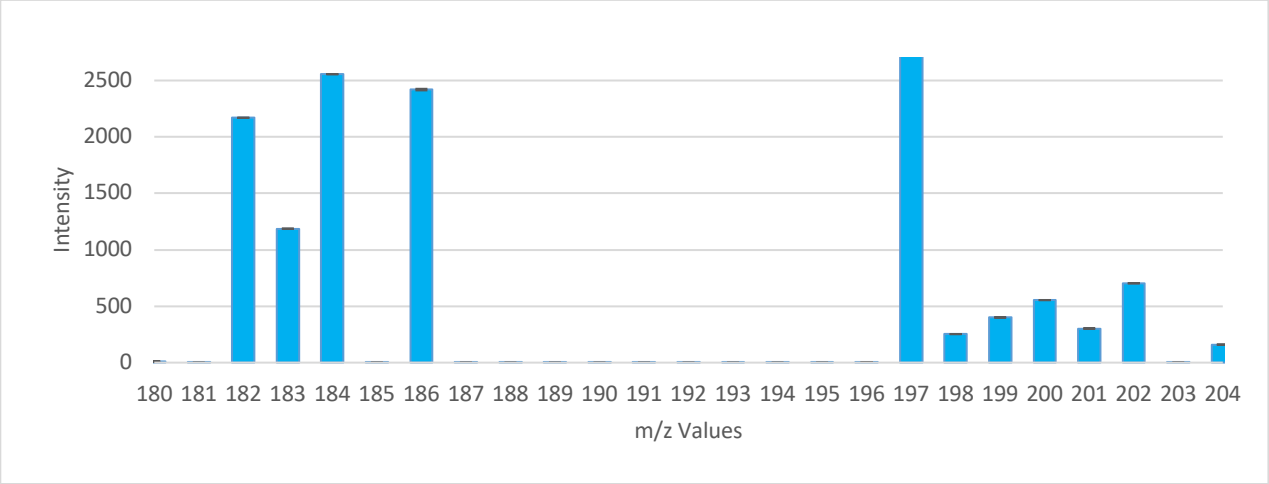


Figure 47. ICP-MS spectrum for Hg and W standards (25 ppb each); (n=3) at the 95% confidence level.

Table 40. Confirmation of isotopic fingerprints for 25 ppb W and Hg standards.[101]

| Isotope | % Abundance | Intensity | % Total Intensity | % Difference |
|---|---|---|---|---|
| W 180 | 0.12 | 6.23 | 0.13 | 4.25 |
| W 182 | 26.50 | 1301.73 | 26.16 | 1.30 |
| W 183 | 14.30 | 709.75 | 14.26 | 0.27 |
| W 184 | 30.64 | 1534.50 | 30.83 | 0.63 |
| W 186 | 28.43 | 1424.61 | 28.62 | 0.69 |
| Total | 99.99 | 4976.80 | - | - |
| Hg 196 | 0.15 | 4.92 | 0.21 | 38.17 |
| Hg 198 | 9.97 | 252.43 | 10.63 | 6.57 |
| Hg 199 | 16.87 | 400.02 | 16.84 | 0.19 |
| Hg 200 | 23.1 | 553.74 | 23.31 | 0.90 |
| Hg 201 | 13.18 | 302.24 | 12.72 | 3.48 |
| Hg 202 | 29.86 | 702.89 | 29.59 | 0.92 |
| Hg 204 | 6.87 | 159.53 | 6.71 | 2.26 |
| Total | 100.00 | 2375.78 | - | - |

To further investigate WO interferences in soil cores, two 1” fractions from Sites 6 (Ridge), 2 (Slope), and 21 (Plain) were extracted using the MAE Hg method with concentrated $HNO_3$, and then analyzed from m/z 50-238 by ICP-MS. Each sample after the initial analysis was spiked with 6 ppb W to investigate if a WO interference would form.

For 21 (Table 41), 6 (Table 42), 2 (Table 43), W and Hg isotopes are compared before and after the spike (the spectra can be found in Figure 141-Figure 146 in Appendix C). There is a significant interference at m/z 204 because $^{204}$Hg and $^{204}$Pb interfere isobarically. The interference is only observed for the soil samples and not the standards because of the presence of Pb in soil. The isotopic fingerprint for Hg is thus

distorted by this interference. The percent differences in the theoretical and observed intensities for $^{202}$Hg (highest abundant isotope), are shown in

Table 41-Table 43. By comparing the intensities for $^{184}$W (highest abundant isotope), shown in Table 41-Table 43, the difference is ~190%. It can be speculated that if a significant WO interference were present, the increases for Hg would follow a consistent trend, as seen for W. Therefore, because of the inconsistency, this suggests that the percent differences are due to instrument variability confirming that a WO interference is not present. From these findings, it can be concluded that the WO interferences were not observed in this study.

Table 41. Comparison of the spiked and un-spiked for Site 21. Relative isotopic abundances for W and Hg are shown.

| Isotope | Abundance | Un-spiked Intensity | Spiked Intensity | % Difference |
|---|---|---|---|---|
| W 180 | 0.12 | 33.94 | 30.45 | 10.86 |
| W 182 | 26.50 | 14.81 | 598.11 | 190.34 |
| W 183 | 14.30 | 8.20 | 329.33 | 190.28 |
| W 184 | 30.64 | 16.85 | 710.42 | 190.74 |
| W 186 | 28.43 | 15.41 | 667.94 | 190.98 |
| Hg 196 | 0.15 | 2.05 | 1.57 | 26.53 |
| Hg 198 | 9.97 | 5.14 | 7.18 | 33.25 |
| Hg 199 | 16.87 | 5.28 | 5.36 | 1.45 |
| Hg 200 | 23.10 | 7.13 | 9.02 | 23.37 |
| Hg 201 | 13.18 | 4.02 | 2.56 | 44.27 |
| Hg 202 | 29.86 | 9.17 | 10.08 | 9.47 |
| Hg 204 | 6.87 | 221.91 | 177.68 | 22.14 |

Table 42. Comparison of the spiked and un-spiked for Site 6. Relative isotopic abundances for W and Hg are shown.

| Isotope | Abundance | Un-spiked Intensity | Spiked Intensity | % Difference |
|---|---|---|---|---|
| W 180 | 0.12 | 25.35 | 33.47 | 27.62 |
| W 182 | 26.50 | 23.60 | 527.45 | 182.87 |
| W 183 | 14.30 | 12.16 | 291.26 | 183.97 |
| W 184 | 30.64 | 28.31 | 677.39 | 183.95 |
| W 186 | 28.43 | 26.31 | 664.50 | 184.77 |
| Hg 196 | 0.15 | 1.81 | 1.91 | 5.12 |
| Hg 198 | 9.97 | 3.63 | 7.60 | 70.65 |
| Hg 199 | 16.87 | 3.16 | 5.70 | 57.53 |
| Hg 200 | 23.10 | 4.32 | 9.32 | 73.31 |
| Hg 201 | 13.18 | 2.41 | 2.83 | 15.97 |
| Hg 202 | 29.86 | 5.58 | 10.57 | 61.83 |
| Hg 204 | 6.87 | 260.30 | 321.54 | 21.05 |

Table 43. Comparison of the spiked and un-spiked for Site 2. Relative isotopic abundances for W and Hg are shown.

| Isotope | Abundance | Un-spiked Intensity | Spiked Intensity | % Difference |
|---|---|---|---|---|
| W 180 | 0.12 | 51.20 | 45.09 | 12.70 |
| W 182 | 26.50 | 8.81 | 585.95 | 194.08 |
| W 183 | 14.30 | 5.01 | 322.95 | 193.89 |
| W 184 | 30.64 | 10.20 | 699.93 | 194.26 |
| W 186 | 28.43 | 9.14 | 654.72 | 194.49 |
| Hg 196 | 0.15 | 2.06 | 1.63 | 23.38 |
| Hg 198 | 9.97 | 3.76 | 6.60 | 54.81 |
| Hg 199 | 16.87 | 3.22 | 4.74 | 38.19 |
| Hg 200 | 23.10 | 4.46 | 7.99 | 56.74 |
| Hg 201 | 13.18 | 2.53 | 2.03 | 21.62 |
| Hg 202 | 29.86 | 5.73 | 8.85 | 42.75 |
| Hg 204 | 6.87 | 81.67 | 67.49 | 19.02 |

## 3.2 Study of the Environmental Chemistry

In this section, evaluation of the trends in abundance, distribution, and transport of Cu, Pb, and Hg in soil fractions obtained by sequential extraction will be discussed. Radiometric dating of the soil is evaluated and compared to historical descriptions of the troop movements and positions, as well as a comparison of rate constants for Cu and Pb in soil.

### 3.2.1 Radiometric Dating of the Soil

To address the rate and mechanisms of transport involved for Cu, Pb, and Hg it is essential to correlate the depth of the soil with age. Radiometric dating of the soil was performed by Mr. Dustin M. Ottman and Professor Erik R. Christensen in the Department of Civil Engineering & Mechanics at the University of Wisconsin-Milwaukee.[74] Seven combined (because of their proximity to each other) and individual soil cores were analyzed for $^{210}Pb$ and $^{137}Cs$ activity using alpha and gamma spectrometry. Deposition velocities for the soil core samples were determined by plotting log excess $^{210}Pb$ versus the depth of the core (cm) and then comparing to $^{137}Cs$ activity versus depth (cm).[74] A sample depositional velocity plot is shown in Figure 48.

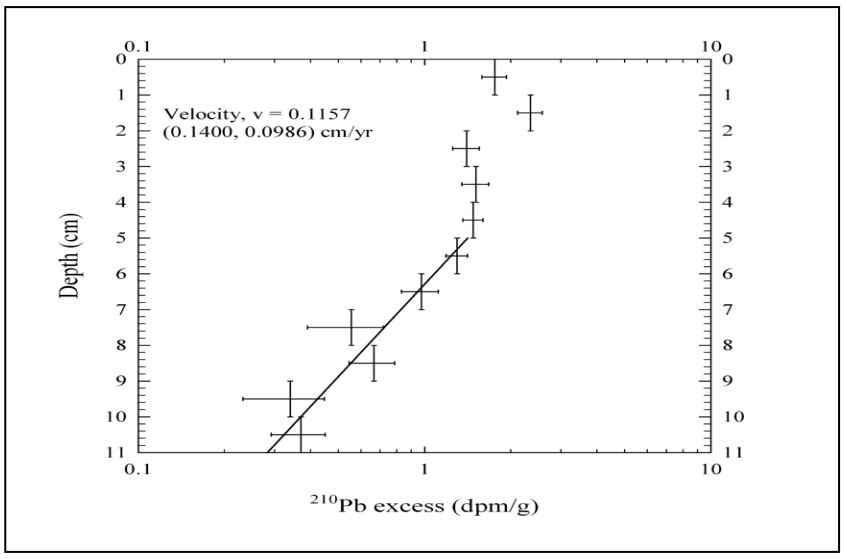


Figure 48. Measurement of the excess $^{210}$Pb vs. depth by weighted regression for sample core 2004-06B.[74] Depositional velocities were used to determine the age of soil layers within the cores.

A comparison of the depositional velocities for the soil cores is shown in Figure 51 in Appendix D. Each radiometric core has an exclusive depositional velocity (rate) based on its position, that is, where the core was located along the transect. Figure 51 is organized in a manner to compare the radiometrically analyzed cores (in respect to their position along the transect), to the cores used to for Cu and Pb speciation. For this method, inherent error exists because it was not practical to radiometrically date each core because of the destructive nature of the process. Thus, there is an error in selecting the depositional velocity for a given core relative to its proximity to a radiometrically analyzed core.

### 3.2.2 Sampling Area

To understand the variations in Cu, Pb, and Hg movement in the battlefield soil, defining the exact dimensions of the source input are critical. The precise troop

movements during the battle are unknown, thereby making this a difficult task. However, the battle was noted by several participants as one which had little tactical maneuvering. General Taliaferro, who commanded the Stonewall Brigade that opposed the 19th Indiana, described the battle as having “no maneuvering and very little tactics”.[17] Some shifting of the infantry lines undoubtedly occurred, in particular, the 19th Indiana occupied two positions, though the latter for a relatively brief period as they withdrew upon nightfall occurred.[17] Therefore, in this study the dimensions of their primary position was defined. First, a typical American Civil War (ACW) infantry regiment was nominally composed of 10 companies forming two parallel lines of soldiers to face the enemy. These lines were within arm's length of one another, so the width of a regimental formation was approximately 3-4 m.[106] Adding movement forwards and backwards that occurred during the fighting, another 2-3 m in each direction would be a reasonable estimate if "little maneuvering" is assumed. Therefore, the assumption will be made that the total variation of the "input source" perpendicular to the sampling transect (Figure 49 and Figure 50) was approximately 10 m.

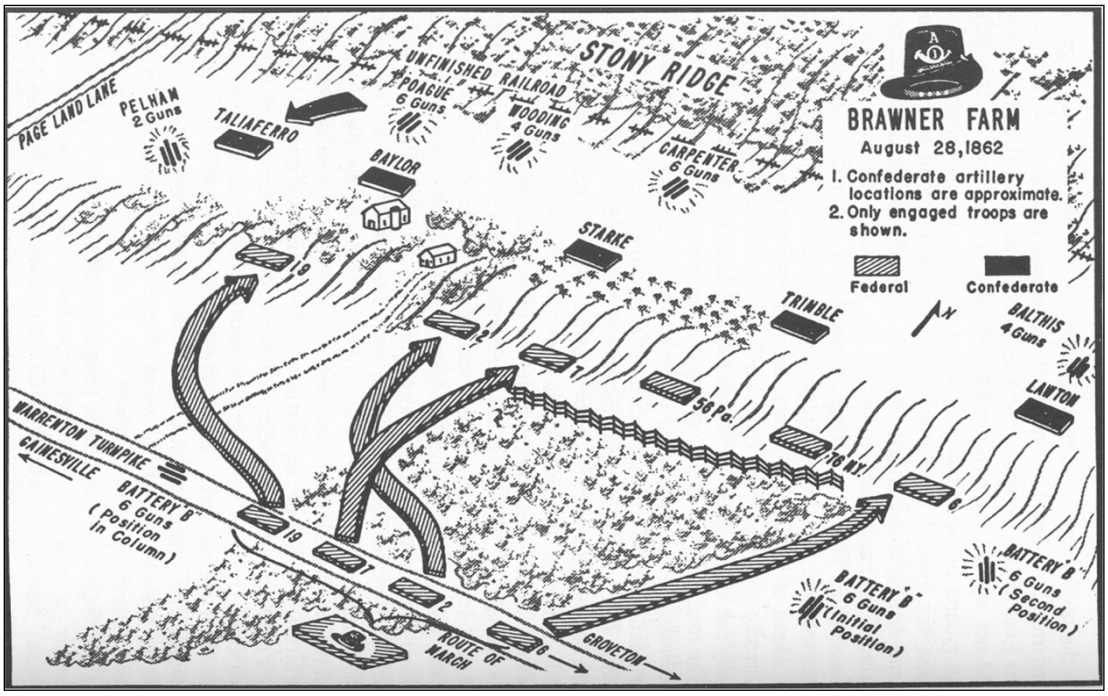


Figure 49**.** Troop movements and positions at Brawner Farm.[18]

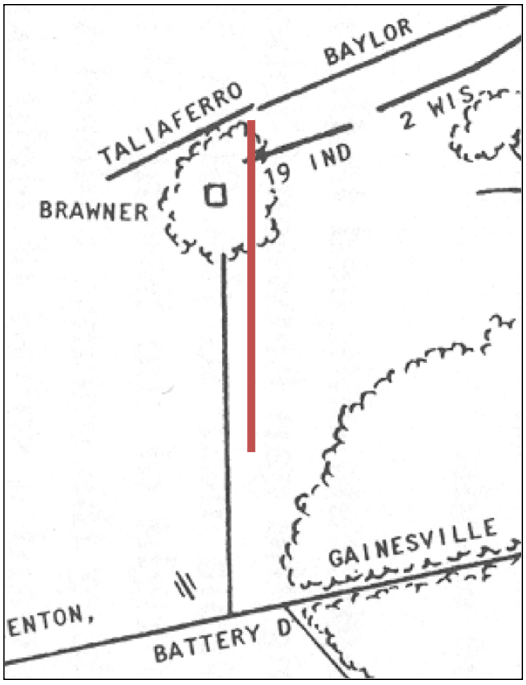


Figure 50. Transect of the battle where soil core samples were taken indicated by the red line.[17]

To gain a better understanding of where the soil cores were sampled on the battlefield, Figure 51 shows a profile of the landscape. The profile is divided into three different regions of interest: Region A is the ridge where the battle lines were drawn, Region B is the slope behind the infantry formations, and Region C is the plain which extends for approximately 150 m to the Warrenton Turnpike (today named the Lee Highway). The soil core numbers are labeled along with the distance (m) in relation to the first sampled site 9 at 0 m. Figure 52 displays the depth of the cores in regions A and B.

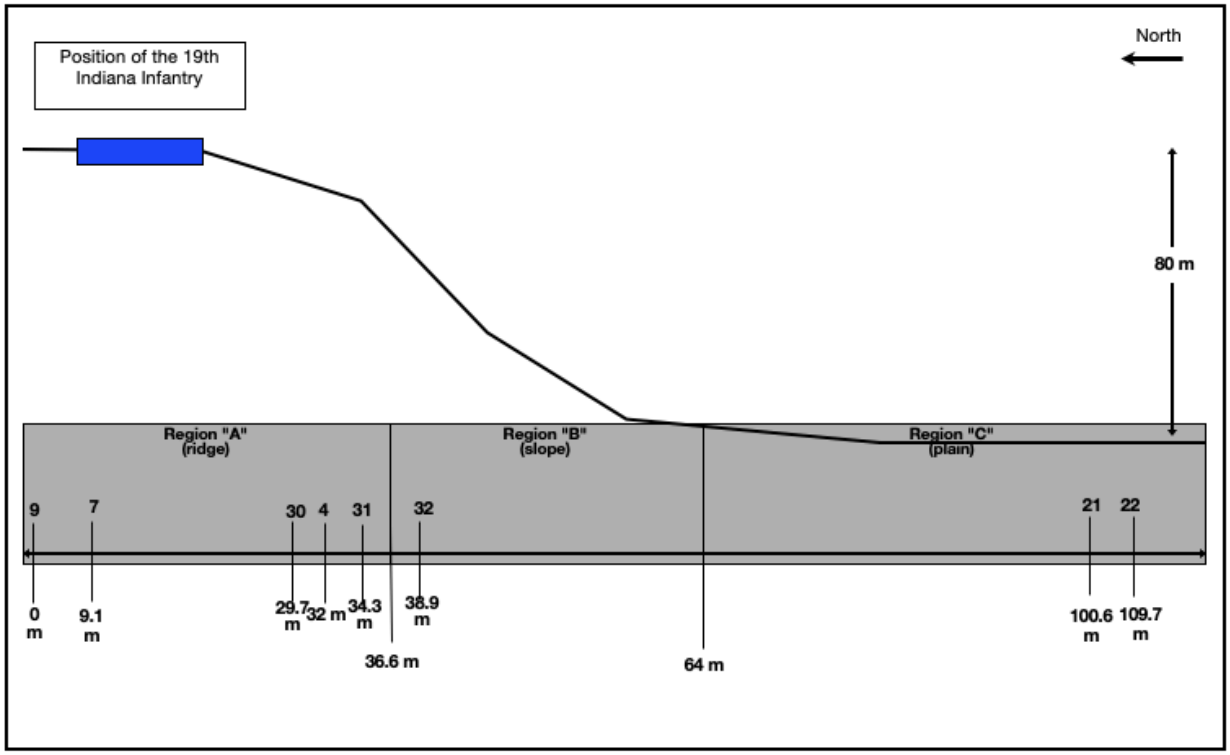


Figure 51. Profile of the sampling sites in relation to their position on the battlefield. Numbers above the distance (m) indicate where a soil core was collected.

The soil on the Ridge was relatively compact (Figure 52), and thus only shallow cores (<7 in) could be collected, whereas on the Slope and Plain the soil was relatively loose and deeper cores (>10 in) could be collected.

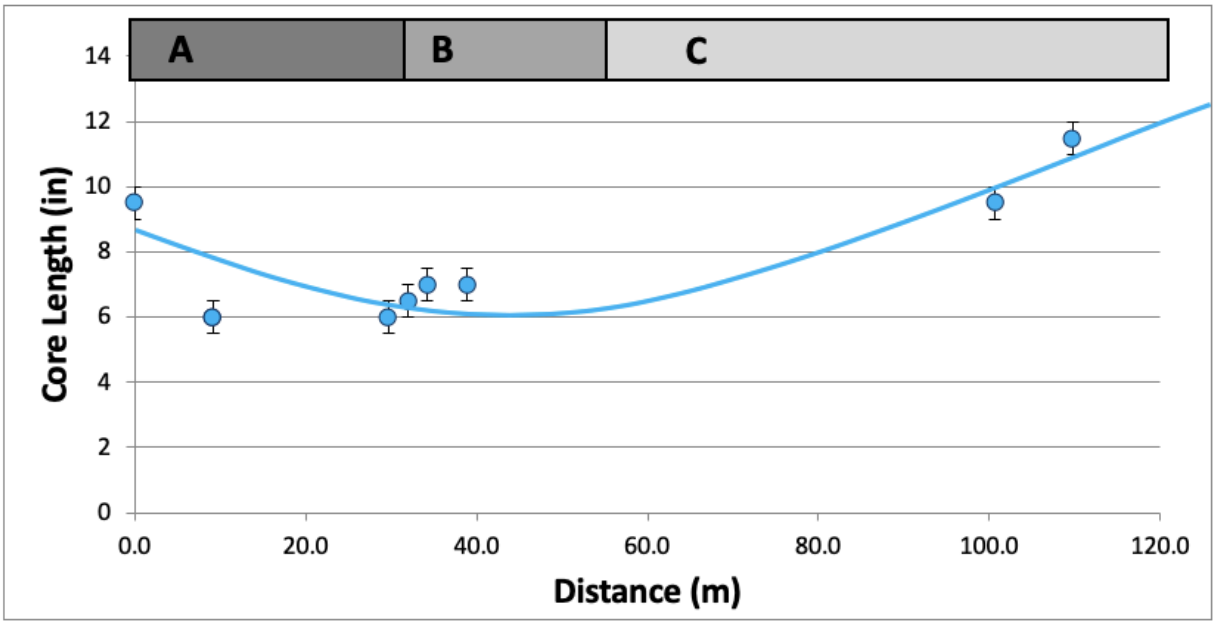


Figure 52. The depth of the soil cores that were collected in Regions A and B was also a measure of the relative compactness of the soil; (n=3) at the 95% confidence level.

From prior studies, for geochemical characterization of the soils using standard methods, it was found that the properties of the soil were: pH (4.9-6.8), ORG C (0.70-3.70%(w/w), averaging 0.17 ± 0.08), ORG N (0.10-0.27%(w/w), averaging 1.73 ± 1.07), cation-exchange capacity (hereafter denoted "μ") (13.0 ±3.3 meq 100 $g^{-1}$), total iron oxides (1420-2010 mg $kg^{-1}$, averaging 1702 ± 217 mg $kg^{-1}$), and the crystalline and amorphous iron oxides were 20.1%(w/w) and 79.9%(w/w), respectively (±12.2%)[73]

#### 3.2.2.1 Exchangeable Cu

The exchangeable Cu is defined as very weakly-sorbed species that are retained on the soil surface exclusively by electrostatic interactions.[42] The BCR reagent for releasing the exchangeable Cu (10 mM $CaCl_2$) is intended to mimic rainwater, that is, an aqueous solution of low ionic strength. As mentioned earlier in Section 3.1, exchangeable Cu was not detected in any of the soil core samples. The minimum detectable limit (MDL) of the GF-AAS method for exchangeable Cu was 0.73 ng $g^{-}1$. As mentioned earlier in section 3.1, EXΔ-[Cu] was not detected in any of the soil core samples. This is not surprising given that $Cu^{2+}$ on the soil surface would be expected to rapidly "wash-off" because of weathering.

#### 3.2.2.2 Carbonate-bound Cu

CO3-[Cu] was extracted from the soil cores by using acetic acid (0.11 M), the MDL for the CO3-[Cu] by the GF-AAS method was 0.88 ng $g^{-1}$. The results for all of the soil core samples and the [Cu] vs. depth profiles for each sampling site can be found in the Appendix (Table A-1, Figure A-1 (a - h) respectively). The concentration of Cu for all of the soil cores studied was near the MDL, except for the more recent layers (<100 yr), i.e., at the top of the core samples. Some of the core fractions displayed high RSD values because the denominator was small.

Interesting trends were observed in terms of the position of the infantry firing line relative to the terrain profile. The soil cores from the ridgeline that transect the position of the 19th Indiana displayed distinct peaks in the recent layers for the CO3-[Cu]

(Figure 78, Appendix A-1). The cores collected in Region B, moving away from the battle line, show peaks compared to the Region A soil cores (Figure 79, Appendix A-1). Moving from the ridge (Region A) down the slope of the hill (Region B), a major peak is observed at 34.3 m. Continuing down the slope into Region C, a second major peak is observed at 110 m. Interestingly, the [Cu] increases from Site 7 (9.1 m) to Site 4 (32 m), which would be moving from the firing line (7) down the slope (Region B), and then the [Cu] decreases from the infantry line at Site 9 (0 m).

Figure 54 shows the horizontal distribution in Regions A, B, and C of the CO3-[Cu] for different ages of soil (the concentrations were interpolated with respect to time). Three peaks in Figure 54 show relatively higher concentrations of CO3-[Cu]. To understand why these peaks are found in specific locations, it is important to first note that, according to historical records, apparently no anthropogenic disruption (i.e., tillage) of the sampling area has occurred since the battle.[20] Therefore, one can safely assume that these trends can be interpreted purely in terms of natural weathering processes. The transport behavior of Cu — or *any* pollutant in soil — is a complex process (Figure 53).[107,108]

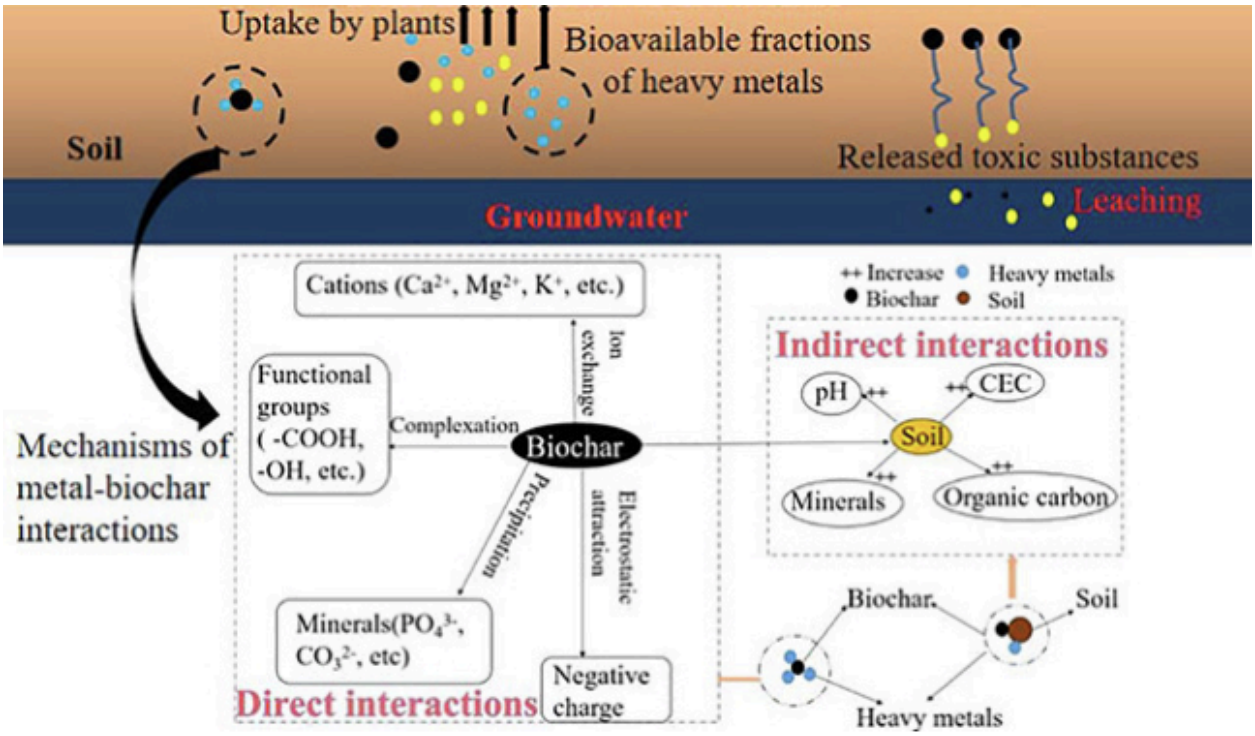


Figure 53. Possible mechanisms of heavy metal transport and the use of biochar-metal interactions to immobilize metals in contaminated soils.[108]

Cu will migrate vertically as well as horizontally through the soil as a function of the convective and diffusive forces that act upon it.[109] The location of the prominent peak at 34.4 m found in the center of Region A corresponds to the 19th Indiana's primary position. Furthermore, as shown in Figure 55, because the vertical distribution of Cu in the core increases with depth, the relatively high concentrations observed at 34.4 m suggest the downward (diffusive and convective) movement of Cu deposited during the battle through older layers that correspond to approximately 60 yr before the battle.

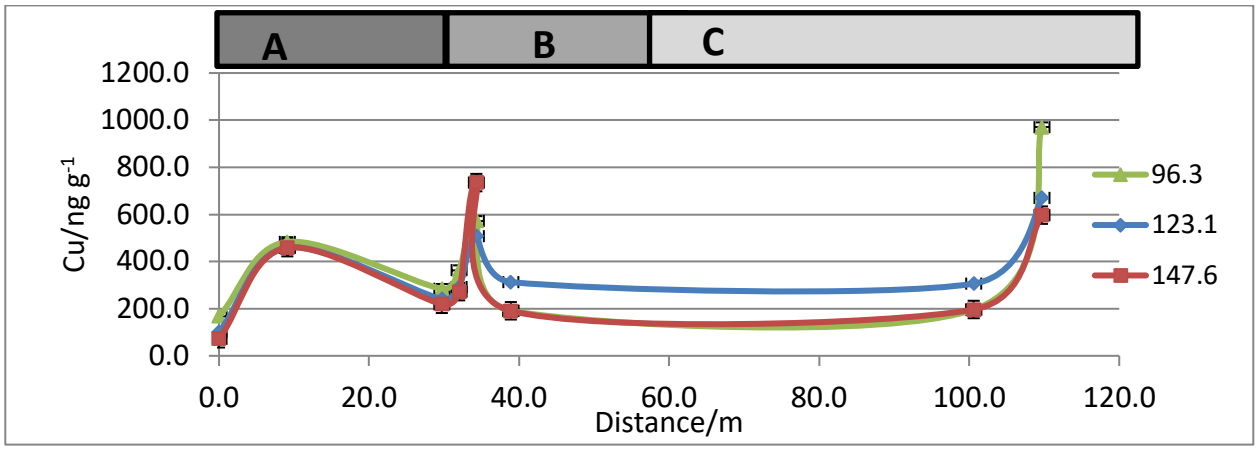


Figure 54. Horizontal distribution of CO3-[Cu] along the entire transect for ~50 yr after the battle; (n=3) at the 95% confidence level.

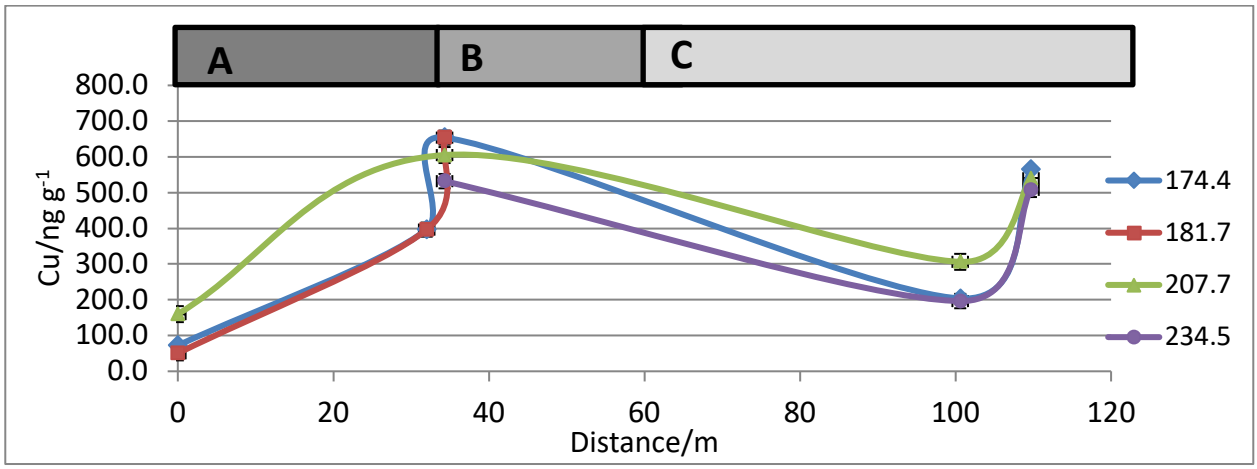


Figure 55. Horizontal distribution of CO3-[Cu] along the entire transect for ~90 yr before the battle; (n=3) at the 95% confidence level.

From Figure 54 the initial peak at 9.1 m can be rationalized as the southern edge of the Confederate infantry firing line (i.e., closest to the Union line) while the primary peak at 34.3 m corresponds to the 19th Indiana's approximate primary position during the battle in 1862. Interestingly, in Figure 54, the CO3-[Cu] shows remarkable consistency in the horizontal distribution along the transect. Minor differences appear in the concentration of CO3-[Cu] in the older (>150 yr) layers, suggesting perhaps that the CO3-[Cu] migrated horizontally at a consistent rate over time. During one of the

sampling trips, a typical summer-time Virginia thunderstorm occurred, and the volume and rate at which water washed down the slope was remarkable (there were even "white-capped waves"). The torrent formed large pools of standing water at the beginning of the plain (northern end of Region C). Therefore, it can be speculated that the peak at ~110 m shown in Figure 54 and Figure 55 is formed from these occasional massive puddling events, a soil profile on a hillslope is shown in Figure 56.

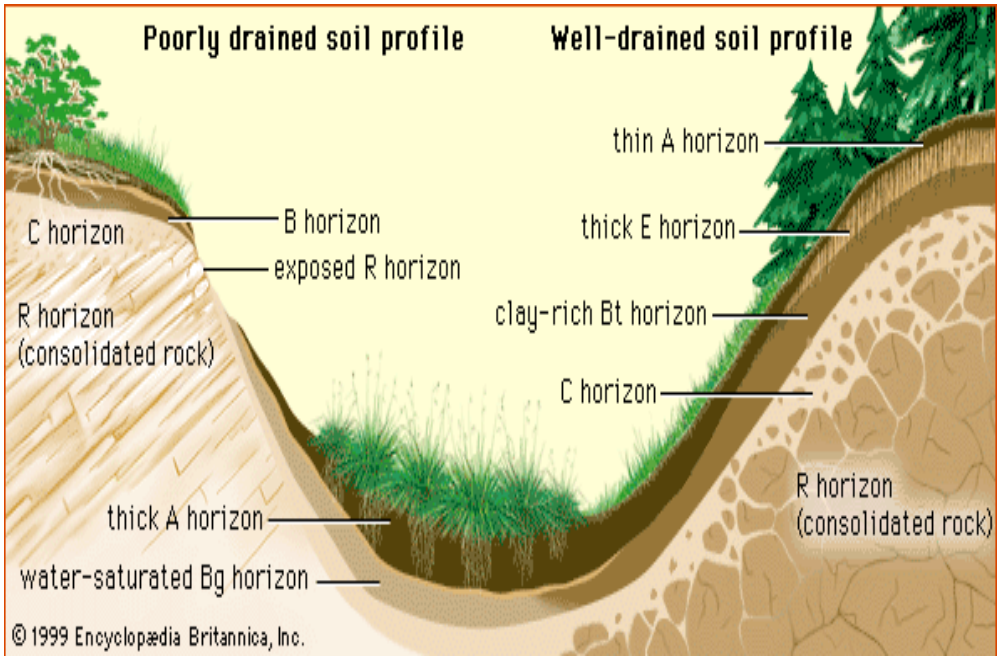


Figure 56. Soil profiles on hillslopes.[110]

The more recent layers at Site 32B (38.9 m) do not display large differences in CO3-[Cu] because the surface and sub-surface water flow washed the CO3-[Cu] down the slope. Due to weathering along the slope, the CO3-[Cu] decreases because it is washed away. Thus, the horizontal migration of the CO3-[Cu] would have been increased even more over time, positioned in the middle of the slope.

The third, broad peak located further into the plain (Region C) indicates surface water migration from the rapid flow of rainwater that had pooled at the bottom of the slope, thereby distributing CO3-[Cu] over a broader area. At the bottom of the slope, water would pool and then slowly percolate through the soil. Therefore, an increase in CO3-[Cu] would be expected in the older core layers because vertical water flow would be much slower because Region C is relatively flat. This conclusion is supported by noting that from Figure 54 and Figure 55, one can see that there is not an increase in CO3-[Cu] above the battle layer. With a steady decrease in CO3-[Cu] in the recent layers and a steady increase in the older soil core layers, it can be concluded that the CO3-[Cu] is migrating downwards at a faster rate than at either the ridgeline (Region A) or the slope (Region B).

#### 3.2.2.3 Metal Oxide-bound Cu

MOX-[Cu] was extracted from the soil cores by using $NH_2OH$•HCl (0.5 M), The MDL by the GF-AAS method was 0.39 ng $g^{-1.}$ The results for all of the soil core samples and the [Cu] vs. depth profiles for each sampling site can be found in the Appendix (Table A-2 and Figure A-2 (a – h), respectively). The distribution of the MOX-[Cu] extracted from the soil core samples revealed interesting depositional trends in relation to the terrain profile across all regions of the transect (A, B, and C). The soil cores from the ridgeline (Region A) that transect the position of the 19th Indiana display distinct peaks in the recent shallow layers (Figure 81, Appendix A-2). By comparison, the trends in Region A appear to be similar for both the MOX- and the CO3-[Cu]. Figure 82

(Appendix A-2) shows that the MOX-[Cu] soil core profiles in Region B are similar to the trends in Region A, with the highest concentrations observed at Site 4 (32m).

Soil layers deeper than 1862 (>140 yr) were found in Region A at Sites 9 (0 m), 7 (9.1 m), 30A (29.7 m), 4 (32 m), and 31 (34.3 m). The profiles of these older layers show that the MOX-[Cu] migrated downward (vertically) through the soil, with the [Cu] gradually decreasing in the layers that are ~50 yr older than the date of the battle (> ~200 yr). This trend suggests that the steep concentration gradient that was created in 1862 resulted in significant transport of the MOX-[Cu] in both vertical directions.

Trends in the abundance and distribution of MOX-[Cu] in Region B and C are much broader, with wide range of distribution (Figure 82 and Figure 83, Appendix A-2). This distribution of the MOX-[Cu] levels in the soil core profiles suggests that surface rainwater washed the MOX-[Cu] down the slope where the Cu accumulated over a wide area and subsequently migrated down (vertically) through the soil core profile. Because the Fe and Mn oxides in particular have a well-known high affinity for heavy metal cations,[111] this would suggest that the MOX-[Cu] is particularly mobile and thus accounts for the significant spreading of the Cu in Regions B and C. This trend suggests that MOX-[Cu] migrated horizontally from the sub-surface flow of water, thereby causing Cu to accumulate in Region B. Additional support for this hypothesis can be seen in the horizontal distributions shown in Figure 57 that also have the same peak signature at 32 m.

Figure 57 shows the horizontal distribution in Regions A through C of the MOX-[Cu] for different ages of the soil. Overall, the levels for MOX-[Cu] are >10X than for CO3-[Cu] fraction. Figure 57 is similar to Figure 54 (Appendix A-2) in that the [Cu] are

relatively the same along the entire transect with a noticeable peak at 32 m where the [Cu] was relatively high, corresponding to the 19th Indiana's position during the battle. In addition, the lowest levels of MOX-[Cu] are found at 38.9 m, on the slope (Region B) directly after battle line. The third peak (101 m) indicates that the MOX-[Cu] was mobile in Region B but was forming a cluster — "pooling" in Region C — which is further proof of the bulk migration of Cu into the plain during the acute episodes of high precipitation.

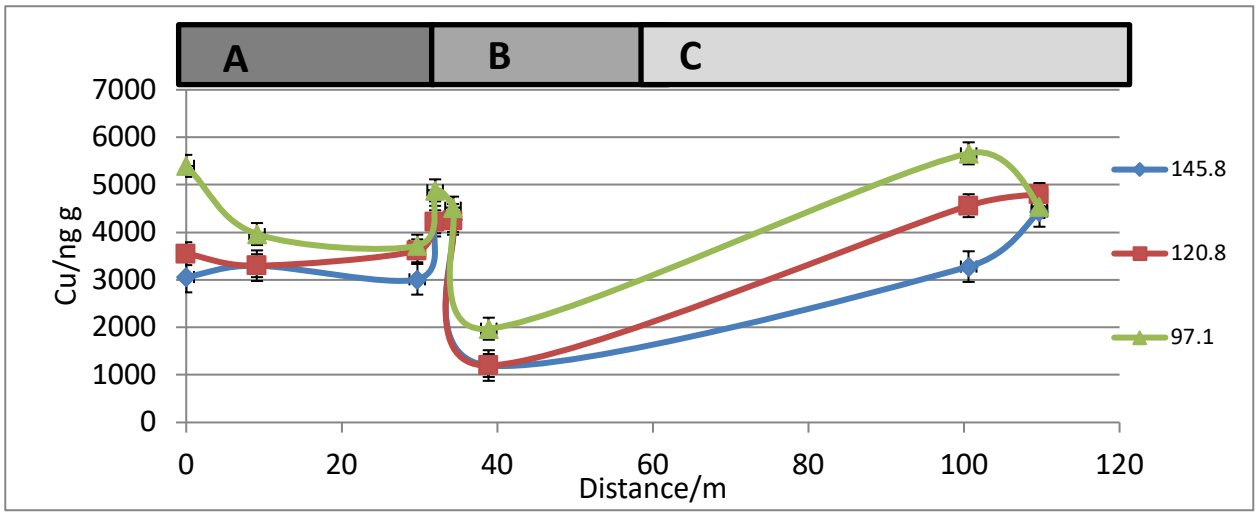


Figure 57. Horizontal distribution of MOX-[Cu] along the entire transect for ~50 yr after the battle; (n=3) at the 95% confidence level.

The horizontal distribution of MOX-[Cu] in Regions A through C for soil core layers older than 1862 are shown in Figure 58. In comparing Figure 58 to the more recent Cu deposition in Figure 57, the migration of the MOX-[Cu] in the soil core profile was similar for both in the vertical direction, in particular the increases observed at ~32 m and at ~110 m which indicates that the downward migration of the MOX-[Cu] follows a bulk migration, as it accumulates in Region C. However, the rate downwards was faster ~40

yr after the battle compared to the rate upwards ~25 yr after the battle, as shown in Figure 57 by the change in the slope from 40 m to 110 m. In Region C (Figure 58), it was again apparent that surface rainwater pooled, and the downward migration also apparently occurred at a steady rate, with a relatively high MOX-[Cu] in layers that are ~90 yr before the time of the battle.

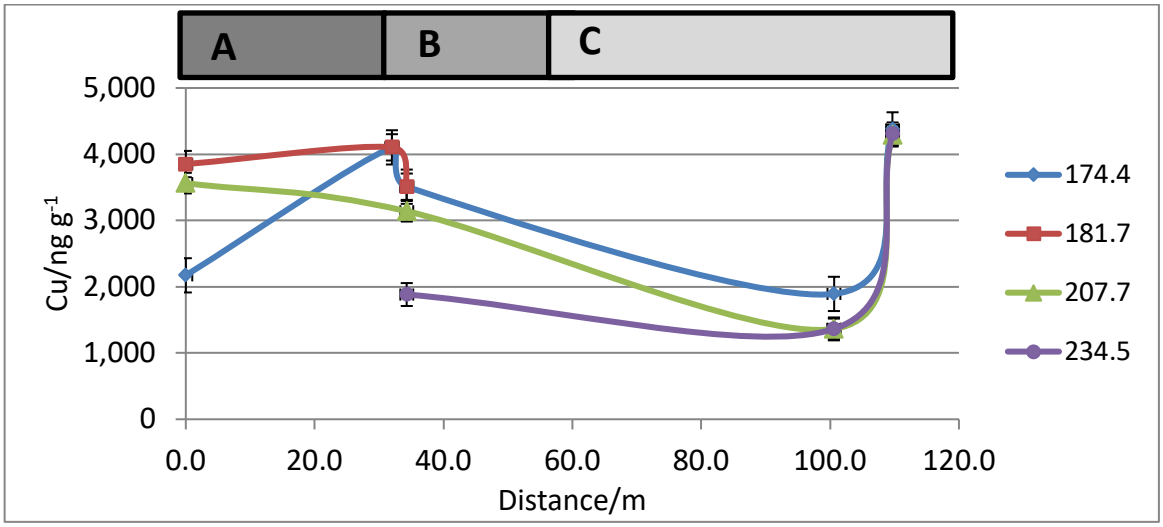


Figure 58. Horizontal distribution of MOX-[Cu] along the entire transect for ~90 yr before the battle; (n=3) at the 95% confidence level.

### 3.2.2.4 Organic-bound Cu

ORG-[Cu] was extracted from the soil cores by using $H_2O_2$ (35% v/v) followed by $NH_4CH_3CO_2$ (1.0 M), the MDL by the GF-AAS method was 1.54 ng $g^{-1}$. The results for all of the soil core samples and the [Cu] vs. depth profiles for each sampling site can be found in the Appendix (Table A-3 and Figure A-3 (a - h), respectively). The soil cores from the ridgeline (Region A) that transect the position of the 19th Indiana display distinctive peaks in the recent, shallow layers for ORG-[Cu].

The ORG-[Cu] from the leading edge of the slope (interface of Region A/B) at Site 32 (38.9 m) is lower than the profiles in Region A (Figure 84 and Figure 85 Appendix A-3). The observed trends between Regions A and B for ORG-[Cu] are: (a) the highest levels are on the ridge (Region A), (b) the highest levels are in the shallow layers < 100 yr, and (c) the vertical profiles are similar in the distribution of Cu. This distribution suggests that a bulk migration of the ORG-[Cu] occurred as a result of chronic convective-diffusive forces, thereby causing Cu to accumulate in these layers. This suggests that Cu is migrating horizontally because the contour of the landscape sharply changes at the Region A/B interface (Figure 51).

The concentrations of ORG-[Cu] at the Region B/C interface are shown in Figure 86 (Appendix A-3). The [Cu] varies significantly (five-fold) from 100.6 m (Site 21) to 109.6 m (Site 22). This points towards a more mobile form of Cu because of three factors: (a) the soil is low in NOM thereby decreasing the capacity of the soil to retain Cu, (b) the soil is high in pH causing an increased solubility of ORG-[Cu] and (c) the soil is high in ionic strength increasing the desorption of Cu from soil, thus decreasing the capacity of the soil to retain Cu.[29,112-115] Two primary forms of Cu were associated with NOM: (a) Cu(I) was predominantly coordinated with a N and/or S ligand group, and (b) Cu(II) was predominantly coordinated with five- to-six-membered ring chelates formed by closely spaced carboxyl and hydroxyl groups.[120]

From the literature, maximum Cu sorption was obtained at pH > 5.8, in which more than 99% of Cu could be sorbed by soils.[114] This was caused mainly by the formation of $Cu(OH)_2$ because the pH at which $Cu(OH)_2$ precipitation occurred was calculated as 5.77 based upon on the $Cu(OH)_2$ solubility product ($K_{SP} = 2.2 \times 10^{-20}$).[114]

Furthermore, the addition of NOM reduced the Cu sorption at each respective pH for both soils. The reduction was especially obvious with an increase in pH, which implied that NOM could bind with Cu more readily and strongly at a higher pH. However, at pH > 6.8, Cu sorption decreased with increases in pH in the presence of NOM.[114] As shown in Figure 59, a model organic compound complexes with Cu in different binding forms as a function of pH. Hydroxyl ions bind to Cu at high pH to yield a complex ion. The Cu complex ion would be repelled by the soils of the same charge through which Cu was moving. Cu sorption by soils is thus simultaneously affected by both pH and NOM concentration at lower soil pH (<6.8).[114] At a high-pH condition (>6.8), however, Cu sorption was predominantly affected by NOM due to a strong binding affinity of NOM with Cu.[114]

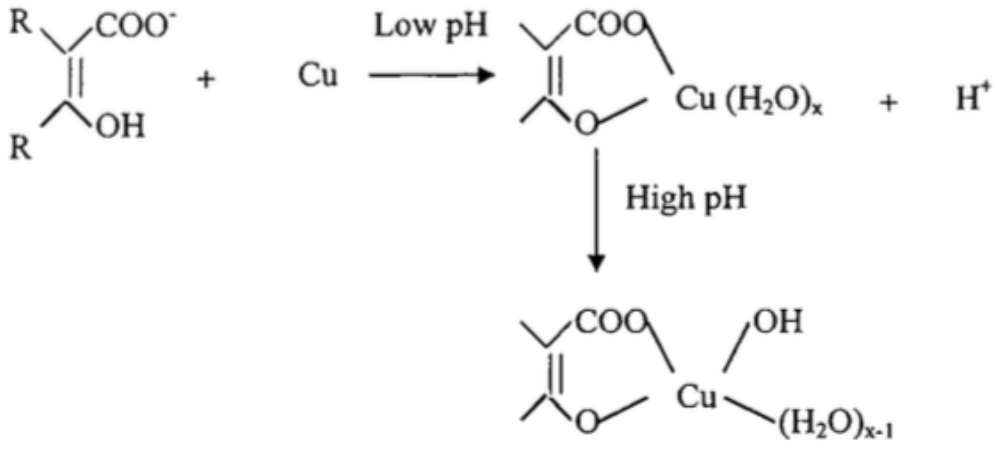


Figure 59. An example of an ORG-[Cu] complex with different binding forms low and high pH values.[114]

In this study, the pH is in the range from 4.9-6.8 and has high ORG-[Cu] in shallower layers, meaning that the sorption is affected by both pH and NOM, whereas

in the deeper layers sorption is predominantly affected by pH.[73,114] The cation-exchange capacity (ionic strength) of the soil (13.0 ±3.3 meq 100 $g^{-1}$) is relatively low, therefore increasing the capacity of the soil to retain Cu.[73]

High NOM in soil provides for a larger surface area for the Cu to sorb, thereby immobilizing the ORG-[Cu] that forms in the humic material.[41,112] Also, if the soil pH is low, the ORG-[Cu] will not dissolve and consequently become retained in the sub-surface soil layers. There is high accumulation of Cu in Region C (109.6 m, Site 22), suggesting that the ORG-[Cu] has a high mobility and has pooled further down the slope (Region B) and into the plain (Region C).

For comparison, the horizontal distribution of ORG-[Cu] along the entire transect for ~50 yr after the battle is shown in Figure 60, where there is high accumulation of ORG-[Cu] at the Region A/B interface (34.3 m) which also confirms the location of the 19th Indiana's position during the battle. The second peak at ~110 m (Region C) is sharper, indicating the horizontal movement of the ORG-[Cu] as it was transported down the slope, and eventually pooling in the plain (Region C).

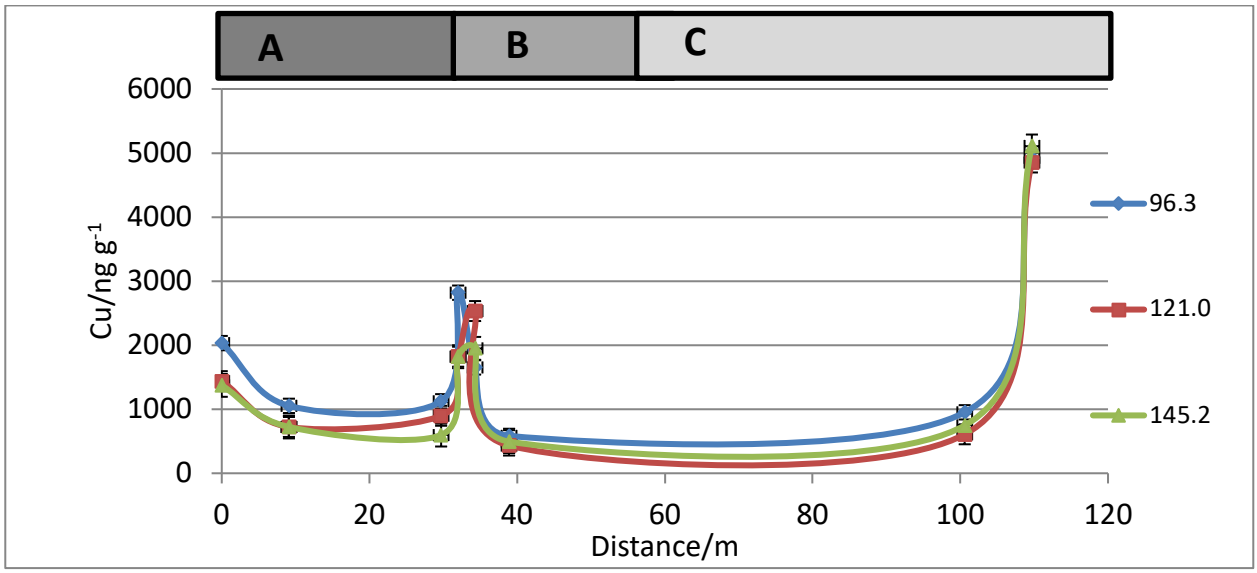

Figure 60. Horizontal distribution of ORG-[Cu] along the entire transect for ~50 yr after the battle; (n=3) at the 95% confidence level.

The high [Cu] in the shallow soil layers of Region A/B interface correspond to the vertical movement of the ORG-[Cu] from the deeper layers of soil. At the Region A/B interface the older layers of soil have ~60% lower levels of ORG-[Cu] (comparing ~50 yr after the battle to ~90 years before the battle (Figure 60, Figure 61). This suggests that the ORG-[Cu] that accumulated on the slope migrated to the bottom of the slope, or that the Cu migrated so quickly and deeply for it to be undetectable in the cores collected in this study. Thus, Cu appears to preferentially accumulate in the plain (Region C).

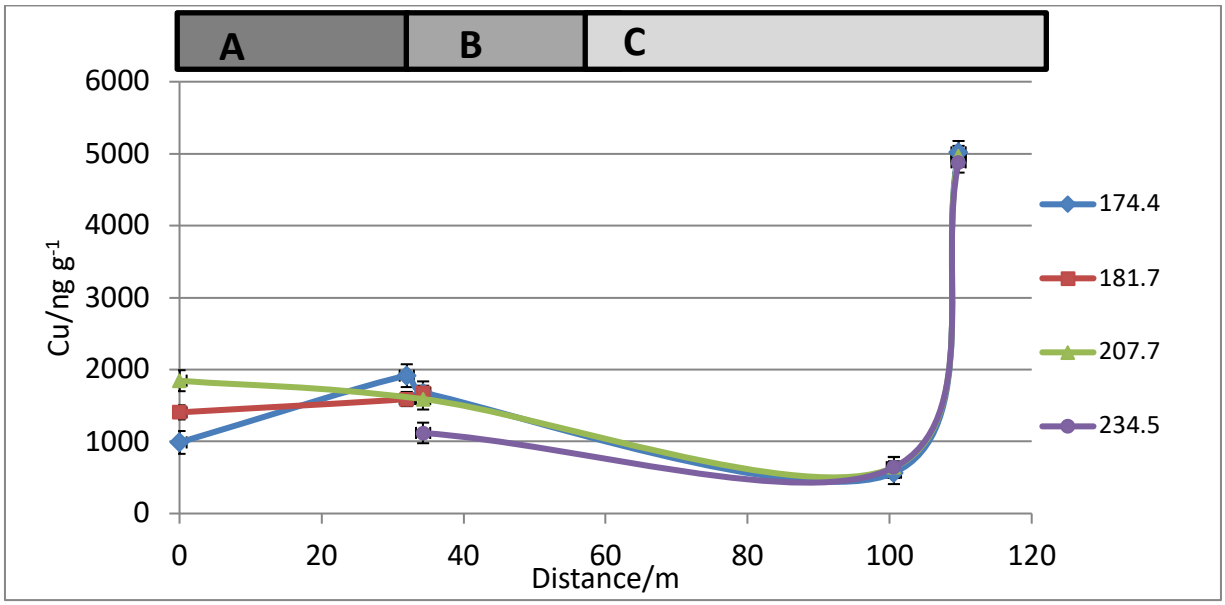


Figure 61. Horizontal distribution of ORG-[Cu] along the entire transect for ~90 yr before the battle; (n=3) at the 95% confidence level.

NOM transforms metallic Cu into more mobile forms of Cu compounds in the soil, suggesting that the observed increased mobility is due to the presence of high levels of ORG-[Cu].[30,112] Organic acids (i.e., humic and fulvic acids) strongly bind metal ions and the oxidation of NOM to $CO_2$ leads to the transformation of the Cu(II) to $CuCO_3$.[116,117] Thus soil that contains high levels of NOM will have more carbonate functionalities, thereby supporting the trend observed in this study that CO3-[Cu] was also found at significant levels and was very mobile.[117]

### 3.2.2.5 Determination of Total Cu by *Aqua-Regia* Extraction

As described in the Experimental chapter, soil core 9 (Region A, 0 m) was extracted for total Cu by *Aqua Regia* extraction. This procedure is designed to extract the RFC-[Cu] (hereafter referred to as RFC-[Cu]) from the soil, meaning the Cu is so

tightly bound to minerals that it is immobile under natural (BCR-simulated) conditions.[9] The extraction procedure and the determination method are described in Chapter 2.3.1.6 and Chapter 3.1.5, respectively. The results for the core sample and the [Cu] vs. depth profiles can be found in the Appendix (Table A-4 and Figure A-4 (a), respectively).

In Figure 62, the sum of the concentrations for the total speciated Cu was calculated — that is, the sum of the EXΔ-, CO3-, MOX-, ORG-, and RFC-[Cu] for Core 9 (Region A, 0 m). The maximum Cu input from these cores is: 67.3 wt% from RFC-[Cu], 22.1 wt% MOX-[Cu], 9.40 wt% ORG-[Cu], and 1.25 wt% CO3-[Cu] (the EXΔ-[Cu] was below the MDL).

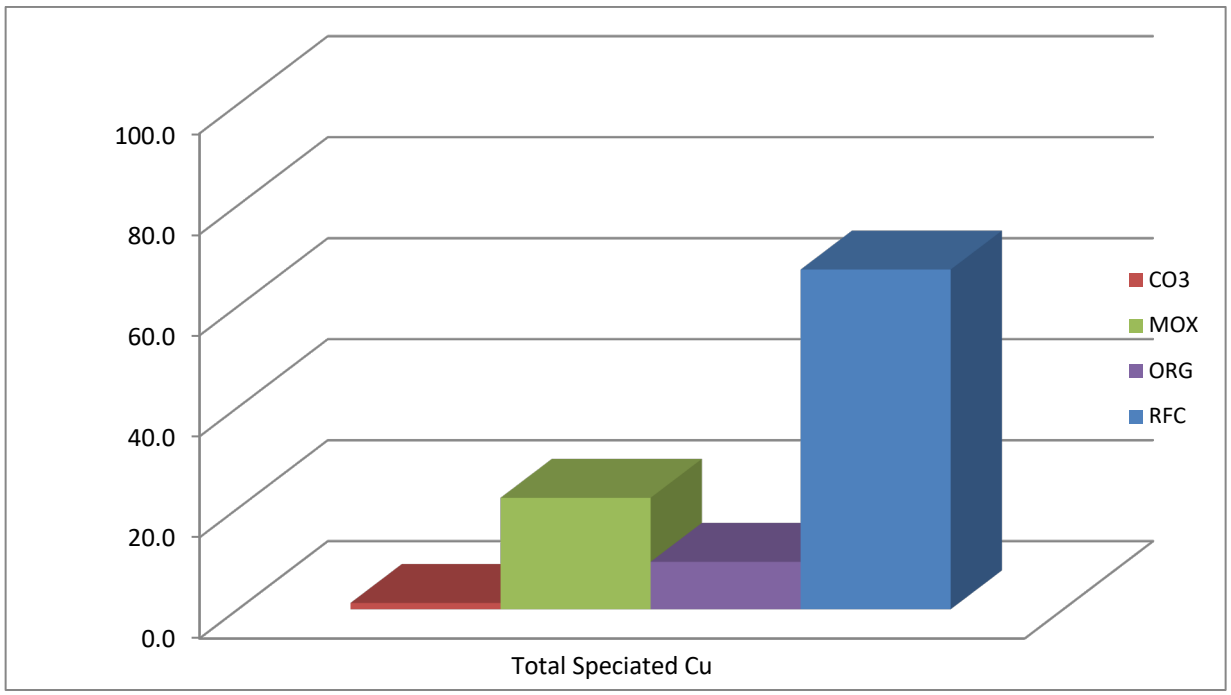


Figure 62. Mass balance for the sum of the speciated forms of Cu along the battle-line transect for core 9 (0 m); (n=3) at the 95% confidence level.

From Figure 62 it can be interpreted that the vast majority (> 67%) is RFC-[Cu]. For soil near an urban area, this is not unusual because RFC-bound is commonly >99 wt%.[8] This result is intriguing in that the MAE BCR method extracted much more than the typical <1 wt% that is typically extracted by the conventional BCR. This suggests that with the MAE BCR method, especially for the MOX-[Cu] but also for the ORG-[Cu], the RFC-[Cu] is also being extracted because of the more energetic conditions within the microwave vessel. Thus, as stated earlier in this chapter, the goal of the BCR method in revealing the "bioavailable Cu" is severely compromised when using MAE, thereby creating a significant bias in the results. A bimodal release of Cu was observed which may provide insight into how Cu species are sequestered within the crystal lattice of the soil minerals. This should be studied in future investigations to improve the understanding of the molecular structures that are binding Cu and the mechanism of its release by the application of microwave energy.

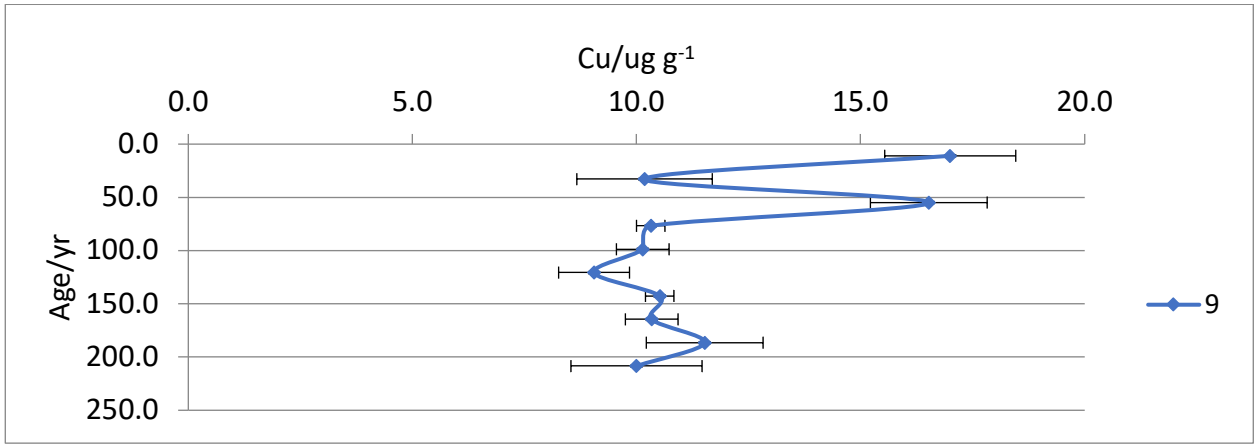

Figure 63. Vertical distribution at Site 9 of RFC-[Cu], where it is primarily found near the surface; (n=3) at the 95% confidence level.

From Figure 63, the RFC-[Cu] was found in the more shallow soil layers. RFC-[Cu] is highest at the surface, peaks at ~75 yr and remains relatively low thereafter. The fluctuation in [Cu] in recent layers of soil may be understood as a competing kinetic process, where the formation of CO3-, MOX-, and ORG-[Cu] species is out-competing RFC-[Cu] formation processes. That is, the RFC-[Cu] is more thermodynamically stable but slower to form than CO3-, MOX-, and ORG-[Cu] species.

In this work, Cu-contaminated soils originating from single-use, brass ignition devices have been examined and interesting depositional trends for Cu have been observed. Next, this study focused on investigating residual Hg from the explosive compound $Hg(CNO)_2$ used in these percussion caps.

#### 3.2.2.6 Speciated Hg

EXΔ-, CO3-, MOX-, and ORG-[Hg] were extracted from the soil cores by using the same extractants as used for Cu. The MDL by the ICP-MS method was 0.002 ng $g^{-1}$. The results for all of the soil core samples and the [Cu] vs. depth profiles for each sampling site can be found in the Appendix (Table A-5 and Figure A-5 (a - d), respectively).

The distribution of Hg revealed an interesting depositional trend in relation to the terrain profile. To study the speciation of Hg in Region B, Core 2 (36.6 m) was examined by the MAE BCR method for bioavailable Hg (i.e., the first four steps). Figure 64 shows the distributions of EXΔ-, CO3-, MOX-, ORG-[Hg] for soil core 2, in Region B (Slope) determined by ICP-MS. Essentially the Hg levels are the same throughout the

core with an increase of ORG-[Hg] in the shallow layers that is similar to the results found for Cu.

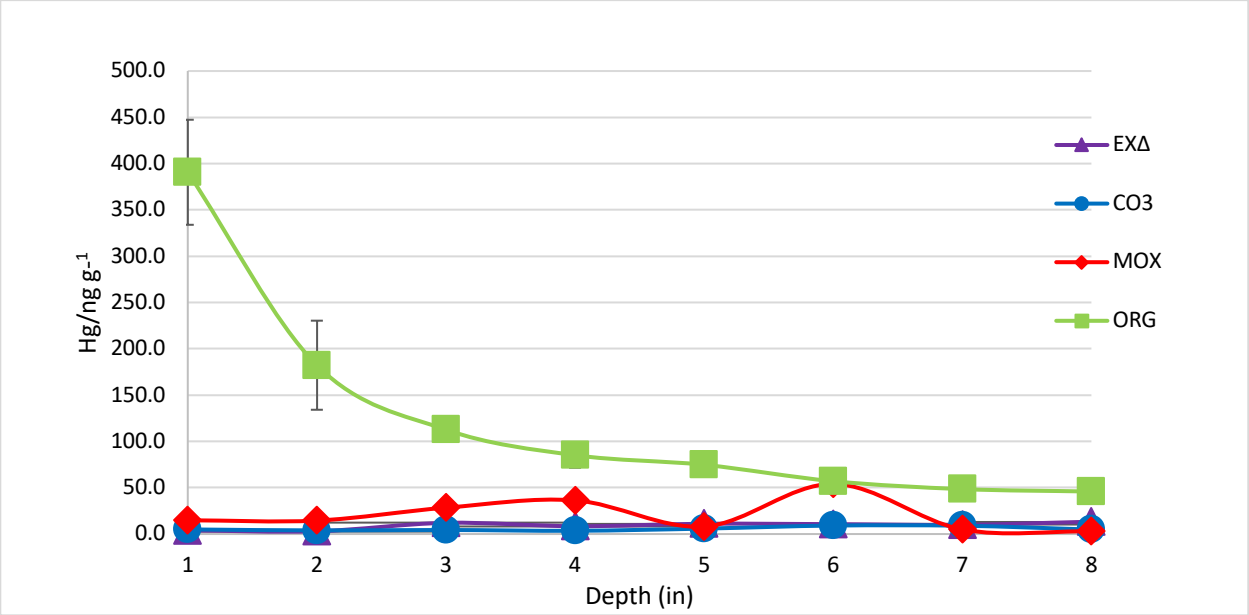


Figure 64. Vertical distribution of [Hg] for soil core 2 in Region B (Slope) as determined by the MAE BCR ICP-MS method; n=3 at the 95% confidence level.

By comparison, the trends shown for site 2 (36.6 m, Slope) in Region B display distinct peaks in the soil layers for EXΔ-, CO3-, MOX-, and ORG-[Hg] (Figure 87-Figure 90 in Appendix A-5). An overlay of the extraction steps is shown in Figure 65. EXΔ-[Hg] and CO3-[Hg] in Figure 87 and Figure 88, respectively show that [Hg] is essentially constant at low ppb levels, with variation presumably because of the noise being pronounced. MOX-[Hg] in Figure 89 shows a significant peak near 1860 (~150 yr) and a lesser one at ~1900 (~100 yr). While the peak circa 1860 corresponds to the battle, the circa 1900 peak is of unknown origin. ORG-[Hg] in Figure 90 shows that there is a high [Hg] at the surface, presumably related to the deposition of Hg from coal-fired power plants.

Intriguingly, the high NOM content near the surface has the highest overall [Hg] (Figure 90 and Figure 65). High amounts of NOM in soil provides for a larger surface area for the Hg to sorb, thereby immobilizing the ORG-[Hg].[41] This rationalization follows the trend that this study has observed, in that the concentration of ORG-[Hg] in the shallow layers is elevated while the deposition of Hg in the deeper layers is low. This indicates that the deeper layers have lower quantities of NOM, thus increasing the migration of Hg because of the weaker ORG-[Hg] complexes that form at depth. Note that what appears to be an increase (~65%) in the ORG-[Hg] at ~200 yr is probably attributable to experimental uncertainty at the low levels that were measured. On the other hand, it may indicate the relatively fast transport of Hg to deeper layers, but in the absence of cores with depths >250 yr that cannot be assumed.

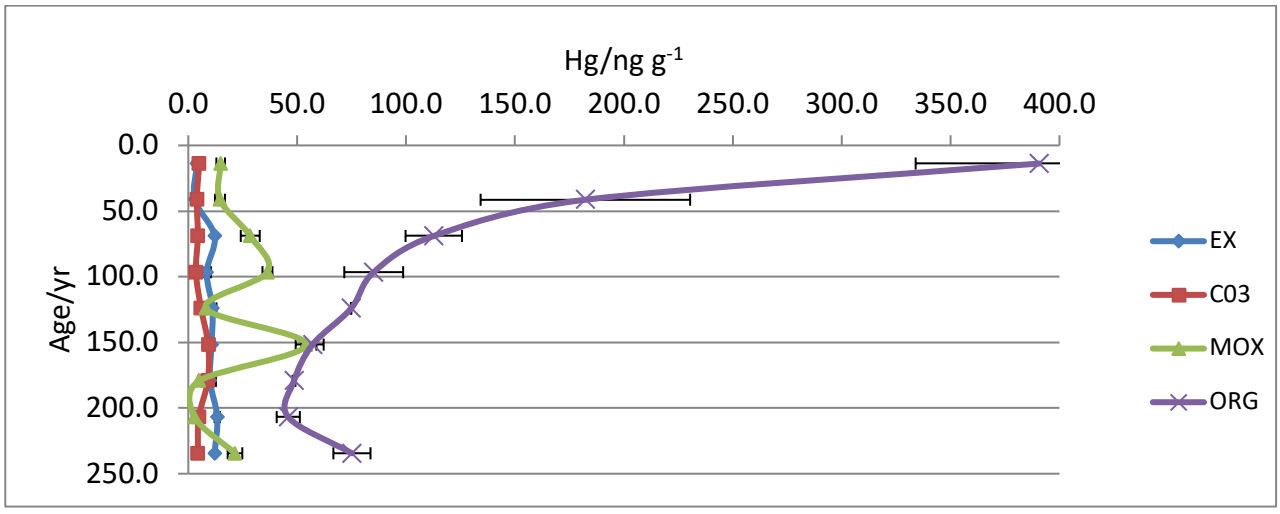


Figure 65. Overlay of soil core profile for EXΔ-, CO3-, MOX-, and ORG-[Hg] in Region B, site 2 (36.6 m); (n=3) at the 95% confidence level.

#### 3.2.2.7 Hg Extraction with Nitric Acid

Hg extracted from the soil core samples with concentrated $HNO_3$ (CAT-[Hg]) was used to understand the overall trend in its abundance and distribution. CAT-[Hg] was extracted from the soil cores by using concentrated $HNO_3$ and the MDL by the ICP-MS method was 0.002 ng $g^{-1}$. The results for all of the soil core samples and the [Cu] vs. depth profiles for each sampling site can be found in the Appendix (Table A-6 and Figure A-6 (a - c), respectively). CAT-[Hg] extracts Hg differently than the BCR method or the *Aqua Regia* method. The $HNO_3$ method acts as both acidifying reagent and oxidizing agent by dissolving and then oxidizing inorganic and organic compounds. In general, it can be assumed that the $HNO_3$ method extracts all of the speciated forms of Hg except those that are bound to refractory matter.

The results for the CAT-[Hg] method revealed an interesting depositional trend in relation to the terrain profile. The soil cores from the ridgeline (Region A) that transect the position of the 19th Indiana display distinct peaks for Hg in the recent shallow layers, as shown in Figure 91 (Appendix A-6). By comparison, the trends shown in Region A appear to be similar to those observed for the CO3-[Cu] (Figure 78), MOX-[Cu] (Figure 81), and ORG-[Cu] forms.

The levels for Hg are dramatically lower in the shallow layers, with relatively high levels at greater depth. (Figure 84) (Shown in Appendix A-3, a-e respectively) forms. Figure 92 (Appendix A-6) shows the Hg soil core profile in Region B — both Region A and B show a relatively steady decrease in [Hg] from 100-150 yr (presumably, the peak at ~100 yr can be attributed to method error). The peak at ~200 yr is not seen in

Regions B or C (Appendix A-6), perhaps because Hg migrates more slowly in the more compact soil. In Region C, a similar increase is observed at a depth corresponding to ~250 yr which is not seen in Region B, which indicates that Hg species are vertically more mobile.

Vertical distributions in Regions B (Figure 92, 36.6 m) and C (Figure 93, 100.6 m) both display a linear decrease in [Hg] over time. The [Hg] in Region B is higher than Region C, again suggesting that the bulk migration of Hg from the sub-surface flow of water caused Hg to accumulate on the slope. The combined soil core profiles for Hg in Regions A, B, and C are shown in Figure 66.

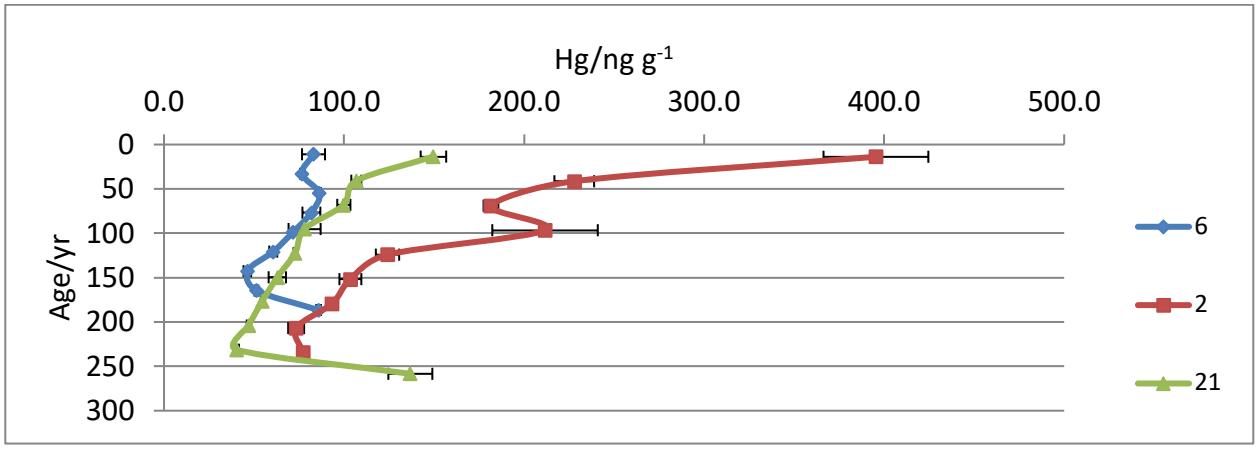


Figure 66. Soil core profiles for Hg in Regions A (Site 6), Region B (Site 2), and Region C (Site 21); (n=3) at the 95% confidence level.

Figure 67 shows the horizontal distribution of Hg in Regions A through C for soil ~50 yr after the battle. Figure 67 is similar to Figure 66 in that there are higher levels of Hg in Region B (Slope). The horizontal distribution of Hg in Regions A through C for ~90 yr before the battle are shown in Figure 68. In comparing Figure 68 to Figure 67, the migration of Hg in the soil core profiles from the peak in Region B to C (Figure 67)

for ~50 yr after the battle has a 66% decrease in [Hg] while ~90 yr before the battle, the [Hg] decreased 50%. Both trends (±15%) are in the vertical direction suggesting that the migration rate did not appreciably change. As described in Section 3.2.2.5 for RFC-[Cu], a similar process is apparently occurring here as well. The increased fluctuation in [Hg] within recent layers of soil can also be described as a competing kinetic process, as observed for RFC-[Cu].

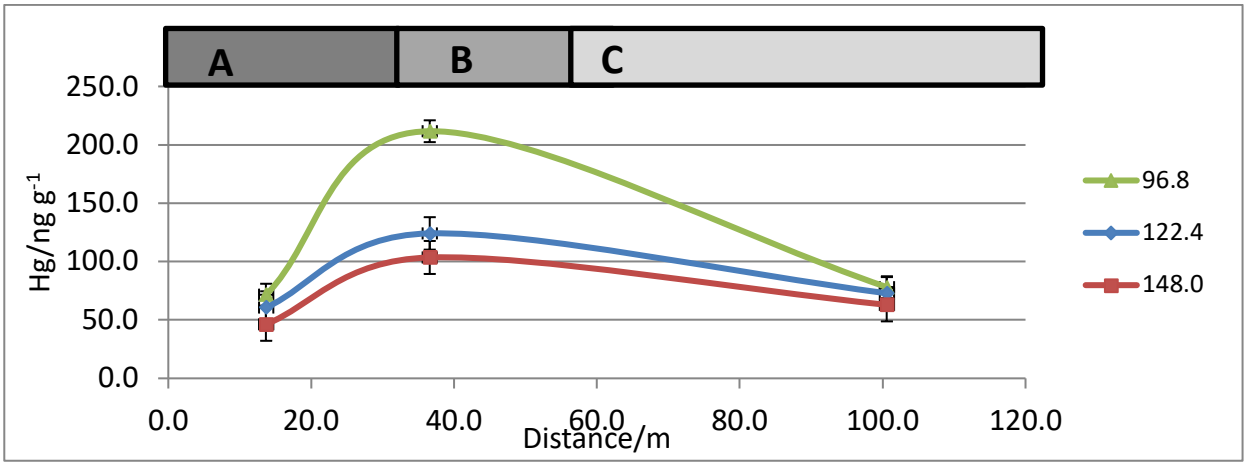


Figure 67. Horizontal distribution of CAT-[Hg] along the entire transect for ~50 yr after the battle in Regions A (Site 6), Region B (Site 2), and Region C (Site 21); (n=3) at the 95% confidence level.

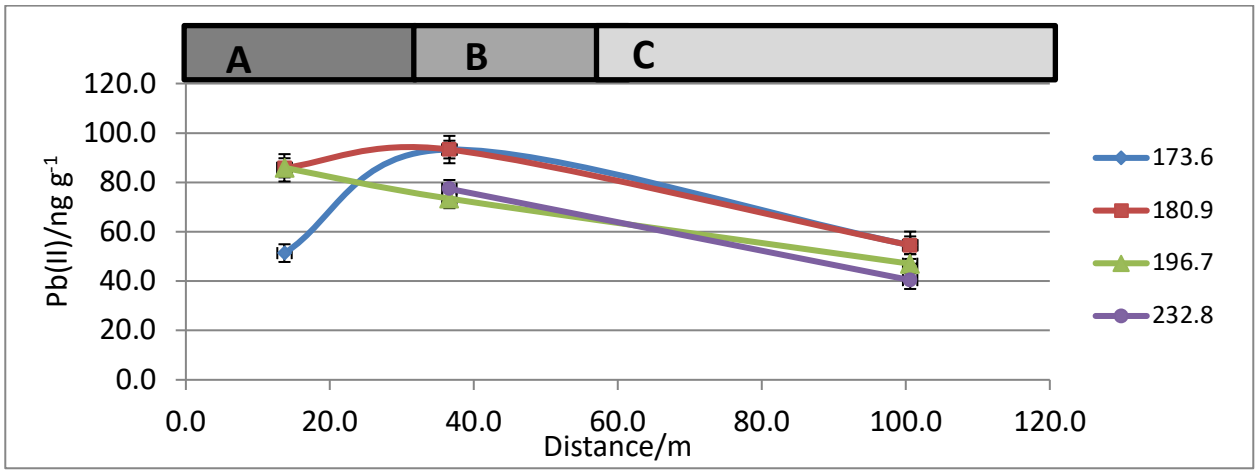


Figure 68. Horizontal distribution of [Hg] along the entire transect for ~90 yr before the battle in Regions A (Site 6), B (Site 2), and C (Site 21), (n=3) at the 95% confidence level.

#### 3.2.2.7.1 Mass Balance for CAT-[Hg]

In Figure 69, the sum of the [CAT]-Hg was calculated — that is, the sum of Hg for the soil layers corresponding to Region A, B, and C separated by region and compared to one another. The Hg input from these cores Figure 69 is as follows: 22.2% remained on the ridgeline (Region A), 51.4% migrated down the slope (Region B), and 26.4% moved into the plain (Region C).

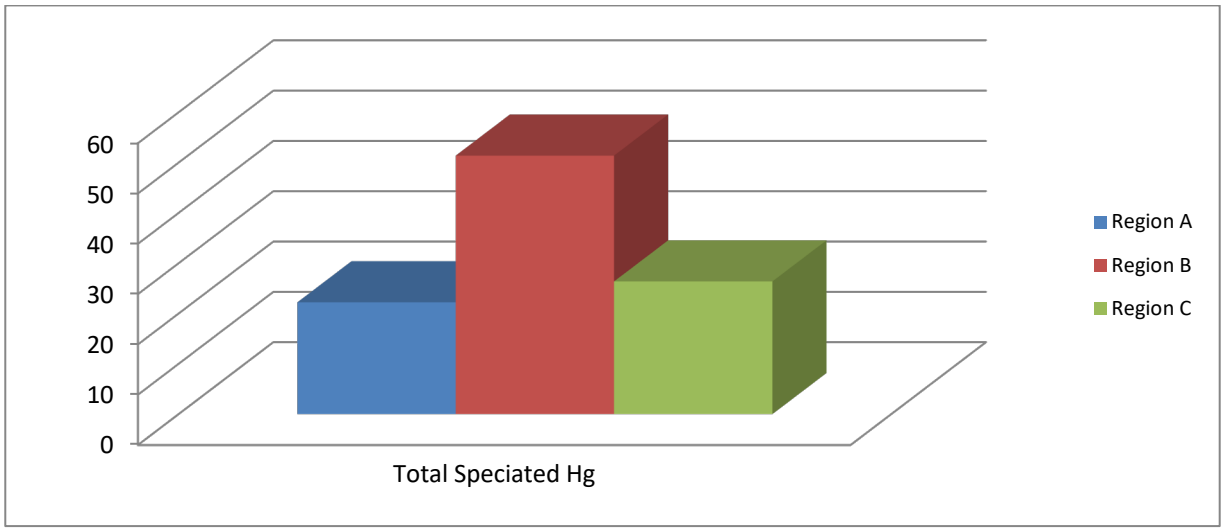


Figure 69. Mass balance for the sum of CAT-[Hg] along the battle-line transect.

Figure 69 shows that Hg is moving at a constant rate for the CO3-, MOX-, and ORG-[Hg] — that is, the CAT-[Hg] method extracts all of the BCR-speciated forms of Hg. By the time of sample collection (2004-2007), most of the Hg had migrated to Region B. If re-sampled today, it is expected that the Hg will have migrated further into Region C.

Nevertheless, it is interesting that the migrating CAT-[Hg] is significantly increased in Region B. As described in Section 3.2.2.4, he maximum Cu sorption (>99%) will occur at pH 5.8, but beyond pH 6.8 the sorption will decrease in the presence of NOM.[114] This trend may also apply for Hg because the soil pH ranged from 4.9 to 6.8 and the soil in Region B is relatively high in NOM in the shallow layers but less in the deeper layers (>4 in).[73] It can be speculated that because the soil pH on the Slope is >5.8, perhaps the sorption of Hg would decrease on the Ridge and increase on the Slope at the low end of the measured pH range.[29,112-114,]

### 3.2.3 Transport and Fate

In this study it has been shown that the analytical method is robust and that the comparison of the Cu and Hg results to the earlier Pb findings is interesting. Now beyond speciation, transport will be examined as a means to understand the fate of the speciated forms of Cu and Hg compared to Pb.

For calculation of the first-order rates of the speciated forms of Cu, the two primary concentration peaks from the horizontal distributions (Figure 54-Figure 55 for CO3, Figure 57-Figure 58 for MOX, and Figure 60-Figure 61 for ORG) were used. Region A is the source input of the Cu, based not only upon the historical evidence but also from the data analysis described in this study. Therefore, the first step in developing a first-order rate is to use the highest concentration peak on the ridgeline as the initial input location, which would be Site 31 at 34.3 ± 5 m (the variability is based on an estimate of the width of the infantry firing line, as described in Section 1.1.3). Based on the description of the trends described earlier in this chapter for the Cu migration, there are two primary accumulation points: in the southern part of Region A (Site 31 at 34.3 m) and in Region C (Site 22 at 109.7 m) with no accumulation point in Region B.

The rates for the migration of the CO3-, MOX-, ORG-[Cu] were calculated from the apparent center of the 19th Indiana's position in Region A (Site 31) to the accumulation point in the plain Region C (Site 22). Region A (34.3 ± 5 m) to Region C (109.6 ± 5 m) for each speciated form of Cu. The calculated rate is based on the average concentration for the entire core for Sites 31 and 22 for each speciated form of

Cu to determine the two primary accumulation points. Since several trips to BF were made to collect cores at these sites (9 in August 2004, 31 in November 2007, and 22 in July 2007), the most recent trip in November 2007 was used as the representative date in the kinetic calculations. With the difference of three years between the visits, this is within the error associated in radiometrically dating the cores is ±10 yr.[74] A sample calculation is shown in Equation 12 for Region A → C. The difference between accumulation points refers to the difference between Region C to Region A (109.6 m - 34.3 m), the deposition to collection refers to the difference of the time of collection and time of deposition (November of 2007 to August 1862, i.e., 145.25 yr). The variability of the infantry firing line is based on an estimate of the width of the infantry firing line (± 5 m) divided by the deposition to collection (145.25 yr).

$$Rate\ \frac{m}{yr} = \frac{difference\ between\ acumulation\ points\ (m)}{Deposition\ to\ colletion\ (yr)} \pm \frac{\text{variability of infantry firing line (m)}}{Deposition\ to\ colletion\ (yr)} \quad [12]$$

$$Rate\ \frac{m}{yr} = \frac{75.3\ m}{145.25\ yr} \pm \frac{5\ \text{m}}{145.25\ yr} = 0.518 \pm 0.034\ \frac{m}{yr}$$

The calculated first-order rate constant from Region A to C shown in Table 44 is the same for CO3-, MOX-, ORG-[Cu] (0.519 ± 0.034 m $yr^{-1}$). Results from prior studies of Pb is shown in Table 45, where the first-order rate constants from Region A to C for CO3-, MOX-, ORG-[Cu] are 26.7%, 32.6%, and 22.9% higher than observed previously for Pb. This provides insight into how these metals are transported through the soil — Cu contamination will impact a larger area in a given time compared to Pb. This will

need to be studied in future work for Hg to compare the rates of transport among the speciated forms of the three metals.

Table 44. Calculated first-order rates for the three speciated forms of Cu.

| Form of Cu | Rates (m $yr^{-1}$) | |
|---|---|---|
| | Region A → B | Region A → C |
| CO3-[Cu] | N/A[1] | 0.52 ± 0.03 |
| MOX-[Cu] | N/A[1] | 0.52 ± 0.03 |
| ORG-[Cu] | N/A[1] | 0.52 ± 0.03 |

[1] There was not an accumulation point in Region B to calculate rate constants.

Table 45. Calculated first-order rates for the three speciated forms of Pb.[73]

| Form of Pb(II) | Rates (m $yr^{-1}$) | |
|---|---|---|
| | Region A → B | Region A → C |
| CO3-[Pb] | 0.24 ± 0.02 | 0.38 ± 0.03 |
| MOX-[Pb] | 0.23 ± 0.02 | 0.35 ± 0.03 |
| ORG-[Pb] | 0.25 ± 0.02 | 0.40 ± 0.03 |

### 3.2.4 Overall Trends in the Abundance and Distribution of Speciated Cu and Hg

#### 3.2.4.1 Mass Balance for Cu

As shown earlier for the mass balance of RFC-[Cu] (Figure 62) and CAT-[Hg] (Figure 69), in this section the sum of the concentrations of the total speciated Cu is calculated (Figure 70). That is, the sum of the CO3-, MOX-, and ORG-[Cu] for the soil layers corresponding to the soil core samples separated by region and compared to one another. Figure 70 shows the maximum Cu input from these cores: 63.7% remained on the ridgeline (Region A), 6.86% migrated down the slope (Region B), and 29.5% moved into the plain (Region C).

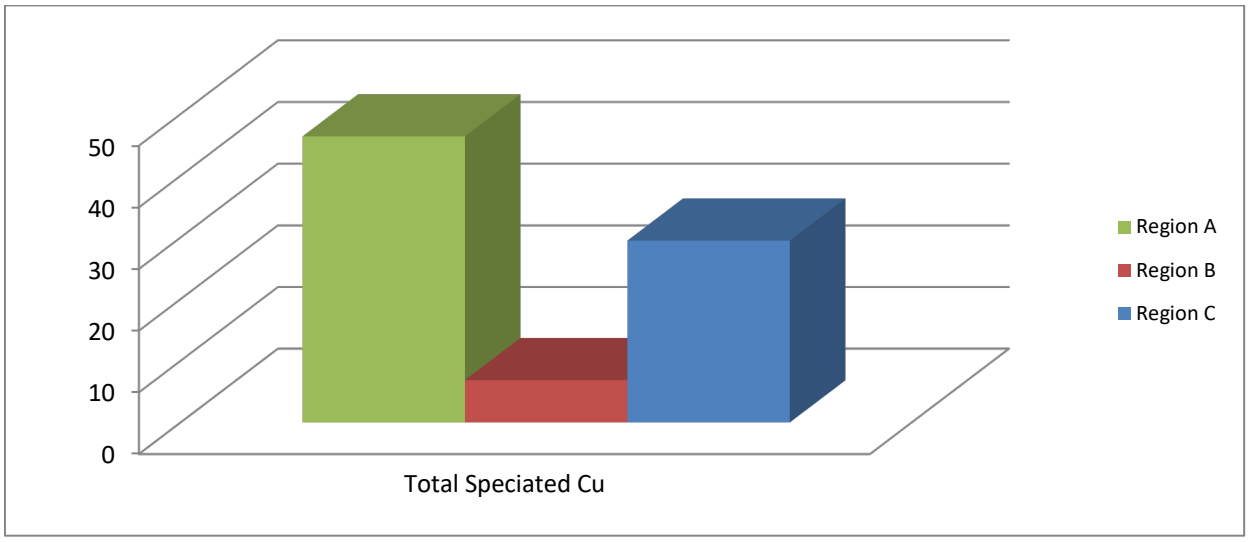


Figure 70. Mass balance for the sum of the speciated forms of Cu along the battle-line transect.

From Figure 70, for Cu moving at a constant rate, by the time of collection (2004-2007) the Cu had migrated to Region C. Figure 71 breaks down the total Cu migration into its individual speciated forms. Most of the Cu is in the MOX form on the Ridge and Plain.

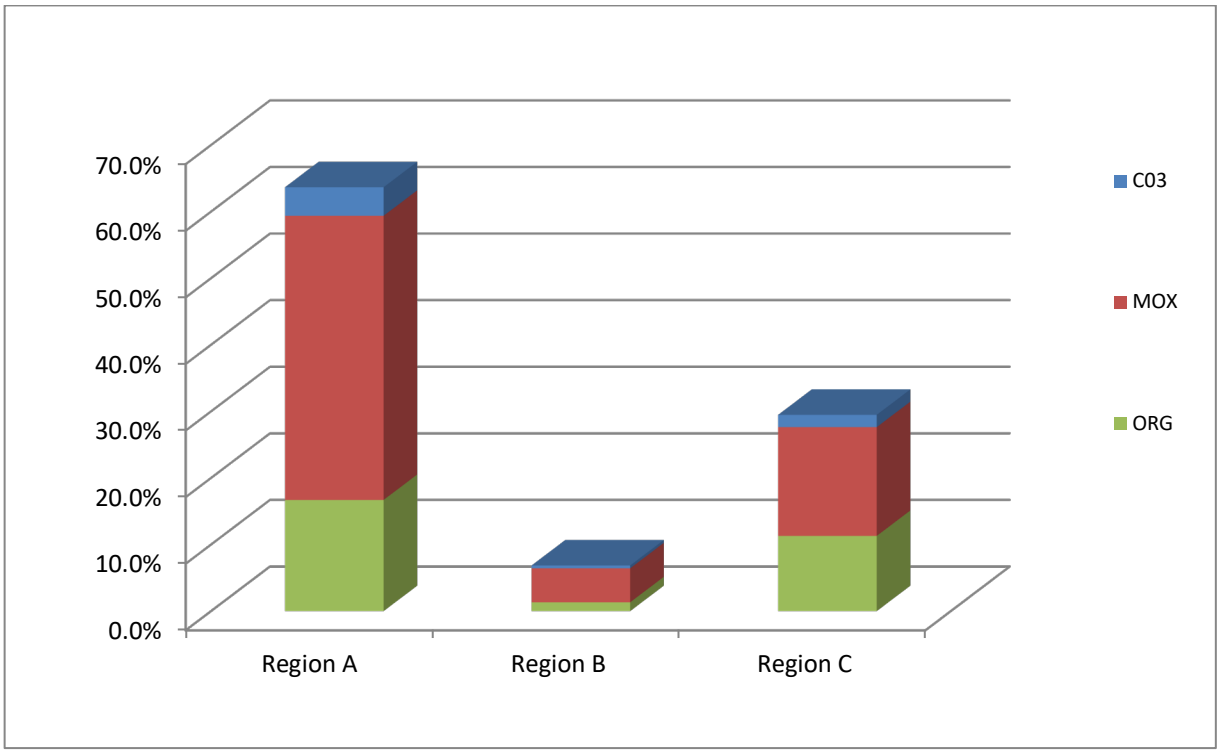

Figure 71. Mass balance for the sum of the speciated Cu along the battle-line transect.

Overall, the Cu is mobile horizontally with more than half of the overall input migrating to the plain. The individual soil profiles also showed the vertical migration of Cu into pre-1862 layers. In this study, whether the migration was vertical or horizontal, similar trends were observed for each speciated form of Cu. That is, the observed speciated forms migrated *together* — regardless of position along the transect or the age of the soil. As mentioned earlier, this suggests a bulk horizontal migration down the slope into the plain occurred, accumulating at the interface where the landscape changed sharply — that is, where the slope became the plain ("pooling" area). Cu transport was thus apparently the result of a combination of acute and chronic weathering events, as described earlier.

The major form of speciated Cu was MOX-bound (42.7%, Figure 71). The next highest level of speciated Cu was ORG-bound, which had high accumulation on the plain Region C (11.3%, Figure 71). The migrating ORG-[Cu] also showed a slow downward (vertical) migration through the soil core profile. Because the soil in Region C is relatively high in NOM in the shallow layers but less so in the deeper layers (>4 in), Cu sorption to soil would be increased in these layers as described earlier in Section 3.2.2.4.[29,73,112-115] Nevertheless, the ORG-[Cu] could be exceptionally mobile, thus making it detectable only at greater depth than sampled — that is, the ORG-[Cu] on the slope migrated to the bottom of the slope or that the Cu migrated so quickly and deeply for it to be undetectable in the cores that were collected.

Pollutant migration can be defined as a three-dimensional process, a function of fluid dynamics, solution chemistry, and matrix properties such as soil porosity.[41] To explain the vertical movement of Cu in soil, consider that narrow capillaries will draw liquids, and this model can be extended to soil pores in that smaller pores will increase the vertical transport of water. Thus, if an aqueous fluid reaches a more compacted zone (i.e., with smaller pore diameters), the solution will move more horizontally — rather than vertically — along this denser layer.[41] In Region A and at the Region A/B interface, the soil is very compacted (Figure 52) leading to the horizontal migration of the Cu. Thus, the heterogeneity of the soil in the regions that were studied can explain the observed Cu transport.

### 3.2.4.2 Mass Balance Hg — MAE BCR

In this section, the sum of the total speciated Hg was also examined — that is, the sum of the EXΔ-, CO3-, MOX-, and ORG-[Hg] for the soil layers corresponding to the soil core sample 2 (Region B) compared to one another. Site 2 was chosen because the depositional trend in relation to the terrain profile from Region A to Region C showed the highest [Hg]. The complete transect was not examined because only a representative comparison of Hg to the detailed results for Cu was sought.

Figure 72 shows that Region B was dominated by the ORG-[Hg] (77.1%). The MOX-[Hg] made up 13.3%, the EXΔ-[Hg] was 6.08%, and the CO3-[Hg] 3.59%.

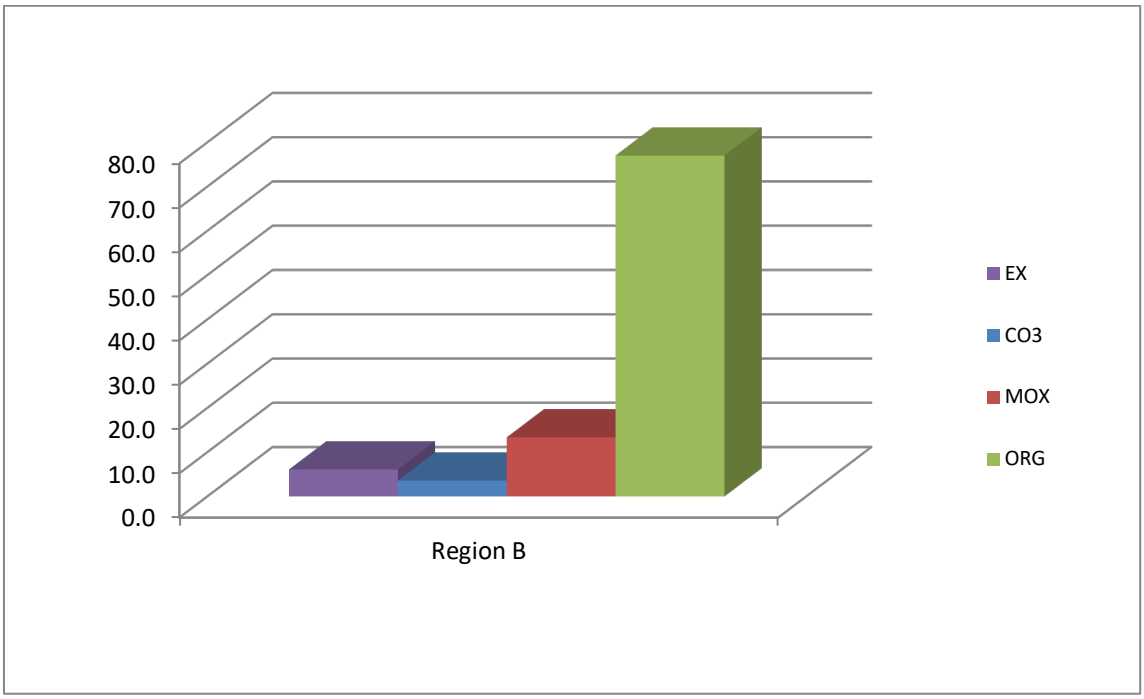


Figure 72. Mass balance for the sum of the speciated Hg along the battle-line transect in Region B.

Most of the [Hg] was found in the shallow (more recent) layers of soil (Figures 76 and 77), and as noted earlier, Hg was readily immobilized by humic material.[41] The ORG-[Hg] is highest in the first inch because that is where the humic acid concentrations are the highest (essentially pure humic acid) from vegetation on the surface as well as the dwelling place for microbes as well as other fauna.[99]

### 3.2.5 Comparison of Overall Trends in the Speciated Forms of Cu and Pb

A comparison of the overall horizontal distribution of Cu and Pb along the transect (Figure 74 and Figure 75) is interesting. The location of the 19th Indiana was definitively shown at 34.3 m and there are two primary accumulation points for Cu: Region A (34.3 m) and Region C (109.7 m). Comparing the trends for Pb from Figure 75 reveals that there are three primary accumulation points: in Region A (~9-18 m), in the center of Region B (~55 m), and Region C (101 m). As mentioned above (3.2.3), this suggests that Cu and Pb underwent distinctive transport mechanisms causing Cu and Pb to accumulate at dissimilar points on the transect.

The Pb extracted by the BCR method is generally ~3-5 times higher than the Cu levels determined in the present study.[73] This can be explained by the relative size and mass of a 0.54 caliber Pb bullet (14.2 g) to a percussion cap (0.10 g, 0.07 g Cu) with a ratio of 70% (w/w) Cu and 30% (w/w) Zn.[21] One bullet is thus 200 times heavier than the mass of Cu in a percussion cap, and therefore potentially releases a much higher amount into the environment through weathering over ~150 years. For every bullet that was fired, one percussion was deposited over the course of the 2-hr. battle. The major

"unknown" is the frequency of dropped bullets, which are assumed to have been the primary source of Pb in the soil. To calculate and compare the deposition of caps to bullets, some assumptions are shown in Table 46.

Table 46. Assumptions in the calculation of the numbers of deposited percussion caps and bullets.

| Assumptions: | Uncertainty / Description | ref |
|---|---|---|
| Number of Union Soldiers | Low / 2100 | 20 |
| Number of Confederate Soldiers | Low / 5200 | 20 |
| Soldiers Engaged: 50% | High / Difficult to accurately estimate | 106 |
| Firing Rate: 2 per min | Low / Reference [20] states 3 rounds $min^{-1}$; re-supply rate of the firing lines is unknown. | 20 |
| Length of Battle: 120 min | Low / Reference [18] | 18 |
| Number of Dropped Bullets: 10 % | High / Difficult to accurately estimate | 106 |
| % of Percussion Cap made of Cu: 70% | Low / Reference [21] | 21 |

The calculation for the number of fired bullets is shown in Equation 13, which is also valid for the number of percussions caps deposited.

$$n_b = n_s * \%S * r * l \quad [13]$$

Where:

$n_b$ is the number of fired bullets

$n_s$ is the number soldiers

$\%S$ is the % of soldiers engaged

$r$ is the rate of fire in $(\frac{bullets}{min})$

$l$ is the length of battle (min)

$$n_b = 7300 * 50\% * (\frac{2}{min}) * 120\ min = 876{,}000\ bullets$$

The calculation of the mass of bullets to caps is shown in Equation 14 and 15, respectively.

$$T_{Pb} = n_b * m_{Pb} \quad [14]$$

Where:

$T_{Pb}$ is total mass of Pb bullets (g)

$n_b$ is the number of fired bullets

$m_{Pb}$ is the mass of a single Pb bullet (g)

$T_{Pb} = 876{,}000 * 14.2\ g * (\frac{1\ kg}{1000\ g})$ = 12,439.2 kg

$$T_{Cu} = n_c * m_{PC} * \%Cu \quad [15]$$

Where:

$T_{Cu}$ is total mass of Cu in percussion caps (g)

$n_c$ is the number of caps

$m_{PC}$ is the mass of a single percussion cap (g)

$\%Cu$ is the % of Cu in a single percussion cap

$$T_{Cu} = 876{,}000 * 0.050g * 0.70 * \left(\frac{1\ kg}{1000g}\right) = 63.1\ \text{kg}$$

To compare the estimated mass of Pb from bullets and Cu from percussion caps to results from this study for Cu and previous studies of Pb, the sum of the CO3-, MOX-, and ORG-bound Cu and Pb is compared in Figure 73. It is assumed that RFC-bound Cu and Pb should be excluded because they may not have been from the battle. The estimated mass of Pb from dropped bullets is about 5 times higher than the mass of Cu from spent percussion caps. This calculation thus generally confirms the observed differences in the [Cu] and [Pb] measured in the soil.

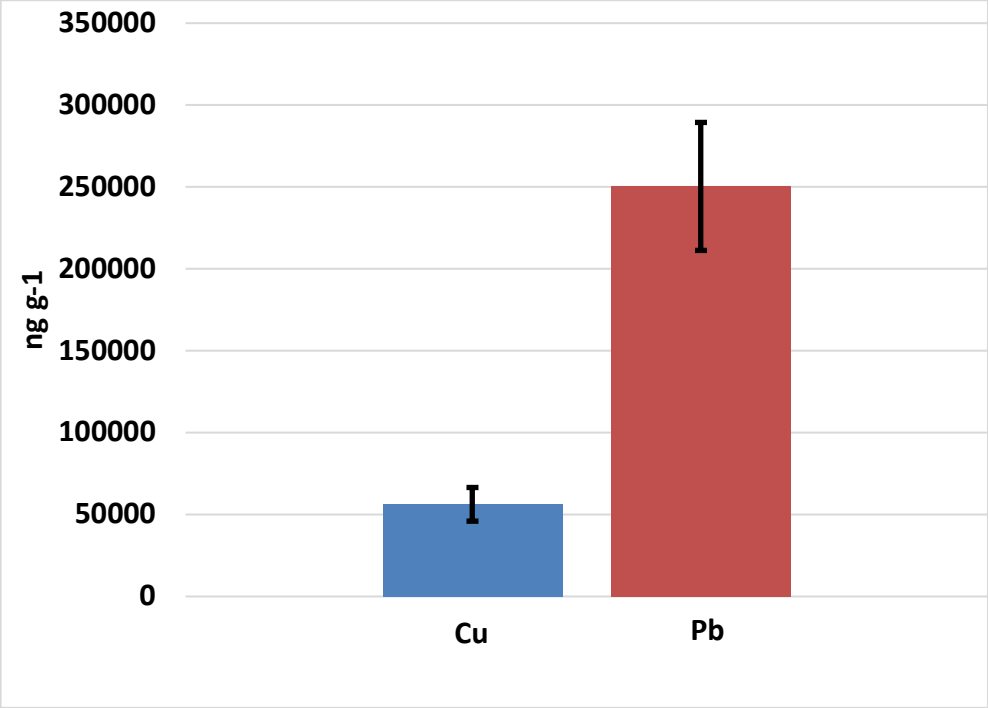


Figure 73. The sum of the CO3-, MOX-, and ORG-bound, excluding the RFC-bound Cu and Pb; (n=3) at the 95% confidence level.[73]

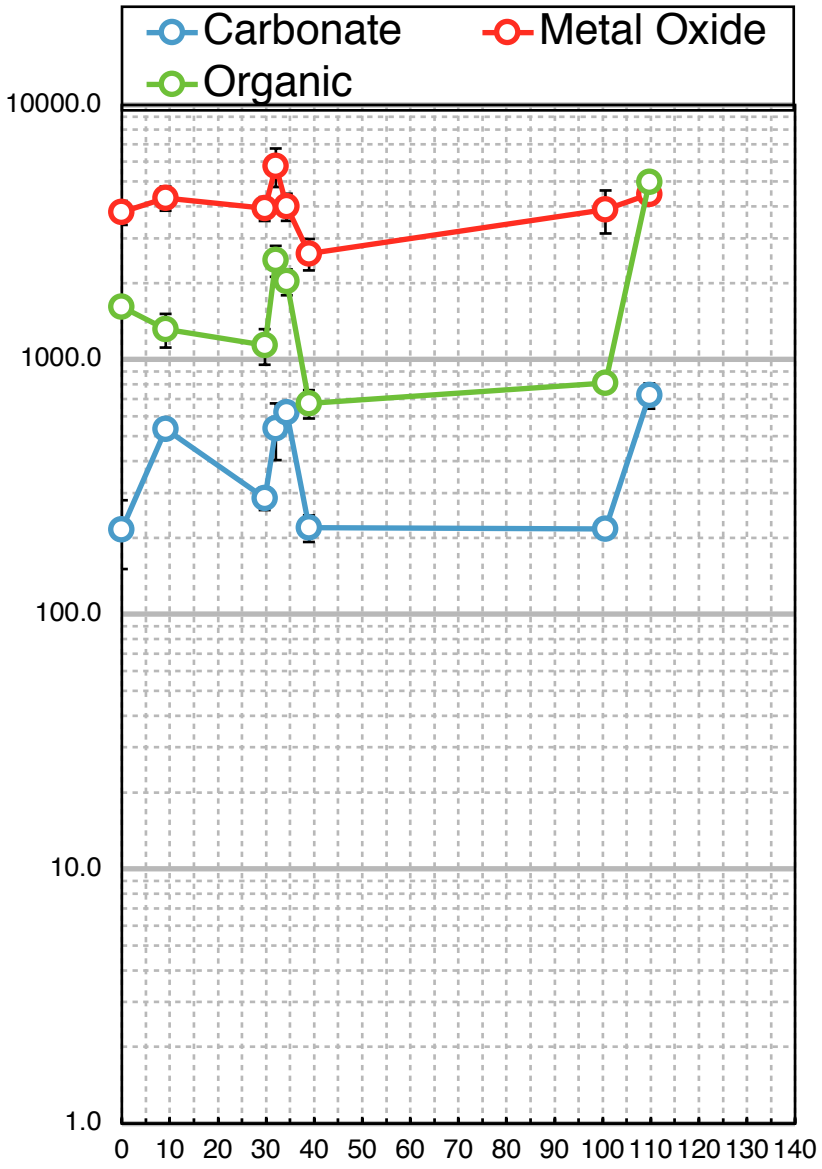


Figure 74. Distribution of the speciated forms of Cu along the transect. The primary regions of migration are ~32 m (Region A) and 110 m (Region C), (n=3) at the 95% confidence level.

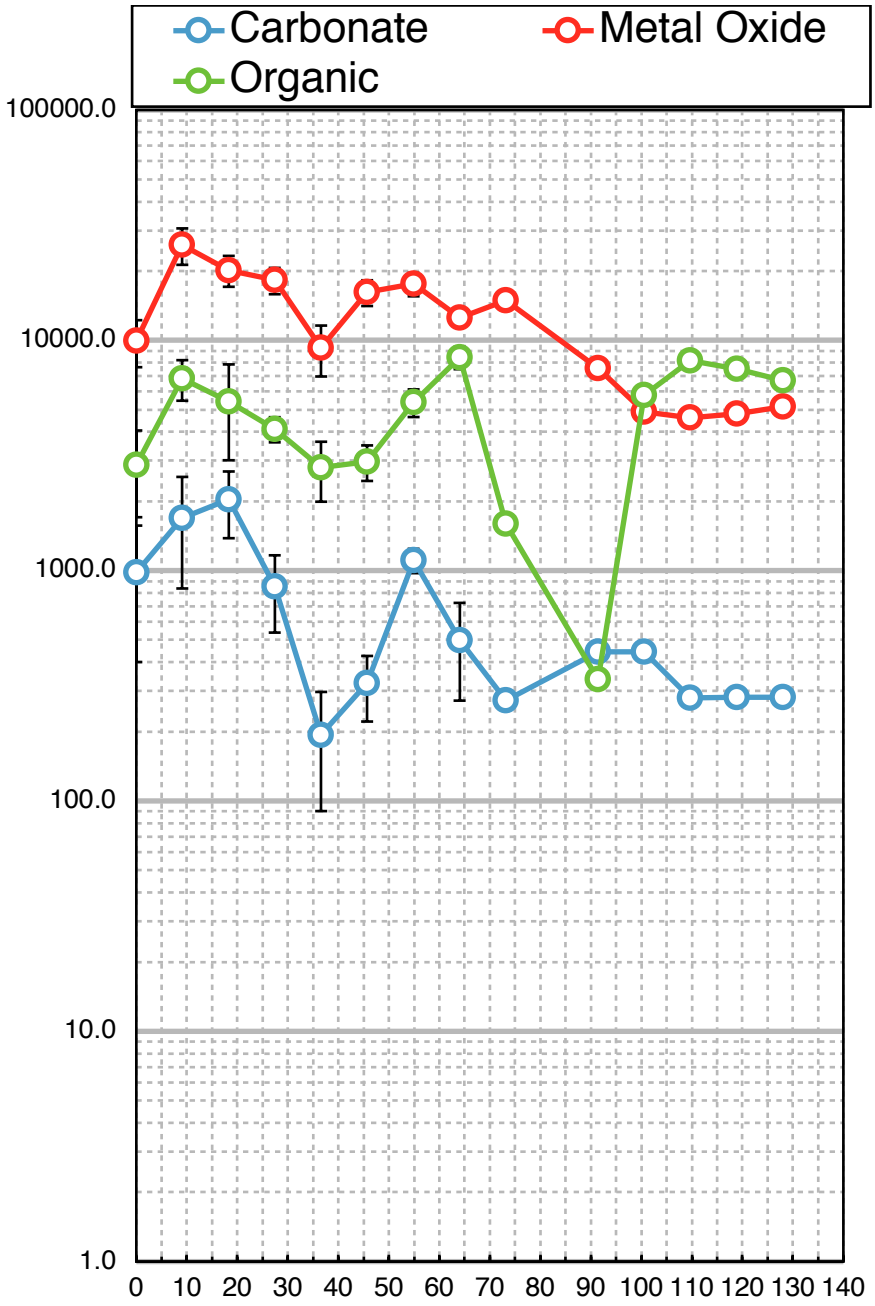


Figure 75. Distribution of the speciated forms of Pb along the transect. The primary regions of migration are 0-18 m (Region A), 37-64 m (Region B) and 101 m (Region C) particularly for the ORG-[Pb], at the bottom of the slope. Raw data is shown in the Appendix in Table A-7, (n=3) at the 95% confidence level.

From prior studies it was found that for the sum of speciated Pb, 33.1% remained on the Ridge (Region A), 38.2% migrated down the Slope (Region B), and 28.7% moved into the Plain (Region C), as shown in Figure 76.[73] Additionally, it was

found that Region A was mainly MOX-[Pb] (26.0%) with low relative amounts of CO3-[Pb] (0.4%) and ORG-[Pb] (6.7%). In Region B, similar results were observed: MOX-[Pb] (28.9%), CO3-[Pb] (0.5%), and ORG-[Pb] (8.8%) as well as in Region C: MOX-[Pb] (24.6%), CO3-[Pb] (0.9%), and the ORG-[Pb] (3.2%) (Figure 77).[73]

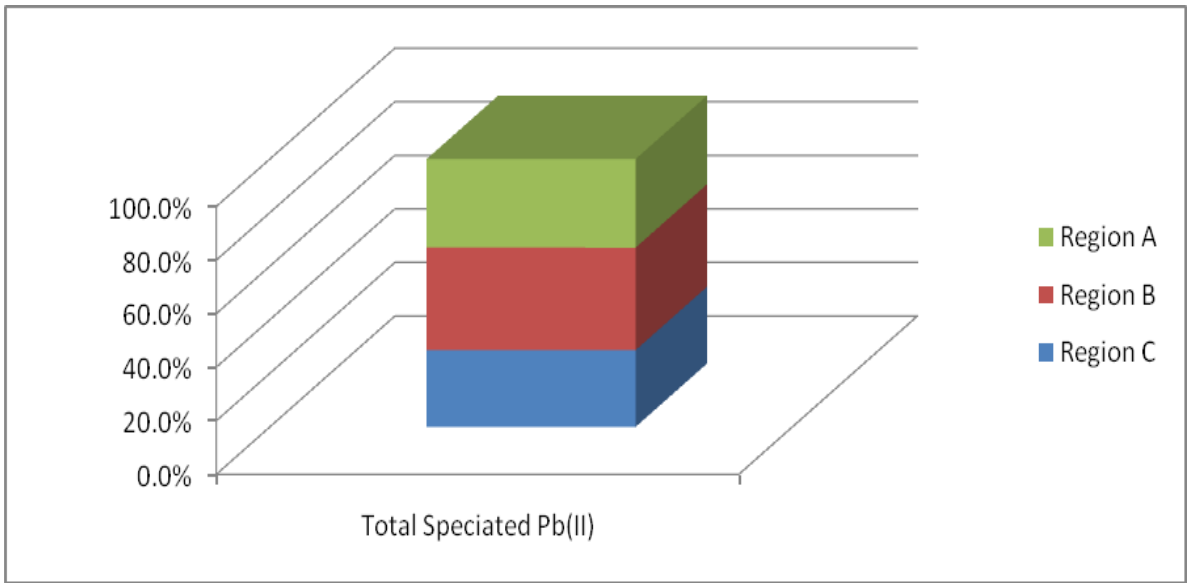


Figure 76. Mass balance for the sum of the speciated Pb along the battle-line transect.[73]

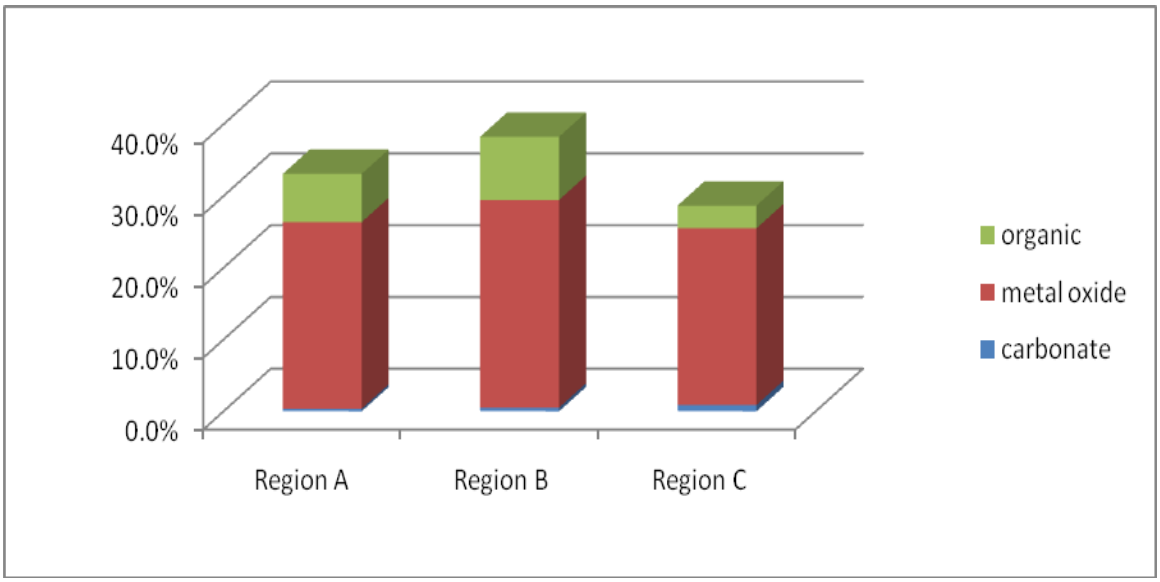


Figure 77. Mass balance for the sum of the speciated Pb along the battle-line transect.[73]

## 3.3 Conclusions

In this study, the development of a MAE GF-AAS method for Cu revealed interesting characteristics in the way Cu is extracted from soil by microwave energy and its speciation, complexation by soil, and transport. The most significant conclusion from this work is that with the use of microwave energy extracts RFC-[Cu], creating a major analytical method bias. Transport from Region A to C was undoubtedly dependent upon the frequency and intensity of atmospheric precipitation as well as the elevation, slope, and orientation of terrain features that affected surface water flow and distribution. From the two primary accumulation points along the transect, Cu was transported ~27% faster than Pb, allowing for a better assessment of the risk imposed by Cu in contaminated soils. This study was also able to pin-point the firing line location, thereby augmenting archaeologic methods. By comparing the relative amount of Cu deposited to Pb, the conditions of the battle and ability to reenact the narrative can be considered, i.e., to imagine the intensity of the battle and step directly inside of the shoes of the soldiers on the battlefield.

Pb and Cu were primarily transformed into MOX- and ORG-bound species, and their abundance and distribution, along with rates of transport, could be defined with high precision. The major differences found were: (a) Pb transport rates are ~27% slower than Cu, (b) Pb deposits were ~78% higher than Cu, (c) total speciated [Pb] is more evenly distributed along the transect while [Cu] is more variable. The exact molecular structures and mechanisms of transport for Cu and Pb in soil are unknown, arising from a variety of factors, including pH, NOM, CEC, and the various minerals

present. Because of the complex nature of soil, the results from this type of study allow for the description of overall general trends.

The abundance and distribution of Hg was examined, and its rate was more similar to Pb than Cu. Hg species moved at a decreased rate compared to Cu and also accumulated preferentially on the Slope. The source of Hg is less clear to assign than for Cu and Pb, i.e., Hg from the detonator in percussion caps or from the release of Hg by coal-burning power plants or other atmospheric sources (e.g., volcanoes). In general, soils with "low background [Hg]" are typically 14 ng $g^{-1}$,[118] while "high background [Hg]" areas range from 69 to 416 ng $g^{-1}$.[119] From the results of the present study, the [Hg] is within the range of both these studies so that one cannot necessarily conclude that the Hg measured was solely from the battle. Further studies of the distribution of Hg isotopes, as done previously for Pb,[73] would be worth pursuing to attempt to answer this question.

# Chapter 4 Conclusions and Future Work

## 4.1 Conclusions

The objective of this study was to develop a robust method for the speciation of Cu, Pb, and Hg at trace levels in soil and to apply it to soil for which the spatial and temporal dimensions could be well-defined. The abundance, distribution, speciation, and transport of these trace metal species could then be studied with confidence, and accurate first-order rate constants could be calculated. By defining accurate and precise rate constants for the transport of heavy metals in soil, the environmental risk to society from contaminated soil could be more reliably assessed.

This study was able to effectively develop and optimize a novel MAE-GF-AAS method for each of the BCR extracts at trace levels, with validation of the method by the use of an SRM. The use of a permanent modifier in combination with a conventional modifier worked well to improve the performance and lifetime of the graphite furnace for measuring Cu and Pb from the sequential extraction of soil samples. Also, in this work an optimized MAE-ICP-MS method for Hg extraction was developed and applied to the soil samples, and the method was also validated for Hg by the use of an SRM.

Significant concentrations of Cu and Pb (> 1 parts per million) were found in the samples that were collected throughout the battle line transect. The Cu and Pb clearly migrated predominantly as the MOX- and ORG-bound species. Hg was predominantly an ORG-complexed species that was found primarily in the shallow layers. Trends in transport and fate were realized for the physico-chemical speciation of Cu, Pb, and Hg through the transect of the battlefield.

The results correlated well with historical descriptions of unit position, therefore providing archaeologically relevant information as well as demonstrating that the novel methodology used in this work provides a sensitive, selective, and low-impact method to study trace metals in soil.

## 4.2 Future Work

In the future, additional field work should be done at Brawner Farm to develop a better model of the vertical migration of Cu, Pb, and Hg by increasing the sampling depth of the cores to reach well beyond the depth of the battlefield layer

throughout the transect. Specifically, new cores should be collected on the ridge (Region A) and plain (Region C), particularly on the ridge where the compactness of the soil made the collection of deeper cores difficult in previous visits to the battlefield. Also, a higher number of sampling sites should be examined across the entire transect to gain an enhanced understanding of the horizontal migration, as well as to replenish archival cores for future studies. With the presence of Hg identified in this study, apparently from residues originating from the deposition of percussion caps, a model for the vertical and horizonal migration of Hg can be developed.

To better understand the physico-chemical speciation of trace metals in the soil, specifically for the fractions in which the metals were bound to organic compounds, other analytical techniques could also be explored. For example, to gain a better understanding of the nature of the particles present (Flow Field-Flow Fractionation), soil geochemistry (Ion Chromatography), and organic structures (Pyrolysis Gas Chromatography-Mass Spectrometry).

As a means to simplify the GF-AAS method developed herein, more work should be done with "permanent" chemical modifiers to the graphite furnace. The 1:1 mixture of Ru and W (500 mg $kg^{-1}$) was simply prepared from AA standards of W and Ru, but it would be interesting to explore the effect upon furnace performance for a modifier prepared from W (using sodium tungstate dihydrate) and Rh (using ammonium hexachlororhodate(III)), which have recently been reported to be superior to AA standards for W and Ru.

To improve the determination of Hg, Atomic Fluorescence Spectroscopy (AFS) could be employed because of several advantages. AFS is considered to be superior to AAS in sensitivity and calibration range for Hg species, including organomercurials for which direct ICP-MS measurements are difficult ("cold" plasmas). Analytical features such as very low detection limits (MDL of pg $g^{-1}$), wide linear calibration ranges (up to mg $L^{-1}$), as well as simplicity, small footprint, and lower acquisition and operating costs make AFS an attractive atomic detector in speciation studies.[123] Another simpler alternative to consider is the Cold Vapor GF-AAS method for Hg implemented by using Sequential Injection Analysis because of its greater sensitivity and selectivity compared to the other techniques, as well as its convenient adaptation to the current GF-AAS system.

To provide insight into the complexation of toxic metals with the various forms of Fe and Mn oxides as well as other minerals present at Brawner Farm, additional work could be performed by using MAE ICP-MS. Future studies could also consider the abundance, distribution, speciation, and mobility of Zn, given its presence in the brass percussion caps (70% Cu, 30% Zn). There is a need to more thoroughly investigate the release of RFC-[Cu] at longer MAE times, increased power and higher temperature. MAE of MOX-[Cu] showed its release from Fe oxides, and in future studies an investigation if this release is a uniquely associated with Cu, or if the same trend is found with Pb, Hg, and/or other metals for each of the BCR steps.

To study other soil types, as well as to identify the exact locations of unit positions on ACW battlefields, new sites with different soil chemistry should be investigated. These sites would be good tests of the methodology used at Brawner

Farm. A prime candidate is the Wilson’s Creek battlefield (near Springfield, MO, USA), which meets the criteria for a "pristine" (non-tilled) sampling area as well as one in which unit positions were relatively static and a high volume of rifle fire occurred. Additionally Wilson's Creek, like Brawner Farm, has also been extensively studied by archaeologists so unit positions could also be confirmed using the methods developed in the present work. Furthermore, the terrain at Wilson's Creek has a longer, gentler slope than Brawner Farm which would be ideal for studying the horizontal migration of metal species without the complication of "pooling" across a broad plain which interrupted the migration at Brawner Farm.

## References


1. Acar, O. “Electrothermal atomic absorption spectrometric determination of cadmium and lead in environmental, botanic and biological samples by different permanent modifiers”, *Journal of Analytical Atomic Spectrometry* **2004,** *19*.
2. United States Environmental Protection Agency. *Lead in Paint, Dust, and Soil.* http://www.epa.gov/lead/index.html (accessed May 22, 2020).
3. United States Environmental Protection Agency. *Copper Facts*. https://archive.epa.gov/pesticides/reregistration/web/pdf/copper (accessed May 22, 2020).
4. United States Environmental Protection Agency. *Mercury*. https://www.epa.gov/mercury (accessed May 22, 2020).
5. Sheetz, C.D., Rimstidt, D.J. “Dissolution, transport, and fate of lead on a shooting range in the Jefferson National Forest near Blacksburg, VA, USA”, *Journal of Environmental Geology* **2009,** *58*, 655-665.
6. Noriagu, J.O., “*The Biogeochemistry of Lead in the Environment”*, Elsevier North-Holland Biomedical Press: Amsterdam, 1978.
7. Emsley, J., “*Nature's Building Blocks : Everything You Need To Know About The Elements”*, Oxford University Press: Oxford, 2011.
8. Ewers, W., Schlipkoter, H.W., Merian, E., “*Metals and Their Compounds in the Environment: Occurrence, Analysis, and Biological Relevance*”, VCH: Weinheim, New York, Basel, Cambridge, 1990; pp 971-1014.
9. Tessier, A., Campbell, P.G.C., Bisson, M. “Sequential Extraction Procedure for the Speciation of Particulate Trace Metals”, *Analyitical Chemistry* **1979,** *51*, 844-851.
10. Suave, S., McBride, M.B., Hendershot, W.H. “Speciation of Lead in Contaminated Soils”, *Journal of Environmental Pollution* **1998,** *98*, 149-155.
11. Wuana, R.A., Okieimen, F.E. “Heavy Metals in Contaminated Soils: A Review of Sources, Chemistry, Risks and Best Available Strategies for Remediation”, **2011**.
12. Dijkstra, J.J., Meeussen, J.C.L., Comans, R.N. “Leaching of Heavy Metals from Contaminated Soils: An Experimental and Modeling Study”, *Environmental Science & Technology* **2004,** *38*, 4390-4395.
13. Bacon, J.R., Hewitt, I.R., Cooper, P. “Origin of Lead Associated With Different Reactive Phases in Scottish Upland Soils: An Assessment Made Using Sequential Extraction and Isotope Analysis”, *Journal of Environmental Monitoring* **2004,** *6*, 766-773.
14. Kobler, J., Fitz, W.J., Dirnbock, T., Mirtl, M. “Soil Type Affects Migration Pattern of Airborne Pb and Cd Under a Spruce-Beech Forest of the UN-ECE Integrated Monitoring Site Zöbelboden, Austria”, *Journal of Environmental Pollution* **2010,** *158*, 849-854.
15. McPherson, J.M., “*Battle Cry of Freedom: The Civil War Era”*, Oxford University Press: 2003.
16. Davis, W.C., Wiley, B.I., “*Civil War Album: Complete Photographic History of the Civil War, Fort Sumter to Appomattox”*, Tess Press: New York, 2000.
17. Gaff, A.D., “*Brave Men's Tears: The Iron Brigade at Brawner Farm”*, 2nd ed.; Morningside Press: Dayton, 1988.
18. Nolan, A.T., “*The Iron Brigade, A Military History”*, Indiana University Press: Bloomington, IN, 1961.
19. Stackpole, E.J., “*From Cedar Mountain to Antietam”*, Stackpole Co.: Harrisburg, PA, 1959.
20. Potter, S.R., Sonderman, R.C., Creveling, M.C., Dean, S.L., “*No Maneuvering and Very Little Tactics: Archaeology and the Battle of Brawner Farm”*, Gainesville, FL, 2000.

21. Fadala, S., "*The Complete Blackpowder Handbook"*, 5th ed.; DBI Books: 1996; Vol. 41.
22. Lorraine, D., Dill, D.B., "*Structure, Stratigraphic Controls, and Genisis of Balmat Zinc Deposits"*, Geological Association of Canada: Northwest Adirondacks, NY, 1982; Vol. 25, p 571-596.
23. Whisonant, R.C., "*Geology and the Civil War in Southwestern Virginia: The Wythe County Lead Mines"*, Division of Mineral Resources: Richmond, 1996; Vol. 42, p 13-20.
24. Winant, L., "*Early Percussion Firearms; a History of Early Percussion Firearms Ignition, from Forsyth to Winchester"*, N.Y. Morrow: 1959.
25. Kurzer, F. "The Life and Work of Edward Charles Howard FRS", *Annals of Science* **1999,** *56*, 113-141.
26. Edward H. "On a New Fulminating Mercury. By Edward Howard, Esq. F. R. S", *Philosophical Transactions of the Royal Society of London* **1800,** *90*, 204-238.
27. Masta, C., Luis, R.L., Manuel, B., Felipe, M. "Assessment of Mercury-Polluted Soils Adjacent to an Old Mercury-Fulminate Production Plant", *Journal of Applied and Environmental Soil Science* **2009,** *- 2009*.
28. Emsley, J., "*The Elements"*, 3rd ed.; Oxford: Clarendon Press: 1998.
29. Cao, X., Lena, Q.M., Chen, M., Hardison, D.W., Harris, W.G. "Weathering of Lead Bullets and Their Environmental Effects at Outdoor Shooting Ranges", *Journal of Environmental Quality* **2003,** *32*, 526-534.
30. Lena, Q.M., Hardison. D.W., Harris, W.G., Cao, A., Zhou, Q. "Effects of Soil Property and Soil Amendment on Weathering of Abraded Metallic Pb in Shooting Ranges", *Water, Air, & Soil Pollution* **2006,** *178*, 297-307.
31. Strawn, D.G., Sparks, D.L. "Effects of Soil Organic Matter on the Kinetics and Mechanisms of Pb(II) Sorption and Desorption in Soil", *Soil Science Society of America Journal* **2000,** *64*, 144-156.
32. Gerberding J.L. U.S. Department of Health and Human Services, Agency for Toxic Substance and Disease Registry. *Toxicological Profile For Copper*. https://www.atsdr.cdc.gov/ToxProfiles/tp132.pdf.
33. Code of Federal Regulations. *Drinking Water Requirements for States and Public Water Systems, CFR-141.88*. https://www.epa.gov/dwreginfo/lead-and-copper-rule (accessed May 22, 2020).
34. Rice, K.M., Walker, M.E., Wu, M., Gillette, C., Blough, E.R. "Environmental mercury and its toxic effects", *Journal of Preventive Medicine and Public Health* **2014,** *47*, 74-83.
35. Borum, D., Manibusan, K.M., Schoeny, R., Winchester, E.L. U.S. Environmental Protection Agency, Office of Water. *Water Quality Criterion for the Protection of Human Health: Methylmercury*. https://www.epa.gov/sites/production/files/2020-01/documents/methylmercury-criterion-2001.pdf.
36. Koplan J.P. U.S. Department of Health and Human Services, Agency for Toxic Substance and Disease Registry. *Toxicological Profile For Mercury*. https://www.atsdr.cdc.gov/ToxProfiles/tp46.pdf.
37. Éder C. Lima, E.C., Ronílson V. Barbosa, R.V., Jorge L. Brasila, J.L., Ana H. D. P. Santos, A.D.P. "Evaluation of different permanent modifiers for the determination of arsenic, cadmium and lead in environmental samples by electrothermal atomic absorption spectrometry", *Journal of Analytical Atomic Spectrometry* **2002,** *17*, 1523-1529.
38. U.S. Department of Health and Human Services, Agency for Toxic Substance and Disease Registry. *Toxicological Profile For Lead*. https://www.atsdr.cdc.gov/toxprofiles/tp13.pdf.
39. Davidson, C.M., Duncan, A.L., Littlejohn, D., Ure, A.M., Garden, L.M. "A critical evaluation of the three-stage BCR sequential extraction procedure to assess the potential

mobility and toxicity of heavy metals in industrially-contaminated land", *Analytica Chimica Acta* **1998,** *363*, 45-55.
40. Sutherland, R.A., Tack, F.M. "Sequential Extraction of Lead from Grain Size Fractionated River Sediments Using the Optimized BCR Procedure", *Water, Air, & Soil Pollution* **2007,** *184*, 269-284.
41. Conklin, A.R., "*Introduction to Soil Chemistry Analysis and Instrumentation"*, John Wiley & Sons, Inc.: New Jersey, 2005; Vol. 167, p 218.
42. Gleyzes, C., Tellier, S., Astruc, S. "Fractionation studies of trace elements in contaminated soils and sediments: a review of sequential extraction procedures", *Trends in Analytical Chemistry* **2002,** *21*, 451-467.
43. Rauret, G., Sanchez, L.J.F., Sahuquillo, A., Rubio, R., Davidson, C., Ure, A., Quevauviller, P. "Improvement of the BCR three step sequential extraction procedure prior to the certification of new sediment and soil reference materials", *Journal of Environmental Monitoring* **1999,** *1*, 57-61.
44. Quevauviller, P., "*Methodologies in Soil and Sediment Fractionation Studies: Single and Sequential Extraction Procedures"*, Royal Society of Chemistry: Cambridge, UK, 2002.
45. Yusuf, K.A. "Evaluation of the Three-Stage BCR (European Community Bureau of Reference) Sequential Extraction Procedure to Assess the Potential Mobility and Toxicity of Heavy Metals in Roadside Soils", *Pakistan Journal of Scientific and Industrial Research* **2006,** *49 (3)*, 181-183.
46. Giacomelli, M.B.O., Lima, M.C., Dias, L.F., Welzb, B., Curtius, A.J. "Fractionation of Cd and Pb in BCR No. 601 sediment reference material following the BCR protocol for sequential extraction and determination by electrothermal atomic absorption spectrometry using permanent modifiers", *Journal of Analytical Atomic Spectrometry* **2002,** *17*, 1339-1343.
47. Adel, A.S., Steven, M.J., Koirtyohann, S.R. "Wet Ashing of Some Biological Samples in a Microwave oven", *Analytical Chemistry* **1975,** *47*, 1475-1477.
48. "*CEM Corporation MARS 5 Microwave Accelerated Reaction System Operation Manual"*, Rev. 0 ed.; CEM Corporation: Matthews, North Carolina, 1999.
49. Cornthwaite, H.M., Watterson, J.H. "Microwave Assisted Extraction of Ketamine and its Metabolites From Skeletal Tissues", *Analytical Methods* **2014,** *6*, 1142-1148.
50. Kitchen, J.H., Vallance, S.R., Kennedy, J.L., Tapia-Ruiz, N.T., Carassiti, L., Harrison, A., Whittaker, A.G., Drysdale, T.D., Kingman, S.W., Gregory, D.H. "Modern Microwave Methods in Solid-State Inorganic Materials Chemistry: From Fundamentals to Manufacturing", *Chemical Reviews* **2014,** *114*, 1170-1206.
51. Letellier, M., Budzinski, H. "Influence of Sediment Grain Size on the Efficiency of Focused Microwave Extraction of Polycyclic Aromatic Hydrocarbons", *Analyst Journal* **1999,** *124*, 5-14.
52. Gulmini, M., Ostacoli, G., Zelano, V., Torazzo, A. "Comparison between microwave and conventional heating procedures in Tessier's extractions of calcium, copper, iron and manganese in a Lagoon sediment", *Analyst Journal* **1994,** *119*, 2075-2080.
53. Cid, P.B.P., Lavilla, I., Bendicho, C. "Application of microwave extraction for partitioning of heavy metals in sewage sludge", *Analytica Chimica Acta* **1999,** *378*, 201-210.
54. Bahattin, G., Gulsen, O. "Chemical speciation of heavy metals in the Tigris River sediment", *Chemical Speciation & Bioavailability* **2001,** *13*, 25-29.
55. Mili, D., Chandrasekhar, K., Suparna, D., Arabinda K., D. "Microwave-assisted speciation studies in fly ash by AAS and ICP-MS: comparison between Tessier and BCR sequential extraction schemes", *Journal of Atomic Spectroscopy* **2005,** *26*, 137.

56. Jackson, K.W., "*Electrothermal Atomization for Analytical Atomic Spectrometry"*, John Wiley & Sons, Ltd.: West Sussex, 1999; p 470.
57. L'vov, B.V., "*Atomic Absorption Spectroscopy"*, The U.S. Atomic Energy Commission and The National Science Foundation: Washington, D.C., 1969; p 251.
58. L'vov, B.V. "A Personal View of the Evolution of Graphite Furnace Atomic", *Analyitical Chemistry* **1991,** *63*, 924-931.
59. Koirtyohann, S.R., Kaiser, M.L. "Furnace Atomic Absorption-A Method Approaching Maturity", *Analytical Chemistry* **1982,** *54*, 1515-1524.
60. Chakrabarti, C.L., Wan, C.C., Hamed, H.A., Bertels, P.C. "Matrix Interferences in Graphite Furnace Atomic Absorption Spectrometry bu capacitive Discharge Heating", *Analyitical Chemistry* **1981,** *53*, 444-450.
61. Slavin, W., Manning, D.C. "Atomic Absorption Spectroscopy the Present and the Future", *Analytical Chemistry* **1982,** *54*, 685-694.
62. Slavin, W., Manning, D.C. "Reduction of Matrix Interferences for Lead Determination withthe L'vov Platform and the Graphite Furnace", *Analyitical Chemistry* **1979,** *51*, 261-265.
63. Sturgeon, R.E., Chakrabarti, C.L. "Evaluation of pyrolytic-graphite-coated tubes for graphite furnace atomic absorption spectrometry", *Analytical Chemistry* **1977,** *49*, 90-97.
64. Robinson, J.W., "*Atomic Spectroscopy"*, 2nd ed.; Marcel Dekker. Inc.: New York, 1996; p 391.
65. Butcher, D.J., Sneddon, J., "*A Practical Guide to Graphite Furnace Atomic Absorption Spectrometry"*, John Wiley & Sons, Inc.: New York, 1998; Vol. 149, p 250.
66. Jackson, K. "Electrothermal Atomic Absorption Spectrometry and Related Techniques", *Analytical Chemistry* **2000,** *72*.
67. Thermo Electron Spectroscopy Ltd. *Design Considerations for High Performance Background Correction Systems*; Thermo Electron Corporation: Cambridge, 2003.
68. Beach, L.M. *Varian SpectrAA Zeeman graphite furnace methods for environmental samples*; 1989.
69. Beauchemin, D. "Inductively Coupled Plasma Mass Spectrometry", *Analytical Chemistry* **2010,** *82*, 4786-4810.
70. Kennedy, J.F., Xu, L. "Practical Guide to ICP-MS by Robert Thomas", *Journal of Carbohydrate Polymers* **2005,** *62*, 392-393.
71. Skoog, D.A., Holler, J.F., Crouch, S.R., 4th ed.; Saunders College Publishing: Orlando, FL, 1992.
72. Houk, R.S. "Mass Spectrometry of Inductively Coupled Plasmas", *Analytical Chemistry* **1986,** *58*, 97A-105A.
73. Schlipp, S. "Determination of Trace Level of Pb(II) in Battlefield Soil Extracts By Sequential Extraction and Electrothermal Atomic Absorption Spectroscopy", University of Wisconsin-Milwaukee, 2011.
74. Ottman, D.M. "210Pb and 137Cs Radiochemistry and Dating for Soil Cores from Brawner Farm Battlefield Manassas, Virginia", University of Wisconsin-Milwaukee, 2009.
75. Vazquez, M.J., Carro, A.M., Lorenzo, R.A., Cela, R. "Optimization of Methylmercury Microwave-Assisted Extraction from Aquatic Sediments", *Analytical Chemistry* **1997,** *69*, 221-225.
76. Bass, D.A., Holcombe, J.A. "Mechanisms of Lead Vaporization from an Oxygenated Graphite Surface Using Mass Spectrometry and Atomic Absorption", *Analytical Chemistry* **1988,** *60*, 578-582.
77. Frech, W., Li, K., Berglund, M., Baxter, D.C. "Effects of Modifier Mass and Temperature Gradients on Analyte Sensitivity in Electrothermal Atomic Absorption Spectrometry", *Journal of Analytical Atomic Spectrometry* **1992,** *7*, 141-145.

78. Gilchrist, G.F.R., Chakrabarti, C.L., Byrne, J.P., Lamoureux, M. “Gas-phase thermodynamic model and chemical modification in graphite furnace atomic absorption spectrometry”, *Journal of Analytical Atomic Spectrometry* **1990,** *5*, 175-181.
79. Cedergren, A., Frech, W., Lundberg, E. “Estimation of oxygen pressure in graphite furnaces for atomic absorption spectrometry”, *Analyitical Chemistry* **1984,** *56*, 1382-1387.
80. Vogt, G.M., Hahn, L., Muller, H., Wendl, W., Roux, D.J. “Role of oxygen in the determination of oxide forming elements by electrothermal atomic absorption spectrometry”, *Journal of Analytical Atomic Spectrometry* **1995,** *10*, 777-783.
81. Sturgeon, R.E., Mitchell, D.F., Berman, S.S. “Atomization of Lead in Graphite Furnace Atomic Absorption Spectrometry”, *Analyitical Chemistry* **1983,** *55*, 1059-1064.
82. Voth, L.M. *Dealing with Matrix Interferences in the Determination of the Priority Pollutant Metals by Furnace AA*; Varian Resource Centre: Park Ridge, IL, 1983; pp 1-6.
83. Krasowski, J.A., Copeland, T.R. “Matrix interference in furnace atomic absorption spectrometry”, *Analyitical Chemistry* **1979,** *51*, 1843-1849.
84. Erspamer, J.P., Niemczyk, T.M. “Vaporization of some chloride matrices in graphite furnace atomic absorption spectrometry”, *Analyitical Chemistry* **1982,** *54*, 538-540.
85. Silva, J.B.B., Silva, M.A.M., Curtius, A.J., Welz, B. “Determination of Ag, Pb and Sn in *aqua regia* extracts from sediments by electrothermal atomic absorption spectrometry using Ru as a permanent modifier”, *Journal of Analytical Atomic Spectrometry* **1999,** *14*, 1737-1742.
86. Yasuda, K., Hirano, Y., Kamino, T., Kichinosuke, D. “Relationship between the formation of intermetallic compounds by matrix modifiers and atomization in graphite furnace-atomic absorption spectrometry, and an observation of the vaporization of intermetallic compounds by means of electron microscopy”, *Journal of Analytical Sciences* **1994,** *10*, 623-631.
87. Ortner, H.M., Bulska, E., Rohr, U., Schlemmer, G., Weinbruch, S., Welze, B. “Modifiers and coatings in graphite furnace atomic absorption spectrometry—mechanisms of action (A tutorial review)”, *Spectrochimica Acta Part B: Atomic Spectroscopy* **2002,** *57*, 1835-1853.
88. CEM Corporation, MARS 5 Operation Manual. In *Method Parameters*, CEM Corporation: United States Of America, 1999.
89. Reid, M.K., Spencer, K.L., Shotbolt, L. “An appraisal of microwave-assisted Tessier and BCR sequential extraction methods for the analysis of metals in sediments and soils”, *Journal of Soils and Sediments* **2011,** *11*, 518-528.
90. Ipolyi, I., Brunori, C., Cremisini, C., Fodor, P., Macaluso, L., Morabito, R. “Evaluation of performance of time-saving extraction devices in the BCR three-step sequential extraction procedure”, *Journal of Environmental Monitoring* **2002,** *4*, 541-548.
91. Jamali, K.J., Kazi, G.T., Arain, B.A., Hassan, I.A., Nusrat, J., Ghulam, A.K., Abdul, Q.S., Jameel, A.B. “Speciation of heavy metals in untreated sewage sludge by using microwave assisted sequential extraction procedure”, *Journal of Hazardous Materials* **2009,** *163*, 1157-1164.
92. Tipping, E., Hetherington, N.B., Hilton, J., Thompson, D.W., Bowles, E., Hamilton, J.T. “Artifacts in the use of selective chemical extraction to determine distributions of metals between oxides of manganese and iron”, *Analytical Chemistry* **1985,** *57*, 1944-1946.
93. Arrigo, T., Laurel, K., Byrne, J.M., Kappler, A., Kretzschmar, R. “Impact of Organic Matter on Iron(II)-Catalyzed Mineral Transformations in Ferrihydrite–Organic Matter Coprecipitates”, *Environmental Science & Technology* **2018,** *52*, 12316-12326.
94. Nevado, J.J.B., Doimeadios, R.C.R., Bernardo, F.J.G., Moreno, M.J. “Determination of monomethylmercury in low- and high-polluted sediments by microwave extraction and gas chromatography with atomic fluorescence detection”, *Analytica Chimica Acta* **2008,** *608*, 30-37.

95. Rahmana, G.M., Kingston, H.M. “Development of a microwave-assisted extraction method and isotopic validation of mercury species in soils and sediments”, *Journal of Analytical Atomic Spectrometry* **2005,** *20*, 183-191.
96. García, M.L.M., Carlosena, A., Mahía, P.L., Muniategui, S., Prada, D. “Determination of mercury in estuarine sediments by flow injection-cold vapour atomic absorption spectrometry after microwave extraction”, *Analusis* **1999,** *27*, 61-64.
97. Niessen, S., Mikac, N., Fischer, J.C. “Microwave-assisted determination of total mercury and methylmercury in sediment and porewater”, *Analusis* **1999,** *27*, 871-875.
98. Park, M., Yoon, H., Yoon, C., Yu, J.Y. “Estimation of Mercury Speciation in Soil Standard Reference Materials With Different Extraction Methods by Ion Chromatography Coupled With ICP-MS”, *Journal of Environmental Geochemistry and Health* **2011,** *33*, 49-56.
99. Liping, W., Temminghoff, E.J.M., Lofts, S., Tipping, E., Willem, H.V.R. “Complexation with Dissolved Organic Matter and Solubility Control of Heavy Metals in a Sandy Soil”, *Environmental Science & Technology* **2002,** *36*, 4804-4810.
100. Wei, G., Shenghong, G., Xiuji, W., Jiangyi, Z., Lanlan, J., Zhenli, Z., Hongfei, Z. “Application of ion molecule reaction to eliminate WO interference on mercury determination in soil and sediment samples by ICP-MS”, *Journal of Analytical Atomic Spectrometry* **2011,** *26*, 1198-1203.
101. Montaser, A., “*Inductively Coupled Plasma Mass Spectrometry”*, Wiley: 1998.
102. Planchon, F.A.M., Gabrielli, P., Gauchard, P.A., Dommergue, A., Barbante, C., Cairns, W.R.L., Cozzi, G., Nagorski, S.A., Ferrari, C.P., Boutron, C.F., Capodaglio, G., Cescon, P., Varga, A., Wolff, E.W. “Direct determination of mercury at the sub-picogram per gram level in polar snow and ice by ICP-SFMS”, *Journal of Analytical Atomic Spectrometry* **2004,** *19*, 823-830.
103. Long, S.E., Kelly, R.W. “Determination of Mercury in Coal by Isotope Dilution Cold-Vapor Generation Inductively Coupled Plasma Mass Spectrometry”, *Analytical Chemistry* **2002,** *74*, 1477-1483.
104. Shimadzu, *Shimadzu ICP Mass Spectrometer ICPMS-2030 (Instruction Manual)*. Japan, 2017.
105. Chen, J.K., Hsu, I.H., Sun, Y.C. “Determination of methylmercury and inorganic mercury by coupling short-column ion chromatographic separation, on-line photocatalyst-assisted vapor generation, and inductively coupled plasma mass spectrometry”, *Journal of Chromatography A* **2009,** *1216*, 8933-8938.
106. Nelson J.W.L., “*U.S. Army War College Guide to the Battle of Gettysburg”*, South Mountain Press: Carslisle, PA, 1987; Vol. Appendix I.
107. McBride, M.B., “*Environmental Chemistry of Soils”*, Oxford University Press 1994.
108. He, L., Zhong, H., Liu, G., Dai, Z., Brookes, P.C., Xu, J. “Remediation of heavy metal contaminated soils by biochar: Mechanisms, potential risks and applications in China”, *Journal of Environmental Pollution* **2019,** *252*, 846-855.
109. Flowers, T.C., Hunt, J.R. “Viscous and gravitational contributions to mixing during vertical brine transport in water-saturated porous media”, *Water resources research* **2007,** *43*, W01407.1-W01407.18.
110. Sposito, G., “*The Chemistry of Soils Second edition”*, Oxford University Press, New York: 2008.
111. Manchanda, J.S., Nayyar, V.K., Chhibba, I.M. “Speciation of exchangeable and crystalline Fe oxide bound Zn, Cu, Fe and Mn ions from calcareous soils during sequential fractionation”, *Chemical Speciation & Bioavailability* **2006,** *18*, 27-37.

112. Weng, L., Temminghoff, E.J.M., Lofts, S., Tipping, E., Riemsdijk, W.H.V. “Complexation with Dissolved Organic Matter and Solubility Control of Heavy Metals in a Sandy Soil”, *Environmental Science & Technology* **2002,** *36*, 4804-4810.
113. Fulda, B.F., Voegelin, A.V., Maurer, F., Christl, I., Kretzschmar, R. “Copper Redox Transformation and Complexation by Reduced and Oxidized Soil Humic Acid. 1. X-ray Absorption Spectroscopy Study”, *Environmental Science & Technology* **2013,** *47*, 10903-10911.
114. Zhou, L.X., Wong, J.W.C. “Effect of Dissolved Organic Matter from Sludge and Sludge Compost on Soil Copper Sorption”, *Journal of Environmental Quality* **2001,** *30*, 878-883.
115. Yuan, S., Xi, Z., Jiang, Y., Wan, J., Wu, C., Zheng, Z., Lu, X. “Desorption of copper and cadmium from soils enhanced by organic acids”, *Chemosphere* **2007,** *68*, 1289-1297.
116. Jorgensen, S.S., Willems, M. “The fate of lead in soils: The transformation of lead pellets in shooting range soils.”, *Ambio* **1987,** *16*, 11-15.
117. Mehlhorn, J., Besold, J., Pacheco, J.S.L., Gustafsson, J.P., Kretzschmar, R., Friedrich, B.P. “Copper Mobilization and Immobilization along an Organic Matter and Redox Gradient—Insights from a Mofette Site”, *Environmental Science & Technology* **2018,** *52*, 13698-13707.
118. Xin, M., Gustin, M., Johnson, D. “Laboratory Investigation of the Potential for Re-emission of Atmospherically Derived Hg from Soils”, *Environmental Science & Technology* **2007,** *41*, 4946-4951.
119. Blackwell, B.D., Driscoll, C.T. “Deposition of Mercury in Forests along a Montane Elevation Gradient”, *Environmental Science & Technology* **2015,** *49*, 5363-5370.
120. Harris, D., “*Quantitative Chemical Analysis”*, 5th ed.; W.H. Freeman and Company: New York, 1999.

## APPENDIX A-1: Raw Data

**Table A-1.** Data for the CO3-[Cu] MAE BCR extractions.

| Depth/in (Core#) | Age (yr) | Cu (ng $g^{-1}$) | RSD | | Depth/in (Core#) | Age (yr) | Cu (ng $g^{-1}$) | RSD |
|---|---|---|---|---|---|---|---|---|
| 30A 0.5 | 13.8 | 335.8 | 6.5 | | 9B 0.5 | 11.0 | 145.3 | 31.4 |
| 30A 1.5 | 41.4 | 343.2 | 9.8 | | 9B 1.5 | 32.9 | 474.5 | 9.6 |
| 30A 2.5 | 69.0 | 291.9 | 15.0 | | 9B 2.5 | 54.9 | 474.5 | 11.6 |
| 30A 3.5 | 96.5 | 284.6 | 11.8 | | 9B 3.5 | 76.8 | 437.9 | 10.4 |
| 30A 4.5 | 124.1 | 240.7 | 32.0 | | 9B 4.5 | 98.8 | 167.3 | 15.1 |
| 30A 5.5 | 151.7 | 218.7 | 5.8 | | 9B 5.5 | 120.7 | 101.4 | 76.0 |
| | | | | | 9B 6.5 | 142.6 | 72.2 | 30.4 |
| 4A 0.5 | 13.8 | 944.9 | 6.3 | | 9B 7.5 | 164.6 | 72.2 | 80.4 |
| 4A 1.5 | 41.4 | 1016.7 | 4.0 | | 9B 8.5 | 186.5 | 50.2 | 43.7 |
| 4A 2.5 | 69.0 | 481.3 | 14.1 | | 9B 9.5 | 208.5 | 160.0 | 47.5 |
| 4A 3.5 | 96.5 | 363.8 | 5.4 | | | | | |
| 4A 4.5 | 124.1 | 292.0 | 7.7 | | 13B 0.5 | 17.4 | 291.9 | 0.0 |
| 4A 5.5 | 151.7 | 272.4 | 4.2 | | 13B 1.5 | 52.2 | 233.4 | 19.6 |
| 4A 6.5 | 179.3 | 396.4 | 7.5 | | 13B 2.5 | 86.9 | 248.0 | 8.9 |
| | | | | | 13B 3.5 | 121.7 | 182.1 | 12.1 |
| 31A 0.5 | 13.8 | 751.2 | 6.7 | | 13B 4.5 | 156.5 | 174.8 | 7.3 |
| 31A 1.5 | 41.4 | 653.8 | 9.4 | | 13B 5.5 | 191.2 | 182.1 | 12.1 |
| 31A 2.5 | 69.0 | 580.7 | 2.4 | | 13B 6.5 | 226.0 | 138.2 | 15.9 |
| 31A 3.5 | 96.5 | 572.6 | 4.3 | | 13B 7.5 | 260.8 | 138.2 | 27.5 |
| 31A 4.5 | 124.1 | 507.7 | 2.8 | | 13B 8.5 | 295.6 | 108.9 | 23.3 |
| 31A 5.5 | 151.7 | 735.0 | 6.9 | | | | | |
| 31A 6.5 | 179.3 | 653.8 | 8.6 | | 28E 0.5 | 6.3 | 729.4 | 9.7 |
| 31A 7.5 | 206.9 | 605.1 | 8.4 | | 28E 1.5 | 19.0 | 853.5 | 4.8 |
| 31A 8.5 | 234.5 | 532.0 | 9.5 | | 28E 2.5 | 31.6 | 905.7 | 3.7 |
| | | | | | 28E 3.5 | 44.3 | 820.8 | 13.8 |
| 32B 0.5 | 8.4 | 199.2 | 17.3 | | 28E 4.5 | 56.9 | 814.3 | 5.6 |
| 32B 1.5 | 25.3 | 191.1 | 7.4 | | 28E 5.5 | 69.6 | 781.6 | 6.3 |
| 32B 2.5 | 42.1 | 193.1 | 12.1 | | 28E 6.5 | 82.2 | 1258.3 | 2.7 |
| 32B 3.5 | 58.9 | 191.1 | 7.4 | | 28E 7.5 | 94.9 | 905.7 | 2.2 |
| 32B 4.5 | 75.8 | 312.8 | 22.5 | | | | | |

| | | | | | | | | |
|---|---|---|---|---|---|---|---|---|
| 32B 5.5 | 92.6 | 191.1 | 7.4 | | 7B 0.5 | 11.0 | 588.9 | 4.1 |
| 32B 6.5 | 109.5 | 199.2 | 32.3 | | 7B 1.5 | 32.9 | 597.0 | 6.2 |
| 32B 7.5 | 126.3 | 312.8 | 22.5 | | 7B 2.5 | 54.9 | 540.1 | 9.0 |
| 32B 8.5 | 143.1 | 191.1 | 7.4 | | 7B 3.5 | 76.8 | 532.0 | 7.0 |
| | | | | | 7B 4.5 | 98.8 | 483.3 | 17.7 |
| | | | | | 7B 5.5 | 120.7 | 459.0 | 3.1 |
| | | | | | | | | |
| 22A 0.5 | 13.6 | 645.7 | 7.9 | | 21A 0.5 | 13.6 | 203.8 | 15.2 |
| 22A 1.5 | 40.8 | 1011.0 | 5.0 | | 21A 1.5 | 40.8 | 196.5 | 6.4 |
| 22A 2.5 | 68.0 | 1011.0 | 6.1 | | 21A 2.5 | 68.0 | 198.4 | 10.6 |
| 22A 3.5 | 95.2 | 970.4 | 5.2 | | 21A 3.5 | 95.2 | 196.5 | 6.4 |
| 22A 4.5 | 122.4 | 670.0 | 4.2 | | 21A 4.5 | 122.4 | 306.2 | 20.7 |
| 22A 5.5 | 149.6 | 597.0 | 14.3 | | 21A 5.5 | 149.6 | 196.5 | 6.4 |
| 22A 6.5 | 176.8 | 564.5 | 4.3 | | 21A 6.5 | 176.8 | 203.8 | 28.5 |
| 22A 7.5 | 204.0 | 540.1 | 16.3 | | 21A 7.5 | 204.0 | 306.2 | 20.7 |
| 22A 8.5 | 231.2 | 507.7 | 2.8 | | 21A 8.5 | 231.2 | 196.5 | 6.4 |
| | | | | | 21A 9.5 | 258.4 | 196.5 | 6.4 |
| | | | | | 21A 10.5 | 285.6 | 143.6 | 11.0 |

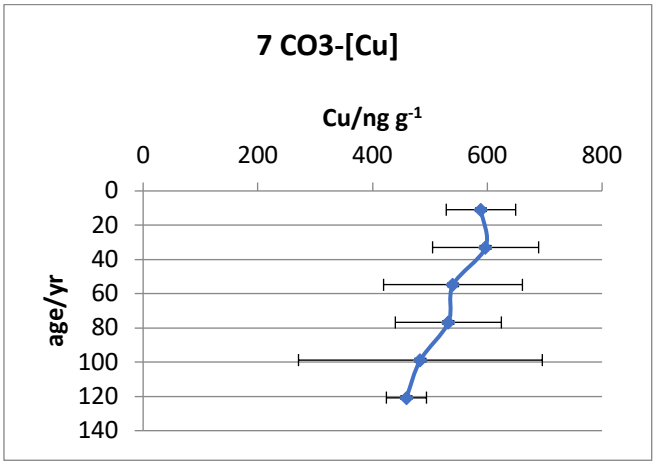


Figure A-1 (a). Soil core profile 7 for CO3-[Cu]; (n=3) at the 95% confidence level.

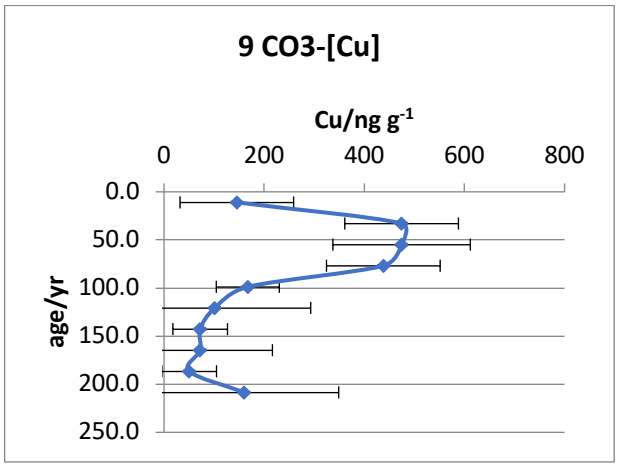


Figure A-1 (b). Soil core profile 9 for CO3-[Cu]; at the (n=3) at the 95% confidence level.

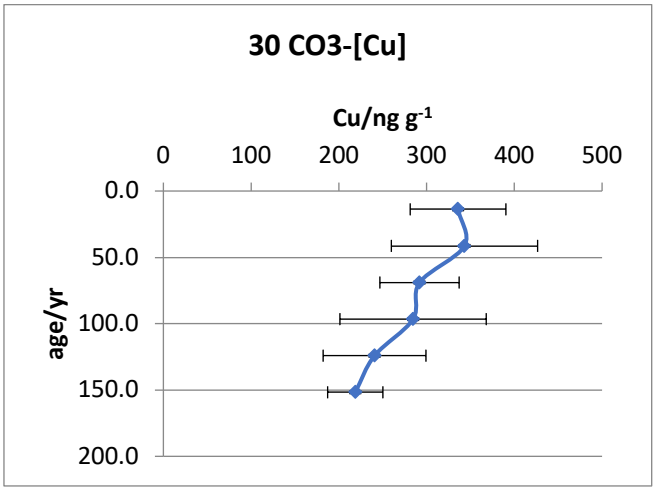


Figure A-1 (c). Soil core profile 30 for CO3-[Cu]; (n=3) at the 95% confidence level.

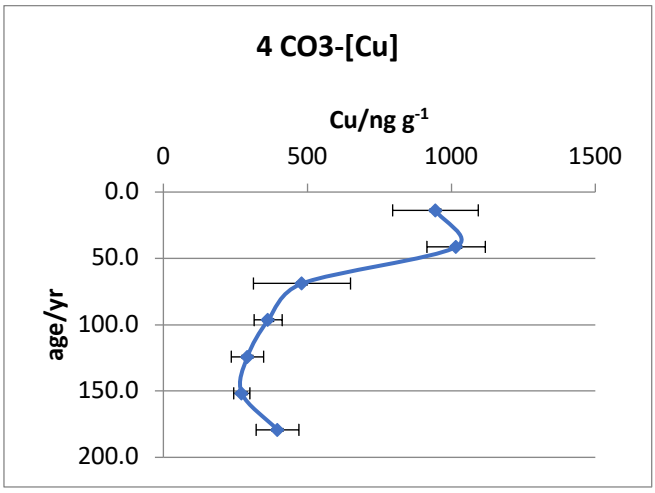


Figure A-1 (d). Soil core profile 30 for CO3-[Cu]; (n=3) at the 95% confidence level.

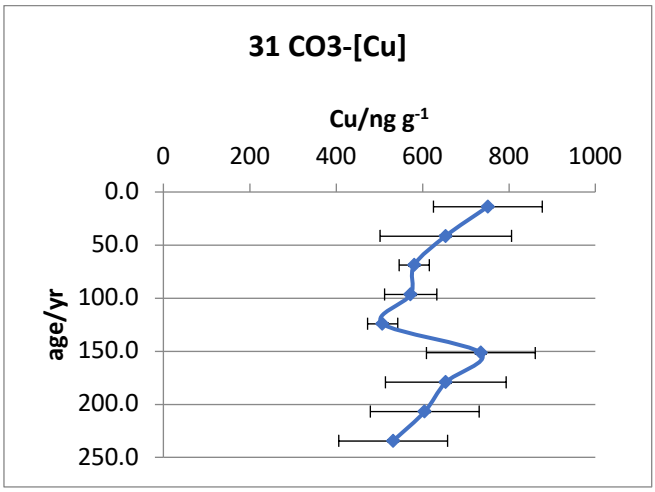


Figure A-1 (e). Soil core profile 31 for CO3-[Cu]; (n=3) at the 95% confidence level.

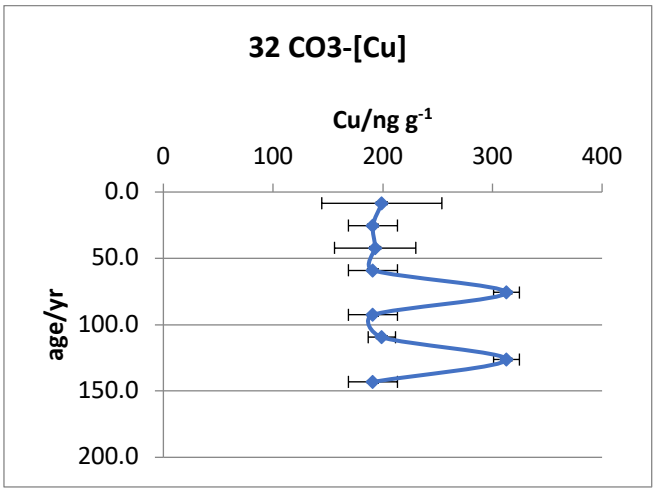


Figure A-1 (f). Soil core profile 32 for CO3-[Cu]; (n=3) at the 95% confidence level.

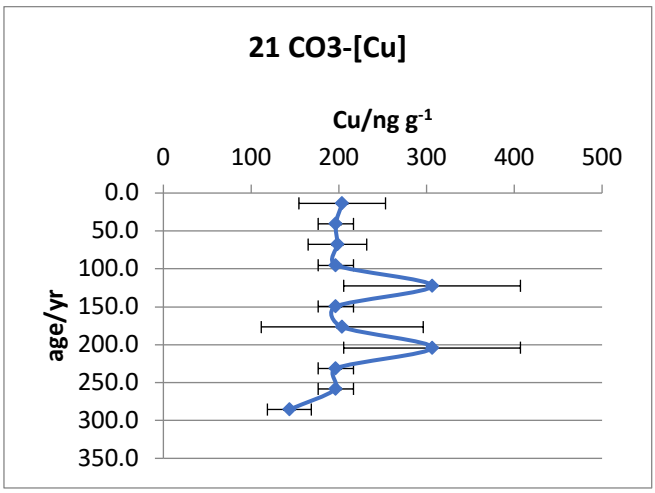


Figure A-1 (g). Soil core profile 21 for CO3-[Cu]; (n=3) at the 95% confidence level.

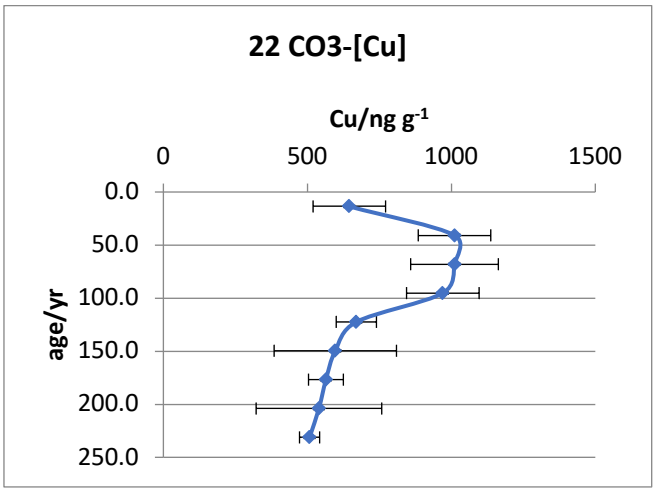


Figure A-1 (h). Soil core profile 21 for CO3-[Cu]; (n=3) at the 95% confidence level.

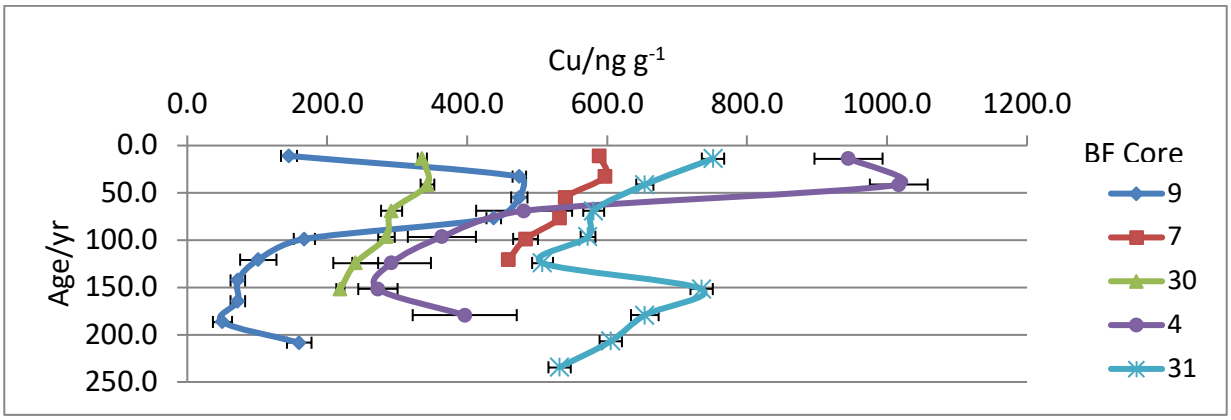


Figure 78**.** Vertical CO3-[Cu] profiles in Region A for five separate core sampling sites; (n=3) at the 95% confidence level.

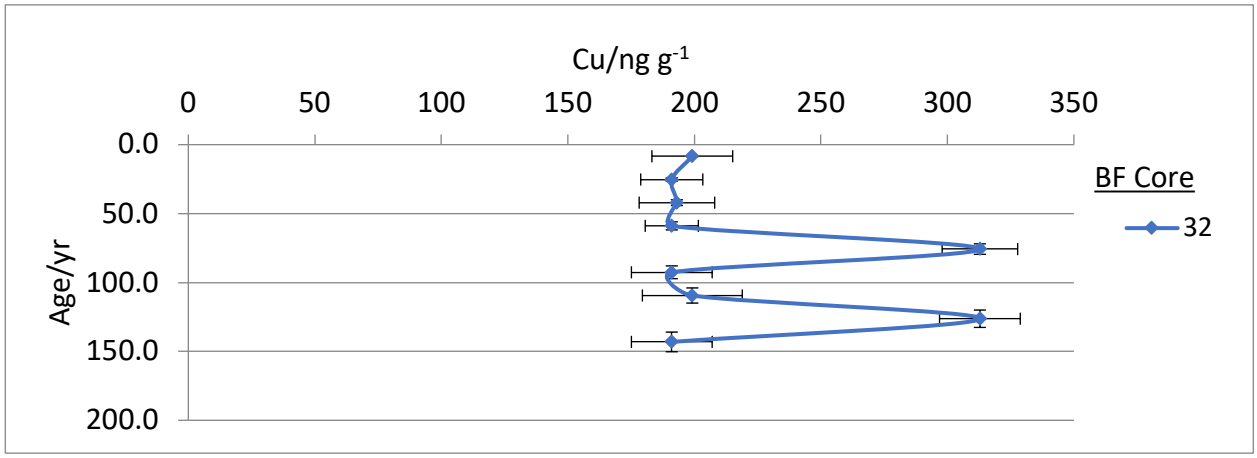


Figure 79. Soil core profiles for CO3-[Cu] at Site 32 (38.9 m) in Region B; (n=3) at the 95% confidence level.

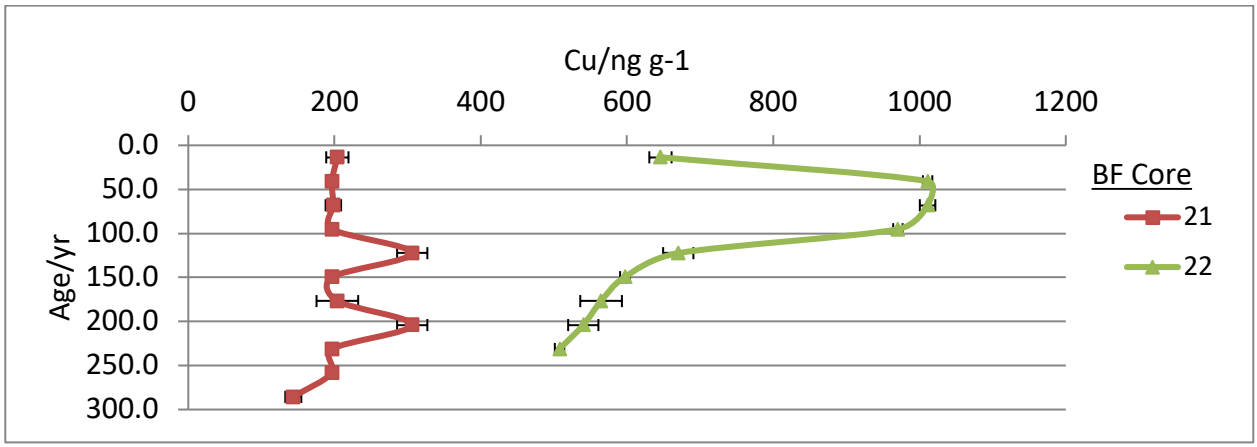


Figure 80. Soil core profiles for CO3-[Cu] in Region C; (n=3) at the 95% confidence level.

## APPENDIX A-2: Raw Data

**Table A-2.** Data for the MOX-[Cu] MAE BCR extractions.

| Depth/in (Core#) | Age (yr) | Cu (ng $g^{-1}$) | RSD | | Depth/in (Core#) | Age (yr) | Cu (ng $g^{-1}$) | RSD |
|---|---|---|---|---|---|---|---|---|
| 30A 0.5 | 13.8 | 3479.8 | 11.9 | | 9B 0.5 | 11.0 | 3635.7 | 10.4 |
| 30A 1.5 | 41.4 | 5339.1 | 12.1 | | 9B 1.5 | 32.9 | 2616.2 | 9.4 |
| 30A 2.5 | 69.0 | 4391.4 | 7.6 | | 9B 2.5 | 54.9 | 4523.4 | 8.3 |
| 30A 3.5 | 96.5 | 3719.7 | 8.8 | | 9B 3.5 | 76.8 | 5555.0 | 4.6 |
| 30A 4.5 | 124.1 | 3611.8 | 9.6 | | 9B 4.5 | 98.8 | 5399.0 | 11.6 |
| 30A 5.5 | 151.7 | 3012.0 | 11.0 | | 9B 5.5 | 120.7 | 3551.8 | 6.7 |
| | | | | | 9B 6.5 | 142.6 | 3060.0 | 1.2 |
| 4A 0.5 | 13.8 | 5162.0 | 2.2 | | 9B 7.5 | 164.6 | 2172.3 | 8.3 |
| 4A 1.5 | 41.4 | 10162.2 | 5.6 | | 9B 8.5 | 186.5 | 3851.7 | 6.5 |
| 4A 2.5 | 69.0 | 7516.6 | 5.5 | | 9B 9.5 | 208.5 | 3563.8 | 3.0 |
| 4A 3.5 | 96.5 | 4884.2 | 3.3 | | | | | |
| 4A 4.5 | 124.1 | 4222.8 | 12.8 | | 13B 0.5 | 17.4 | 3919.5 | 0.7 |
| 4A 5.5 | 151.7 | 4236.0 | 6.5 | | 13B 1.5 | 52.2 | 3384.4 | 0.3 |
| 4A 6.5 | 179.3 | 4103.8 | 9.0 | | 13B 2.5 | 86.9 | 3271.9 | 0.6 |
| | | | | | 13B 3.5 | 121.7 | 2489.4 | 0.9 |
| 31A 0.5 | 13.8 | 3644.7 | 8.4 | | 13B 4.5 | 156.5 | 2423.1 | 0.5 |
| 31A 1.5 | 41.4 | 4946.5 | 7.5 | | 13B 5.5 | 191.2 | 2142.5 | 1.3 |
| 31A 2.5 | 69.0 | 6383.1 | 8.2 | | 13B 6.5 | 226.0 | 2304.7 | 0.6 |
| 31A 3.5 | 96.5 | 4520.1 | 6.0 | | 13B 7.5 | 260.8 | 2733.2 | 0.5 |

| | | | | | | | | |
|---|---|---|---|---|---|---|---|---|
| 31A 4.5 | 124.1 | 4250.7 | 9.0 | | 13B 8.5 | 295.6 | 2709.6 | 0.3 |
| 31A 5.5 | 151.7 | 4273.1 | 3.9 | | | | | |
| 31A 6.5 | 179.3 | 3510.0 | 8.9 | | 28E 0.5 | 6.3 | 323.7 | 18.7 |
| 31A 7.5 | 206.9 | 3139.6 | 2.5 | | 28E 1.5 | 19.0 | 442.6 | 22.5 |
| 31A 8.5 | 234.5 | 1882.6 | 2.1 | | 28E 2.5 | 31.6 | 323.7 | 7.1 |
| | | | | | 28E 3.5 | 44.3 | 310.5 | 12.8 |
| 32B 0.5 | 8.4 | 2107.1 | 2.6 | | 28E 4.5 | 56.9 | 204.8 | 11.2 |
| 32B 1.5 | 25.3 | 3386.5 | 2.9 | | 28E 5.5 | 69.6 | 574.7 | 14.4 |
| 32B 2.5 | 42.1 | 3857.9 | 4.9 | | 28E 6.5 | 82.2 | 442.6 | 20.7 |
| 32B 3.5 | 58.9 | 3049.8 | 12.0 | | 28E 7.5 | 94.9 | 363.3 | 22.7 |
| 32B 4.5 | 75.8 | 2687.9 | 5.2 | | | | | |
| 32B 5.5 | 92.6 | 1972.4 | 6.4 | | 7B 0.5 | 11.0 | 3817.8 | 12.1 |
| 32B 6.5 | 109.5 | 1198.0 | 9.2 | | 7B 1.5 | 32.9 | 5880.9 | 12.2 |
| 32B 7.5 | 8.4 | 2107.1 | 2.6 | | 7B 2.5 | 54.9 | 4829.4 | 7.7 |
| 32B 8.5 | 25.3 | 3386.5 | 2.9 | | 7B 3.5 | 76.8 | 4084.0 | 8.9 |
| | | | | | 7B 4.5 | 98.8 | 3964.2 | 9.7 |
| 22A 0.5 | 13.6 | 4198.4 | 0.3 | | 7B 5.5 | 120.7 | 3298.7 | 11.1 |
| 22A 1.5 | 40.8 | 4429.0 | 1.4 | | | | | |
| 22A 2.5 | 68.0 | 4678.2 | 0.7 | | 21A 0.5 | 13.6 | 4124.4 | 2.4 |
| 22A 3.5 | 95.2 | 4535.2 | 1.3 | | 21A 1.5 | 40.8 | 6417.3 | 2.8 |
| 22A 4.5 | 122.4 | 4797.1 | 0.7 | | 21A 2.5 | 68.0 | 7262.0 | 4.7 |
| 22A 5.5 | 149.6 | 4440.5 | 0.2 | | 21A 3.5 | 95.2 | 5663.0 | 16.8 |
| 22A 6.5 | 176.8 | 4374.8 | 1.9 | | 21A 4.5 | 122.4 | 4561.9 | 5.4 |
| 22A 7.5 | 204.0 | 4288.2 | 0.6 | | 21A 5.5 | 149.6 | 3279.7 | 6.9 |
| 22A 8.5 | 231.2 | 4306.7 | 0.3 | | 21A 6.5 | 176.8 | 1891.9 | 10.4 |
| | | | | | 21A 7.5 | 204.0 | 1364.0 | 5.6 |
| | | | | | 21A 8.5 | 231.2 | 1364.0 | 5.6 |
| | | | | | 21A 9.5 | 258.4 | 2005.1 | 63.6 |
| | | | | | 21A 10.5 | 13.6 | 4124.4 | 2.4 |

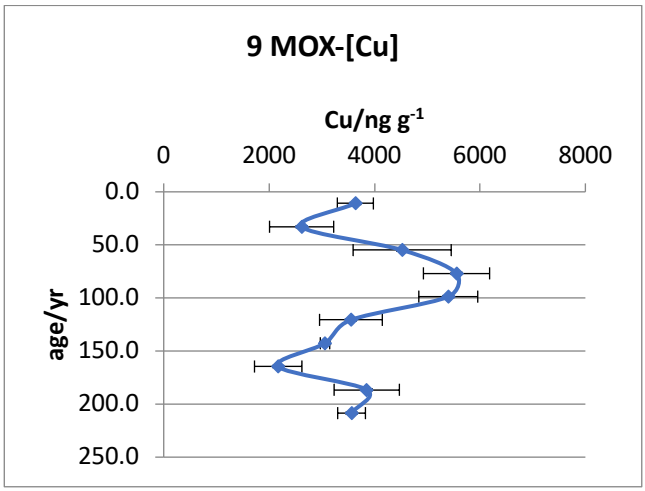

Figure A-2 (a). Soil core profile 9 for MOX-[Cu]; (n=3) at the 95% confidence level.

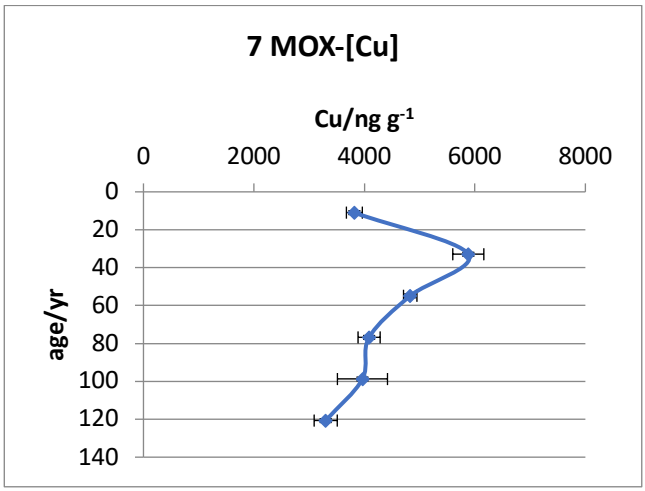

Figure A-2 (b). Soil core profile 7 for MOX-[Cu]; (n=3) at the 95% confidence level.

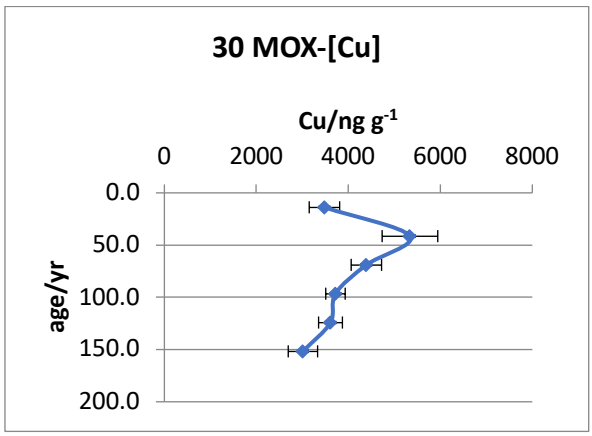

Figure A-2 (c). Soil core profile 30 for MOX-[Cu]; (n=3) at the 95% confidence level.

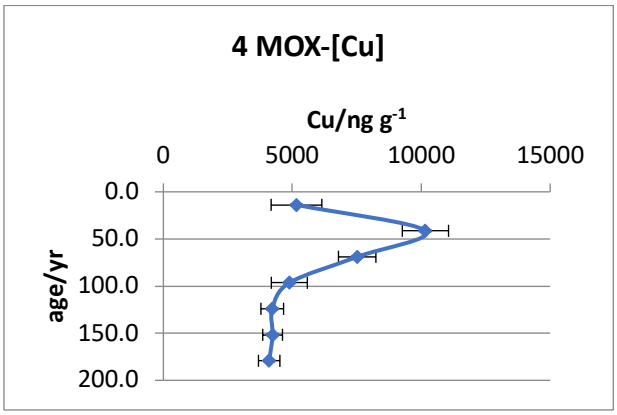

Figure A-2 (d). Soil core profile 4 for MOX-[Cu]; (n=3) at the 95% confidence level.

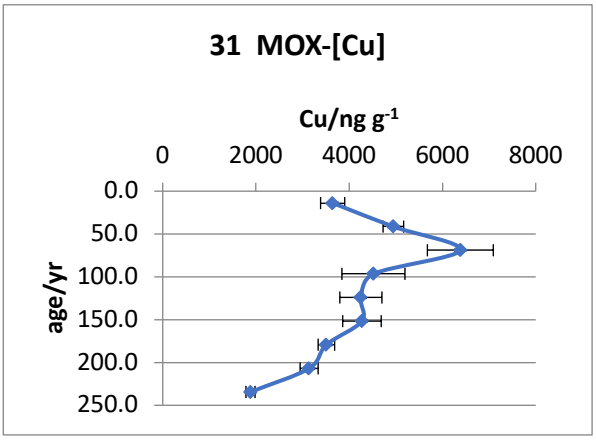

Figure A-2 (e). Soil core profile 31 for MOX-[Cu]; (n=3) at the 95% confidence level.

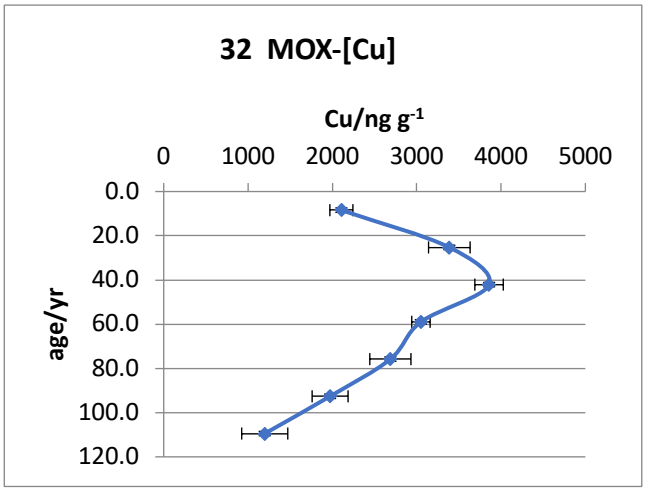

Figure A-2 (f). Soil core profile 32 for MOX-[Cu]; (n=3) at the 95% confidence level.

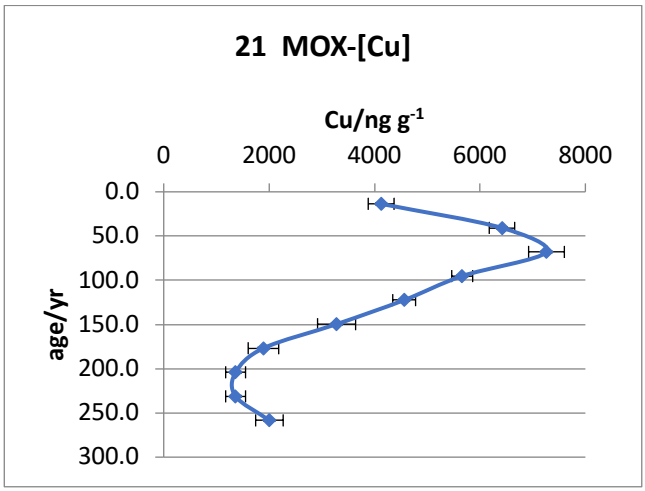


Figure A-2 (g). Soil core profile 21 for MOX-[Cu]; (n=3) at the 95% confidence level.

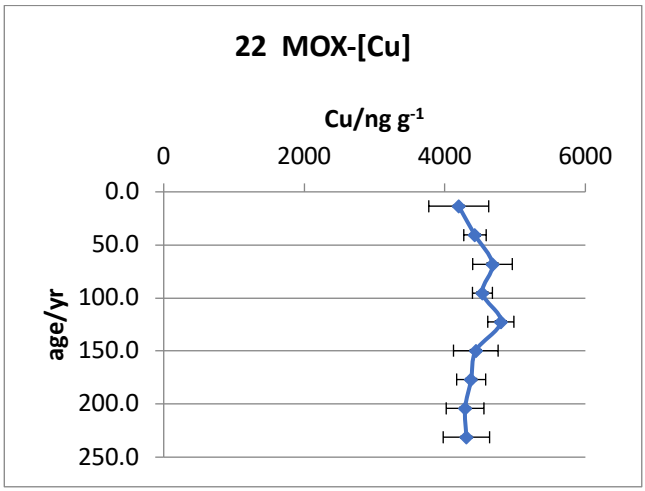


Figure A-2 (h). Soil core profile 22 for MOX-[Cu]; (n=3) at the 95% confidence level.

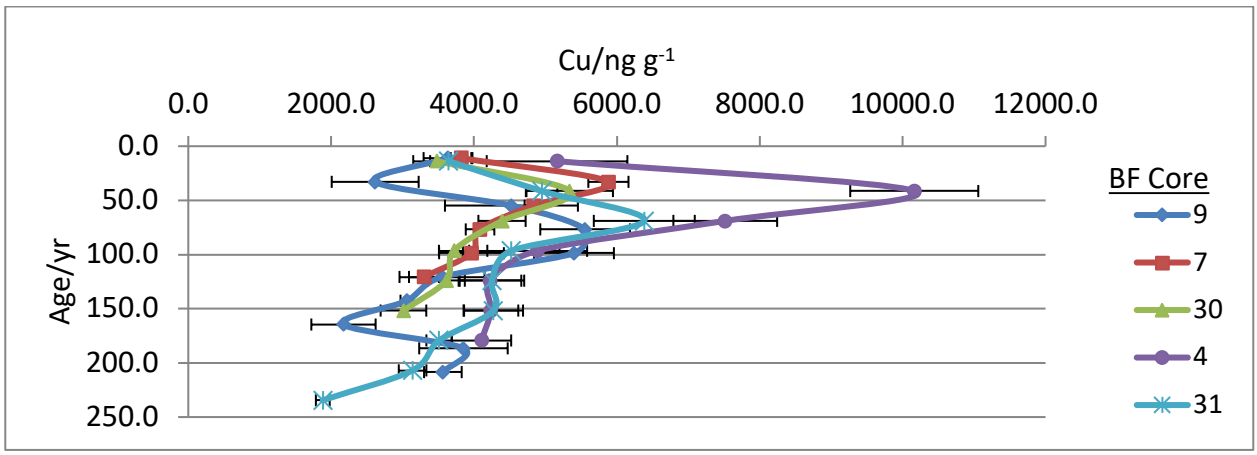


Figure 81. Soil core profiles for MOX-[Cu] in five cores from Region A; (n=3) at the 95% confidence level.

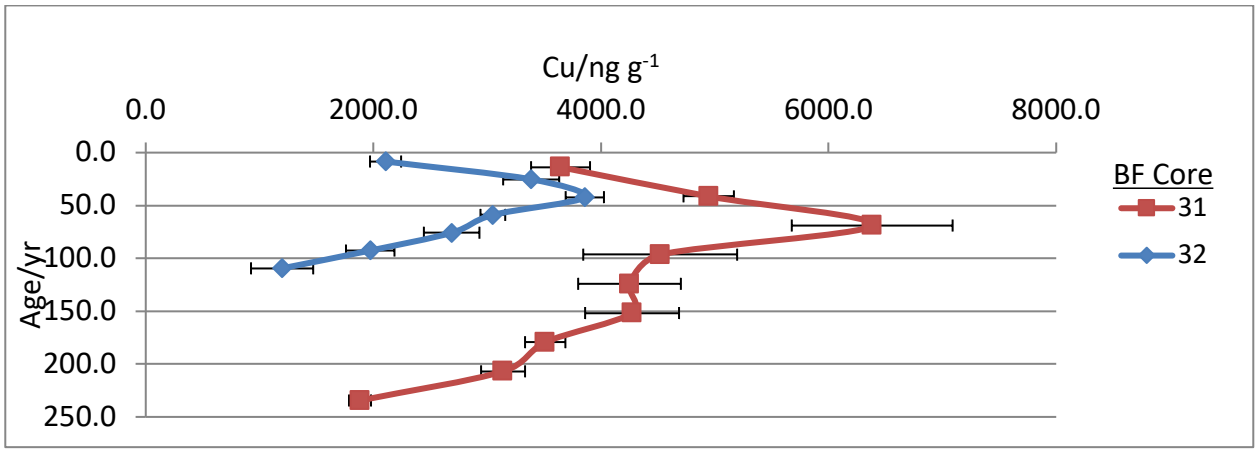


Figure 82. Soil core profiles for MOX-[Cu] in Region A (31) and B (32); (n=3) at the 95% confidence level.

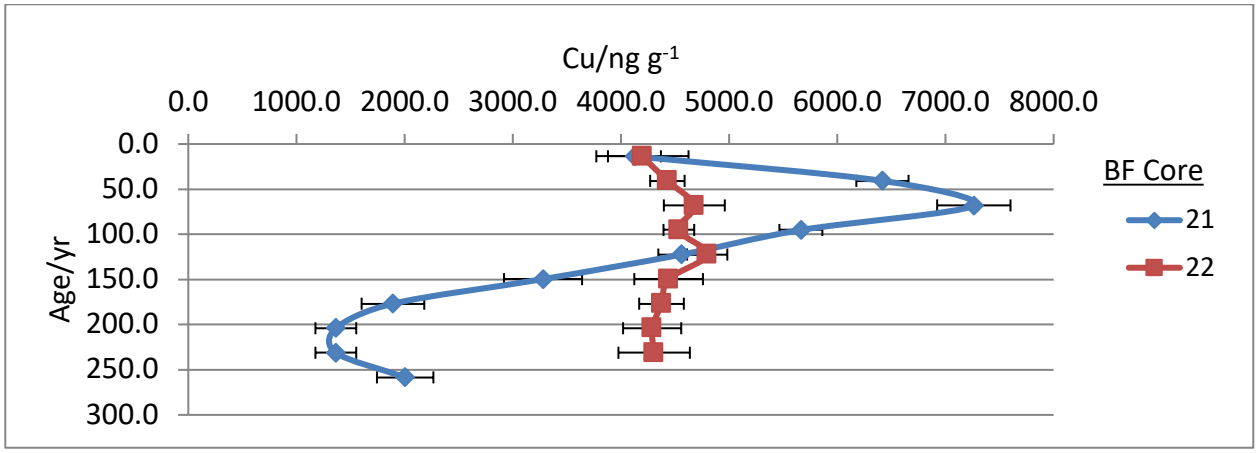


Figure 83. Vertical soil core profiles for MOX-[Cu] at two sites in Region C; (n=3) at the 95% confidence level.

## APPENDIX A-3: Raw Data

**Table A-3.** Data for the ORG-[Cu] MAE BCR extractions.

| Depth/in (Core#) | Age (yr) | Cu (ng $g^{-1}$) | RSD | | Depth/in (Core#) | Age (yr) | Cu (ng $g^{-1}$) | RSD |
|---|---|---|---|---|---|---|---|---|
| 30A 0.5 | 13.8 | 1188.2 | 10.3 | | 9B 0.5 | 11.0 | 1427.6 | 7.1 |
| 30A 1.5 | 41.4 | 1360.2 | 18.4 | | 9B 1.5 | 32.9 | 1757.5 | 8.5 |
| 30A 2.5 | 69.0 | 1650.7 | 10.0 | | 9B 2.5 | 54.9 | 2087.4 | 1.8 |
| 30A 3.5 | 96.5 | 1123.6 | 9.2 | | 9B 3.5 | 76.8 | 1801.4 | 10.7 |
| 30A 4.5 | 124.1 | 897.7 | 5.5 | | 9B 4.5 | 98.8 | 2032.4 | 5.0 |
| 30A 5.5 | 151.7 | 596.6 | 18.7 | | 9B 5.5 | 120.7 | 1438.6 | 8.7 |
| | | | | | 9B 6.5 | 142.6 | 1372.6 | 2.8 |
| 4A 0.5 | 13.8 | 2181.4 | 2.9 | | 9B 7.5 | 164.6 | 987.7 | 5.8 |
| 4A 1.5 | 41.4 | 2766.3 | 8.5 | | 9B 8.5 | 186.5 | 1405.6 | 0.0 |
| 4A 2.5 | 69.0 | 3872.2 | 13.6 | | 9B 9.5 | 208.5 | 1845.4 | 9.3 |
| 4A 3.5 | 96.5 | 2819.4 | 9.8 | | | | | |
| 4A 4.5 | 124.1 | 1819.8 | 5.6 | | 13B 0.5 | 17.4 | 603.2 | 10.1 |
| 4A 5.5 | 151.7 | 1819.8 | 15.8 | | 13B 1.5 | 52.2 | 486.1 | 15.2 |
| 4A 6.5 | 179.3 | 1915.5 | 1.0 | | 13B 2.5 | 86.9 | 398.3 | 4.2 |
| | | | | | 13B 3.5 | 121.7 | 388.5 | 7.5 |
| 31A 0.5 | 13.8 | 2148.5 | 11.5 | | 13B 4.5 | 156.5 | 310.4 | 5.4 |
| 31A 1.5 | 41.4 | 3041.1 | 6.7 | | 13B 5.5 | 191.2 | 583.7 | 10.4 |
| 31A 2.5 | 69.0 | 2520.4 | 6.0 | | 13B 6.5 | 226.0 | 486.1 | 13.9 |
| 31A 3.5 | 96.5 | 1652.7 | 4.7 | | 13B 7.5 | 260.8 | 427.6 | 14.3 |
| 31A 4.5 | 124.1 | 2532.8 | 14.0 | | 13B 8.5 | 295.6 | 339.7 | 17.9 |
| 31A 5.5 | 151.7 | 1950.2 | 12.3 | | | | | |
| 31A 6.5 | 179.3 | 1677.4 | 9.7 | | 28E 0.5 | 6.3 | 401.8 | 28.7 |
| 31A 7.5 | 206.9 | 1590.7 | 12.9 | | 28E 1.5 | 19.0 | 604.5 | 11.0 |
| 31A 8.5 | 234.5 | 1119.6 | 12.0 | | 28E 2.5 | 31.6 | 689.8 | 8.0 |
| | | | | | 28E 3.5 | 44.3 | 551.2 | 33.5 |
| 32B 0.5 | 8.4 | 919.3 | 9.9 | | 28E 4.5 | 56.9 | 540.5 | 13.7 |
| 32B 1.5 | 25.3 | 1008.4 | 9.9 | | 28E 5.5 | 69.6 | 487.1 | 16.5 |
| 32B 2.5 | 42.1 | 775.3 | 7.4 | | 28E 6.5 | 82.2 | 1265.9 | 4.4 |
| 32B 3.5 | 58.9 | 754.8 | 9.6 | | 28E 7.5 | 94.9 | 689.8 | 4.6 |
| 32B 4.5 | 75.8 | 466.9 | 7.4 | | | | | |

| | | | | | | | | |
|---|---|---|---|---|---|---|---|---|
| 32B 5.5 | 92.6 | 583.4 | 14.6 | | 7B 0.5 | 11.0 | 1370.7 | 9.8 |
| 32B 6.5 | 109.5 | 432.6 | 11.6 | | 7B 1.5 | 32.9 | 1559.2 | 17.6 |
| 32B 7.5 | 126.3 | 494.3 | 10.5 | | 7B 2.5 | 54.9 | 1877.2 | 9.7 |
| 32B 8.5 | 8.4 | 919.3 | 9.9 | | 7B 3.5 | 76.8 | 1300.1 | 8.7 |
| | | | | | 7B 4.5 | 98.8 | 1052.7 | 5.1 |
| | | | | | 7B 5.5 | 120.7 | 722.9 | 16.9 |
| | | | | | | | | |
| 22A 0.5 | 13.6 | 5128.4 | 1.1 | | 21A 0.5 | 13.6 | 1147.9 | 9.4 |
| 22A 1.5 | 40.8 | 5017.9 | 1.4 | | 21A 1.5 | 40.8 | 1254.2 | 9.5 |
| 22A 2.5 | 68.0 | 4935.0 | 0.3 | | 21A 2.5 | 68.0 | 976.3 | 7.0 |
| 22A 3.5 | 95.2 | 4925.8 | 0.6 | | 21A 3.5 | 95.2 | 951.7 | 9.0 |
| 22A 4.5 | 122.4 | 4852.1 | 0.3 | | 21A 4.5 | 122.4 | 608.3 | 6.8 |
| 22A 5.5 | 149.6 | 5110.0 | 1.1 | | 21A 5.5 | 149.6 | 747.3 | 13.6 |
| 22A 6.5 | 176.8 | 5017.9 | 1.3 | | 21A 6.5 | 176.8 | 567.5 | 10.5 |
| 22A 7.5 | 204.0 | 4962.6 | 1.2 | | 21A 7.5 | 204.0 | 641.1 | 9.7 |
| 22A 8.5 | 231.2 | 4879.7 | 1.2 | | 21A 8.5 | 231.2 | 641.1 | 9.7 |
| | | | | | 21A 9.5 | 258.4 | 641.1 | 9.7 |
| | | | | | 21A 10.5 | 285.6 | 436.6 | 10.6 |

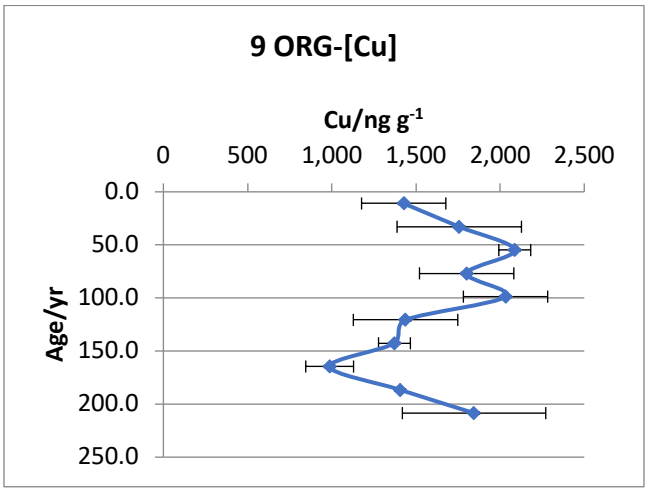


Figure A-3 (a). Soil core profile 9 for ORG-[Cu]; (n=3) at the 95% confidence level.

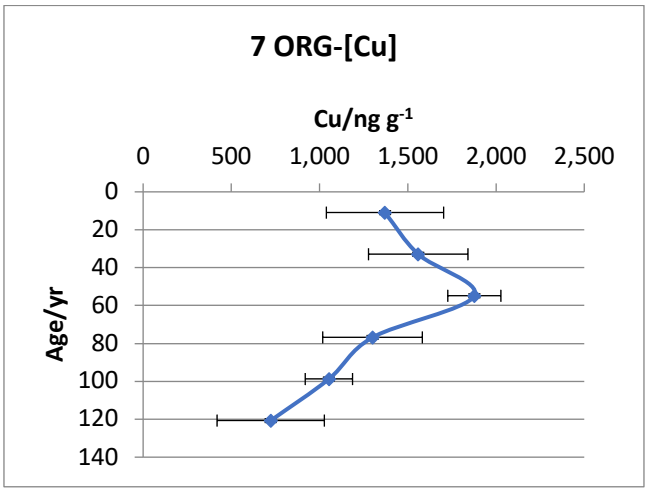


Figure A-3 (b). Soil core profile 7 for ORG-[Cu]; (n=3) at the 95% confidence level.

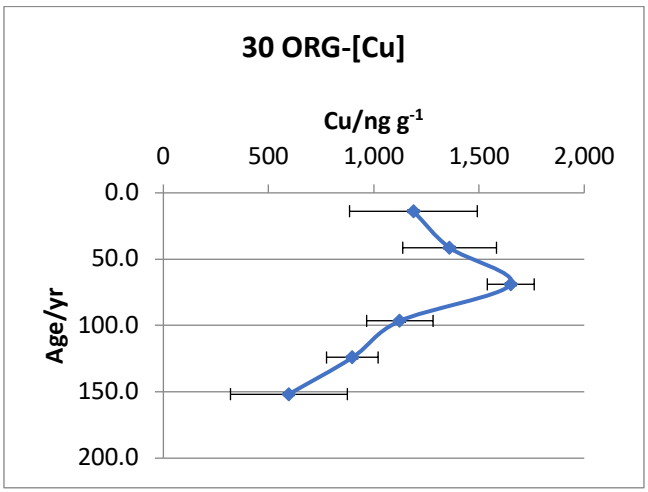


Figure A-3 (c). Soil core profile 30 for ORG-[Cu]; (n=3) at the 95% confidence level.

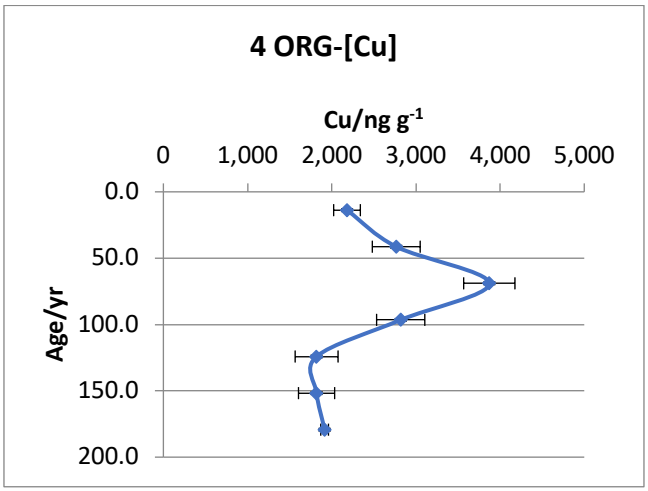


Figure A-3 (d). Soil core profile 4 for ORG-[Cu]; (n=3) at the 95% confidence level.

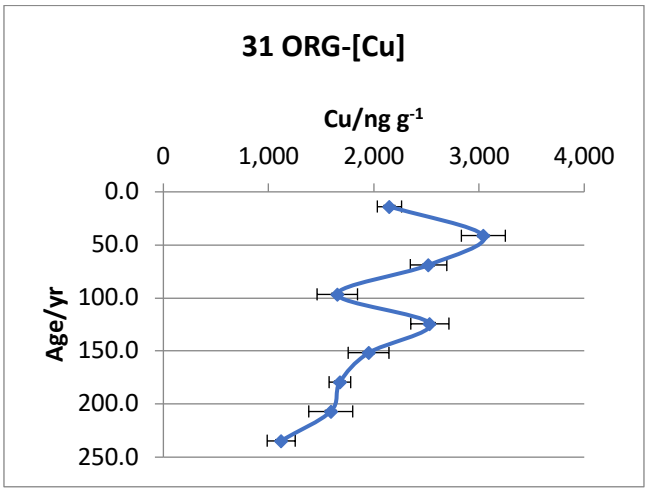


Figure A-3 (e). Soil core profile 31 for ORG-[Cu]; (n=3) at the 95% confidence level.

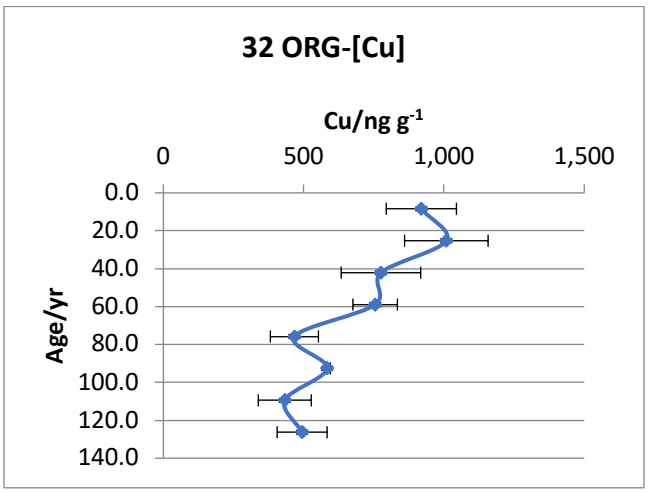


Figure A-3 (f). Soil core profile 32 for ORG-[Cu]; (n=3) at the 95% confidence level.

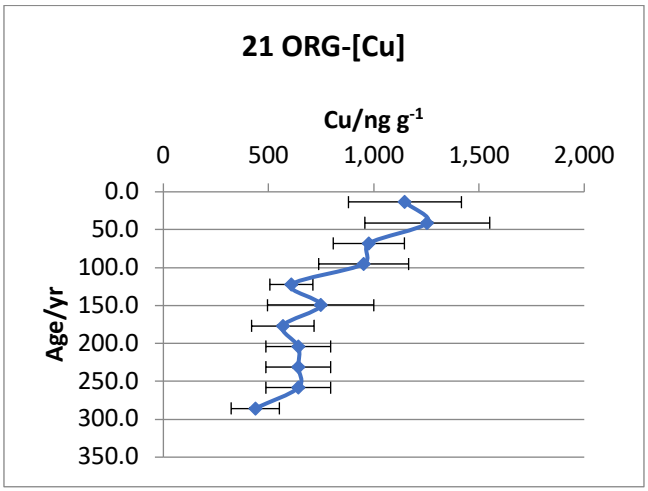


Figure A-3 (g). Soil core profile 21 for ORG-[Cu]; (n=3) at the 95% confidence level.

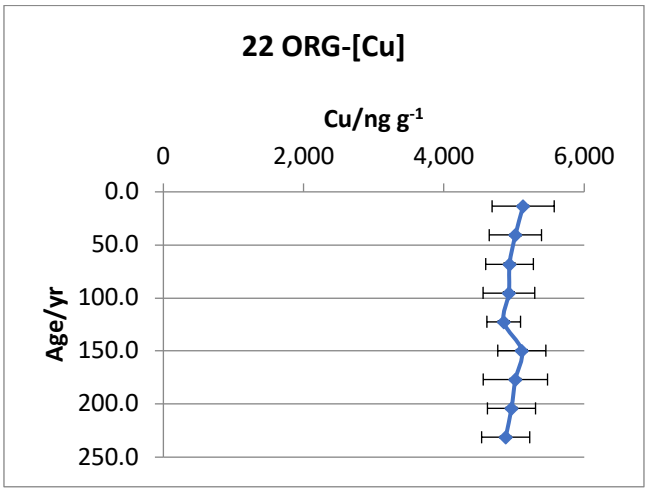


Figure A-3 (h). Soil core profile 22 for ORG-[Cu]; (n=3) at the 95% confidence level.

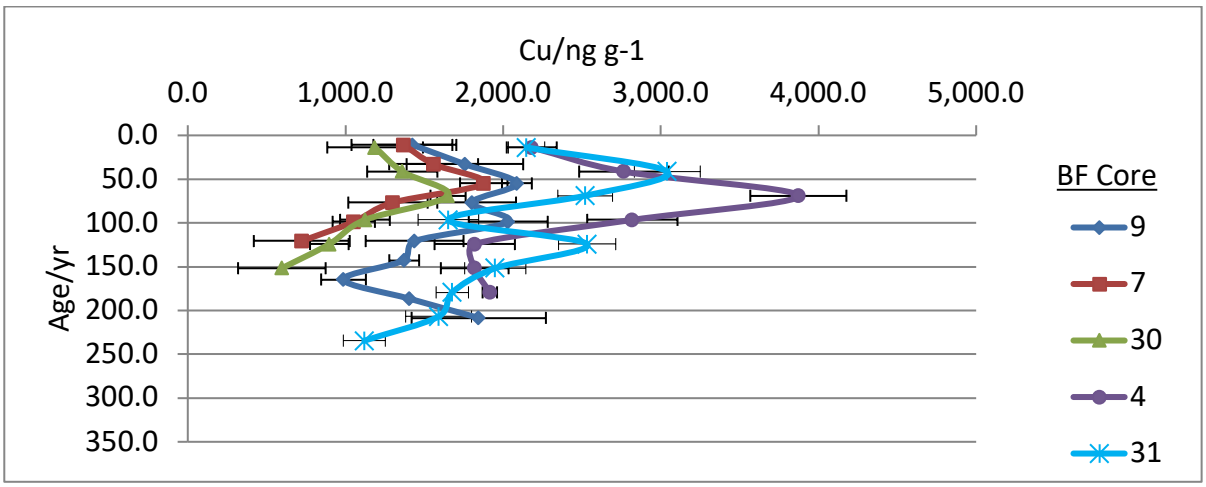


Figure 84. Soil core profiles for ORG-[Cu] in Region A; (n=3) at the 95% confidence level.

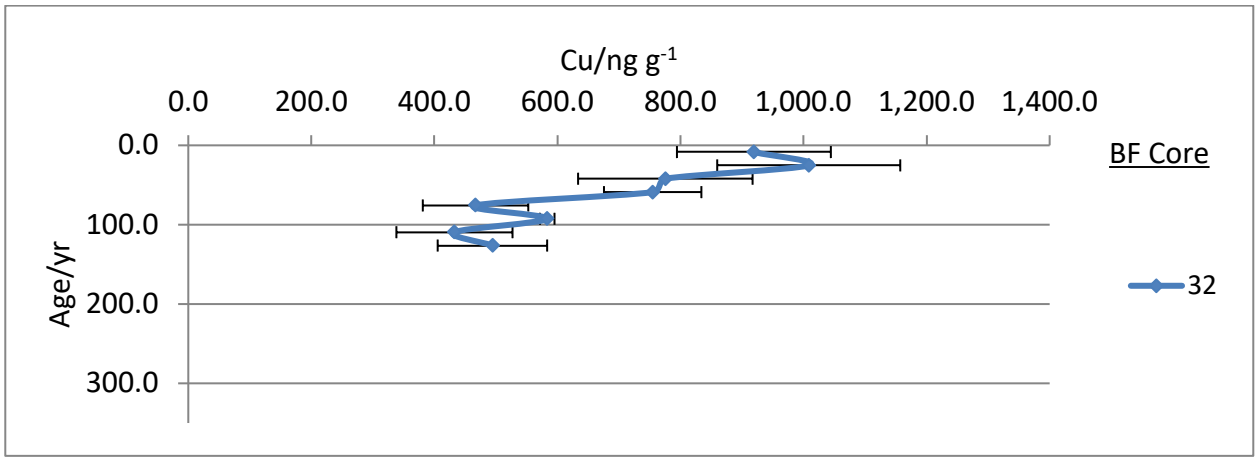


Figure 85. Soil core profiles for ORG-[Cu] in Region B; (n=3) at the 95% confidence level.

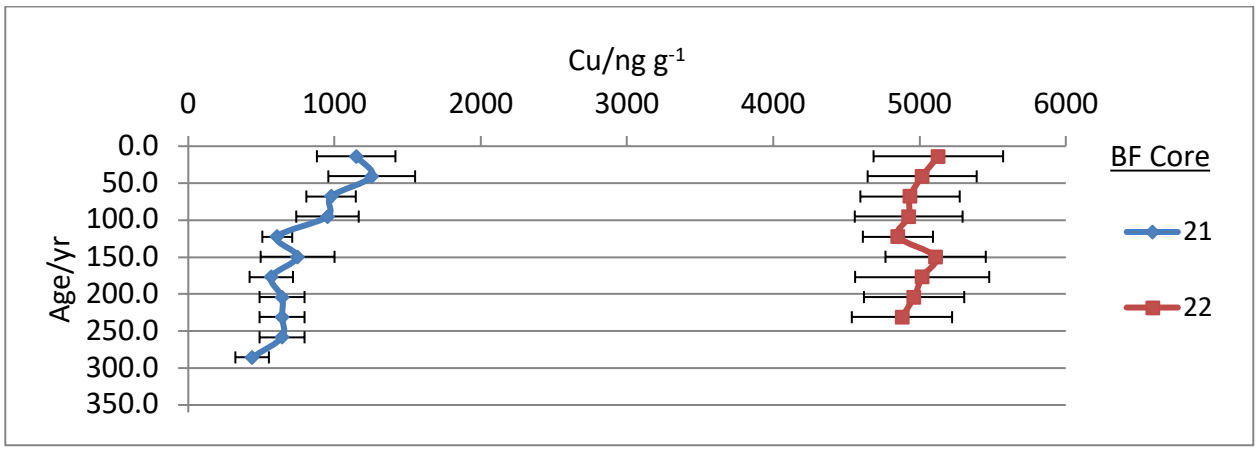


Figure 86. Soil core profiles for ORG-[Cu] in Region C; (n=3) at the 95% confidence level.

## APPENDIX A-4: Raw Data

**Table A-4**. Data for the BF RFC-[Cu] BCR extractions.

| Depth/in (Core#) | Age (yr) | Cu (μg $g^{-1}$) | RSD |
|---|---|---|---|
| 9B 0.5 | 9B 0.5 | 17.0 | 3.2 |
| 9B 1.5 | 9B 1.5 | 10.2 | 3.3 |
| 9B 2.5 | 9B 2.5 | 16.5 | 3.1 |
| 9B 3.5 | 9B 3.5 | 10.3 | 2.1 |
| 9B 4.5 | 9B 4.5 | 10.1 | 2.3 |
| 9B 5.5 | 9B 5.5 | 9.1 | 2.5 |
| 9B 6.5 | 9B 6.5 | 10.5 | 2.1 |
| 9B 7.5 | 9B 7.5 | 10.3 | 2.3 |
| 9B 8.5 | 9B 8.5 | 11.5 | 3.1 |
| 9B 9.5 | 9B 9.5 | 10.0 | 3.2 |

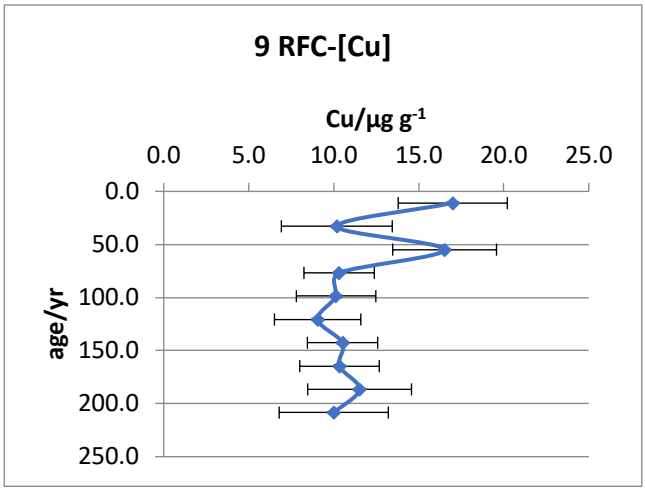


Figure A-4 (a). Soil core profile 9 for RFC-[Cu]; (n=3) at the 95% confidence level.

## APPENDIX A-5: Raw Data

**Table A-5.** Data for the BF Hg MAE-BCR-ICP-MS extractions.

| Depth/in (Core#) | Age (yr) | Hg (ng $g^{-1}$) | RSD | | Depth/in (Core#) | Age (yr) | Hg (ng $g^{-1}$) | RSD |
|---|---|---|---|---|---|---|---|---|
| EXΔ-[Hg] | | | | | MOX-[Hg] | | | |
| 2B 0.5 | 13.8 | 4.0 | 5.8 | | 2B 0.5 | 13.8 | 14.9 | 3.3 |
| 2B 1.5 | 41.4 | 3.0 | 10.2 | | 2B 1.5 | 41.4 | 14.5 | 3.4 |
| 2B 2.5 | 69.0 | 12.1 | 4.4 | | 2B 2.5 | 69.0 | 28.4 | 8.6 |
| 2B 3.5 | 96.5 | 8.5 | 5.9 | | 2B 3.5 | 96.5 | 36.3 | 35.6 |
| 2B 4.5 | 124.1 | 11.1 | 1.1 | | 2B 4.5 | 124.1 | 8.1 | 16.0 |
| 2B 5.5 | 151.7 | 10.7 | 3.3 | | 2B 5.5 | 151.7 | 54.1 | 4.3 |
| 2B 6.5 | 179.3 | 10.0 | 1.6 | | 2B 6.5 | 179.3 | 4.9 | 6.8 |
| 2B 7.5 | 206.9 | 13.3 | 4.1 | | 2B 7.5 | 206.9 | 2.9 | 8.7 |
| 2B 8.5 | 234.5 | 12.1 | 2.3 | | 2B 8.5 | 234.5 | 21.4 | 3.6 |
| | | | | | | | | |
| CO3-[Hg] | | | | | ORG-[Hg] | | | |
| 2B 0.5 | 13.8 | 5.0 | 4.7 | | 2B 0.5 | 13.8 | 390.7 | 8.0 |
| 2B 1.5 | 41.4 | 3.9 | 5.4 | | 2B 1.5 | 41.4 | 182.3 | 2.2 |
| 2B 2.5 | 69.0 | 4.4 | 17.1 | | 2B 2.5 | 69.0 | 112.7 | 37.8 |
| 2B 3.5 | 96.5 | 3.5 | 2.7 | | 2B 3.5 | 96.5 | 85.1 | 7.0 |
| 2B 4.5 | 124.1 | 5.9 | 2.4 | | 2B 4.5 | 124.1 | 74.8 | 2.3 |
| 2B 5.5 | 151.7 | 9.1 | 3.5 | | 2B 5.5 | 151.7 | 57.1 | 2.9 |
| 2B 6.5 | 179.3 | 9.0 | 3.6 | | 2B 6.5 | 179.3 | 48.5 | 4.5 |
| 2B 7.5 | 206.9 | 4.8 | 7.9 | | 2B 7.5 | 206.9 | 45.9 | 2.4 |
| 2B 8.5 | 234.5 | 4.4 | 1.4 | | 2B 8.5 | 234.5 | 75.1 | 3.5 |

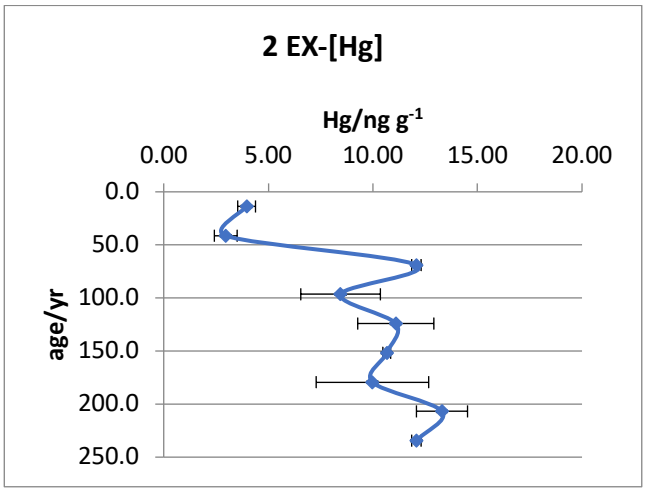


Figure A-5 (a). Soil core profile 2 EXΔ-[Hg]; (n=3) at the 95% confidence level.

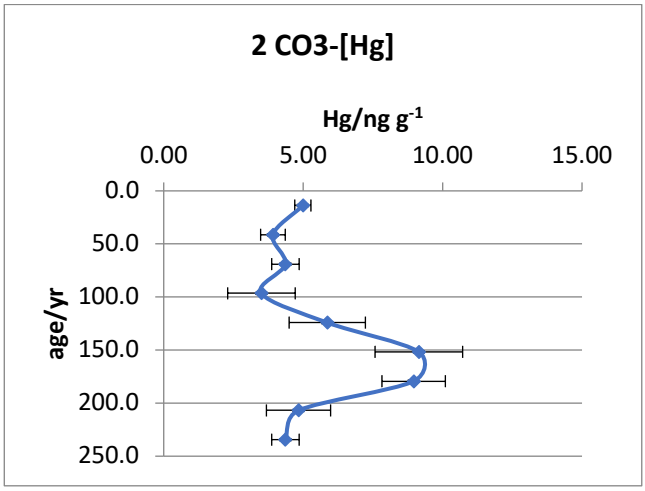


Figure A-5 (b). Soil core profile 2 CO3-[Hg]; (n=3) at the 95% confidence level.

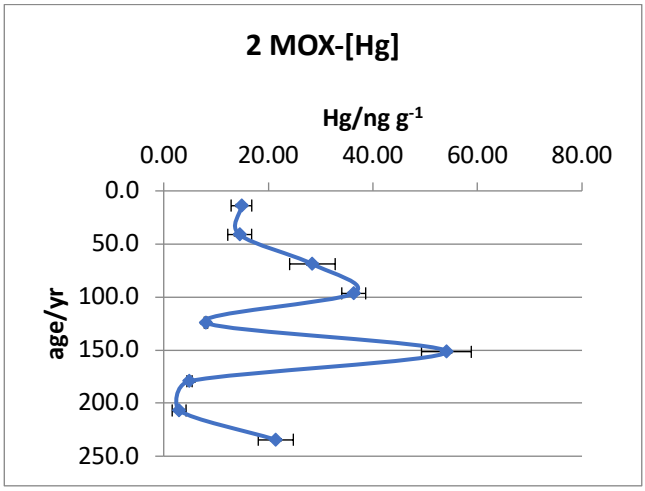


Figure A-5 (c). Soil core profile 2 MOX-[Hg]; (n=3) at the 95% confidence level.

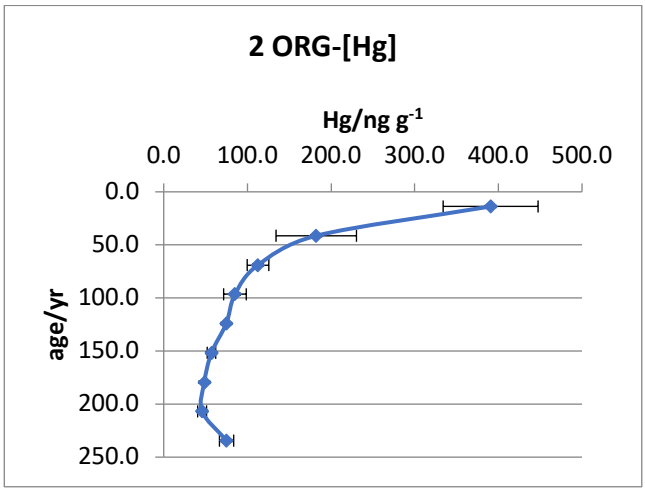


Figure A-5 (d). Soil core profile 2 ORG-[Hg]; (n=3) at the 95% confidence level.

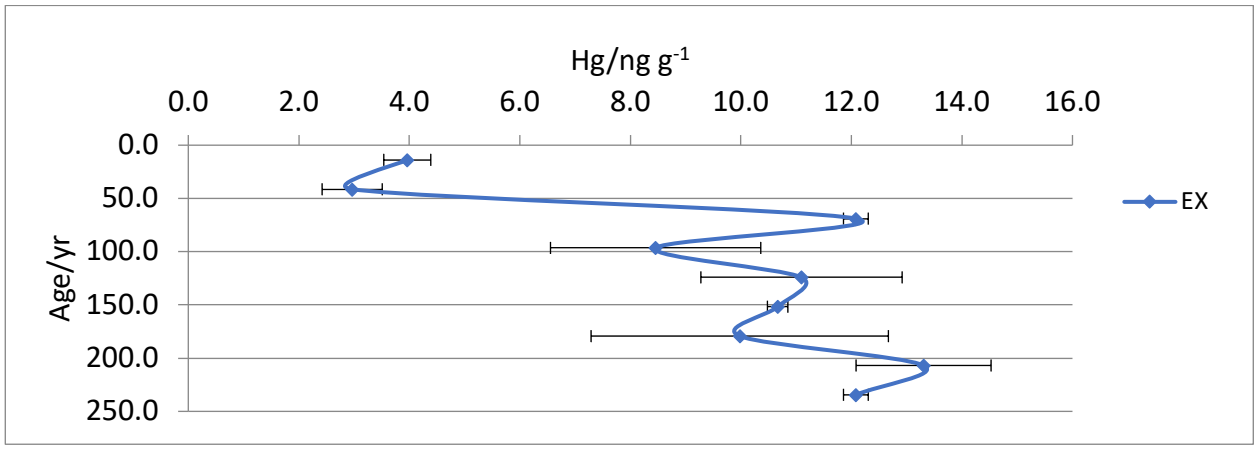


Figure 87. Soil core profile for EXΔ-[Hg] in Region B, site 2 (36.6 m); (n=3) at the 95% confidence level.

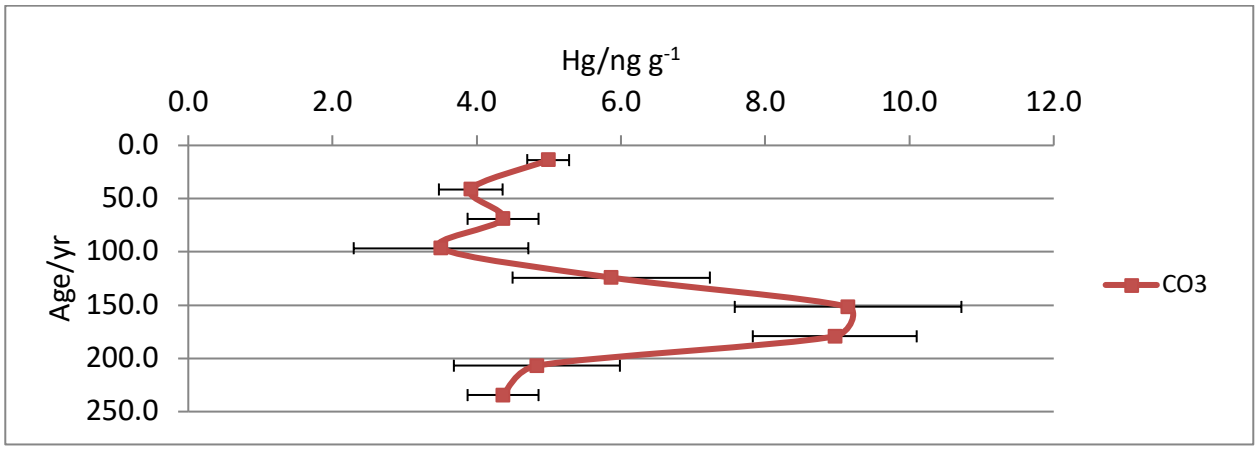


Figure 88. Soil core profile for CO3-[Hg] in Region B, site 2 (36.6 m); (n=3) at the 95% confidence level.

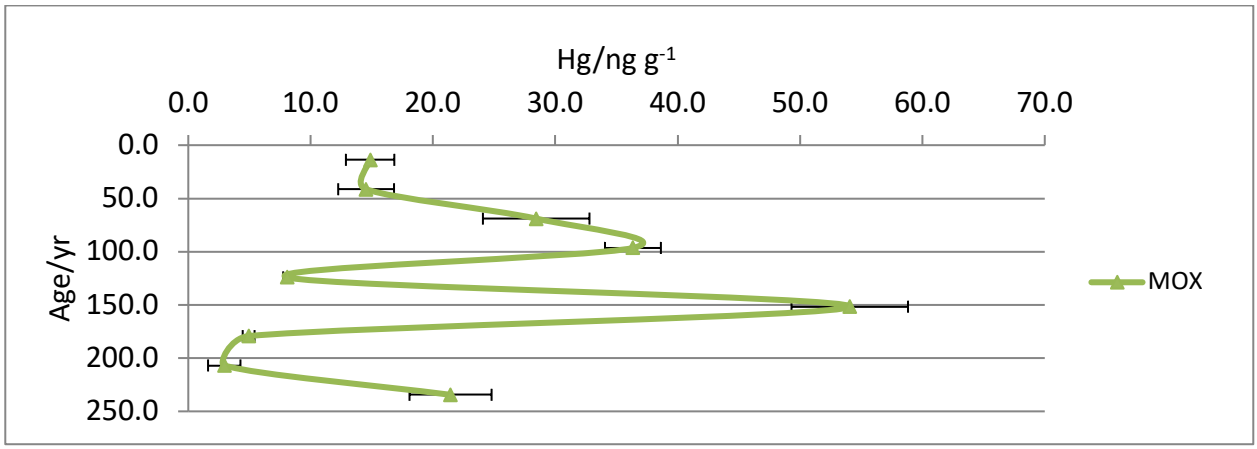


Figure 89. Soil core profile for MOX-[Hg] in Region B, site 2 (36.6 m); (n=3) at the 95% confidence level.

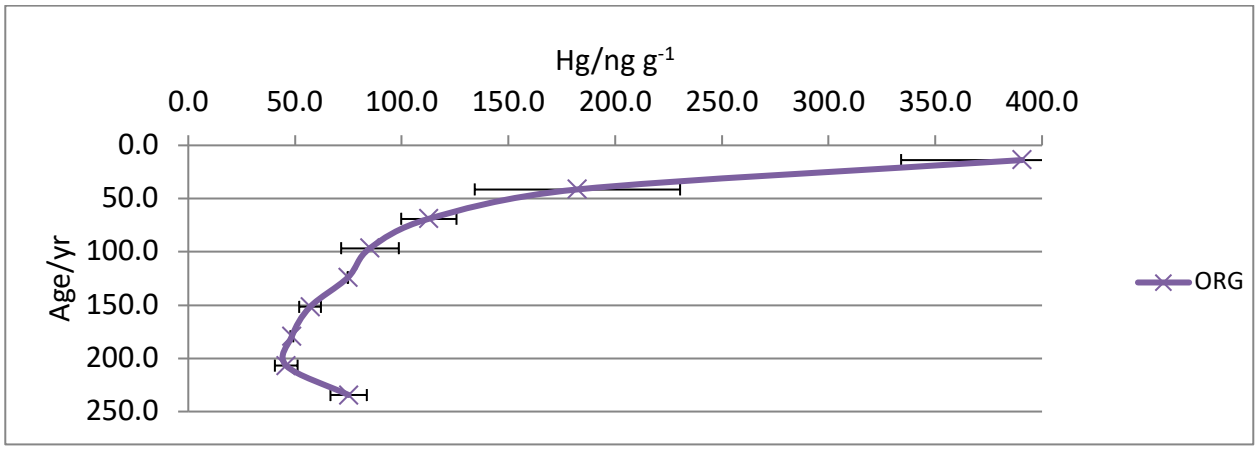


Figure 90. Soil core profile for ORG-[Hg] in Region B, site 2 (36.6 m); (n=3) at the 95% confidence level.

## APPENDIX A-6: Raw Data

**Table A-6**. Data for the CAT-[Hg].

| Depth/in (Core#) | Age (yr) | Hg (ng $g^{-1}$) | RSD | | Depth/in (Core#) | Age (yr) | Hg (ng $g^{-1}$) | RSD |
|---|---|---|---|---|---|---|---|---|
| 2B 0.5 | 13.8 | 395.4 | 3.3 | | 6A 0.5 | 11.0 | 83.0 | 1.1 |
| 2B 1.5 | 41.4 | 227.9 | 3.5 | | 6A 1.5 | 32.9 | 76.7 | 1.8 |
| 2B 2.5 | 69.0 | 181.6 | 2.3 | | 6A 2.5 | 54.9 | 86.4 | 5.6 |
| 2B 3.5 | 96.5 | 211.6 | 12.2 | | 6A 3.5 | 76.8 | 81.9 | 3.0 |
| 2B 4.5 | 124.1 | 124.1 | 6.9 | | 6A 4.5 | 98.8 | 71.7 | 5.3 |
| 2B 5.5 | 151.7 | 103.5 | 7.9 | | 6A 5.5 | 120.7 | 60.7 | 2.8 |
| 2B 6.5 | 179.3 | 93.3 | 5.4 | | 6A 6.5 | 142.6 | 46.3 | 4.3 |
| 2B 7.5 | 206.9 | 73.4 | 4.2 | | 6A 7.5 | 164.6 | 51.3 | 5.7 |
| 2B 8.5 | 234.5 | 77.4 | 7.7 | | 6A 8.5 | 186.5 | 85.9 | 1.2 |
| | | | | | | | | |
| 21A 0.5 | 13.6 | 1147.9 | 9.4 | | | | | |
| 21A 1.5 | 40.8 | 1254.2 | 9.5 | | | | | |
| 21A 2.5 | 68.0 | 976.3 | 7.0 | | | | | |
| 21A 3.5 | 95.2 | 951.7 | 9.0 | | | | | |
| 21A 4.5 | 122.4 | 608.3 | 6.8 | | | | | |
| 21A 5.5 | 149.6 | 747.3 | 13.6 | | | | | |
| 21A 6.5 | 176.8 | 567.5 | 10.5 | | | | | |
| 21A 7.5 | 204.0 | 641.1 | 9.7 | | | | | |
| 21A 8.5 | 231.2 | 641.1 | 9.7 | | | | | |
| 21A 9.5 | 258.4 | 641.1 | 9.7 | | | | | |
| 21A 10.5 | 285.6 | 436.6 | 10.6 | | | | | |

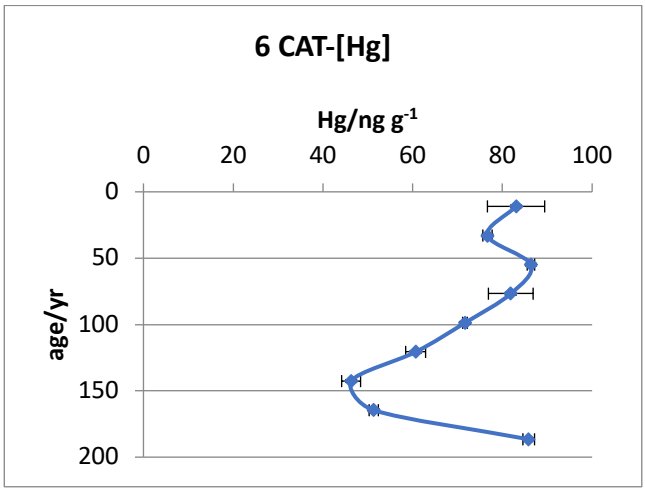


Figure A-6 (a). Soil core profile 6 for CAT-[Hg]; (n=3) at the 95% confidence level.

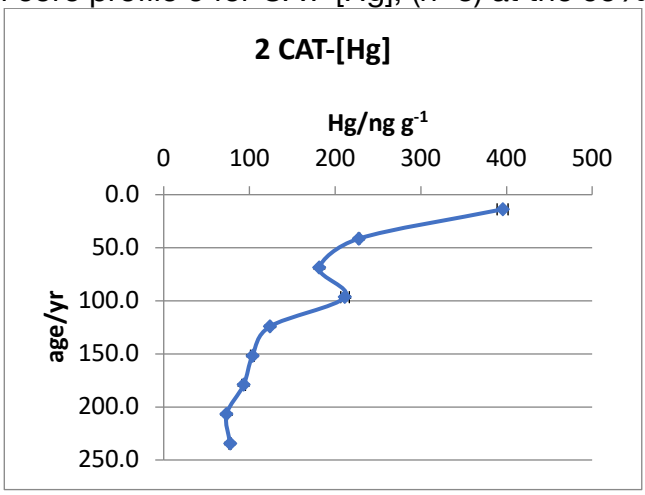


Figure A-6 (b). Soil core profile 2 for CAT-[Hg]; (n=3) at the 95% confidence level.

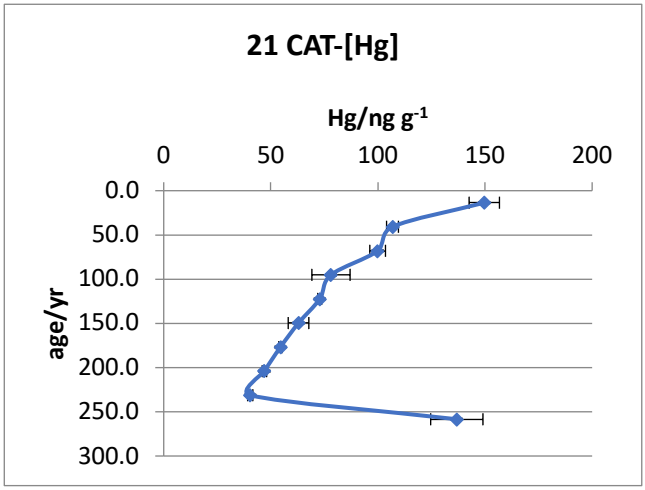


Figure A-6 (c). Soil core profile 21 for CAT-[Hg]; (n=3) at the 95% confidence level.

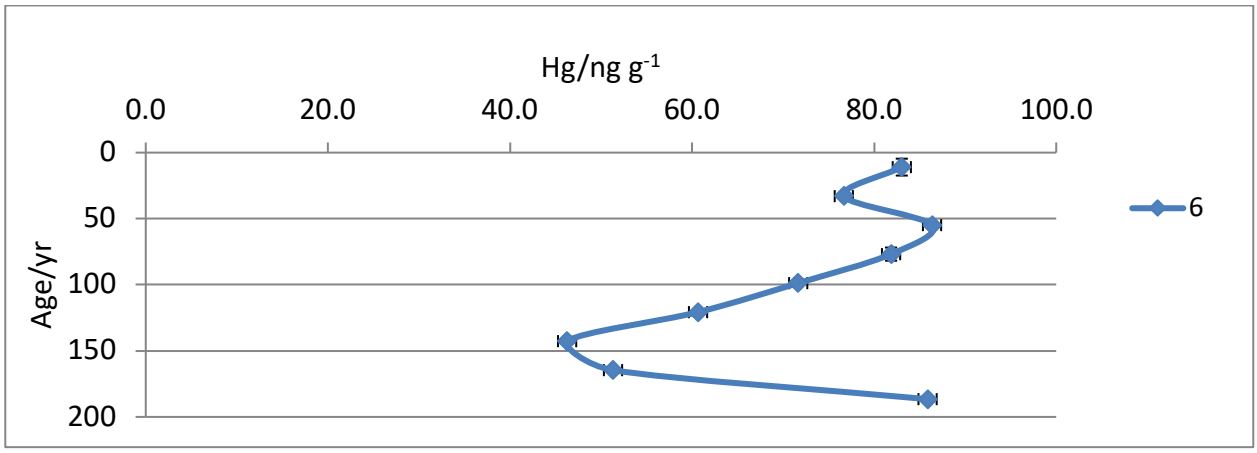


Figure 91. Soil core profile for CAT-[Hg] in Region A (Site 6, 13.7 m); (n=3) at the 95% confidence level.

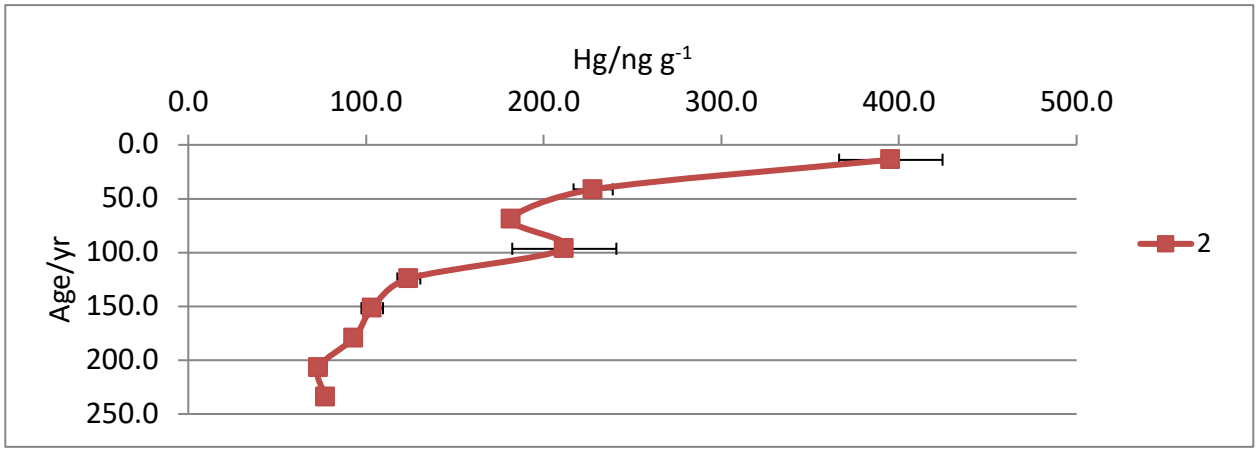


Figure 92. Soil core profile for CAT-[Hg] Hg in Region B (Site 2, 36.6 m); (n=3) at the 95% confidence level.

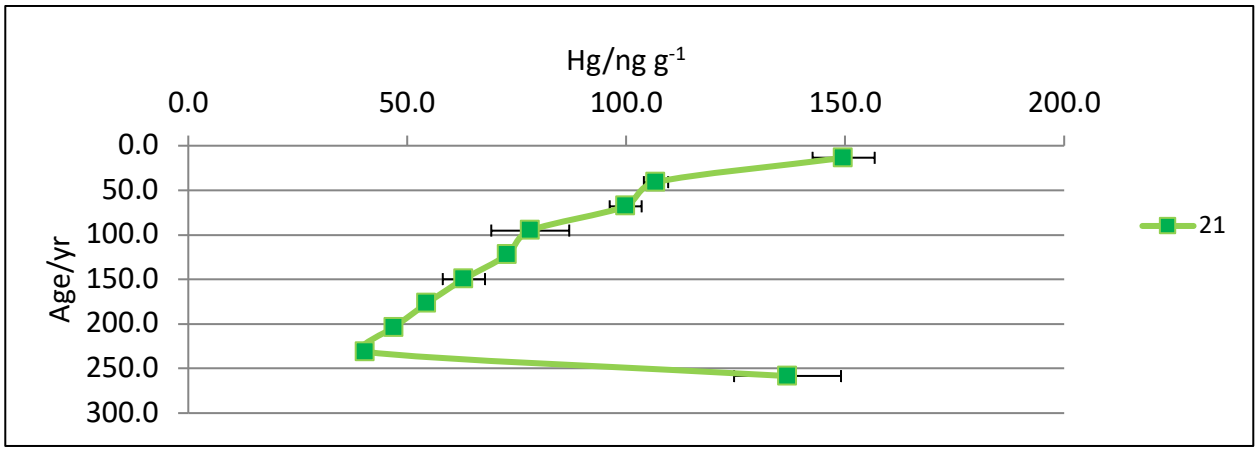


Figure 93. Soil core profile for Hg in Region C (Site 21, 100.6 m; (n=3) at the 95% confidence level.

## APPENDIX A-7: Raw Data

**Table A-7.** Data for the BF CO3-, MOX- and ORG-[Pb] BCR extractions. (n=3); at the 95% confidence interval.

| BF Core | Distance (m) | CO3-[Pb] (ng $g^{-1}$) | Sd (ng $g^{-1}$) | MOX-[Pb] (ng $g^{-1}$) | Sd (ng $g^{-1}$) | ORG-[PB] (ng $g^{-1}$) | Sd (ng $g^{-1}$) |
|---|---|---|---|---|---|---|---|
| 9B | 0 | 984.8 | 583.8 | 9935.0 | 2293.6 | 2882.1 | 1176.5 |
| 7B | 9 | 1694.3 | 857.8 | 25937.6 | 4672.7 | 6832.2 | 1366.2 |
| 5A | 18 | 2038.6 | 655.8 | 20163.7 | 3090.6 | 5436.7 | 2422.5 |
| 3A | 27 | 851.9 | 313.7 | 18237.2 | 2386.3 | 4120.9 | 514.8 |
| 2B | 37 | 193.9 | 103.5 | 9276.0 | 2311.7 | 2809.6 | 817.9 |
| 15A | 46 | 323.7 | 102.5 | 16156.7 | 2068.0 | 2973.8 | 522.9 |
| 16B | 55 | 1109.2 | 134.1 | 17564.9 | 2040.2 | 5382.3 | 739.2 |
| 17A | 64 | 498.4 | 225.8 | 12512.0 | 676.8 | 8428.9 | 937.6 |
| 18A | 73 | 272.7 | 102.1 | 14896.2 | 1746.2 | 1594.8 | 361.0 |
| 20A | 91 | 443.2 | 375.3 | 7559.2 | 1747.2 | 336.9 | 119.8 |
| 21A | 101 | 444 | 5.7 | 4901.2 | 223.3 | 5784.8 | 343.2 |
| 22A | 110 | 280 | 7.3 | 4607.1 | 255.3 | 8160.8 | 983.6 |
| 23A | 119 | 282 | 5.7 | 4790.2 | 234.0 | 7517.3 | 614.4 |
| 24A | 128 | 282 | 5.7 | 5147.8 | 344.3 | 6683.3 | 578.8 |

## APPENDIX B: Calibrations

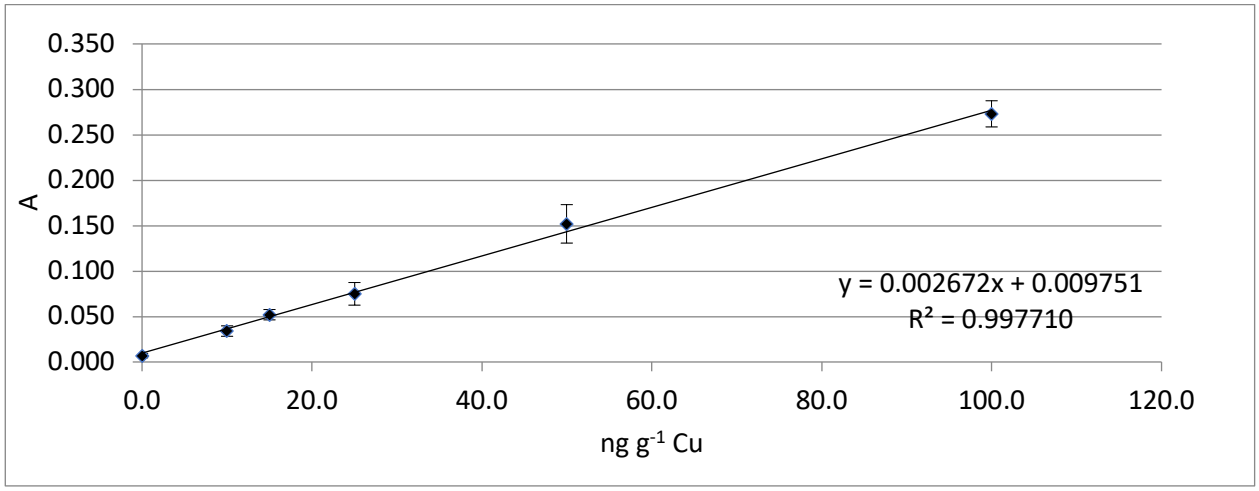


Figure 94. Calibration model for MOX-[Cu] MAE BCR method; (n=3) at the 95% confidence level.

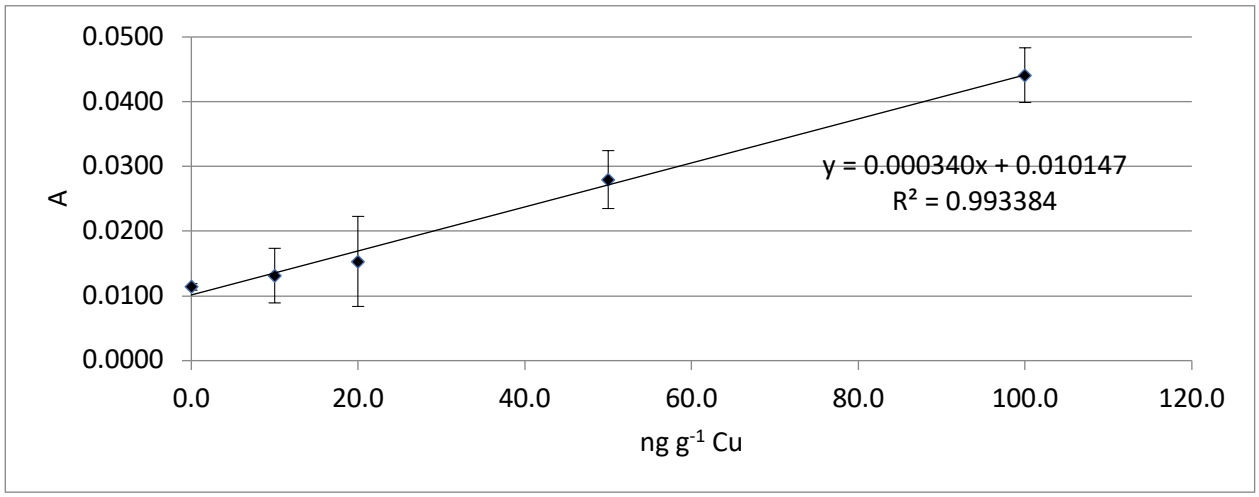


Figure 95. Calibration model for BCR SRM 701 (CO3-[Cu]) MAE BCR method; (n=3) at the 95% confidence level.

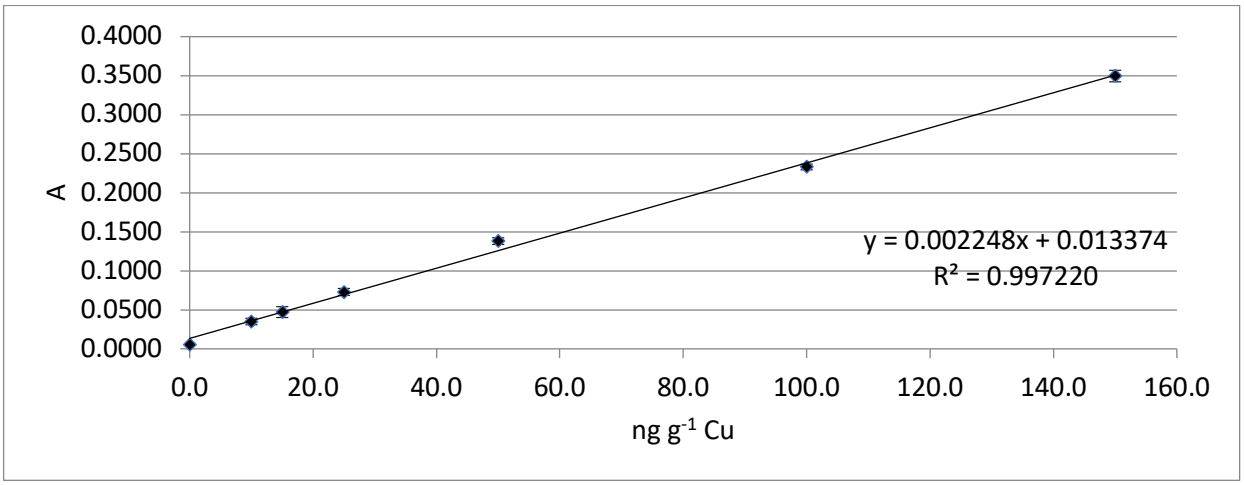


Figure 96. Calibration model for BCR SRM 701 (MOX-[Cu]) MAE BCR method; (n=3) at the 95% confidence level.

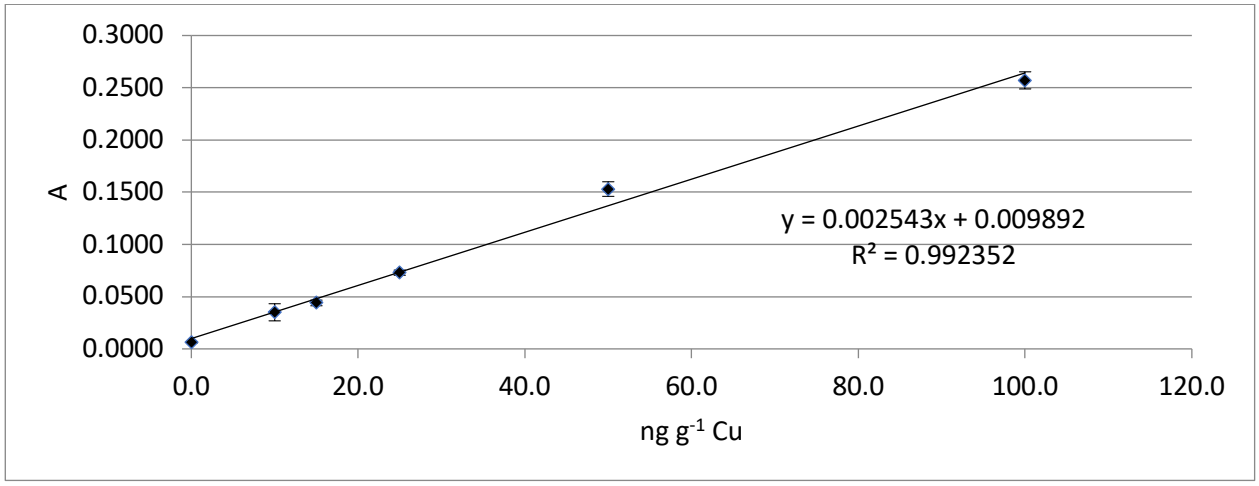


Figure 97. Calibration model for BCR SRM 701 (ORG-[Cu]) MAE BCR method; (n=3) at the 95% confidence level.

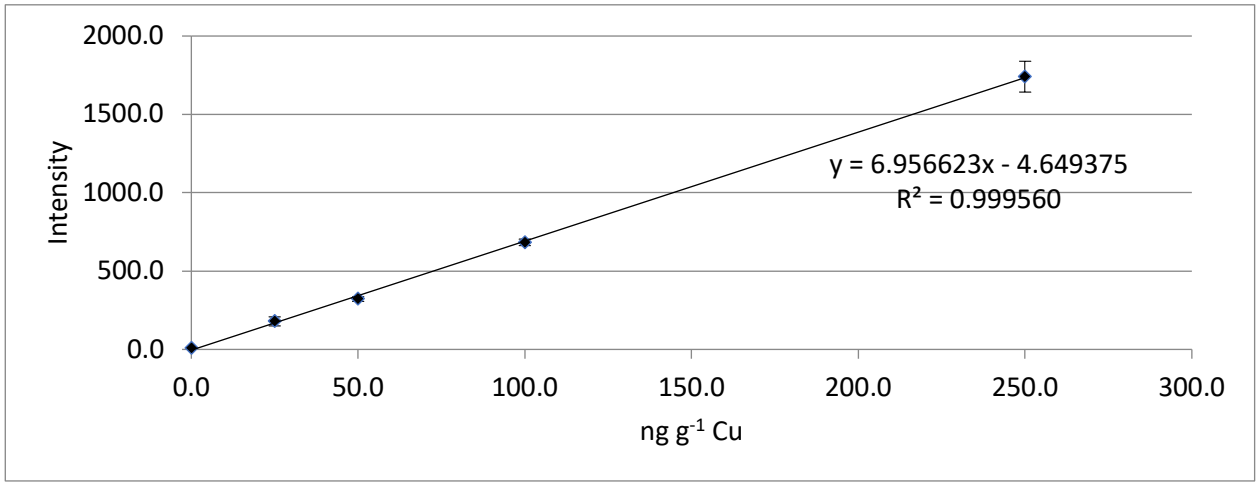

Figure 98. Calibration model for Hg in BCR SRM 1944, using MAE method; (n=3) at the 95% confidence level.

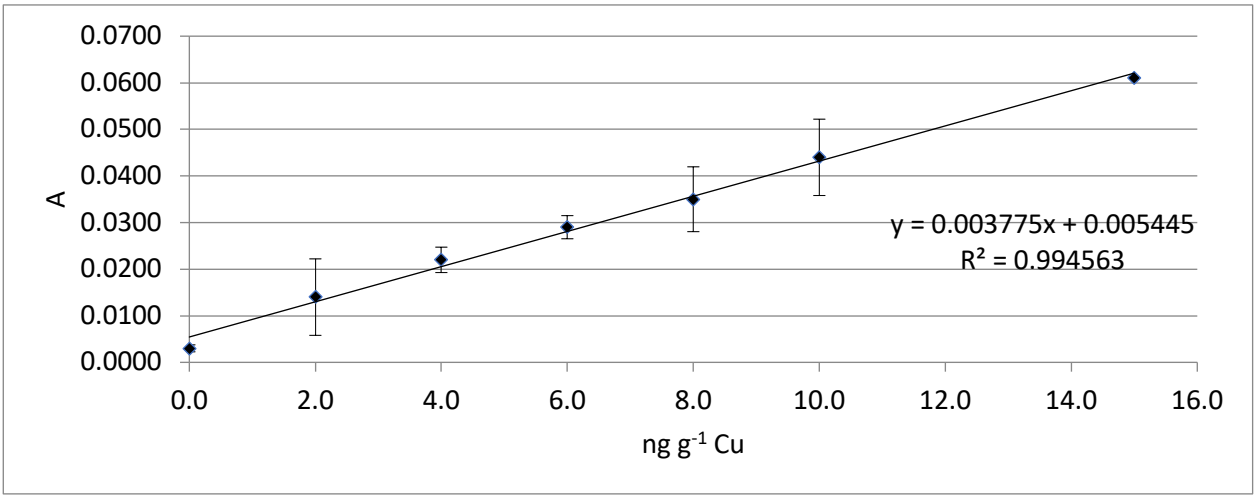


Figure 99. Calibration model for BCR SRM 701 (CO3-[Pb]) Conventional BCR extraction method; (n=3) at the 95% confidence level.

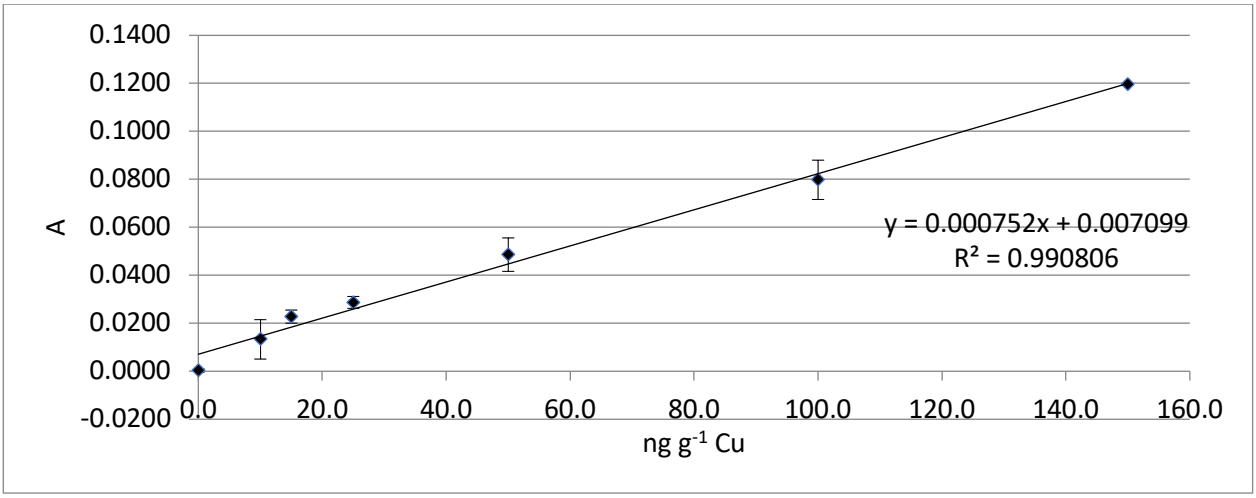


Figure 100. Calibration model for BCR SRM 701 (MOX-[Pb]) Conventional BCR extraction method; (n=3) at the 95% confidence level.

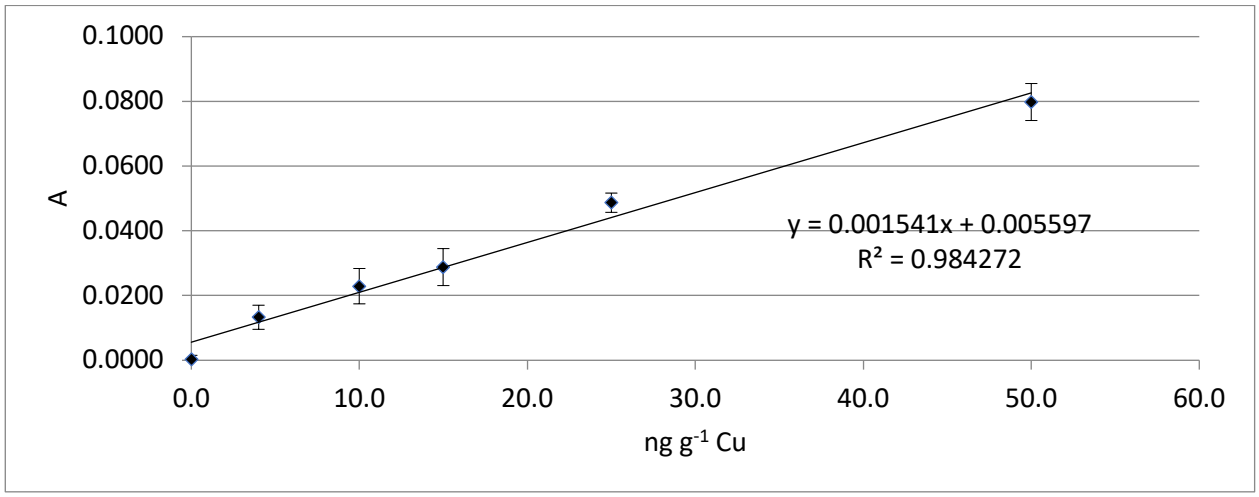


Figure 101. Calibration model for BCR SRM 701 (ORG-[Pb]) Conventional BCR extraction method; (n=3) at the 95% confidence level.

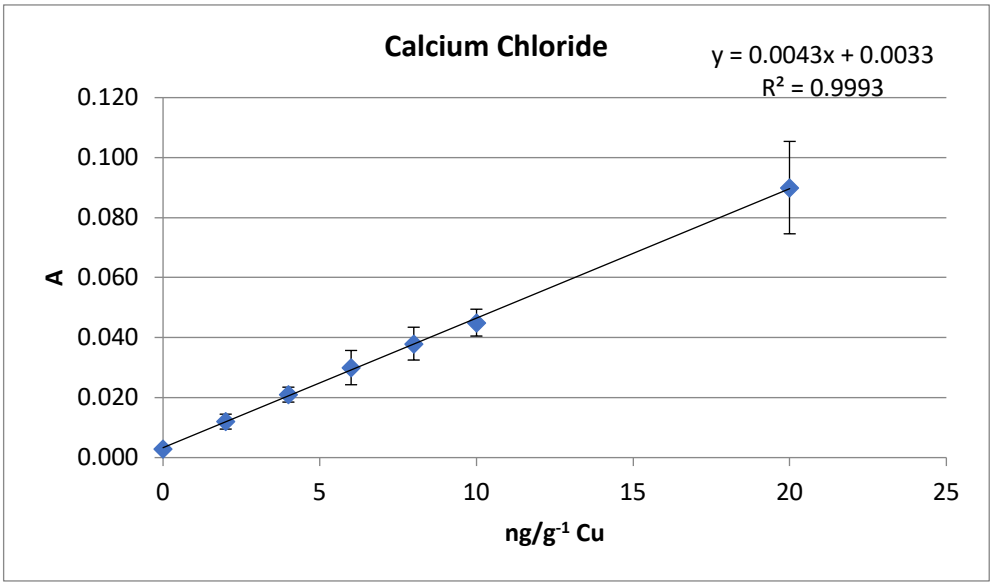


Figure 102. EXΔ-[Cu] calibration model for the soil core samples; (n=3) at the 95% confidence level.

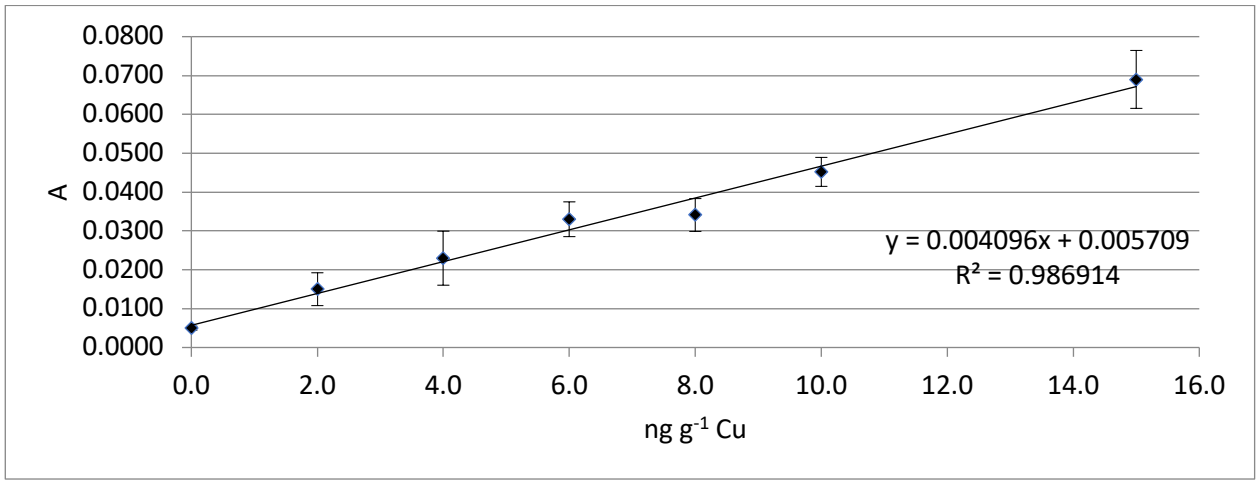


Figure 103. $CH_3COOH$ extraction of the CO3-[Cu] calibration model for soil core samples 13 and 30; (n=3) at the 95% confidence level.

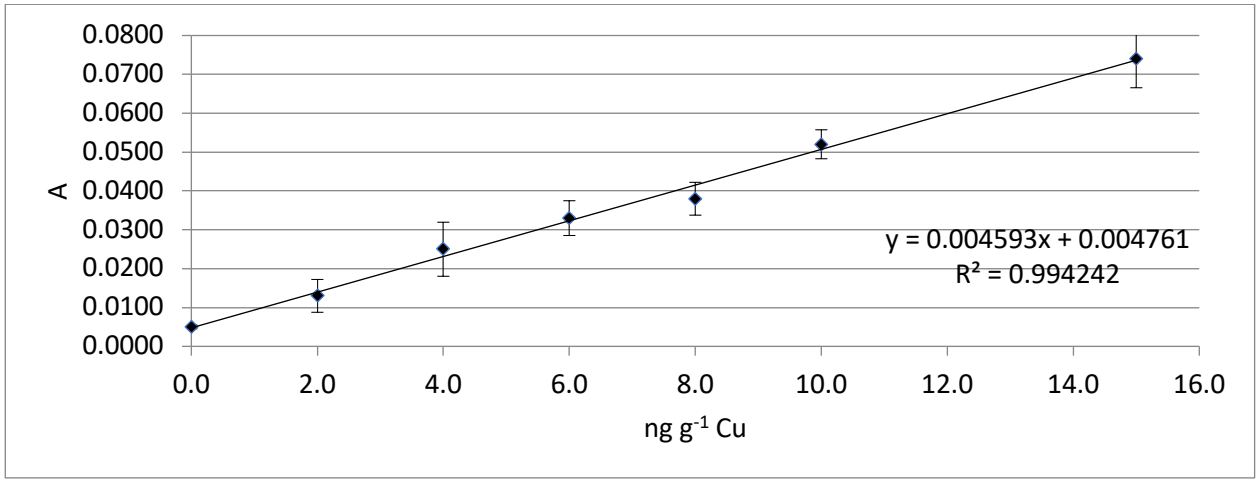


Figure 104. $CH_3COOH$ extraction of the CO3-[Cu] calibration model for soil core samples 4 and 28; (n=3) at the 95% confidence level.

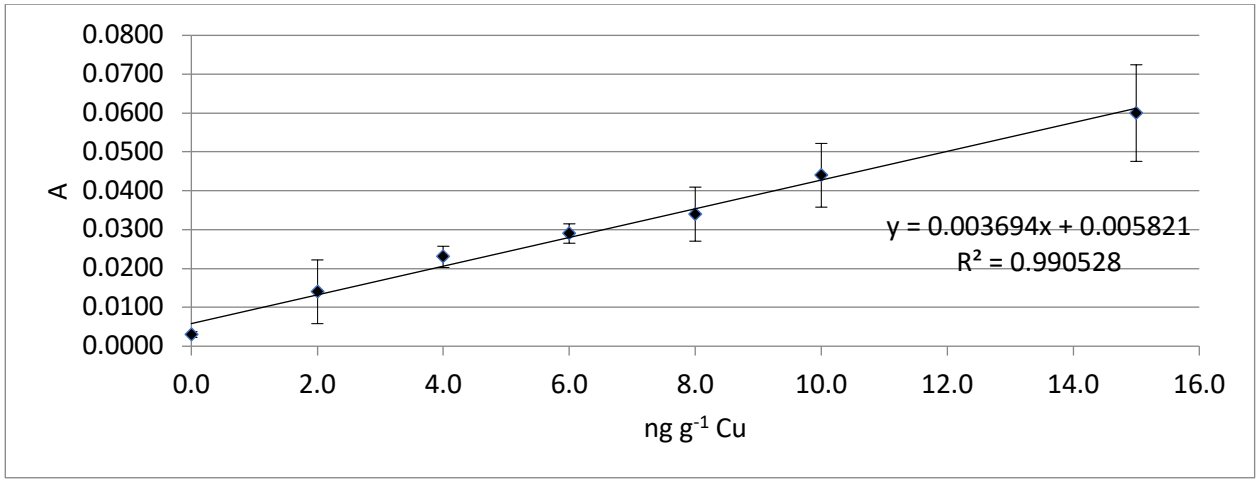

Figure 105. $CH_3COOH$ extraction of the CO3-[Cu] calibration model for soil core samples 22, 31, and 32; (n=3) at the 95% confidence level.

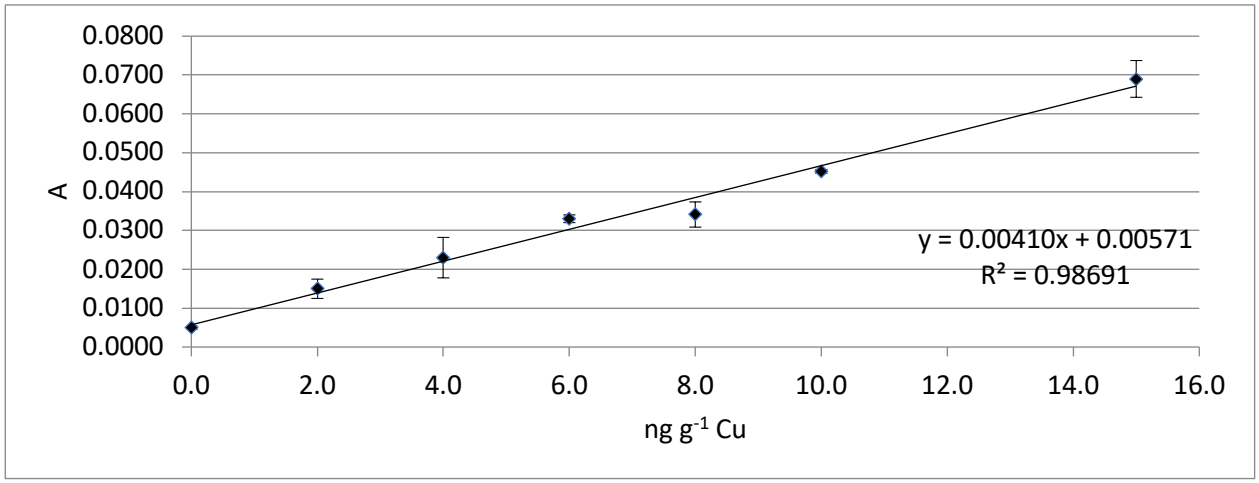


Figure 106. $CH_3COOH$ extraction of the CO3-[Cu] calibration model for soil core samples 9 and 21; (n=3) at the 95% confidence level.

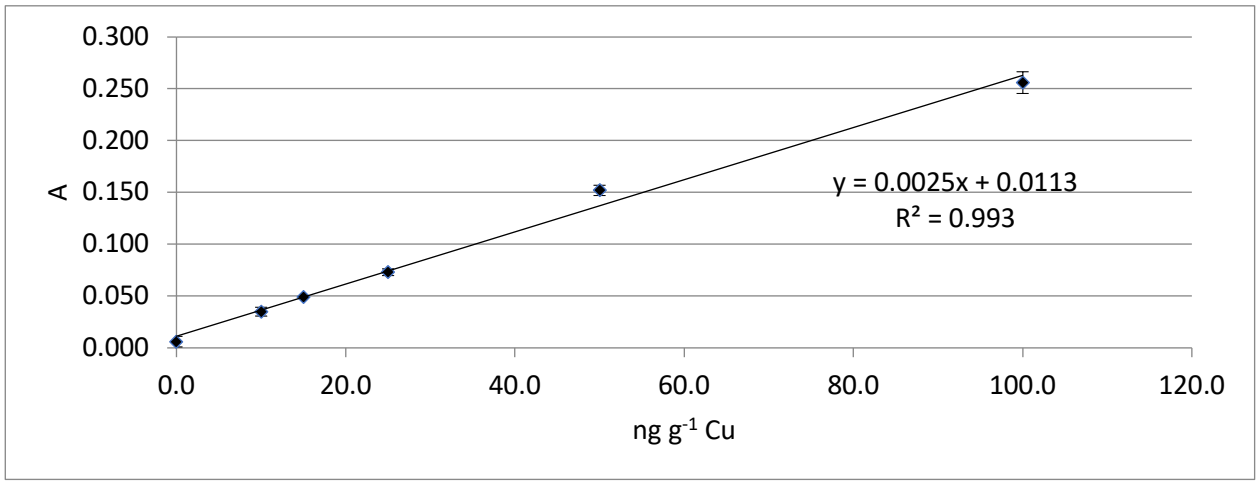


Figure 107. Hydroxylamine-Hydrochloride extraction of MOX-[Cu] calibration model for soil core samples 9 and 30; (n=3) at the 95% confidence level.

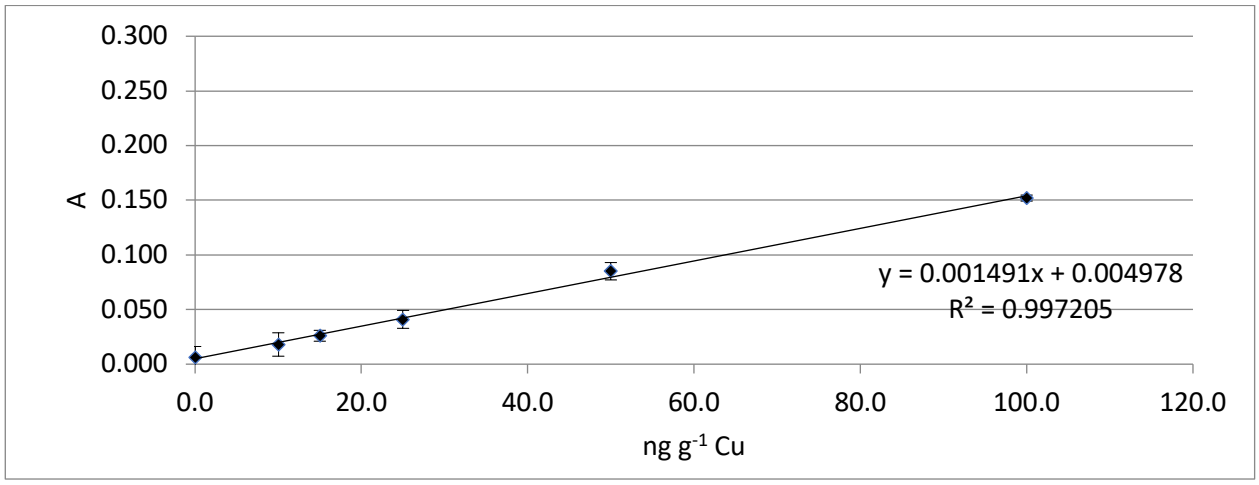


Figure 108. Hydroxylamine-Hydrochloride extraction of MOX-[Cu] calibration model for soil core samples 4; (n=3) at the 95% confidence level.

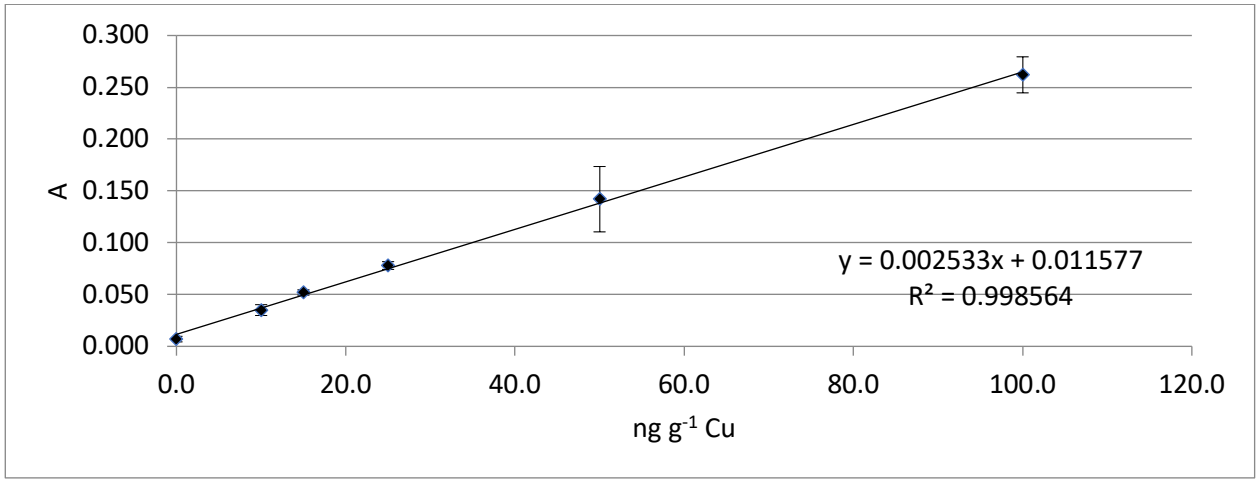


Figure 109. Hydroxylamine-Hydrochloride extraction of MOX-[Cu] calibration model for soil core samples 13; (n=3) at the 95% confidence level.

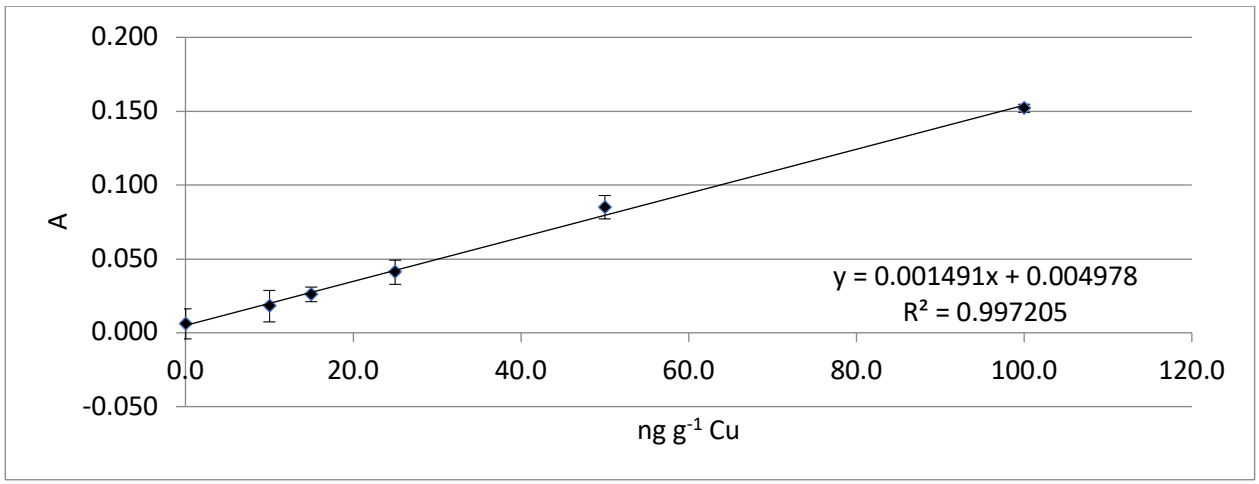

Figure 110. Hydroxylamine-Hydrochloride extraction of MOX-[Cu] calibration model for soil core samples 21; (n=3) at the 95% confidence level.

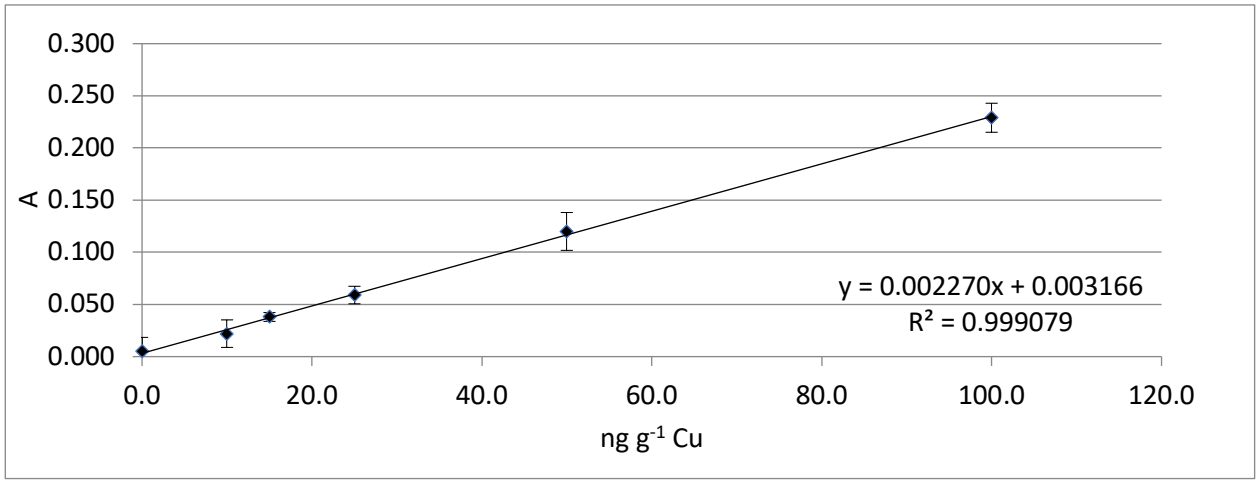


Figure 111. Hydroxylamine-Hydrochloride extraction of MOX-[Cu] calibration model for soil core samples 28; (n=3) at the 95% confidence level.

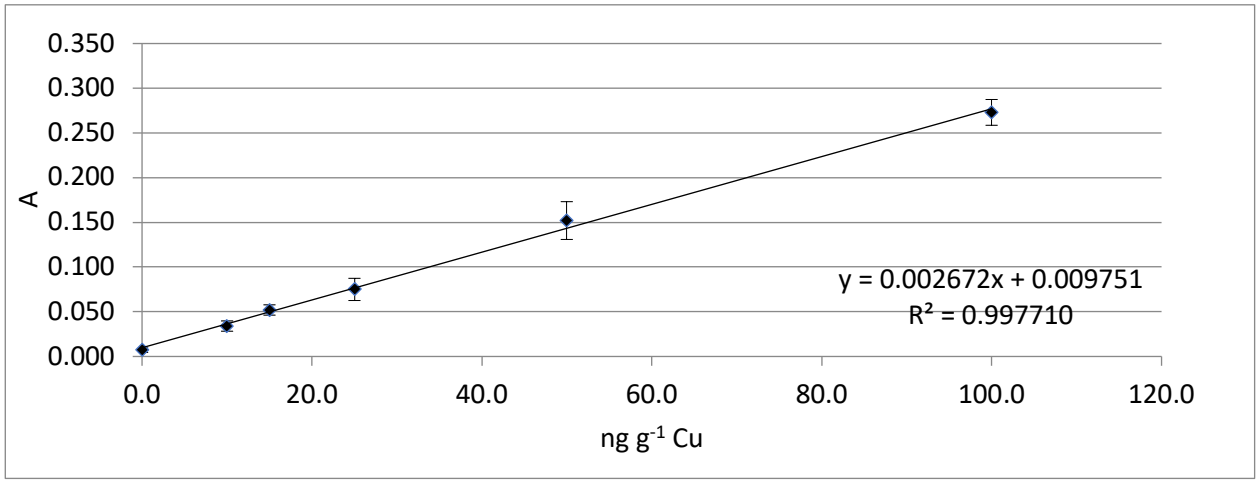


Figure 112. Hydroxylamine-Hydrochloride extraction of MOX-[Cu] calibration model for soil core samples 3 and 32; (n=3) at the 95% confidence level.

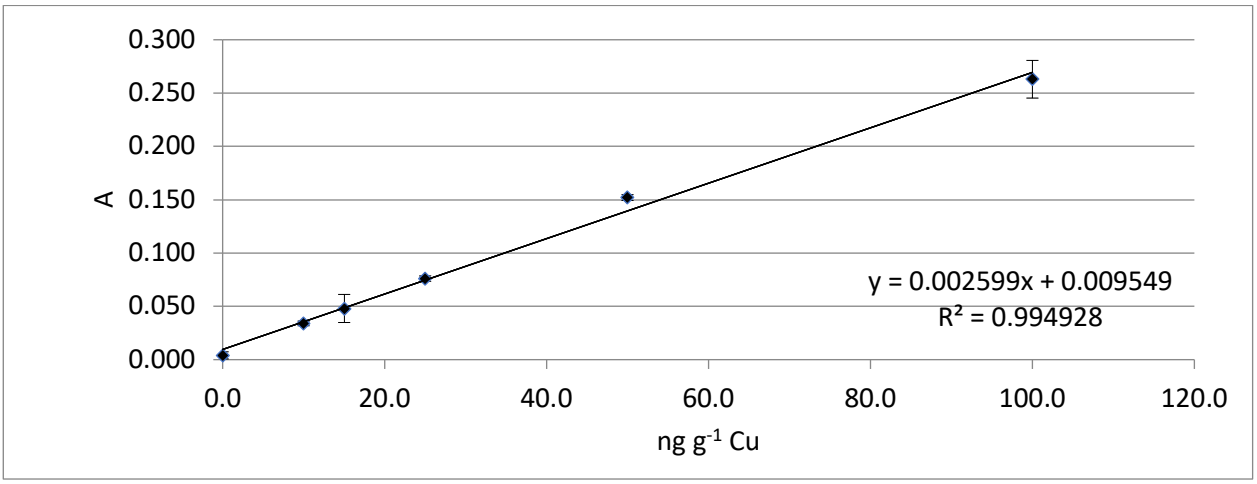


Figure 113. Hydroxylamine-Hydrochloride extraction of MOX-[Cu] calibration model for soil core samples 22; (n=3) at the 95% confidence level.

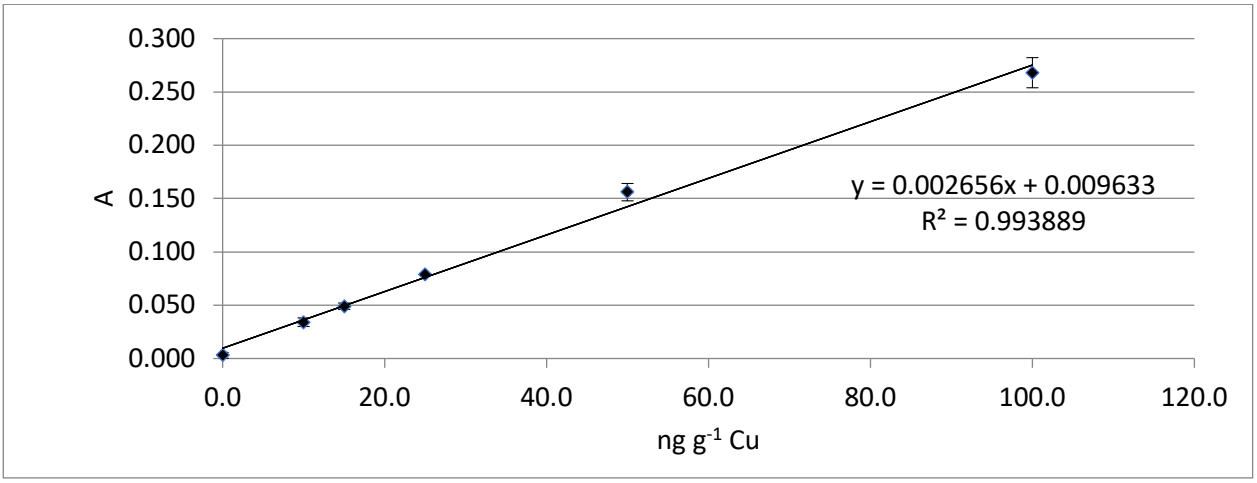


Figure 114. Hydroxylamine-Hydrochloride extraction of MOX-[Cu] calibration model for soil core samples 7; (n=3) at the 95% confidence level.

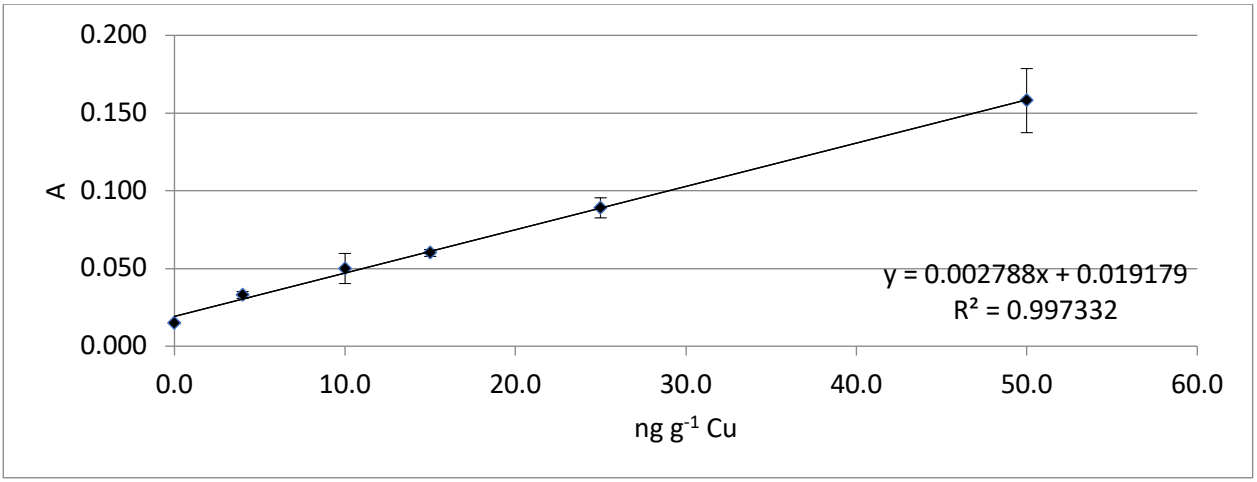

Figure 115. Hydrogen peroxide (oxidative) extraction ORG-[Cu] calibration model for soil samples 30; (n=3) at the 95% confidence level.

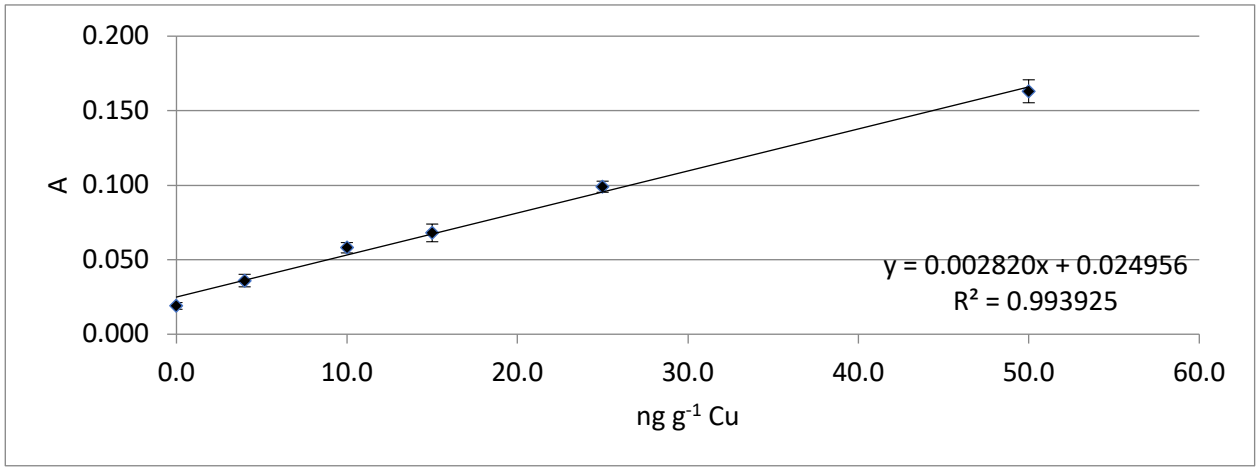


Figure 116. Hydrogen peroxide (oxidative) extraction of ORG-[Cu] calibration model for soil samples 4; (n=3) at the 95% confidence level.

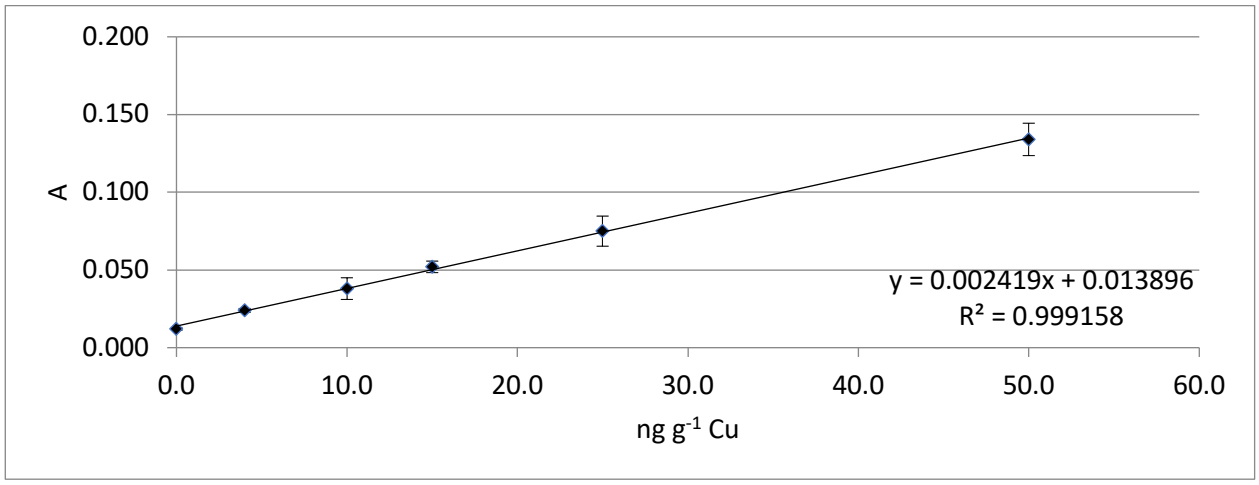


Figure 117. Hydrogen peroxide (oxidative) extraction of ORG-[Cu] calibration model for soil sample 31; (n=3) at the 95% confidence level.

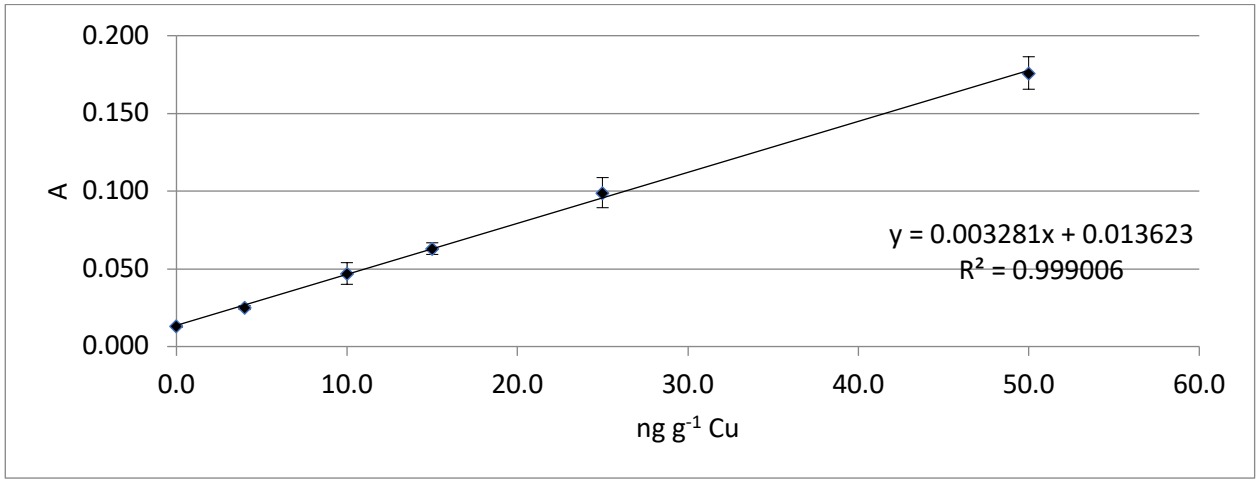


Figure 118. Hydrogen peroxide (oxidative) extraction of ORG-[Cu] calibration model for soil sample 32; (n=3) at the 95% confidence level.

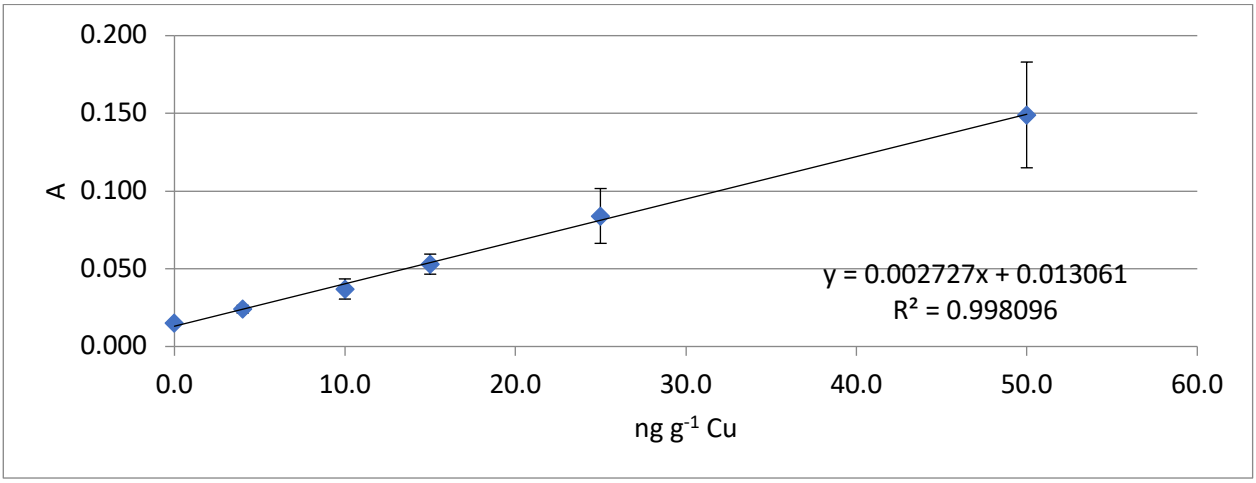


Figure 119. Hydrogen peroxide (oxidative) extraction of ORG-[Cu] calibration model for soil sample 9; (n=3) at the 95% confidence level.

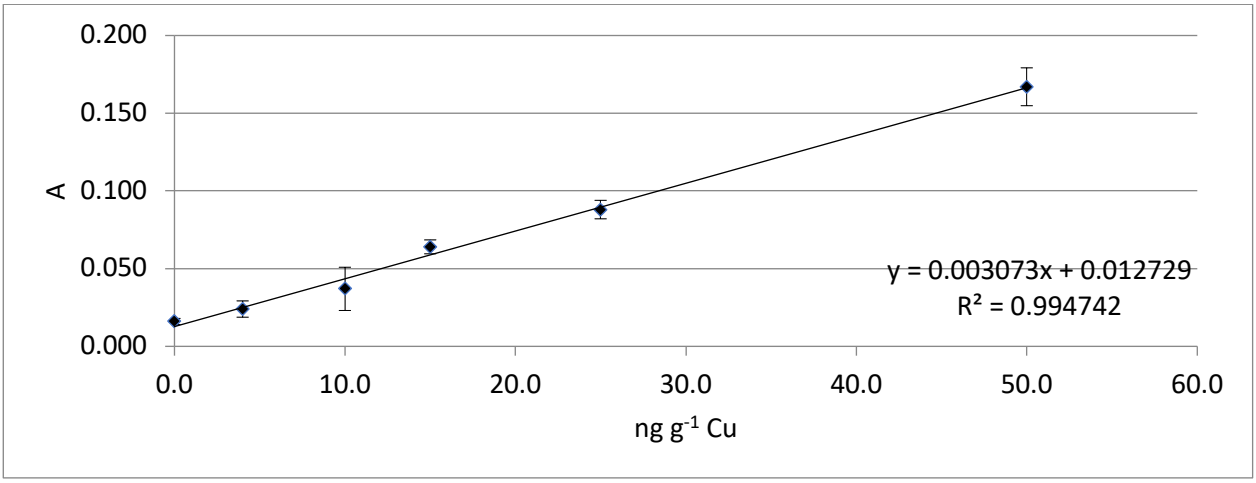


Figure 120. Hydrogen peroxide (oxidative) extraction of ORG-[Cu] calibration model for soil sample 13; (n=3) at the 95% confidence level.

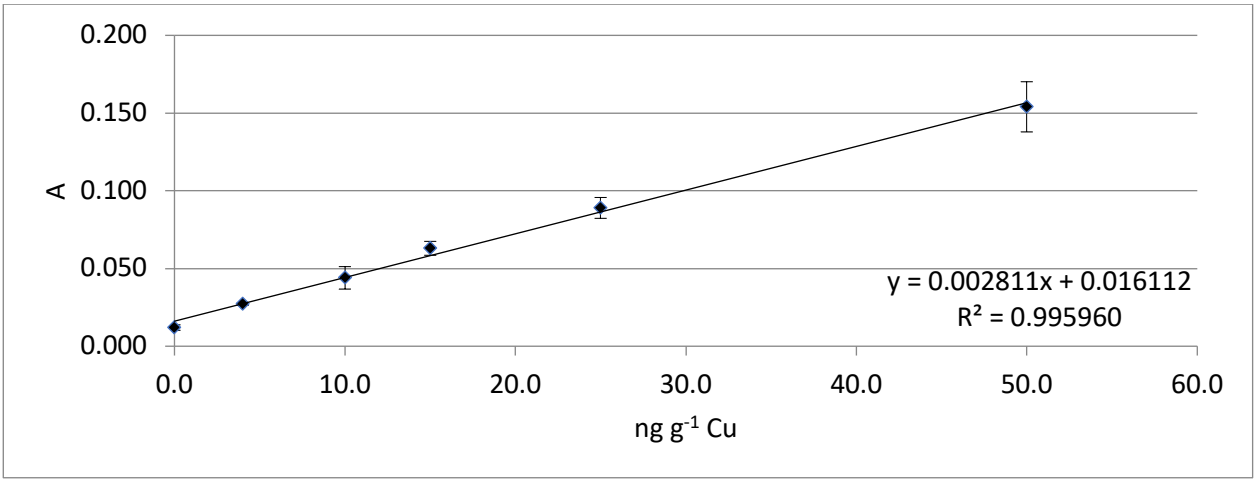

Figure 121. Hydrogen peroxide (oxidative) extraction of ORG-[Cu] calibration model for soil sample 28; (n=3) at the 95% confidence level.

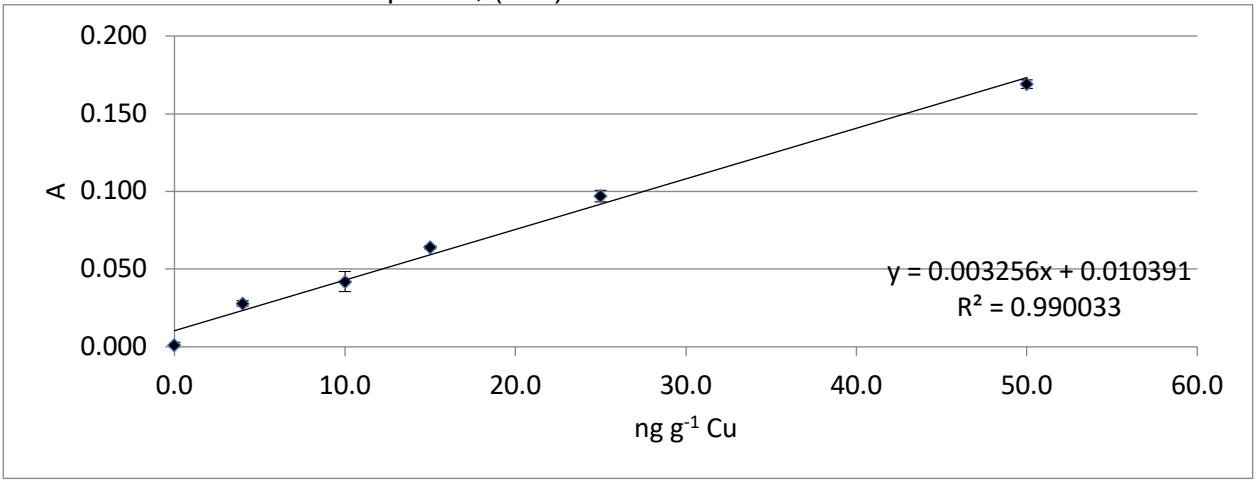


Figure 122. Hydrogen peroxide (oxidative) extraction of ORG-[Cu] calibration model for soil sample 22; (n=3) at the 95% confidence level.

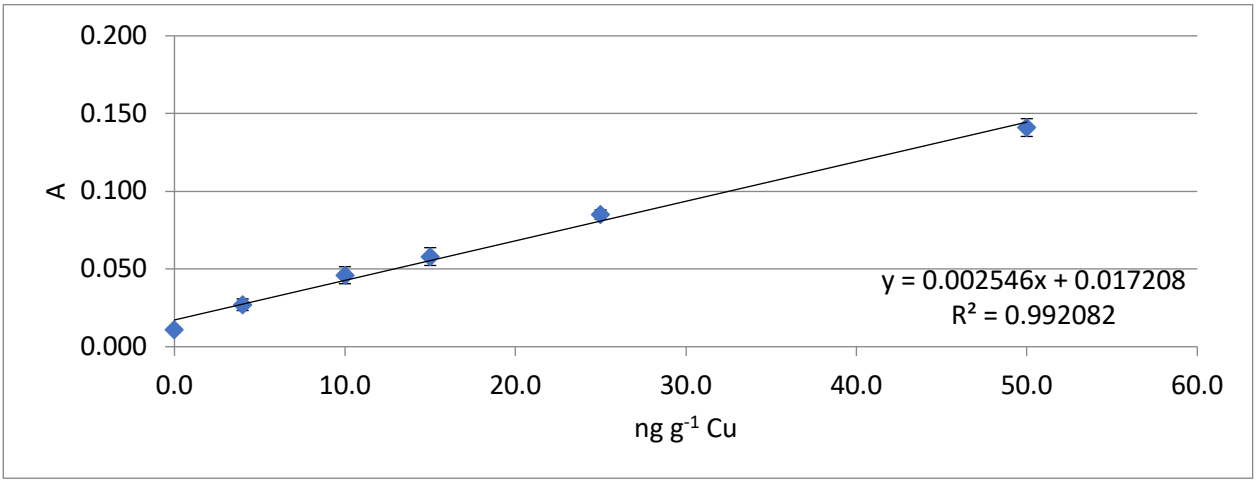


Figure 123. Hydrogen peroxide (oxidative) extraction of ORG-[Cu] calibration model for soil sample 7; (n=3) at the 95% confidence level.

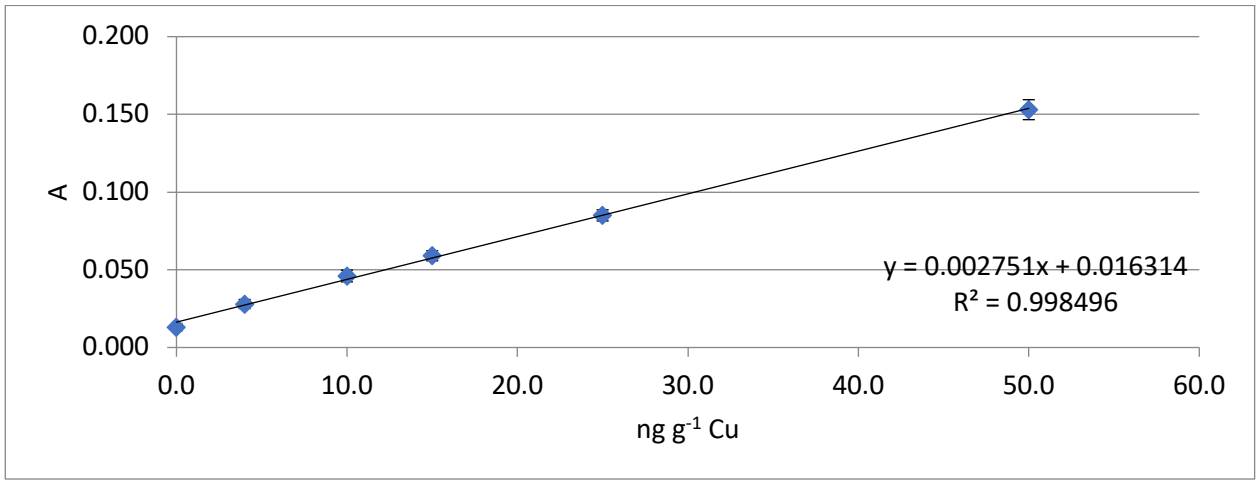


Figure 124. Hydrogen peroxide (oxidative) extraction of ORG-[Cu] calibration model for soil sample 21; (n=3) at the 95% confidence level.

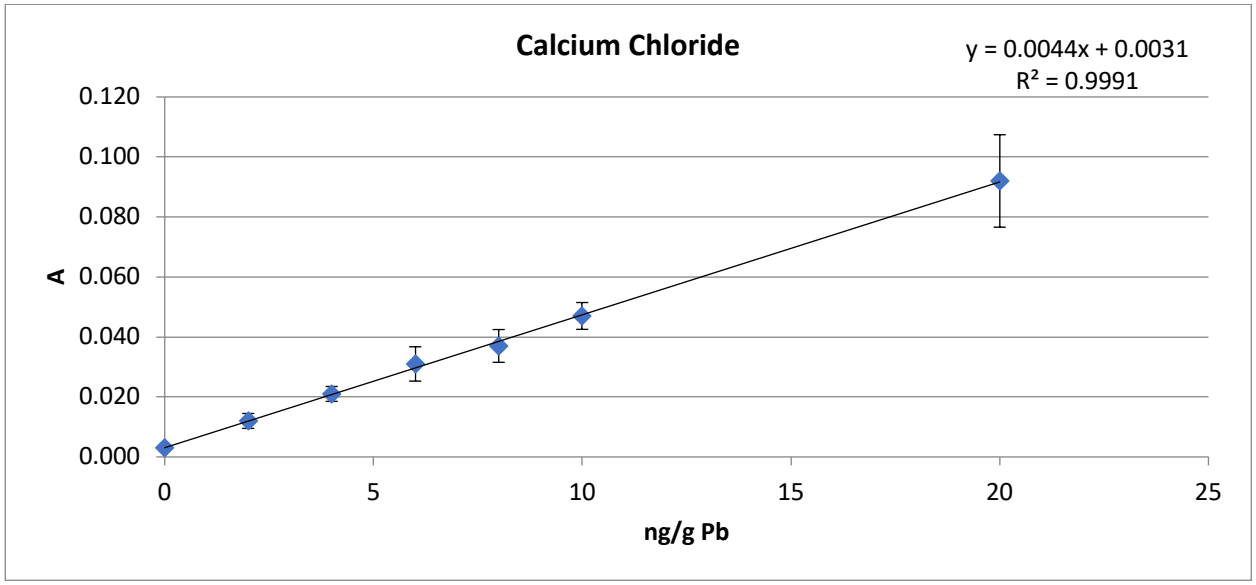


Figure 125. EXΔ-[Pb] calibration model for the soil core samples; (n=3) at the 95% confidence level.

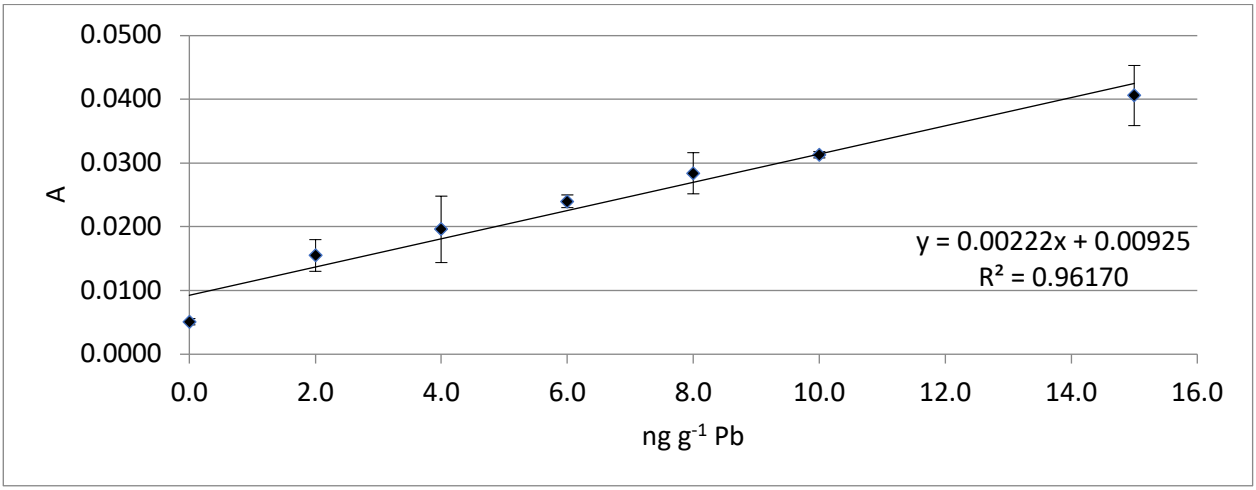


Figure 126. $CH_3COOH$ extraction of the CO3-[Pb] calibration model for soil core samples 21, 22, 23, 24; (n=3) at the 95% confidence level.

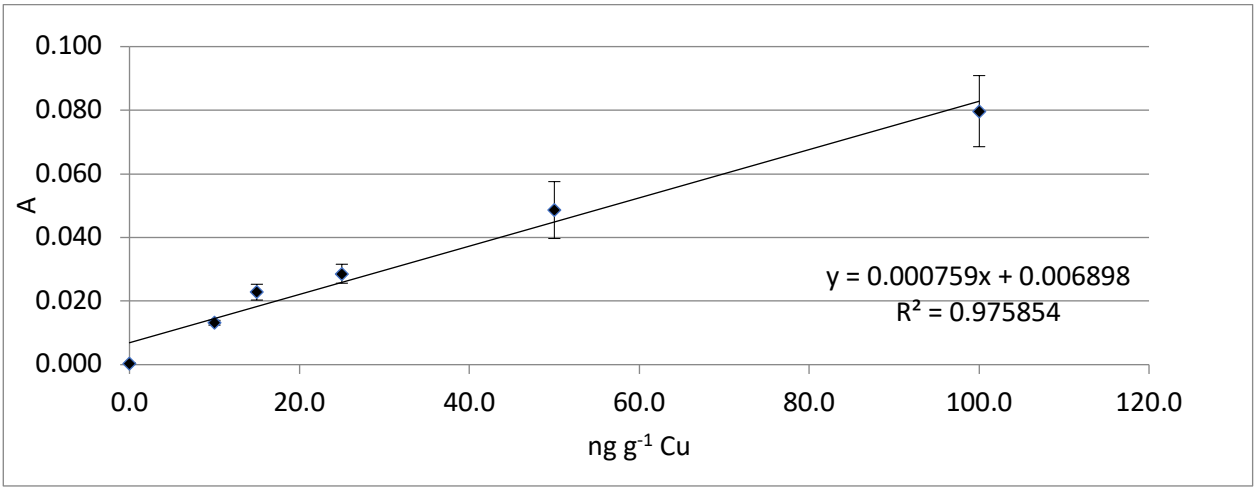


Figure 127. Hydroxylamine-Hydrochloride extraction of MOX-[Pb] calibration model for soil core samples 21, 22, 23, 24; (n=3) at the 95% confidence level.

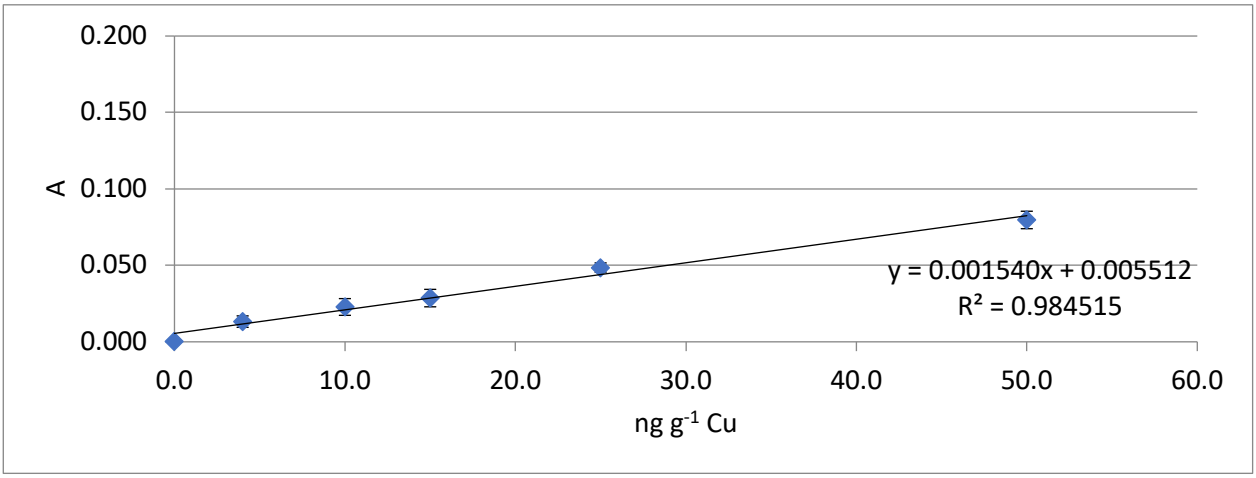

Figure 128. Hydrogen peroxide (oxidative) extraction of ORG-[Pb] calibration model for soil sample 21, 22, 23, 24; (n=3) at the 95% confidence level.

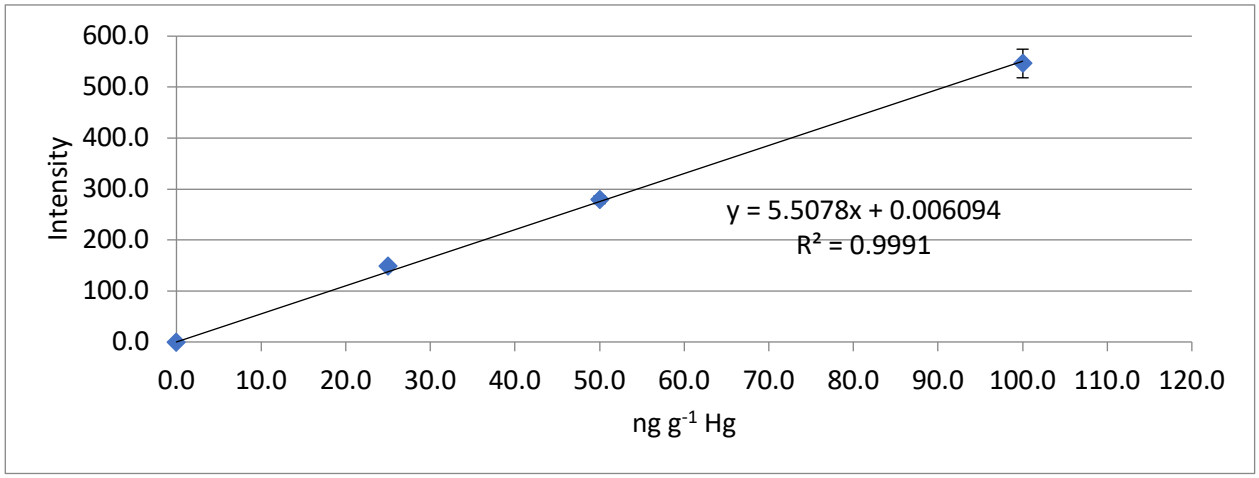


Figure 129. Hg calibration model for soil samples 2, 6, 21; (n=3) at the 95% confidence level.

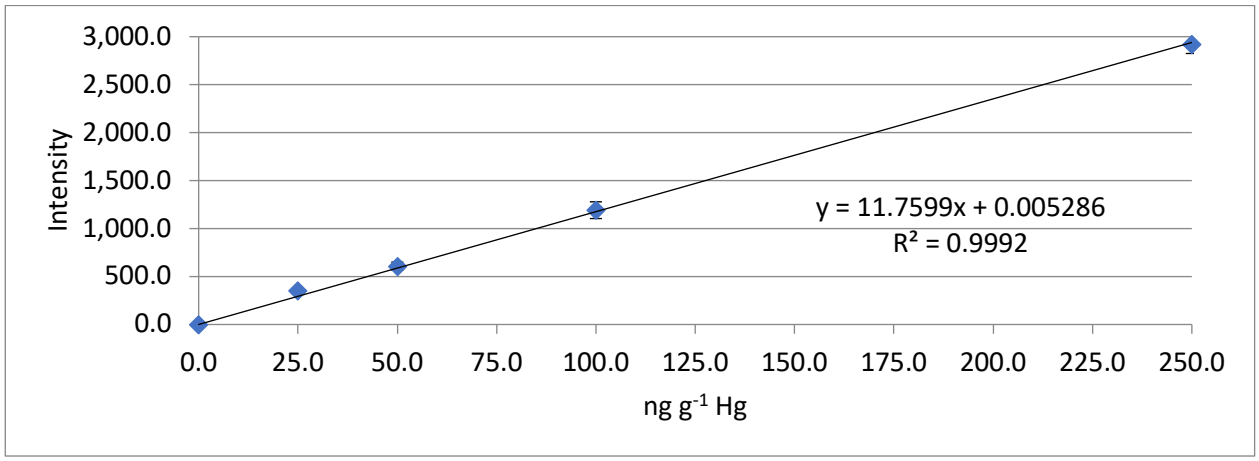


Figure 130. Hg calibration model for soil sample 2, for MAE BCR method; (n=3) at the 95% confidence level.

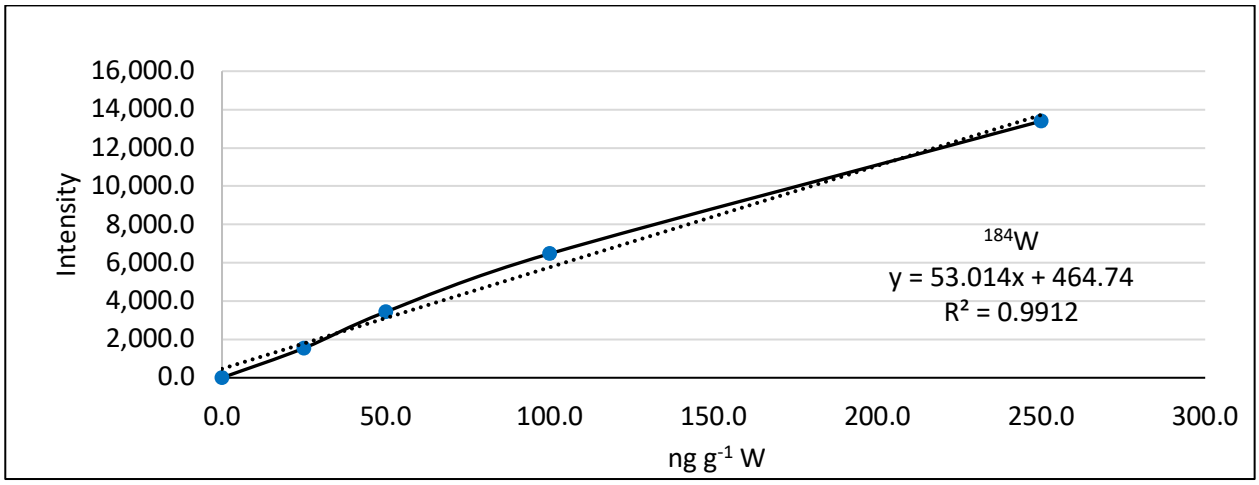


Figure 131. Calibration model for $^{184}W$ isotope in the range from 25-250 ppb. Analyzed from 50-238 m/z, using the quantitative method for ICP-MS; (n=3) at the 95% confidence level.

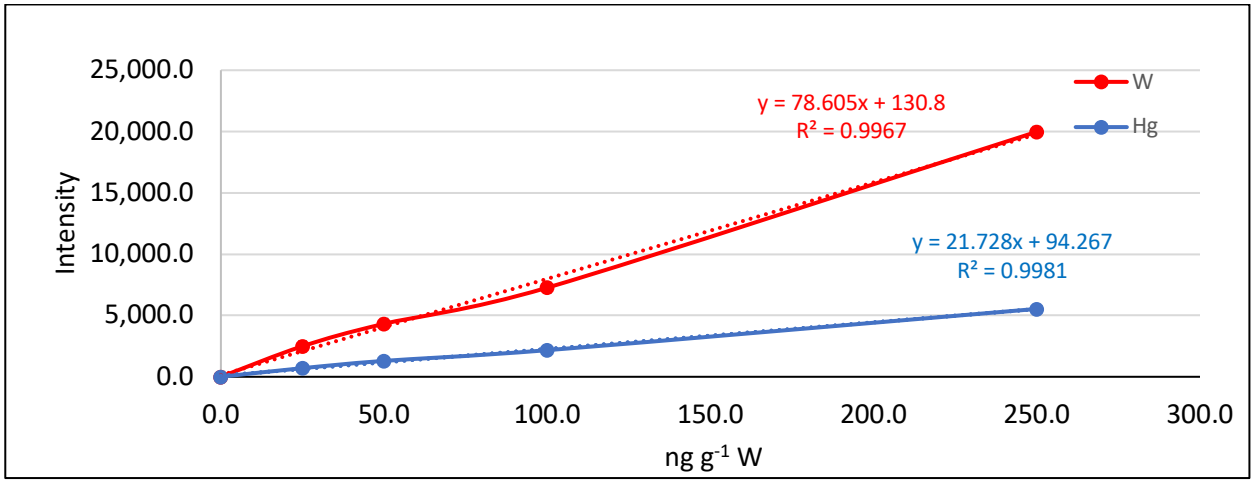


Figure 132. Calibration model for W and Hg in the range from 25-250 ppb. Analyzed from 50-238 m/z, using the quantitative method for ICP-MS; (n=3) at the 95% confidence level.

# APPENDIX C: Mass Spectra

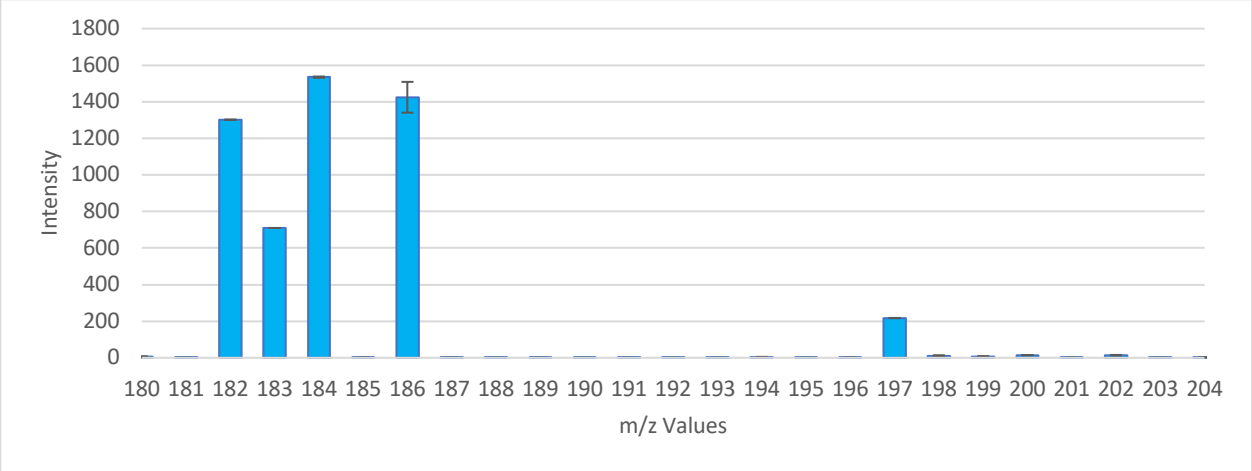


Figure 133. 25 ppb W standard, analyzed from 50-238 m/z, using the quantitative method for ICP-MS. The mass spectrum is focused on the range of interest for WO interferences, from 180-204 m/z to confirm that no WO interferances are present; (n=3) at the 95% confidence level.

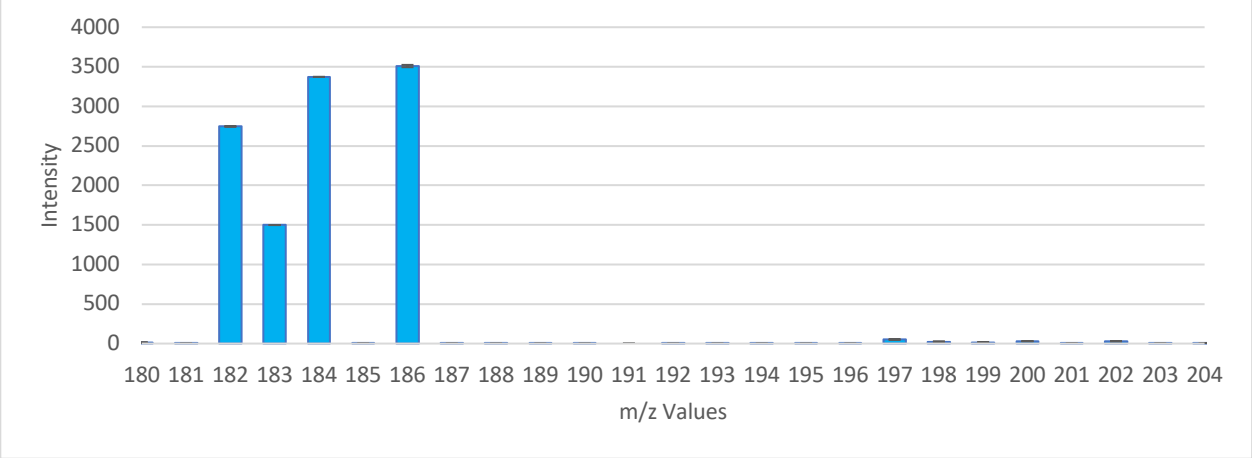


Figure 134. 50 ppb W standard, analyzed from 50-238 m/z, using the quantitative method for ICP-MS. The mass spectrum is focused on the range of interest for WO interferences, from 180-204 m/z to confirm that no WO interferances are present; (n=3) at the 95% confidence level.

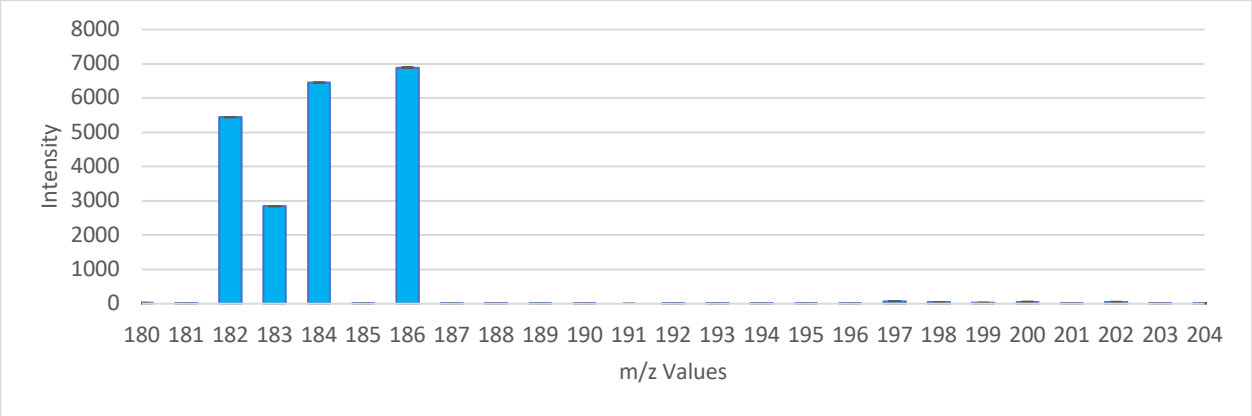

Figure 135. 100 ppb W standard, analyzed from 50-238 m/z, using the quantitative method for ICP-MS. The mass spectrum is focused on the range of interest for WO interferences, from 180-204 m/z to confirm that no WO interferances are present; (n=3) at the 95% confidence level.

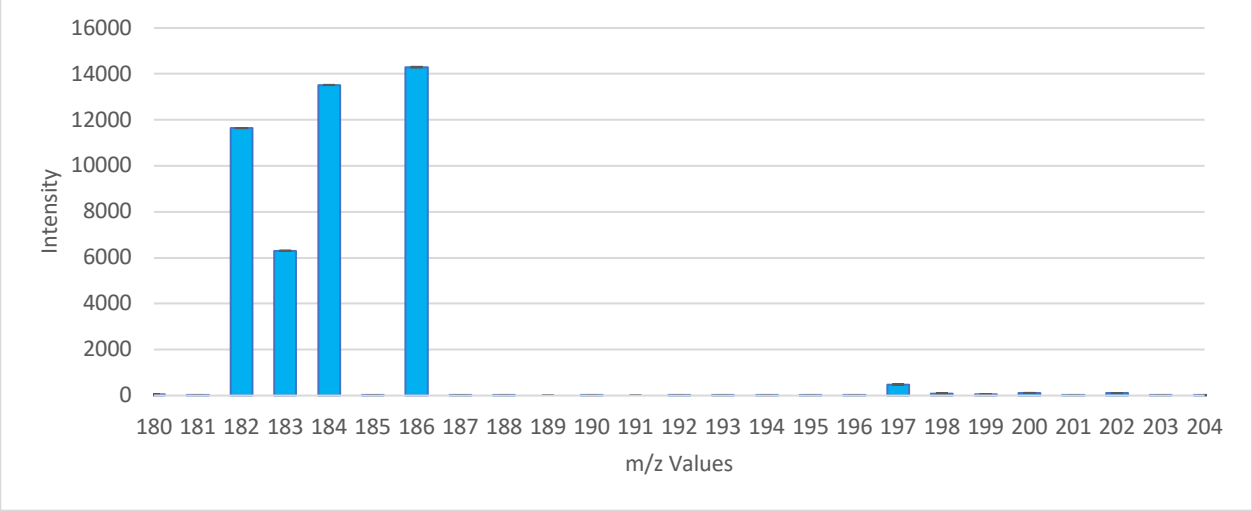


Figure 136. 250 ppb W standard, analyzed from 50-238 m/z, using the quantitative method for ICP-MS. The mass spectrum is focused on the range of interest for WO interferences, from 180-204 m/z to confirm that no WO interferances are present; (n=3) at the 95% confidence level.

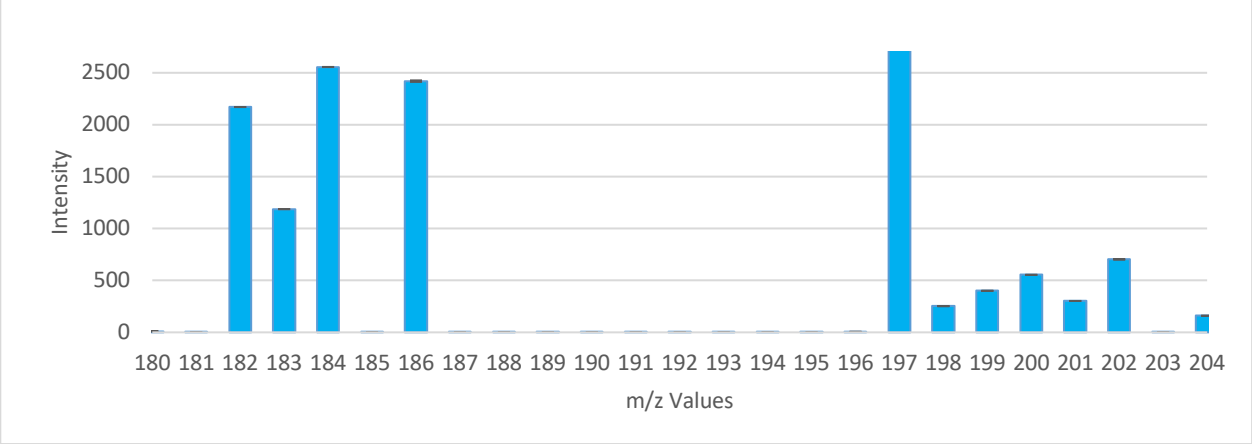


Figure 137. 25 ppb W and Hg standard analyzed from 50-238 m/z, using the quantitative method for ICP-MS. The mass spectrum is focused on the range of interest for W and Hg, from 180-204 m/z to confirm the isotpoic fingerprints and also to confirm that no WO interferances are present; (n=3) at the 95% confidence level.

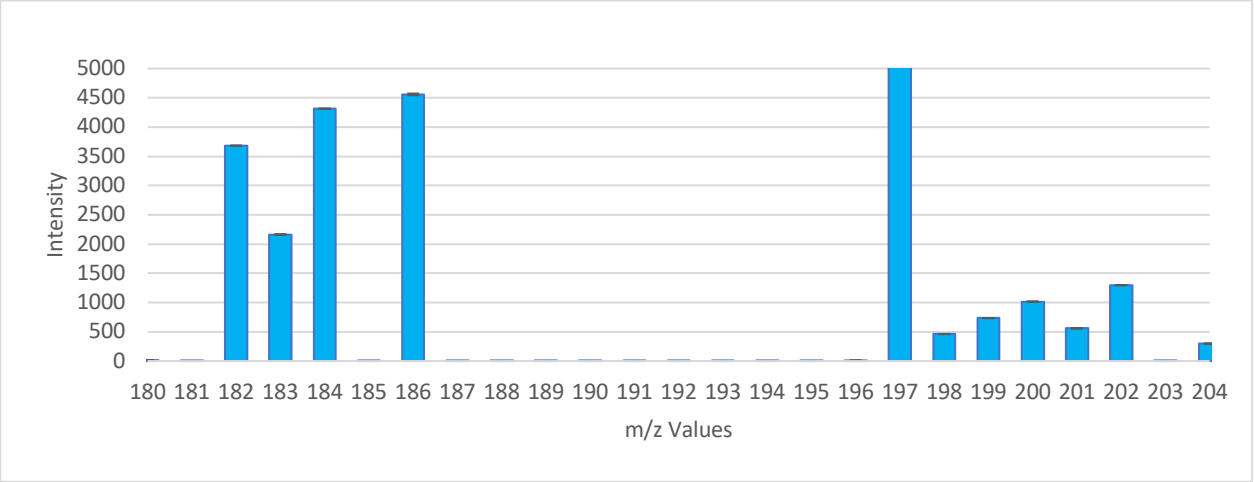


Figure 138. 50 ppb W and Hg standard analyzed from 50-238 m/z, using the quantitative method for ICP-MS. The mass spectrum is focused on the range of interest for W and Hg, from 180-204 m/z to confirm the isotpoic fingerprints and also to confirm that no WO interferances are present; (n=3) at the 95% confidence level.

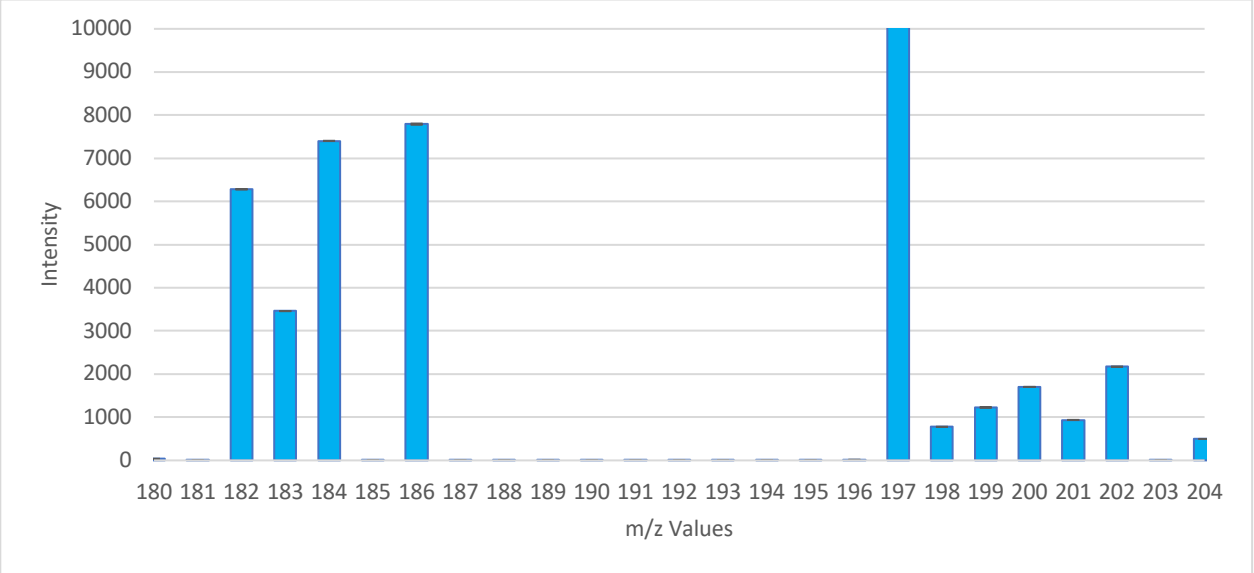


Figure 139. 100 ppb W and Hg standard analyzed from 50-238 m/z, using the quantitative method for ICP-MS. The mass spectrum is focused on the range of interest for W and Hg, from 180-204 m/z to confirm the isotpoic fingerprints and also to confirm that no WO interferances are present; (n=3) at the 95% confidence level.

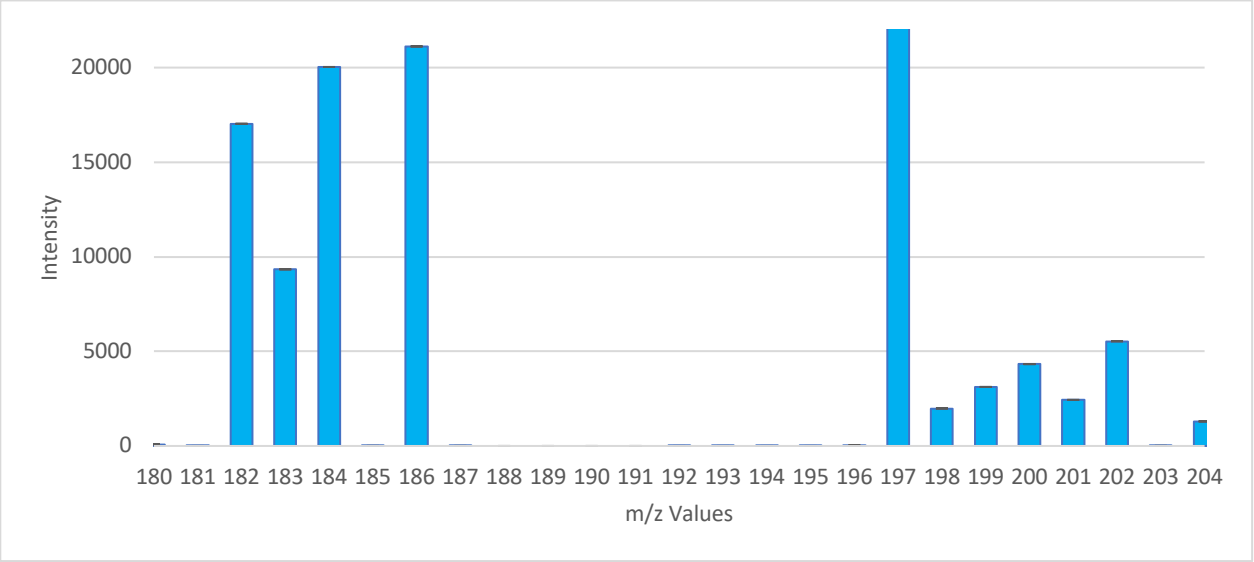


Figure 140. 250 ppb W and Hg standard analyzed from 50-238 m/z, using the quantitative method for ICP-MS. The mass spectrum is focused on the range of interest for W and Hg, from 180-204 m/z to confirm the isotpoic fingerprints and also to confirm that no WO interferances are present; (n=3) at the 95% confidence level.

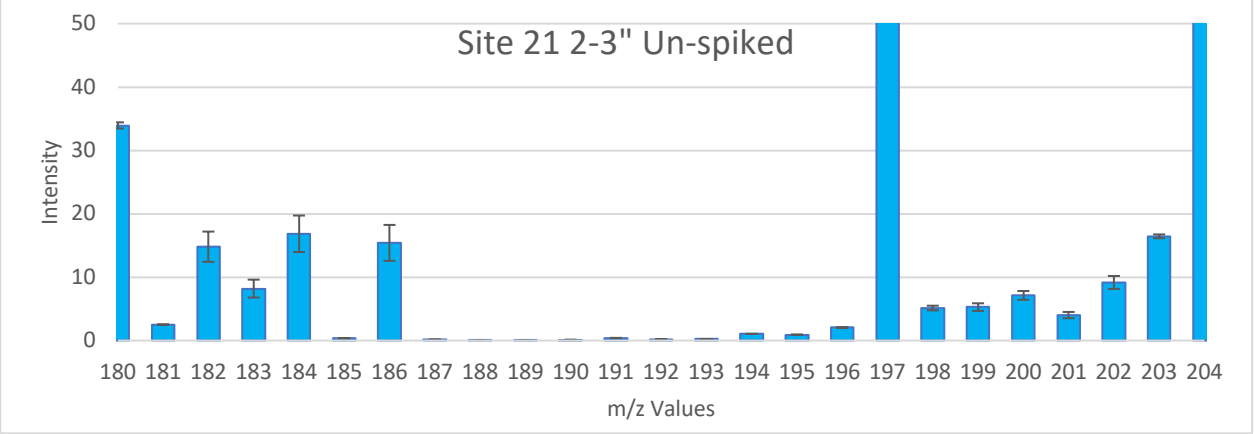


Figure 141. Mass spectrum for Site 21 of the un-spiked sample, analyzed from 50-238 m/z, using the quantitative method for ICP-MS. The mass spectrum is focused on the range of interest for W and Hg, from 180-204 m/z to investigate if WO interfernces are present; (n=3) at the 95% confidence level.

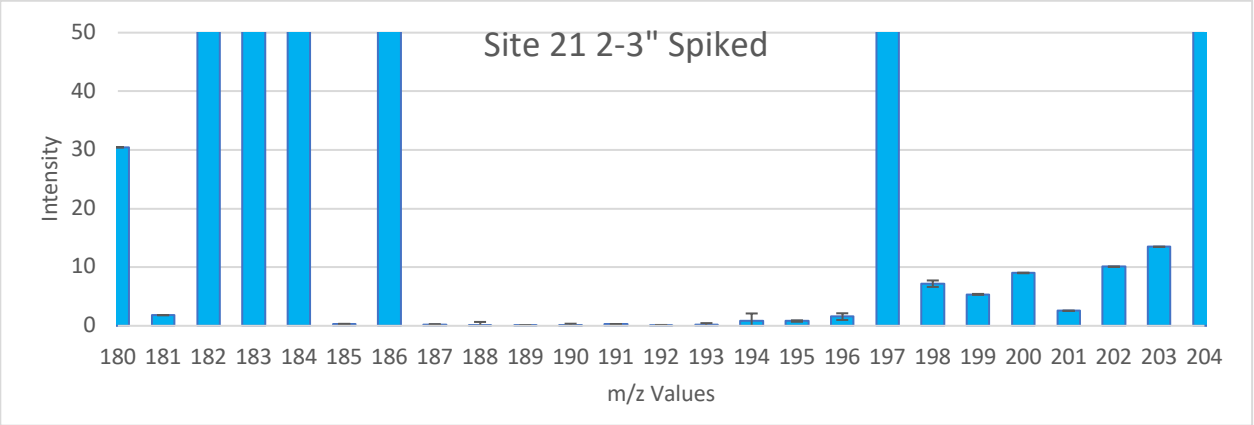

Figure 142. Mass spectrum for 21 of the spiked sample, analyzed from 50-238 m/z, using the quantitative method for ICP-MS. The mass spectrum is focused on the range of interest for W and Hg, from 180-204 m/z to investigate if WO interfernces are present; (n=3) at the 95% confidence level.

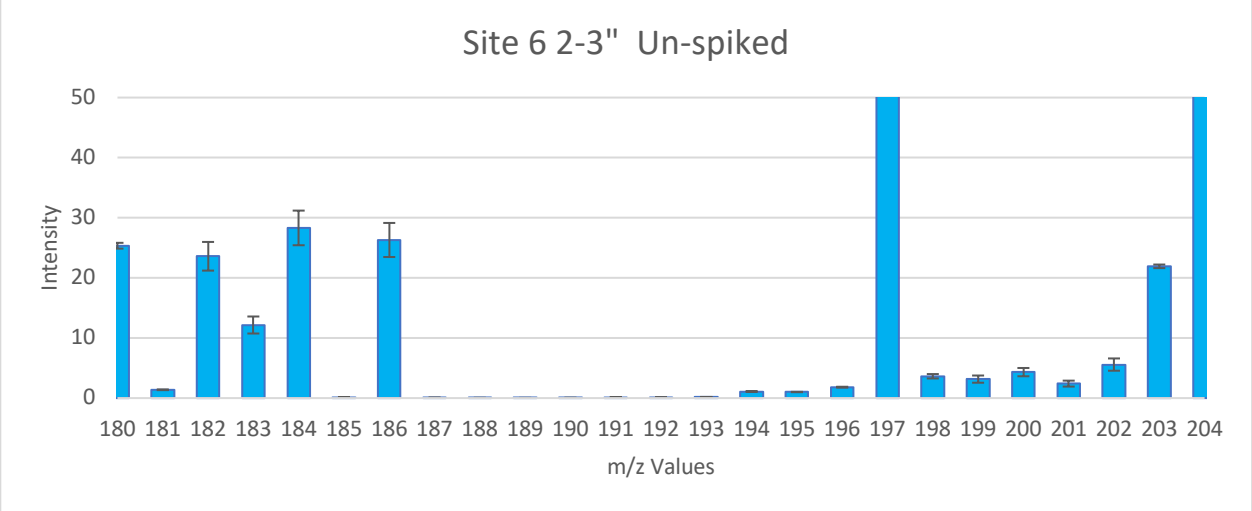


Figure 143. Mass spectrum for Site 6 of the un-spiked sample, analyzed from 50-238 m/z, using the quantitative method for ICP-MS. The mass spectrum is focused on the range of interest for W and Hg, from 180-204 m/z to investigate if WO interfernces are present; (n=3) at the 95% confidence level.

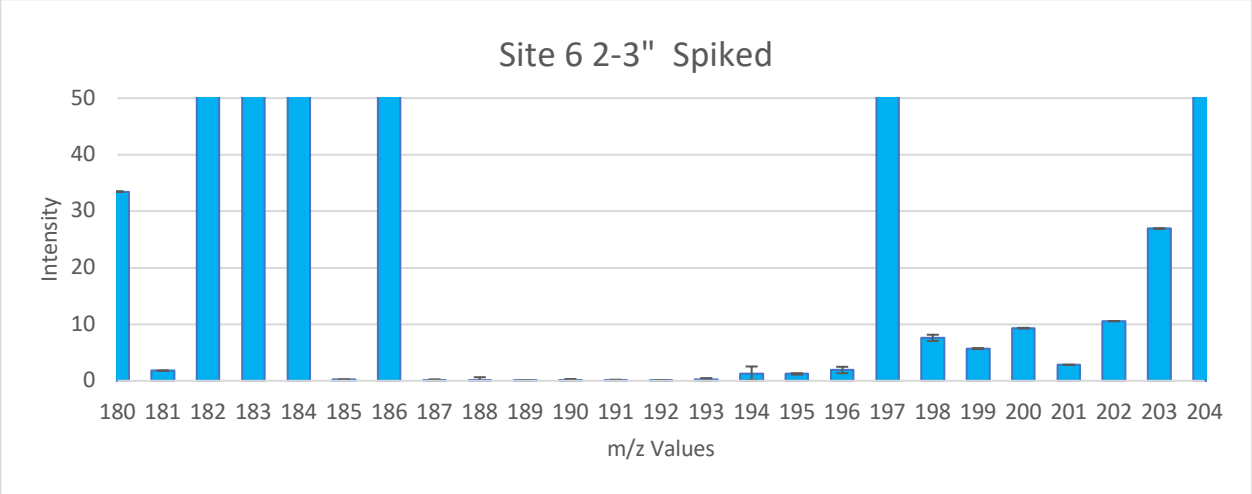


Figure 144. Mass spectrum for Site 6 of the spiked sample, analyzed from 50-238 m/z, using the quantitative method for ICP-MS. The mass spectrum is focused on the range of interest for W and Hg, from 180-204 m/z to investigate if WO interfernces are present; (n=3) at the 95% confidence level.

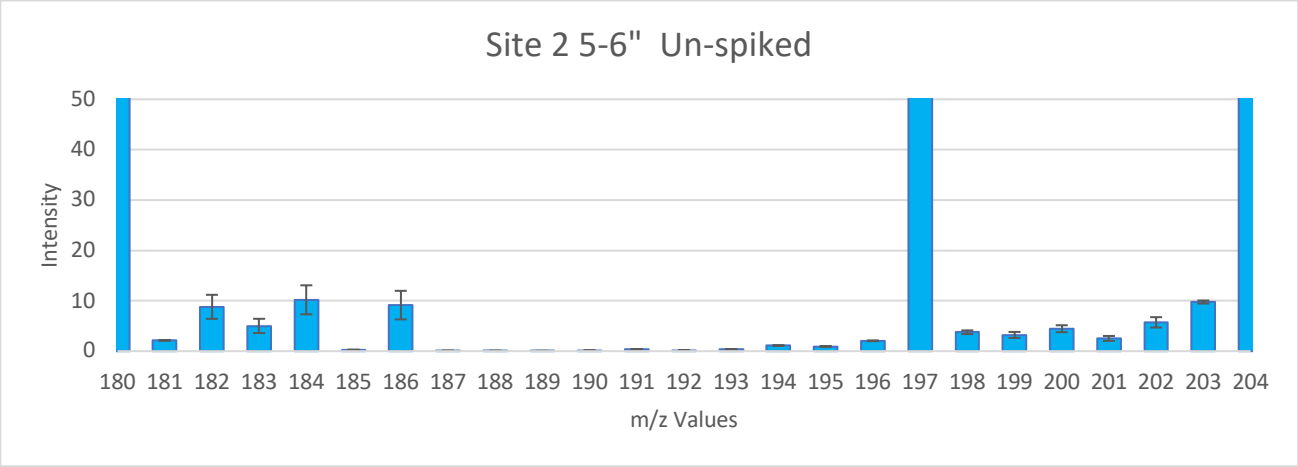


Figure 145. Mass spectrum for Site 2 of the un-spiked sample, analyzed from 50-238 m/z, using the quantitative method for ICP-MS. The mass spectrum is focused on the range of interest for W and Hg, from 180-204 m/z to investigate if WO interfernces are present; (n=3) at the 95% confidence level.

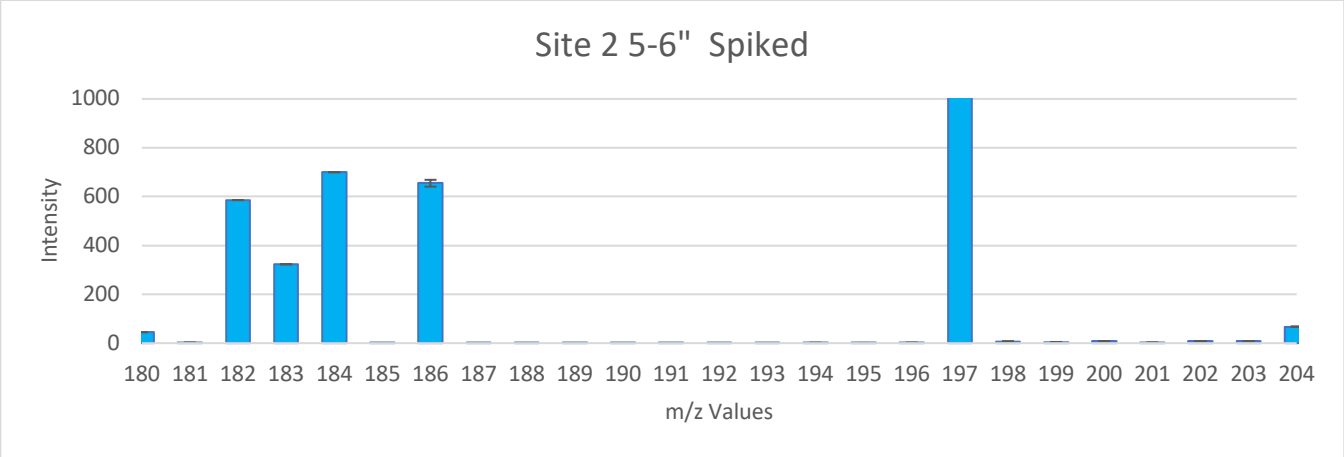


Figure 146. Mass spectrum for Site 2 of the spiked sample, analyzed from 50-238 m/z, using the quantitative method for ICP-MS. The mass spectrum is focused on the range of interest for W and Hg, from 180-204 m/z to investigate if WO interfernces are present; (n=3) at the 95% confidence level.

## APPENDIX D: Deposition Velocities

Table 47. Comparison of deposition velocities for the soil cores. Shown are the radiometrically dated cores and their depositional velocities, as well as the selected rate used for Pb and Cu to determine the age of the soil fractions determined by depth and location of the sampling site.

| Radiometric Distance (m) | Radiometric Site (yr/cm) | Pb Site | Pb Distance (m) | Pb Distance Δ (m) | Cu Site | Cu Distance (m) | Cu Distance Δ (m) |
|---|---|---|---|---|---|---|---|
| 13.7 | 2004-06B/8.64 | 9B, 7B, 5A | 0, 9.1, 18.3 | 13.7, 4.6, 4.6 | 9B, 7A | 0, 9.1 | 13.7, 4.6 |
| 36.6 | 2004-14AB/10.86, 2007-14E/11.25 | 2B, 3A | 36.6, 27.4 | 0, 9.2 | 30A, 4A, 31A | 32.5, 22.9, 34.3 | 4.1, 13.7, 2.3 |
| 45.7 | 2004-1B/6.63 | 15A, 16B, 17A | 45.7, 54.9, 64 | 0, 9.2, 18.3 | 32B | 38.9 | 6.8 |
| Background | 2004-11AB/10.71 | 21A, 22A, 23A, 24A | 100.6, 109.7, 118.9, 128 | 899.4, 890.3, 881.1, 872 | 21A, 22A | 100.6, 109.7 | 899.4, 890.3 |
| Background | 2004-10AB/13.69 | N/A[1] | N/A[1] | N/A[1] | 13B, 28E | 1000, 1000 | 0,0 |
| Background | 2007-28AC/4.98 | N/A[1] | N/A[1] | N/A[1] | N/A[2] | N/A[2] | N/A[2] |

[1]This core was not used for Pb.
[2]This core was not used for Cu.

## APPENDIX E: Figures of Merit

A summary of calibration model parameters for each BCR extraction medium is shown in Table 48. The limit of detection (MDL) for each BCR extraction medium was defined as three times the standard deviation of the blank measurements (99.3% confidence level). The relative standard deviation (RSD) values shown in Table 48 are the average for all of the replicates (n).

Ideally, a Gaussian distribution is formed from experimental data symmetrically cluster about an average value. For example, 68.3% of the measurements will lie within ±1σ of the mean value (μ). Laboratory measurements are normally repeated 3-5 times, which does not provide a reliable means to estimate an "infinite population mean (μ)". From these small sets of data, an experimenter can estimate statistical parameters to approximate what would have been observed for a large data set by applying Student's t-value for low values of n.[120]

Each analytical measurement has two components: the analyte signal and the noise signal.[71] Noise is impossible to eliminate but can be controlled or minimized by several methods, such as ensemble averaging (i.e., simple arithmetic "smoothing"). Noise is typically quantified as the estimate of the standard deviation (s) for a series of replicate measurements. The relative standard deviation (RSD) is the ratio of s to <x>, where <x> is the estimate of the true mean (μ), often expressed as percentage RSD as shown below in Equation 16:

$$\%\boldsymbol{RSD} = \left(\frac{s}{<x>}\right) * \mathbf{100} \qquad [16]$$

The reciprocal of the RSD is the signal-to-noise ratio (S/N). S/N is a commonly used measure of the quality of an analytical measurement. As a common rule, the S/N ratio must be greater than 3 to discriminate a true signal from the noise with confidence, where 3*s is equal to 99.3% of a Gaussian distribution.[120] Thus, for an acceptable S:N value, the RSD should be < 33%. As can be seen from Table 48, the RSD values are less than 33% for the BCR-GF-AAS method used with the soil samples. The slope for BCR step 3 (MOX) and step 4 (ORG) for Cu (Table 48) routinely had a 40% or more decrease in sensitivity, while the y-axis intercept had a ~50% increase (steps 3 & 4). The cause of this loss of sensitivity and observed increase is unknown but apparently "matrix effects" are at work.

The MDL for Pb increased roughly a factor of 6 and 13 from the EXΔ and CO3 to the ORG step, respectively (Table 49). In addition, the MOX step had a relatively poor slope compared to the rest. Because each BCR step uses different conditions, these discrepancies are not unexpected; a matrix effect of unknown mechanism is probably again at work.

Table 48. Analytical figures of merit for the determination of Cu in the different BCR extracts.

| Parameter | EXΔ-[Cu] | CO3-[Cu] | MOX-[Cu] | ORG-[Cu] |
|---|---|---|---|---|
| MDL/ng $g^{-1}$ | 0.73 | 0.88 | 0.39 | 1.54 |
| Number of measurements | 10 | 10 | 10 | 10 |
| Slope | 0.0044 | 0.0041 | 0.0025 | 0.0028 |
| Y-Axis Intercept | 0.0056 | 0.0057 | 0.0113 | 0.019 |
| <x> for blanks | 0.005 | 0.005 | 0.007 | 0.013 |
| s for blanks | 0.001 | 0.001 | 0.002 | 0.003 |
| % RSD | 31.86 | 25.24 | 25.97 | 26.89 |

Table 49. Analytical figures of merit for the determination of Pb in the different BCR extracts.

| Parameter | EXΔ-[Pb] | CO3-[Pb] | MOX-[Pb] | ORG-[Pb] |
|---|---|---|---|---|
| MDL/ng $g^{-1}$ | 0.43 | 0.25 | 1.97 | 3.20 |
| Number of measurements | 10 | 10 | 10 | 10 |
| Slope | 0.0044 | 0.0022 | 0.0008 | 0.0015 |
| Y-Axis Intercept | 0.0031 | 0.0092 | 0.0069 | 0.0055 |
| <x> for blanks | 0.004 | 0.006 | 0.005 | 0.006 |
| s for blanks | 0.001 | 0.001 | 0.001 | 0.002 |
| RSD/% | 24.64 | 26.07 | 27.50 | 26.71 |

Table 50. Analytical figures of merit for the determination of Hg by ICP-MS using the different MAE extraction methods.

| Parameter | MAE BCR ICP-MS |
|---|---|
| MDL/ng $g^{-1}$ | 1.977E-03 |
| Number of measurements | 6 |
| Slope | 5.507 |
| Y-Axis Intercept | 6.097E-03 |
| <x> for blanks | 8.250E-03 |
| s for blanks | 8.803E-04 |
| RSD/% | 10.67 |